



저작자표시-비영리-동일조건변경허락 2.0 대한민국

이용자는 아래의 조건을 따르는 경우에 한하여 자유롭게

- 이 저작물을 복제, 배포, 전송, 전시, 공연 및 방송할 수 있습니다.
- 이차적 저작물을 작성할 수 있습니다.

다음과 같은 조건을 따라야 합니다:



저작자표시. 귀하는 원저작자를 표시하여야 합니다.



비영리. 귀하는 이 저작물을 영리 목적으로 이용할 수 없습니다.



동일조건변경허락. 귀하가 이 저작물을 개작, 변형 또는 가공했을 경우에는, 이 저작물과 동일한 이용허락조건하에서만 배포할 수 있습니다.

- 귀하는, 이 저작물의 재이용이나 배포의 경우, 이 저작물에 적용된 이용허락조건을 명확하게 나타내어야 합니다.
- 저작권자로부터 별도의 허가를 받으면 이러한 조건들은 적용되지 않습니다.

저작권법에 따른 이용자의 권리는 위의 내용에 의하여 영향을 받지 않습니다.

이것은 [이용허락규약\(Legal Code\)](#)을 이해하기 쉽게 요약한 것입니다.

[Disclaimer](#)

理學博士 學位論文

多 帶域 스펙트럼을 放出하는 白色 LED 應用을 위한 混合
소스 HVPE-III-nitride 物質의 研究

Study of the III-nitride materials grown by mixed-source HVPE
for white LED applications emitting multi spectrum range

指導教授 安 亨 洙

2008年 8月

韓國海洋大學校 大學院

應用科學科

黃 善 領

本 論 文 을 黃 善 領 의
理 學 博 士 學 位 論 文 으 로 認 准 함 .

委 員 長 이 삼 녕 印

委 員 심 준 환 印

委 員 장 지 호 印

委 員 하 홍 주 印

委 員 안 형 수 印

2008年 8月

韓 國 海 洋 大 學 校 大 學 院

應 用 科 學 科

TABLE OF CONTENTS

Abstract

Chapter 1. Introduction	1
1.1. Overview of LED	1
1.2. Wide bandgap compound semiconductor	6
1.3. Overview of white LED	10
1.4. Purpose and outline of this project	15
Chapter 2. Fundamentals of Gallium Nitride	21
2.1. Introduction	21
2.1.1. Current Issues in GaN-based LED	23
2.2. Crystallography of Gallium Nitride	26
2.3. Characteristics of Gallium Nitride	32
2.3.1. Doping of Gallium Nitride	33
2.3.2. Optical Properties of Gallium Nitride	35
2.3.3. Polarity in Gallium Nitride	38
2.4. Substrates for GaN Epitaxial Growth	40
2.4.1. Substrate issues	40
2.4.2. Sapphire	41
2.4.3. SiC	45
Chapter 3. Overview of Epitaxial Growth Experimental	57
3.1. Hydride vapor phase epitaxy	57
3.1.1. Introduction to HVPE	57
3.1.2. Mixed source HVPE system	59
3.1.3. Some parameters for optimized GaN growth	62
3.2. Wafer fabrication process	63
3.2.1. Selective area growth	63
3.2.2. Metallization of GaN	64
3.3. Measurements	66
3.3.1. Photoluminescence	66

3.3.2. DXRD	67
3.3.3. SEM/CL	70
3.3.4. E-CV	75
3.3.5. Hall measurement	77
Chapter 4. Mixed Source HVPE Growth Experiment for Bulk Characteristics	82
4.1. GaN growth	82
4.1.1 Buffer growth for GaN layer	83
4.1.2. Mg-doped GaN layer	87
4.2. AlGa _N growth	90
4.3. InGa _N growth	97
Chapter 5. Fabrication of AlInGa_N-Based LED for White Emission	115
5.1. AlInGa _N SAG-DH structure growth	115
5.2. Characterization of AlInGa _N SAG-DH epitaxial structure	123
5.3. Device fabrication	127
Chapter 6. Experimental Results for Active layer's Condition	135
6.1. Performance of AlInGa _N white LED	136
6.2. EL characteristics of AlGa _N and AlInGa _N active	139
6.2.1 GaN active layer	139
6.2.2 Al(0.1g)Ga _N active layer	141
6.2.3 Al(0.3g)Ga _N active layer	144
6.2.4 Al(0.4g)Ga _N active layer	144
6.2.5 Al(0.5g)Ga _N active layer	146
6.2.6 Al(0.6g)Ga _N active layer	149
6.2.7 In(0.1g) Al(0.6g) Ga _N active layer	151
6.2.8 In(0.2g)Al(0.6g)Ga _N active layer	153
6.2.9 In(0.3g)Al(0.6g)Ga _N active layer	155
6.2.10 In(0.4g)Al(0.6g)Ga _N active layer	158
6.2.11 In(0.5g)Al(0.6g)Ga _N active layer	160
6.3. XRD characteristics	163
Chapter 7. Phosphor –Free White LED Lamp	180

<i>7.1. Manufacturing of white LED lamp</i>	180
<i>7.2. Analysis of White LED Spectra and Color Rendering</i>	181
<i>7.3. Measurement of Phosphor free white LED</i>	289
<i>7.4. Future research</i>	297
Chapter 8. Conclusions	200
Publications	202
Conference	204
Biography	209
Acknowledgements	210

List of Figures

<i>Fig.1.1 CIE Chromatic Diagram.....</i>	<i>3</i>
<i>Fig.1.2 Luminous efficiency of light sources.....</i>	<i>5</i>
<i>Fig.1.3 Energy bandgap versus lattice-constant diagram for wurzite nitride semiconductors.....</i>	<i>7</i>
<i>Fig.1.4 Quantum efficiency of compound semiconductors.....</i>	<i>9</i>
<i>Fig.1.5 Evolution of light sources.....</i>	<i>14</i>
<i>Fig.2.1 E-k diagram of gallium nitride.....</i>	<i>27</i>
<i>Fig.2.2 The unit cell of Zinc blende (a = 3.19 Å, c= 5.19 Å).....</i>	<i>28</i>
<i>Fig.2.3 Band structure of zinc blende(cubic) GaN.....</i>	<i>28</i>
<i>Fig.2.4 The unit cell of wurtzite (a = 3.19 Å, c= 5.19 Å).....</i>	<i>30</i>
<i>Fig.2.5 Band structure of zinc wurtzite GaN.....</i>	<i>30</i>
<i>Fig.2.6 Band offsets at nitride semiconductors.....</i>	<i>31</i>
<i>Fig.2.7 Zinc-blende/wurtzite band offsets.....</i>	<i>31</i>
<i>Fig.2.8 Moving away of oxygen atom.....</i>	<i>32</i>
<i>Fig.2.9 (a) GaN, Wurtzite. Band gap energy versus temperature (b) GaN, Zinc Blende(cubic). The Band gap energy versus temperature.....</i>	<i>36</i>
<i>Fig.2.10 The wurtzite-GaN crystal structure showing inequivalent faces.....</i>	<i>39</i>
<i>Fig.2.11 Orientations of sapphire semiconductor substrates.....</i>	<i>41</i>
<i>Fig.2.12 Schematic illustration of GaN growth onto sapphire (0001) surface.....</i>	<i>44</i>
<i>Fig.3.1(a) Mixed Source HVPE system. (b) Schematic diagram of the MS-HVPE reactor.....</i>	<i>60</i>
<i>Fig.3.2 GaN growth by mixed source HVPE.....</i>	<i>61</i>
<i>Fig.3.3 Multi-sliding boat system of the mixed-source HVPE.....</i>	<i>61</i>
<i>Fig.3.4 (a) SAG Growth process on Si substrate. (b) SEM of SAG on Si substrate. (c) GaN SAG types by HVPE.....</i>	<i>63</i>
<i>Fig.3.5. (a) Schematic diagram of the PL measurement (b) Experimental setup of PL system in Lab.....</i>	<i>67</i>
<i>Fig.3.6 SEM/CL system in Lab.....</i>	<i>71</i>
<i>Fig.3.7 Schematic diagram of SEM system.....</i>	<i>73</i>
<i>Fig.3.8 Hall effect device.....</i>	<i>78</i>

<i>Fig.3.9 Hall Measurement in Lab</i>	80
<i>Fig.4.1 the 3D AFM images of GaN buffer layer by mixed source HVPE method</i>	84
<i>Fig.4.2 the RMS roughness of each samples of GaN buffer layer by mixed source HVPE method</i>	84
<i>Fig.4.3 PL measurement of each GaN buffer layer</i>	85
<i>Fig.4.4 the 3D AFM images of AlN buffer layer by mixed source HVPE method</i>	85
<i>Fig.4.5 the RMS roughness of each samples of AlN buffer layer by mixed source HVPE method</i>	86
<i>Fig.4.6 PL measurement of each GaN buffer layer</i>	86
<i>Fig.4.7 (a) The surface of GaN film by MS-HVPE (the Mg atomic fraction ; sample A ~0.026, sample B~0.057) (b) SEM image of cleaved facet of Mg-doped GaN film</i>	87
<i>Fig.4.8 XRD spectrum of Mg-doped GaN On sapphire by mixed source HVPE</i>	88
<i>Fig.4.9 AFM Images of Mg-doped GaN (scan area: $5 \times 5 \mu\text{m}^2$)</i>	88
<i>Fig.4.10 Hole Concentration and Mobility vs. atomic fraction of Mg</i>	89
<i>Fig.4.11 Temperature dependence of Hall measurement</i>	89
<i>Fig.4.12 (a) Typical XRD results of the $\text{Al}_x\text{Ga}_{1-x}\text{N}$ layers grown at source zone temperature of 900 °C. (b) Dependence of the Al composition of the $\text{Al}_x\text{Ga}_{1-x}\text{N}$ layer on source zone temperature</i>	94
<i>Fig.4.13 Typical SEM images of n-type $\text{Al}_{0.16}\text{Ga}_{0.84}\text{N}$ layers grown by mixed-source HVPE. (a) Te-doped $\text{Al}_{0.16}\text{Ga}_{0.84}\text{N}$ layer (b) Si-doped $\text{Al}_{0.16}\text{Ga}_{0.84}\text{N}$ layer</i>	95
<i>Fig.4.14 Dependence of the carrier concentrations of the n- $\text{Al}_{0.16}\text{Ga}_{0.84}\text{N}$ layers on the atomic fraction of Te (or Si). (a) Te-doped $\text{Al}_{0.16}\text{Ga}_{0.84}\text{N}$ layer (b) Si-doped $\text{Al}_{0.16}\text{Ga}_{0.84}\text{N}$ layer</i>	96
<i>Fig.4.15 EL spectra of LEDs of the two different cladding layers at room temperature. (a) SAG-Te-doped $\text{Al}_{0.38}\text{Ga}_{0.62}\text{N}$ cladding layer (b) SAG-Si-doped $\text{Al}_{0.38}\text{Ga}_{0.62}\text{N}$ cladding layer</i>	97
<i>Fig.4.16 CL spectrum of sample grown at 750 °C</i>	100
<i>Fig.4.17 InGaN phase shape on c-plane sapphire</i>	101
<i>Fig.4.18 InGaN phase shape on silicon substrate</i>	101
<i>Fig.4.19 InGaN phase shape on r-plane sapphire</i>	101
<i>Fig.4.20 AFM images of InGaN surfaces grown by mixed-source HVPE</i>	102
<i>Fig.4.21 RMS roughness of InGaN source zone temperature</i>	102
<i>Fig.4.22 Typical surface images of the InGaN layer grown on the GaN templated (111) Si</i>	

<i>substrates by mixed-source HVPE method.....</i>	<i>104</i>
<i>Fig.4.23 (a) Typical PL spectrum of the InGaN layer at 300 K. (b) PL spectrum of GaN templated Si (111) substrates at 300 K.....</i>	<i>105</i>
<i>Fig.4.24 (a) Cross-sectional SEM image, (b) Surface (the sample thickness of the GaN layers in (a) and (b) is 3.5 μm). (c) Cross-sectional SEM image, (d) Surface (the sample thickness of the GaN layer in (c) and (d) is 12 μm).....</i>	<i>106</i>
<i>Fig.4.25 (a) SEM image. The CL images measured at the peak wavelength of (b) 0 and (c) 362 nm at 230 K. Figs. (a), (b), and (c) are images of the GaN layer with 12 μm thickness.....</i>	<i>107</i>
<i>Fig.4.26 SEM images of hexagonal pyramid with height 5 μm obtained by 30 min growth.....</i>	<i>108</i>
<i>Fig.4.27 SEM image of thick InGaN alloy with thickness 12 μm obtained by 60 min growth.....</i>	<i>109</i>
<i>Fig.4.28 (a) XPS spectrum for the SAG-InGaN grown by mixed-source HVPE method. (b) Typical PL spectrum of InGaN.....</i>	<i>109</i>
<i>Fig.4.29 (a) SEM image. The CL intensity images of InGaN grown ($X_{Ga}^I = 0.25$) by mixed-source HVPE method measured at the peak wavelength of (b) 0 nm, (c) 360 nm, and (d) 380 nm at 230 K.....</i>	<i>110</i>
<i>Fig.5.1 Temperature profile of MS-HVPE.....</i>	<i>118</i>
<i>Fig. 5.2 The schematic structure of the AlInGaN/AlGaN DH Structure.....</i>	<i>123</i>
<i>Fig. 5.3 Characterization of Al_{0.16} GaN (a) Te Atomic fraction vs. Carrier concentration (b) Te Atomic fraction vs. Carrier mobility (c) Te Atomic fraction vs. Conductivity.....</i>	<i>123</i>
<i>Fig. 5.4 AES of Mg-doped Bulk Al_{0.16} GaN.....</i>	<i>124</i>
<i>Fig.5.5 TEM of Si-doped Bulk AlGaN (a) Non-optimized growth condition (b) Optimized growth condition.....</i>	<i>125</i>
<i>Fig.5.6 XPS of Si-doped Bulk AlGaN.....</i>	<i>125</i>
<i>Fig.5.7 XPS spectrum of the InAlGaN alloy.....</i>	<i>126</i>
<i>Fig.5.8 5 μm x 5 μm AFM image of InAlGaN layer grown by the mixed-source HVPE.....</i>	<i>126</i>
<i>Fig.5.9 Multi sliding boat system and mixed metal source in MS-HVPE for AlGaN/AlInGaN LED.....</i>	<i>127</i>
<i>Fig.5.10 Top-view image of the SAG-LED chip grown by mixed-source HVPE.....</i>	<i>133</i>
<i>Fig. 6.1 PL spectrum of the SAG-Al(In)GaN/InGaN DH structure.....</i>	<i>137</i>
<i>Fig.6.2 temperature dependance of PL peak for AlGaN/Al(In)GaN DH structure.....</i>	<i>138</i>

<i>Fig.6.3 (a) PL peak at low temperature at 10K (b) temperature dependance of PL peak for AlGa_N/Al(In)Ga_N DH layers.....</i>	<i>138</i>
<i>Fig.6.4. Injection current dependance of EL spectrum for DH structure with Ga_N active layer.....</i>	<i>139</i>
<i>Fig.6.5 Emitting light of DH structure with Ga_N active layer.....</i>	<i>140</i>
<i>Fig.6.6 Injection current dependance of EL (a) intensity and (b) FWHM.....</i>	<i>141</i>
<i>Fig.6.7. Injection current dependance of EL spectrum for DH structure with Al(0.1g)Ga_N active layer.....</i>	<i>141</i>
<i>Fig.6.8 Emitting light of DH structure with Al(0.1g)Ga_N active layer.....</i>	<i>143</i>
<i>Fig.6.9 Injection current dependance of EL (a) intensity and (b) FWHM.....</i>	<i>143</i>
<i>Fig.6.10 Injection current dependance of EL spectrum for DH structure with Al(0.4g)Ga_N active layer.....</i>	<i>144</i>
<i>Fig.6.11 Emitting light of DH structure with Al(0.4g)Ga_N active layer.....</i>	<i>145</i>
<i>Fig.6.12 Injection current dependance of EL (a) intensity and (b) FWHM.....</i>	<i>146</i>
<i>Fig.6.13 Injection current dependance of EL spectrum for DH structure with Al(0.5g)Ga_N active layer.....</i>	<i>147</i>
<i>Fig.6.14 Emitting light of DH structure with Al(0.5g)Ga_N active layer.....</i>	<i>148</i>
<i>Fig.6.15 Injection current dependance of EL (a) intensity and (b) FWHM.....</i>	<i>148</i>
<i>Fig.6.16 Injection current dependance of EL spectrum for DH structure with Al(0.6g)Ga_N active layer.....</i>	<i>149</i>
<i>Fig.6.17 Emitting light of DH structure with Al(0.6g)Ga_N active layer.....</i>	<i>150</i>
<i>Fig.6.18 Injection current dependance of EL (a) intensity and (b) FWHM.....</i>	<i>151</i>
<i>Fig.6.19 Injection current dependance of EL spectrum for DH structure with In(0.1g)Al(0.6g)Ga_N active layer.....</i>	<i>152</i>
<i>Fig.6.20 Emitting light of DH structure with In(0.1g)Al(0.6g)Ga_N active layer.....</i>	<i>153</i>
<i>Fig.6.21 Injection current dependance of EL (a) intensity and (b) FWHM.....</i>	<i>153</i>
<i>Fig.6.22 Injection current dependance of EL spectrum for DH structure with In(0.2g)Al(0.6g)Ga_N active layer.....</i>	<i>154</i>
<i>Fig.6.23 Emitting light of DH structure with In(0.2g)Al(0.6g)Ga_N active layer.....</i>	<i>155</i>
<i>Fig.6.24 Injection current dependance of EL (a) intensity and (b) FWHM.....</i>	<i>155</i>

<i>Fig.6.25 Injection current dependance of EL spectrum for DH structure with In(0.3g)Al(0.6g)GaN active layer.....</i>	<i>156</i>
<i>Fig.6.26 Emitting light of DH structure with In(0.3g)Al(0.6g)GaN active layer.....</i>	<i>157</i>
<i>Fig.6.27 Injection current dependance of EL (a) intensity and (b) FWHM.....</i>	<i>157</i>
<i>Fig.6.28 Injection current dependance of EL spectrum for DH structure with In(0.4g)Al(0.6g)GaN active layer.....</i>	<i>158</i>
<i>Fig.6.29 Emitting light of DH structure with In(0.4g)Al(0.6g)GaN active layer.....</i>	<i>159</i>
<i>Fig.6.30 Injection current dependance of EL (a) intensity and (b) FWHM.....</i>	<i>160</i>
<i>Fig.6.31 Injection current dependance of EL spectrum for DH structure with In(0.5g)Al(0.6g)GaN active layer.....</i>	<i>161</i>
<i>Fig.6.32 Emitting light of DH structure with In(0.5g)Al(0.6g)GaN active layer.....</i>	<i>162</i>
<i>Fig.6.33 Injection current dependance of EL (a) intensity and (b) FWHM.....</i>	<i>162</i>
<i>Fig.6.34 the relation between Al atomic fraction and Poisson's ratio.....</i>	<i>165</i>
<i>Fig.6.35 XRD measurement of AlGa_N layer at Al~0.0127(0.1g).....</i>	<i>166</i>
<i>Fig.6.36 XRD measurement of AlGa_N layer at Al~0.0373(0.3g).....</i>	<i>167</i>
<i>Fig.6.37 XRD measurement of AlGa_N layer at Al~0.0495(0.4g).....</i>	<i>168</i>
<i>Fig.6.38 XRD measurement of AlGa_N layer at Al~0.0607(0.5g).....</i>	<i>169</i>
<i>Fig.6.39 XRD measurement of AlGa_N layer at Al~0.0072(0.6g).....</i>	<i>170</i>
<i>Fig.6.40 The relation of Al atomic fraction and Al mole fraction in AlGa_N layer:</i>	<i>172</i>
<i>Fig.6.41 XRD measurement of AlInGa_N layer at Al~0.0072(0.6g).....</i>	<i>172</i>
<i>Fig.6.42 EL peak at room temperature 20mA of AlGa_N/AlInGa_N DH layers.....</i>	<i>173</i>
<i>Fig.6.43 EL peak as injection current of AlGa_N/AlInGa_N DH layers.....</i>	<i>174</i>
<i>Fig. 6.44. Emitting images at room temperature, 20mA of AlGa_N/AlInGa_N DH.....</i>	<i>174</i>
<i>Fig. 6.45 Wavelength distribution of each samples at I_f=25mA and I_f=30mA (a) AlGa_N active layer (b) InAlGa_N active layer.....</i>	<i>176</i>
<i>Fig. 6.46 Wavelength distribution of InAlGa_N active layer Vs. forward current from 5mA to 30mA.....</i>	<i>177</i>
<i>Fig. 6.47 Growth formation of conventional HVPE(a) and MS-HVPE(b).....</i>	<i>178</i>
<i>Fig. 6.48 CL measurement results of cross section of AlInGa_N DH.....</i>	<i>179</i>
<i>Fig. 7.1 Photopic vision of visual spectrum.....</i>	<i>181</i>

<i>Fig.7.2 Standard spectrum of blue, green, and purple and calculation of chromaticity coordinates.....</i>	<i>183</i>
<i>Fig.7.3 1931 CIE chromaticity coordinates and Black body curve.....</i>	<i>184</i>
<i>Fig.7.4 The eight specified reference source used in the calculation of Ra.....</i>	<i>185</i>
<i>Fig.7.5 Chromaticity Calculations of 1931 Coordinates (2Degree).....</i>	<i>190</i>
<i>Fig.7.6 Spectrum measurement results of phosphor free white LED lamp grown by MS-HVPE at If=30mA and If=50mA.....</i>	<i>191</i>
<i>Fig.7.7 Chromaticity coordinates variation of sample No. 1-1 from If=10mA to If=100mA.....</i>	<i>191</i>
<i>Fig.7.8 Spectrum measurement results of phosphor free white LED lamp grown by MS-HVPE at If=30mA.....</i>	<i>192</i>
<i>Fig.7.9 Chromaticity coordinates variation of sample No. 1-2 from If=10mA to If=100mA.....</i>	<i>192</i>
<i>Fig.7.10 Spectrum measurement results of phosphor free white LED lamp grown by MS-HVPE at If=30mA.....</i>	<i>193</i>
<i>Fig.7.11 Chromaticity coordinates variation of sample No. 2-1 from If=10mA to If=100mA.....</i>	<i>193</i>
<i>Fig.7.12 Chromaticity coordinates variation of Phosphor-converted LED.....</i>	<i>196</i>
<i>Fig.7.13 Chromaticity coordinates variation of Phosphor-free LED.....</i>	<i>196</i>
<i>Fig.7.14 White emission of Phosphor-free LED Lamp.....</i>	<i>197</i>

List of Tables

<i>Table.2.1 GaN Parameters</i>	37
<i>Table.2.2 Physical property of sapphire</i>	43
<i>Table.2.3 Physical property of SiC</i>	46
<i>Table 4.1 Growth conditions of samples</i>	99
<i>Table.5.1 SAG-DH Growth parameters</i>	116
<i>Table.5.2 Experimental conditions and results of SAG-DH growth</i>	119
<i>Table.5.3 AlInGaN/AlGaN SAG-LED making process</i>	129
<i>Table.6.1. Injection current dependance of GaN EL spectrum</i>	140
<i>Table.6.2. Injection current dependance of Al(0.1g)GaN EL spectrum</i>	142
<i>Table.6.3. Injection current dependance of Al(0.4g)GaN EL spectrum</i>	145
<i>Table.6.4. Injection current dependance of Al(0.5g)GaN EL spectrum</i>	147
<i>Table.6.5. Injection current dependance of Al(0.6g)GaN EL spectrum</i>	150
<i>Table.6.6. Injection current dependance of In(0.1g)Al(0.6g)GaN EL spectrum</i>	152
<i>Table.6.7. Injection current dependance of In(0.2g)Al(0.6g)GaN EL spectrum</i>	154
<i>Table.6.8. Injection current dependance of In(0.3g)Al(0.6g)GaN EL spectrum</i>	156
<i>Table.6.9. Injection current dependance of In(0.4g)Al(0.6g)GaN EL spectrum</i>	159
<i>Table.6.10 Injection current dependance of In(0.5g)Al(0.6g)GaN EL spectrum</i>	161
<i>Table.6.11 The relation of Al atomic fraction and Al mole fraction in AlGaN layer</i>	171
<i>Table.7.1. Chromaticity measurement (1931 Coordinates) results of phosphor free white LED lamp grown by MS-HVPE at $I_f=30mA$</i>	190

Study of the III-nitride materials grown by mixed-source HVPE for white LED applications emitting multi spectrum range

Sun-Lyeong Hwang

Major in Applied Sciences

Graduate School, Korea Maritime University

Supervised by Professor Hyung-Soo Ahn

Abstract

The purpose of this study is to explore the possibility of phosphor-free white-emitting LED's based in the gallium nitride material system. The structures are to be grown using mixed source hydride vapor phase epitaxy (MS-HVPE). It is unique crystal growth technology different from conventional HVPE and MOCVD system using mixed metal source of aluminum, indium and gallium.

The first step in this project is the optimization of MS-HVPE growth process. This was achieved successfully, as binary, ternary and quaternary films are demonstrated. Successful n and p-type doping are also demonstrated introducing Te and Mg.

The second step in this project is fabricating broadband spectrum emitting device of phosphor-free white LED by MS-HVPE. The device structure consisted of conventional double-hetero (DH) structure, which was the undoped InAlGa_N active layer and n, p-AlGa_N cladding layers. We observed that the device of AlInGa_N quaternary active grown by MS-HVPE emitted multi spectrum from UV to red area. We also found that its spectrum was variable as indium mole

fraction and controllable. It was nano phase epitaxy phenomenon being only observed in HS-HVPE process. An extensive growth study of GaN based material was also carried out. The effects of several growth parameters on emission characteristics were presented. PL emission wavelengths for each structure were demonstrated. And EL emission wavelengths were also demonstrated after wafer fabrication process. Additionally, x-ray diffraction and x-ray photoelectron spectroscopy (XPS) showed to verify crystal quality of MS-HVPE.

The dissertation presented herein demonstrates achieving phosphor-free solid-state white lighting. But it still has unknown physical characteristics. Continuation of this study will lead to future industry. And hopefully it will be commercialized and applied to residential illumination due to this technology.

Chapter 1.

Introduction

1.1. Overview of LED

Optoelectronic materials and physics represent a deep and broad foundation of knowledge that has an impact on a wide range of important areas of science and technology. Solid-state lighting such as LED is among the most recent of these areas, emerging as a concept only in the past decade, with the sudden development in the mid-1990s of blue and green light-emitting diodes (LEDs) [Nakamura et al. 1994], and with the increase in brightness of red LEDs to the extent of being applied to outdoor applications, such as traffic lights. An important example of the broader impact of the foundational science and technology is the use of heterostructures in optoelectronic and electronic devices. A semiconductor heterostructure consists of two or more layers with different energy bandgaps, formed by changing the composition of the material.

LEDs are p-n junction devices composed of gallium arsenide (GaAs), gallium nitride (GaN), gallium arsenide phosphide (GaAsP), or gallium phosphide (GaP). Silicon and germanium are not suitable because those junctions produce heat and no appreciable IR or visible light. The junction in an LED is forward biased and when electrons cross the junction from the n-type to the p-type material, the electron-hole recombination process produces some photons in the IR or visible range in a process called electroluminescence.

An exposed semiconductor surface can then emit light. When the applied forward voltage on the diode of the LED drives the electrons and holes into the active region between the n-type and p-type material, the energy can be converted into infrared or visible photons. This implies that the electron-hole pair drops into a more stable bound state, releasing energy on the order of electron

volts by emission of a photon. The red extreme of the visible spectrum, near 700 nm, requires an energy release of 1.77 eV to provide the quantum energy of the photon. At the other extreme, 400 nm in the violet, 3.1 eV is required. LEDs are also small extended sources with extra optics added to the chip, which emit a complex intensity spatial distribution [1].

The color of the emitted light depends on the composition and condition of the semiconductor material used, and can be infrared, visible or near-ultraviolet. Rubin Braunstein of the Radio Corporation of America first reported on infrared emission from gallium arsenide (GaAs) and other semiconductor alloys in 1955. Experimenters at Texas Instruments, Bob Biard and Gary Pittman, found in 1961 that gallium arsenide gave off infrared (invisible) light when electric current was applied. Biard and Pittman were able to establish the priority of their work and received the patent for the infrared light-emitting diode. Nick Holonyak Jr. of the General Electric Company developed the first practical visible-spectrum LED made of a compound semiconductor alloy, gallium arsenide phosphide in 1962, which emitted red light. From 1962, compound semiconductors would provide the foundation for the commercial expansion of LEDs. Holonyak's former graduate student, Dr. M. George Craford, invented in 1972 the first yellow LED and 10x brighter red and red-orange LEDs [1]. LED luminous output has been following Haitz's Law doubling every 18–24 months for the past 35 years. The first LEDs became commercially available in the 1970s, and were almost all red. From 1968 when the first commercial LEDs were introduced at 0.001 lm/LED using GaAsP until the mid-1990s commercial LEDs were used exclusively as indicators. In addition to energy savings, LED lifetime and robustness provides lower cost of ownership due to reduction or elimination of source replacement costs. LED white emission is most efficiently generated by mixing light from red, green and blue LEDs. In terms of the number of LEDs sold, indicators and other small signal applications in 2002 still consume the largest volume of LEDs, with the annual global consumption exceeding several LEDs per person on the planet.

The development of AlGaAs LEDs grown on GaAs substrates and employing fully lattice-matched direct bandgap systems and hetero-structure active regions allowed these early red LEDs to exceed the luminous efficiency of a red-filtered incandescent bulb [2]. Efficiency was further doubled by the use of transparent substrate devices [3]. The luminous efficiency of monochromatic LED lamps improved to match and exceed conventional incandescent and halogen sources. More recently, the development of large area “flip-chip” die, and improved package design have resulted in individual red, amber, green, and white LED lamps with flux exceeding 100 lumens, and blue LED lamps with the optical power of greater than 1W.

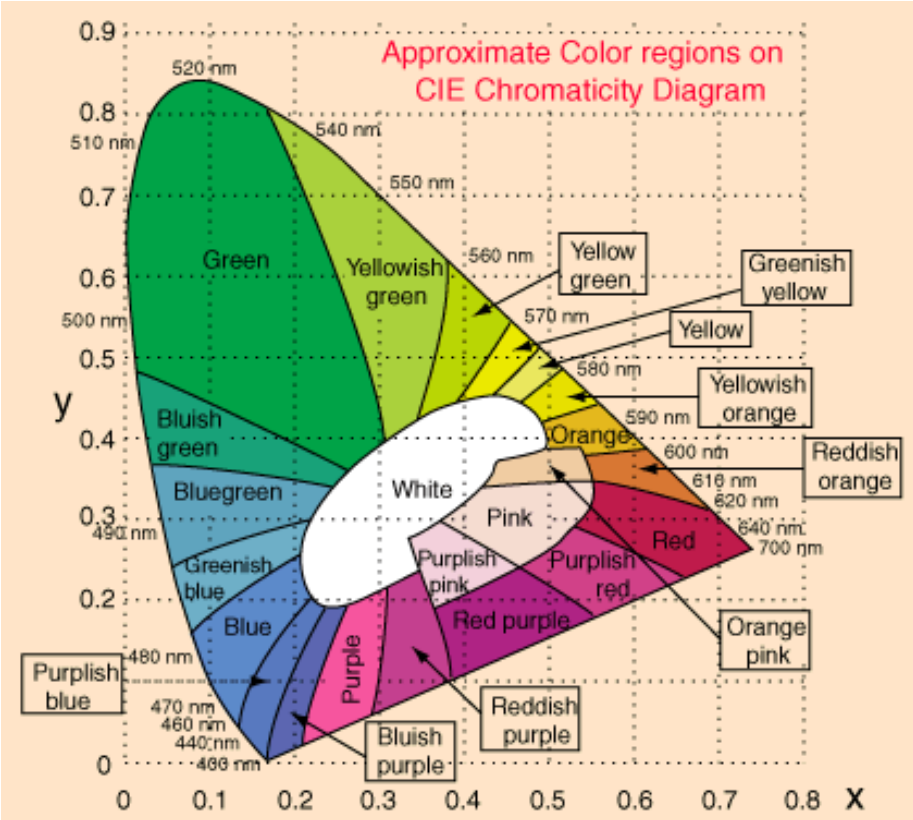


Fig.1.1 CIE Chromatic Diagram

The development of metallic organic vapor phase epitaxy (MOVPE) crystal growth techniques enabled us to introduce a new material system, AlGaInP on GaAs. AlInGaP resulted in the fabrication of high-brightness materials from yellow to red [4]. AlInGaP material system allows the creation of light in the red and amber regions of the spectrum. Alloy ordering, hydrogen passivation of acceptor atoms [5], p–n junction placement and oxygen incorporation into the aluminum-containing semiconductor layers proved to be substantial challenges that required nearly a decade of work to resolve [6]. The result was AlInGaP LEDs with internal quantum efficiencies approaching 100%; nearly every electron and hole pair injected into the device resulted in the creation of a photon. The problem was then how to get the photons that had been generated inside the semiconductor LED out into the world outside the semiconductor where they could be used. The first hurdle was to prevent light from being absorbed in the narrow bandgap (eV nm) GaAs substrate. Techniques such as incorporation in the epitaxial structure of Bragg mirrors, and direct growth on GaP have been tried, but the most successful technique was the removal of the GaAs substrate by etching and replacing GaAs with transparent GaP by wafer bonding. At 25 lm/W efficiency, nearly ten times the efficiency of a red filtered light bulb, and several lumens per LED, these LEDs enabled the first LED stop lights on automobiles, LED red traffic signals, and single color outdoor signs. But 3 lm/LED uses were still limited to those applications where the user was expected to look directly at the LED. Following closely behind the commercialization of AlInGaP, two groups, Shuji Nakamura at Nichia Chemical [7] and Prof. Akasaki and Prof. Amano [8] at Nagoya University and later Meijo University were mastering the complex OMVPE growth process of aluminum indium gallium nitride on sapphire substrates using atmospheric-pressure OMVPE. The AlInGaP material system has a wider bandgap than AlInGaP and allows access to the higher energy green, blue, and UV parts of the color spectrum. As it has been found in AlInGaP, alloy clustering, hydrogen passivation of acceptor atoms [9], p–n junction placement and oxygen

incorporation into the aluminum-containing semiconductor layers proved to be substantial challenges. After a decade of intense research, a bright blue LED was successfully produced by Nichia Chemical of Japan in 1994. The material used for the diode was gallium nitride GaN. Nichia has also produced an InGaN laser diode that lasers in the blue-violet region of the spectrum. The AlInGaN material system is not as well understood as the AlInGaP material system, and today internal quantum efficiencies at typical operating current densities for AlInGaN green devices hover around 20–40 % with blue devices operating in the 40–60 % range. Nevertheless, by taking advantage of the transparent sapphire substrate and the human eye’s greater sensitivity to green light than to either blue or red, Nichia Chemical, Lumileds and others have been able to introduce multilumen green LEDs that together with multilumen red AlInGaP and 1 lumen blue LEDs enables large full color signs to be made entirely from solid state light sources.

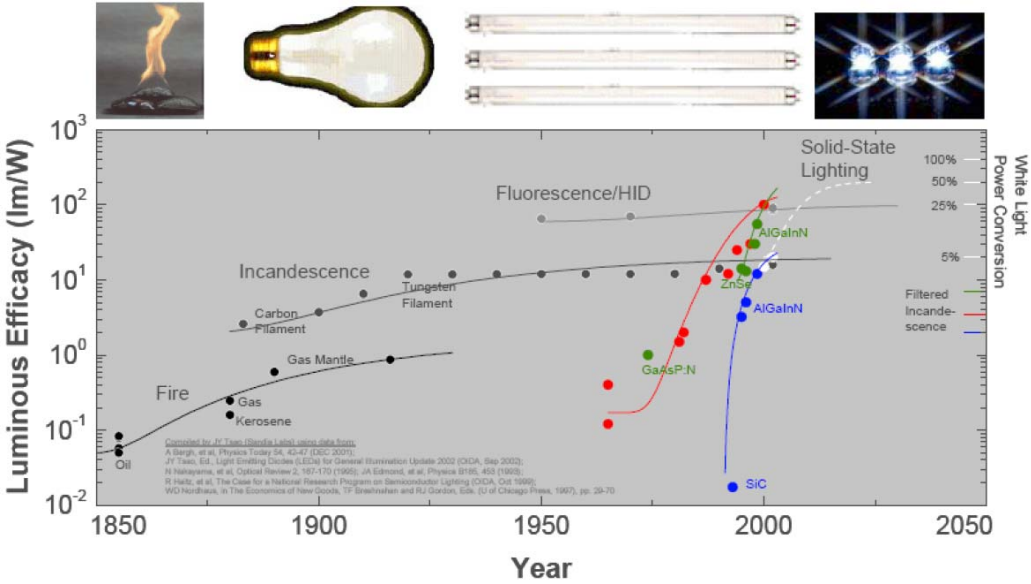


Fig.1.2 Luminous efficiency of light sources
 (IEEE Circuit & Devices Vol 20 No 3 pp 28-37 May/June 2004)

They were commonly used as replacements for incandescent indicators, and in seven-segment displays, first in expensive equipment such as laboratory and electronics test equipment, then later in such appliances as TVs, radios, telephones, calculators, and even watches. These red LEDs were bright enough only to be used as indicators, as the light output was not enough to illuminate an area. Later, other colors became widely available and also appeared in appliances and equipment. As the LED chemistry became more advanced, the light output was increased, and LEDs became bright enough to be used for illumination

Blue LEDs are important for the development of high-information-density storage on optical disks, as well as a host of other applications such as high-resolution television and computer displays, image scanners and color printers, biomedical diagnostic instruments, and remote sensing. Along with the high brightness blue LEDs, white LEDs that use high energy blue photons from a blue AlInGaN LED, and incorporate a phosphor to convert some of the blue photons into yellow, the complementary color to blue, have emerged. The human eye perceives this combination of blue and yellow light as a white light. Finally, 30 years after the introduction of the first commercial LED in 1968 the stage has been set for some new thinking.

1.2. Wide bandgap compound semiconductor

Gallium nitride is a direct, wide bandgap semiconductor that has been intensively investigated and has achieved practical success in optoelectronic devices like green-blue LEDs (Light Emitting Diodes) and the blue laser [10,11].

They are also widely used in many application fields such as optical displays, optical information processing systems, optical sources, and optical detectors. Materials advances in GaN have also had significant impact on high-power, high frequency electronics. III-nitride, AlN, GaN, InN, and their alloys, AlGaN, GaInN, and AlGaInN, are very promising materials for fabricating

blue-green light optoelectrical devices, especially light-emitting diodes (LEDs), laser diodes (LDs) and detectors, because they possess large direct band gap energy from 1.9 eV to 6.2 eV, corresponding to the spectral range from visible to ultraviolet.

This family of materials has direct bandgaps that span a tremendous range of energies, enabling light emission from the near infrared to the deep-ultraviolet region of the spectrum. Nitride-based LEDs employ light emission from $\text{In}_x\text{Ga}_{1-x}\text{N}$ quantum wells (QWs) with $\text{In}_y\text{Ga}_{1-y}\text{N}$ or GaN barriers. Emission wavelengths of these LEDs can be tuned across the entire visible spectrum (see Fig.1.3) by varying the indium composition of the QW. Other structural parameters, such as the thickness of the QW and barrier layers, in addition to the strain and piezoelectric fields of the QW, can also affect the emission wavelength. To date, the most efficient InGaN LEDs emit in the near-UV to blue region, using QWs with relatively low indium compositions. LEDs with higher indium compositions emit at green and longer wavelengths, but have significantly lower efficiencies.

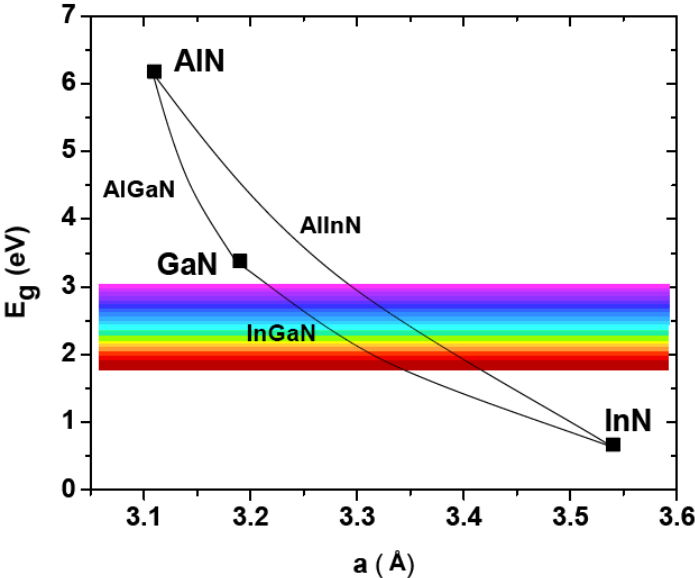


Fig.1.3 Energy bandgap versus lattice-constant diagram for wurzite nitride semiconductors [12].

While the origin of this reduced efficiency is not well understood, it is speculated to arise from the complex interplay of a range of material properties, including localized variation in composition, high defect densities, and the presence of strong piezoelectric fields. Achieving high-efficiency emission across the entire visible region with InGaN alloys is one of the fundamental challenges for LED application. The realization of full-spectrum capability from a single semiconductor alloy family would provide substantial benefit for future SSL architectures and may ultimately be achieved using InGaN alloys.

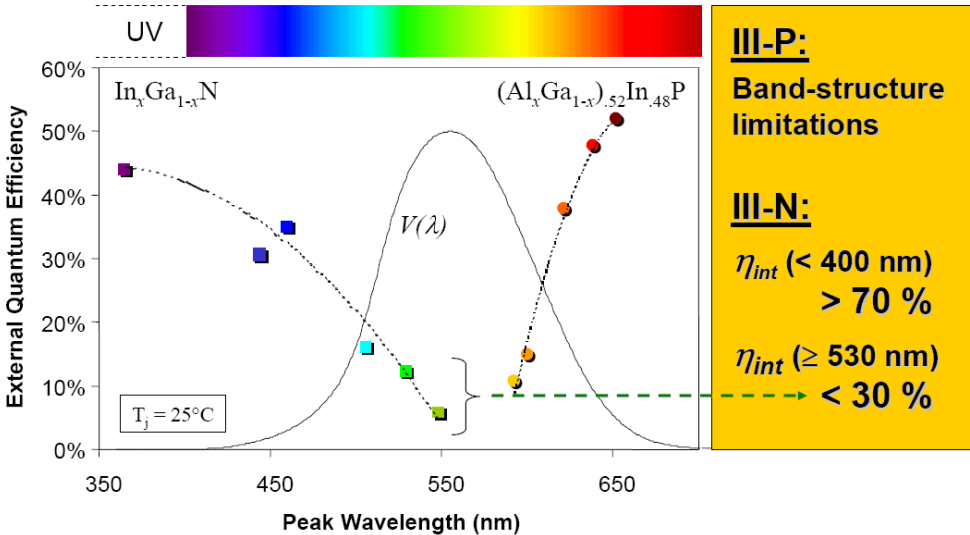
In general, the use of heterostructures allows the energy and flow of electrons in a device to be controlled in a sophisticated manner unobtainable in a single material. Materials advances in GaN have also had significant impact on high-power, high frequency electronics. The electron saturation velocity in GaN is high, and since the bandgap is large, the breakdown voltage of the material is also very high. As a result, these high-power, high frequency transistors are being introduced in state-of-the-art radar systems to replace the large, heavy tube sources used in the past. GaN transistors can also operate in high-temperature environments, where electronics made from conventional materials cannot reliably perform.

Blue LEDs and Lasers based on GaN semiconductor compounds represent one of the most important breakthroughs in electronics and opto-electronics of recent years. GaN based LEDs have started to replace traditional light bulbs in traffic lights and are likely to gain an ever increasing market share for many other lighting applications. GaN based blue lasers allow data storage with much higher density than traditional red lasers. In addition, there are many less obvious applications in medical fields including diagnostics and other areas.

Despite its commercial success, many of the physical properties of GaN and its growth mechanism are still not well known. Usually GaN is grown on highly mismatched substrates like sapphire and silicon carbide using thin, low temperature, polycrystalline AlN or GaN buffer layers

[13,14]. A buffer layer gives dense nucleation on the substrate surface, but introduces strong disorder in the first hundred nanometers and a high density of dislocations in the final film [15]. The difference between the thermal expansion coefficient of the substrate and the film introduces stress during the cooling after the growth. This stress may cause additional dislocations.

Most papers dedicated to GaN heteroepitaxy describe the influence of the buffer layer on properties of the final film. The most important conclusion of these works is that the best film morphology can be obtained by using the thinnest possible buffer layer [14]. This approach is useful, but it does not explain the nature of the defects influencing the quality of the film. For example, the nature of electrically active defects supplying free electrons and defects influencing the electron mobility is still unknown.



(Copyright© Lumileds Lighting LLC)

Fig.1.4 Quantum efficiency of compound semiconductors

Since the first GaN epilayers were grown on sapphire substrates in 1971 [16], various techniques have been applied to optimize the quality of the resulting films, such as nitridation [17] of the substrate, or the growth of a low temperature AlN [18] or GaN buffer layer [19]. Recently significant advances in GaN blue LEDs and LDs technology have been made after the reducing of the background electron concentration and the achievement of the p-GaN since high-brightness blue LEDs were obtained in 1994 [20].

1.3. Overview of white LED

Illumination means white light, and a very particular kind of white light at that. Having evolved under a black body emitter, the sun, with a correlated color temperature (CCT) in the 3000 K–6500 K range depending on time of the day, weather and season, the human eye is quite sensitive to small changes in spectral content of illumination sources. The Planckian locus on the CIE diagram is scaled in Kelvin, denoting the CCT describing the color of a black body source. Sensitivity to color change is a function of location on the CIE curve. Near 3000 K–4000 K where incandescent bulbs and halogen lamps operate typical humans can detect changes in CCT on the order of K–100 K. Multiple illumination sources visible at the same time must therefore have CCTs that are the same to within K–100 K and chromaticity coordinates lying very near the black curve. However, this is still insufficient. Even though a white light source may have color coordinates close to the black body curve, the source may not render true colors when used to illuminate an object. If the wavelengths reflected by a surface are absent in the source, then the surface will appear dark or gray, not colored. Upon reflection or transmission, spectrally incomplete sources will produce less vivid color quality than those with a more complete spectrum. The ability of an illumination source to render true colors is determined by measuring the color rendering index, Ra, scaled 0 to 100 [21]. The noon-day sun, incandescent lamps and other near black body radiators have Ras of near 100.

Fluorescent lamps with choppy emission spectra have lower Ra in the 75–90 range which explains why most people would prefer to see their own reflections when illuminated with incandescent rather than fluorescent lights. Before LEDs can be seriously considered to be sources of “illumination”, CCT variations within a lamp and from lamp to lamp must be homogeneous to within 50 K–100 K, and Ra . There are three general approaches to generate white light from LEDs. The first method directly mixes light from three (or more) monochromatic sources, red, green and blue (RGB), to produce a white source matching with the RGB sensors in the human eye. The second technique uses a blue LED to pump one or more visible light-emitting phosphors integrated into the phosphor-converted LED (pc-LED) package. The pc-LED is designed to leak some of the blue light beyond the phosphor to generate the blue portion of the spectrum, while phosphor converts the remainder of the blue light into the red and green portions of the spectrum. The third technique uses an ultraviolet LED to pump a combination of red, green and blue phosphors in such a way that none of the pump LED light is allowed to escape. Each of these approaches has potential advantages and clear technical challenges.

The most straightforward technique mixes the emission from at least three different colored LEDs. A three-colored (RGB) LED array will be perceived as a color within the triangle depending upon the relative luminance balance of the sources. Properly balanced, the array can produce any particular point within the triangle and in particular along the Planckian black body curve. In more sophisticated versions, onboard electronics adjust the individual drive currents to change the CCT at will [22], or to maintain the color point as each source ages over the life of the array or changes with the ambient temperature. RGB mixing is the most efficient way to make white light from LEDs since there is no quantum deficit (arising from the Stokes shift characteristic of photonic energy down-conversion of the phosphor [23]), and offers infinitely graduated color and white point control. Efficiencies for state of the art devices are in the 30–40 lm/W. Color rendering can be

excellent, 95, but CCT is controlled dynamically by an external detector plus feedback system. For specialized applications such as LCD backlighting or projection images, and applications requiring dynamic color control, RGB mixing is the preferred choice.

By far the most common LED-based white light source is the pc-LED used in a configuration with a blue LED and a complimentary yellow phosphor. The blue LED is used to pump a yellow emitting phosphor integrated into the LED package. Inherently less efficient than an RGB source, simple white sources are made. The phosphor density and thickness are chosen to leak a predetermined fraction of the blue light.

Mixed with phosphor the resulting yellow emission, white light emits. Striking the correct blue/yellow ratio depends upon having the correct amount, density, and particle size of phosphor, distributed evenly around the blue-emitting chip. Variations in any of these parameters will give rise to color or CCT variations at different viewing angles from a single lamp, or between adjacent LED lamps. First generation white pc-LEDs are made by depositing in measured quantities of a slurry mixture of phosphor and epoxy within a containment cup surrounding the pump die during the encapsulation step. Several factors inhibit process uniformity, including the difficulty of measuring precise small quantities of a viscous fluid, slurry settling both before and after dispensing, distribution of the mixture within the cup, and phosphor powder grain size variations. To illustrate typical variations, the circles in Fig.1.1 illustrate typical CCT control within a single LED radiation pattern (viewing angle) using a first generation slurry deposited pc-LED to be very large, K, or 8–16 times the human detectable difference. The triangles indicate results from a second-generation phosphor deposition process developed in which a conformal layer of phosphor is deposited only around the die. In this case, variation within a single LED radiation pattern drops to 80 K, fully 10 times better than first generation pc-LED technology. In effect, the flip-chip LED with the conformal layer of phosphor act as a white light-emitting die.

The conformal deposition process also improves LED to LED color variation. To demonstrate, examine the color locus created from combining a 470 nm pump LED and a 575 nm emitting phosphor as showing the dark tie line. This line crosses the Planckian at a color temperature of 5000 K. Small variations in phosphor thickness, grain size and efficiency create lamps spanning a range large compared to the 50–100 K minimum detectable CCT difference. The Ra for the single phosphor pc-LED is low due to the lack of spectral content in the red. By employing two phosphors, covering a broader emission range, the two-phosphor pc-LED rises to Ra, well above acceptable levels for most illumination. The pc-LED technique with state-of-the art material gives luminous efficacy performance in the 25–30 lm/W. Recently, there has been renewed interest in creating a white source using a UV-emitting LED to pump a trio of RGB-emitting phosphors, the UV-LED. The UV light is completely adsorbed by the phosphors, and the mixed RGB output appears white much the same as an RGB mixed LED array. The quantum deficit between the UV pump and the phosphors, especially the low-energy red phosphor, dissipates significant energy and makes this approach inherently less efficient than either the RGB or the pc-LED schemes for generating white light. Scattering and absorption losses in the package are also considered. The result indicates that an UV-LED must be more than twice the wall plug efficiency of the green LED in an RBG solution in order to overcome packaging and Stokes' losses. Today, there are no ideal blue phosphors that emit efficiently in the 450~470 nm blue range while absorbing efficiently in the 400~430 nm pump range, so actual efficacy numbers are not yet available. The UV-LED approach has the advantage that color can be controlled by the phosphor mix at least at one point in time and at one temperature, so color rendering should be excellent. On the other hand, the high-energy UV light deteriorates the organic LED package materials, limiting the useful lifetime of the lamp. As of today, no UV-LED based RGB white products are in production. Though the basic tradeoffs between the three different approaches to making white LEDs are well established, the long-term winner is hard to

predict. Today most of the LEDs used to make white light are based on the pc-LED with a blue pump plus a single yellow phosphor. The best of these lamps are at least two orders of magnitude too high in cost per lumen to compete in major illumination markets. The major cost driver stems from low yields into the very narrow bins that are required for CCT and color point control. The winning alternative depends upon which set of problems yield most expediently [21] G. Wyszecki and W. S. Stiles, Color Science: Concepts and Methods, Quantitative Data and Formulae, 2nd ed. New York: Wiley, 1982.

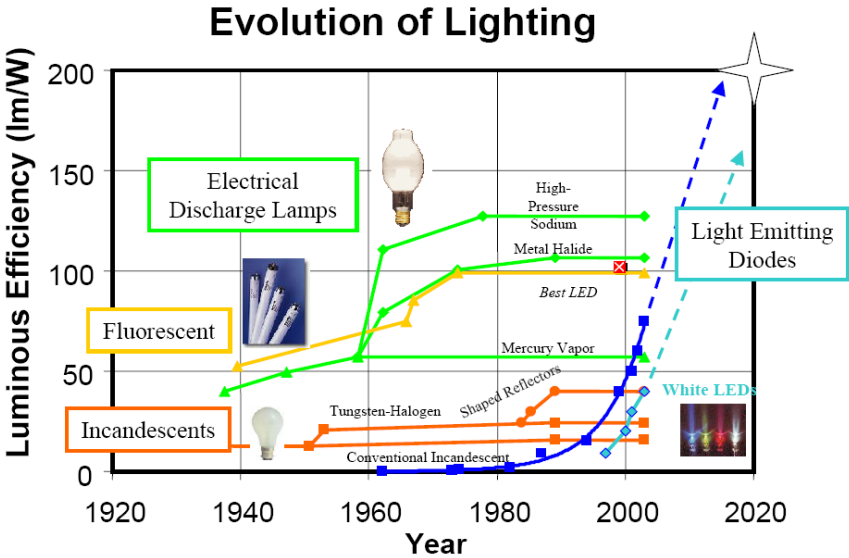


Fig.1.5 Evolution of light sources

In order to provide a stable white light, a blue LED precoated with yellow phosphor. The phosphor YAG:Ce emits yellow light when excited by blue light consequently, the mixing of the yellow light and the blue light can be perceived by human eyes as white light. This blue/yellow white light LED, with characteristics of compact size, high efficiency, long lifetime, low power requirement, and energy savings, has been widely used in various applications such as liquid crystal

display backlighting, full-color displays, cell phones, and traffic signals. However, because the yellow light emitted from the phosphor YAG:Ce lacks sufficient red emission, this white light has a low CRI(color rendering index) around 80. For improvement, red enhanced YAG:Ce and a red phosphor were used in this blue/yellow white light LED.

A new interesting item of research in white light is a three-band white LED. A blue LED is precoated with a green phosphor and a red phosphor, and the phosphors emit green and red emissions when excited by the blue light from the blue LED, respectively. Not all the blue light is absorbed by the phosphors; the remaining blue light is mixed together with the green and red emissions as a three-band white light.

This white light from the combination of the blue, green, and red emissions has an obvious advantage. It has a higher color-rendering index than blue/yellow white light, i.e., colors can be reproduced more vividly. Therefore, it can be more suitably used in museums, galleries, and the medical field.

1.4. Purpose and outline of this project

With the external quantum efficiency of III-V nitride, LED's continuously improved the emission wavelength region widened and covered the area from the ultraviolet region to the infrared region [24]. Thus, white LED's can be created for the first time by combining blue, green, and red LED's, bringing white LED's toward general lighting [25-27]. But various LED's experience is different from light output degradation rates, which will produce unstable white light over time.

Much attention has been given and a huge impact on the solid-state lighting device has been made by GaN-based LEDs that function in the visible or ultraviolet (UV) wavelengths. Commercial white light LEDs are usually composed of GaN LEDs, which function in the blue or UV

wavelengths [28-29], and a mixture of red and yellow phosphor. However, due to loss during the processes of optical pumping and re-emission, the internal quantum efficiency of this kind of phosphor converted white light LED is sacrificed. In addition, the phosphor in discarded LEDs may lead to serious environmental protection problems.

By utilizing the GaN-based ternary (AlGa_N, InGa_N) and quaternary (AlInGa_N) with multi wavelengths, Si and Mg codoped in active and cladding, white-light or near-white-light generation without using phosphor wavelength converter has been demonstrated. However, their output electroluminescence (EL) spectra are seriously dependent on the bias current [30-35]. Only white-light luminescence is exhibited under low bias current due to the nonuniform distribution of injected carriers in the Active layers [30-35] (or the saturation of the donor-to-acceptor transitions [33-34] in the case of Si and Mg co-doped LEDs).

In this paper, we discuss a novel structure for a phosphor-free white-light LED. Transverse p-n junctions are incorporated into GaN-based Multi wavelength (from blue to red) active. The optical spectra of the near white light emitted by the device are little bit variable, from low to high levels of bias current. The bias independent performance of the optical spectra of the demonstrated device can be attributed to the uniform distribution of the injected carriers in active with different center wavelengths. Use of phosphor in fabricating white-light LED has the disadvantages of lower efficiency and lower reliability. This accomplishment should be useful for the developments of solid-state lighting and display.

The problems of nonuniform carrier distribution and bias dependent electroluminescence spectra that occur in phosphor-free white-light or near-white-light LEDs should be improved by optimized process.

References

- [1] N. Holonyak Jr. and S. F. Bevaqua, "Coherent (visible) light emission from GaAs P junctions," *Appl. Phys. Lett.*, vol. 1, pp. 82–83, 1962. In 1995, Nick Holonyak received the Japan Prize for his seminal work on LED's and lasers.
- [2] H. Rupprecht, J. M. Woodall, and G. D. Petit, "Efficient visible electroluminescence at 300 K from Ga Al As p-n junctions grown by liquid-phase epitaxy," *Appl. Phys. Lett.*, vol. 11, pp. 81–83, 1967.
- [3] H. Ishiguro, K. Sawa, S. Nagao, H. Yamanaka, and S. Koike, "High efficiency GaAlAs light-emitting diodes of 660 nm with a double heterostructure on a GaAlAs substrate," *Appl. Phys. Lett.*, vol. 43, pp. 1034–1036, 1983.
- [4] C. P. Kuo, R. M. Fletcher, T. D. Osentowski, M. C. Lardizabal, M. G. Craford, and V. M. Robbins, "High performance AlInGaP visible lightemitting diodes," *Appl. Phys. Lett.*, vol. 57, pp. 2937–2939, 1990.
- [5] S. A. Stockman and G. E. Stillman, "Hydrogen in III-V device structures," *Mater. Sci. Forum*, vol. 148–149, pp. 501–536, 1994.
- [6] M. R. Krames et al., "High-power truncated-inverted-pyramid (Al Ga) In P/GaP light-emitting diodes exhibiting > 50% external quantum efficiency," *Appl. Phys. Lett.*, vol. 75, pp. 2365–2367, 1999.
- [7] S. Nakamura, "GaN Growth using GaN Buffer Layer," *Jpn. J. Appl. Phys.*, pt. 2, p. L1705, 1991.
- [8] H. Amano, N. Sawaki, I. Akasaki, and Y. Toyoda, "Metalorganic vapor phase epitaxial growth of a high quality GaN film using an AlN buffer Layer," *Appl. Phys. Lett.*, vol. 48, p. 353, 1986.
- [9] W. Goetz et al., "Activation of acceptors in Mg doped GaN grown by metalorganic chemical

vapor deposition,” *Appl. Phys. Lett.*, vol. 68, no. 5, pp. 667–669, 1996.

[10] Shuji Nakamura, Takashi Mukai, Masayuki Senoh, *Appl. Phys. Lett.* 64, 1687-1689 (1994).

[text citation]

[11] S Nakamura, M Senoh, S Nagahama, N Iwasa, T Yamada, T Matsushita, Y Sugimoto, H Kiyoku, *Appl. Phys. Lett.* 70, 1417-1419 (1997). [text citation]

[12] Wu, J., W. Walukiewicz, K. M. Yu, J. W. Ager III, S. X. Li, E. E. Haller, H. Lu, and W. J. Schaff, “Universal Bandgap Bowing in Group-III Nitride Alloys,” *Solid State Comm.* 127, 411 (2003).

[13] I. Akasaki, H. Amano, Y. Koide, K. Hiramatsu, N. Sawaki, *J. Cryst. Growth* 98, 209 (1989).

[text citation]

[14] S. Nakamura, *Jpn. J. Appl. Phys.* 30, L1705-L1707 (1991). [text citation]

[15] K. Hiramatsu, S. Itoh, H. Amano, I. Akasaki, N. Kuwano, T. Shiraishi, K. Oki, *J. Cryst. Growth* 115, 628 (1991). [text citation]

[16] H. M. Manasevit, F. M. Erdmann, W. I. Simpson, *J. Electrochem.Soc.* 118, 1864 (1971). [text citation]

[17] O. Briot, in *Group III Nitride Semiconductor Compounds Physics and Applications*, Edited by: B. Gil, (Oxford, 1998) 70-122. [text citation]

[18] S. Yoshida, S. Misawa, S. Gonda, *Appl. Phys. Lett.* 42, 427 (1983). [text citation]

[19] S. Nakamura, *Jpn. J. Appl. Phys.* 30, L1705-L1707 (1991). [text citation]

[20] Shuji Nakamura, Takashi Mukai, Masayuki Senoh, *Appl. Phys. Lett.* 64, 1687-1689 (1994).

[text citation]

[21] G. Wyszecki and W. S. Stiles, *Color Science: Concepts and Methods, Quantitative Data and Formulae*, 2nd ed. New York: Wiley, 1982.

[22] Lumileds Corporate Website [Online]. Available: www.lumileds.com/solutions/LCD/LCDindex.html

- [23] R. Mueller-Mach, G. O. Mueller, M. R. Krames, and T. Trottier, "High-Power Phosphor-Converted Light-Emitting Diodes Based on III-Nitrides," *IEEE J. Select. Topics Quantum Electron.*, vol. 8, pp. 339–345, Mar.–Apr. 2002.
- [24] T. Mukai, M. Yamada, T. Mitani, Y. Narukawa, S. Shioji, I. Niki, S. Sonobe, K. Izuno, and R. Suenaga, *Proc. SPIE 4996*, 156 _2003_.
- [25] M. Yamada, Y. Narukawa, and T. Mukai, *Jpn. J. Appl. Phys., Part 2* 41, L246 _2002_.
- [26] R. Mueller-Mach and G. O. Mueller, *Proc. SPIE 3938*, 30 _2000_.
- [27] G. O. Mueller and R. Mueller-Mach, *Proc. SPIE 4776*, 122 _2002_.
- [28] S. J. Chang, W. C. Lai, Y. K. Su, J. F. Chen, C. H. Liu, and U. H. Liaw, "InGaN/GaN multiquantum well blue and green light emitting diodes," *IEEE J. Sel. Topics Quantum Electron.*, vol. 8, pp. 278–283, Mar./Apr. 2002.
- [29] J. K. Sheu, S. J. Chang, C. H. Kuo, Y. K. Su, L. W. Wu, Y. C. Lin, W. C. Lai, J. M. Tsai, G. C. Chi, and R. K. Wu, "White-light emission from near UV InGaN-GaN LED chip precoated with blue/green/red phosphors," *IEEE Photon. Technol. Lett.*, vol. 15, no. 1, pp. 18–20, Jan. 2003.
- [30] Y.-L. Li, Th. Gessmann, E. F. Schubert, and J. K. Sheu, "Carrier dynamics in nitride-based light-emitting p-n junction diodes with two active regions emitting at different wavelengths," *J. Appl. Phys.*, vol. 94, pp. 2167–2172, Aug. 2003.
- [31] S. C. Shei, J. K. Sheu, C. M. Tsai, W. C. Lai, M. L. Lee, and C. H. Kuo, "Emission mechanism of mixed-color InGaN/GaN multi-quantum-well light-emitting diodes," *Jpn. J. Appl. Phys.*, vol. 45, no. 4A, pp. 2463–2466, Apr. 2006.
- [32] H.-S. Chen, D.-M. Yeh, C.-F. Lu, C.-F. Huang, W.-Y. Shiao, J.-J. Huang, C. C. Yang, I.-S. Liu, and W.-F. Su, "White light generation with CdSe-ZnS nanocrystals coated on an InGaN-GaN quantum-well blue/green two-wavelength light-emitting diode," *IEEE Photon. Technol. Lett.*, vol. 18, no. 13, pp. 1430–1432, Jul. 1, 2006.

- [33] S. J. Chang, L. W. Wu, Y. K. Su, C. H. Kuo, W. C. Lai, Y. P. Hsu, J. K. Sheu, J. F. Chen, and J. M. Tsai, "Si and Zn co-doped InGaN-GaN white light-emitting diodes," *IEEE Trans. Electron Devices*, vol. 50, no. 2, pp. 519–521, Feb. 2003.
- [34] J. K. Sheu, C. J. Pan, G. C. Chi, C. H. Kuo, L. W. Wu, C. H. Chen, S. J. Chang, and Y. K. Su, "White-light emission from InGaN/GaN multi-quantum well light-emitting diodes with Si and Zn codoped active layer," *IEEE Photon. Technol. Lett.*, vol. 14, no. 4, pp. 450–452, Apr. 2002.
- [35] C. H. Chen, S. J. Chang, Y. K. Su, J. K. Sheu, J. F. Chen, C. H. Kuo, and Y. C. Lin, "Nitride-based cascade near white light-emitting diodes," *IEEE Photon. Technol. Lett.*, vol. 14, no. 7, pp. 908–910, Jul. 2002.

Chapter 2.

Fundamentals of Gallium Nitride

2.1. Introduction

Gallium nitride (GaN) is a direct-bandgap semiconductor material of wurtzite crystal structure with a wide (3.4 eV) band gap, used in optoelectronic, high-power and high-frequency devices. It is a binary group III/group V direct bandgap semiconductor. Its sensitivity to ionize radiation is low (like other group III nitrides), making it a suitable material for solar cell arrays for satellites. Because GaN transistors can operate at much hotter temperatures and work at much higher voltages than GaAs transistors, they make ideal power amplifiers at microwave frequencies. GaN is a very hard, mechanically stable material with large heat capacity [1]. In its pure form it resists cracking and can be deposited in thin film on sapphire or silicon carbide, despite the mismatch in their lattice constants [1]. GaN can be doped with silicon (Si) or with oxygen [2] to N-type and with magnesium (Mg) to P-type [3], however the Si and Mg atoms change the way the GaN crystals grow, introducing tensile stresses and making them brittle [4]. GaN crystals are also rich in defects; 100 million to 10 billion per cm^2 [5].

GaN based parts are very sensitive to electrostatic discharge [6]. To develop such novel devices and clarify the intrinsic materials properties of nitrides, it is essential to grow high-quality single crystals and control their electrical conductivity. However, high-quality epitaxial GaN is difficult to grow and its conductivity is hard to control. These problems have prevented the development of GaN-based p-n junction blue-light-emitting devices for many years.

The high crystalline quality of GaN can be realized by low temperature deposited buffer layer technology [7]. This high crystalline quality GaN led to the discovery of p-type GaN, p-n junction

blue/UV-LEDs [3] and room-temperature stimulated emission [8] (indispensable for laser action) [9]. This has led to the commercialization of high-performance blue LEDs and long-lifetime violet-laser diodes (LDs), and to the development of nitride-based devices such as UV detectors and high-speed field-effect transistors. High-brightness GaN light-emitting diodes (LEDs) completed the range of primary colors, and made applications such as daylight visible full-color LED displays, white LEDs and blue laser devices possible. The first GaN-based high-brightness LEDs were being used a thin film of GaN deposited via MOCVD on sapphire. Other substrates used are zinc oxide, with lattice constant mismatch only 2 %, and silicon carbide (SiC).

Group III nitride semiconductors are recognized as one of the most promising materials for fabricating optical devices in the visible short-wavelength and UV region. Potential markets for high-power/high-frequency devices based on GaN include microwave radio-frequency power amplifiers (such as used in high-speed wireless data transmission) and high-voltage switching devices for power grids. A potential mass-market application for GaN-based RF transistors is used as the microwave source for microwave ovens, replacing the magnetrons currently used. The large band gap means that the performance of GaN transistors is maintained up to higher temperatures than silicon transistors. GaN, when doped with a suitable transition metal such as manganese, is a promising spintronics material (magnetic semiconductors).

Nanotubes of GaN are proposed for applications in nanoscale electronics, optoelectronics and biochemical-sensing applications [10]. GaN-based blue laser diodes are used in the Blu-ray disc technology.

The mixture of GaN with In (InGaN) or Al (AlGaN) with a band gap dependent on ratio of In or Al to GaN allows to build Light Emitting Diodes (LEDs) with colors that can go from red to blue. The toxicology of GaN has not been fully investigated. The dust is an irritant to skin, eyes and lungs. The environment, health and safety aspects of gallium nitride sources (such as

trimethylgallium and ammonia) and industrial hygiene monitoring studies of MOVPE sources have been reported recently in a review [11].

2.1.1. Current Issues in GaN-based LED

A great deal of development has already been achieved in the field of GaN-based emitters, yielding the new generation of lighting and optical storage options. However, there are yet many challenges that must be addressed in order to make it available the full range of possibilities seemingly offered by a materials system covering such a large swath of bandgap energies. In terms of wavelengths made available by the AlGaInN system, there are reasons for pushing the devices to perform at both longer and shorter wavelengths than the blue to near-UV spectrum in which one can currently find the best performing devices. Pushing to longer wavelengths to address the problem of the “green gap”, especially for the sake of creating more efficient white lighting, also occupies a prominent place in the research space. In terms of enabling technologies, one finds that film quality, growth methods and substrate engineering still occupy a prominent place in the research space, as does research into p-type doping of materials does. These issues continue to show a need for improvement, while some qualitatively different developments have emerged that continue to stoke the progress of GaN-based materials.

One of the crucial steps in developing the current generation of GaN-based emitters was the development of film growth techniques allowing adequate material quality on non-native substrates. While, epitaxial lateral overgrowth (ELO, LEO, ELOG) has established itself so far to be a critical technique in achieving long lifetime lasers [12], tuning of planar growth technologies still yields valuable steps forward. One interesting example of the latter is a very recent paper focusing on using a multi-step technique for optimizing the earliest stages of film nucleation and coalescence to improve resulting dislocation densities [13]. The most recently presented results show a reduction

in dislocations from 10^9 cm^{-2} down to the mid- 10^7 cm^{-2} levels without using any sort of lateral epitaxy [14]. Other important improvements have been made using versions of pulsed atomic layer epitaxy, wherein the flows of group III and group V precursors are not always concurrent. For one example of the success enabled by such methods, consult the cited paper by Prof. Asif Khan's group [15].

One of the other developments in non-overgrowth epitaxy that has allowed for significant improvements is the use of superlattices of AlGaIn/GaN and AlN/GaN. According to theory, the use of such superlattices can lead to strain relaxation unavailable without the modulated strain fields present in such a structure. Using these structures one aims to increase dislocation annihilation and increase the thickness one can grow before cracking or other strain-related morphological degradation occurs [16,17] Many groups have successfully applied this concept to the challenge of making the thick, transparent, and therefore high Al-content, layers necessary to serve as the cladding to deep UV emitters. One particularly successful recent example of this is cited here [18].

Given the successes achieved using ELO for devices in the blue and violet spectrum, ELO for the high Al-content AlGaIn compounds needed for deep UV devices is currently a high research priority. Similar to the work mentioned above where nucleation and coalescence control were used to improve planar growth quality, variations on ELO have emerged in which growth interruptions and growth rate tuning are used to increase the amount of dislocation filtering afforded by the ELO process [17, 19]. As it stands ELO GaN currently shows defect densities estimated to be around $10^6 \sim 10^7 \text{ cm}^{-2}$ and represents a fairly mature technology. However its utility for devices using high Al-content AlGaIn layers is hampered by the mismatch strain between the GaN underlayers and the subsequent AlGaIn layers. Unfortunately, lateral overgrowth of layers has proven problematic because of observed tendencies of Al-containing nitrides to grow without much lateral growth front propagation. Some successfully coalesced layers of ELO AlN or AlGaIn with >90 % Al

content have been achieved only very recently [20,21] and one finds that the vertical growth needed to achieve film coalescence is very large compared to that of GaN ELO. Finding methods to increase the rate of lateral growth would definitely be a boon to the growth of higher quality AlGaIn-based devices. One alternative that has been used to produce a successful laser is the use of a hetero-ELO technique in which part of the lateral growth is undertaken using GaN before completing the film coalescence using AlGaIn. One noteworthy result achieved using this method is the 350.9 nm laser described earlier.

One final area of interest related to film growth for deep UV emitters in the GaN materials system concerns the fine structure of the grown layers. As discussed earlier, much of the success of current GaN-based emitters owes to the Indium localization that occurs in In-containing compounds. While the lack of In in deep UV active regions precludes the possibility of such In localization, a very recent paper could show that there is promise in creating AlGaIn layers showing similar localization effects. Though the precise growth procedure is not yet published, MBE layers of 20~50 % Al content AlGaIn have been grown that show improved photoluminescence and long carrier lifetimes on the order of those in low dislocation density (10^8 cm^{-2}) GaN films despite the high (10^{10} cm^{-2}) dislocation content of the films [22]. Such behavior, along with observed redshifting from the bandedge and inhomogeneous CL emission, make a strong case for localization similar to that found in InGaIn active regions.

A. P-type doping:

The problem of p-type doping is still an important issue, with doping levels becoming even lower with increasing Al content in device layers. Researchers continue to attempt to improve p-type doping, and the current state of the art shows doping levels of about 10^{17} cm^{-3} in AlGaIn containing up to 50 % aluminum [23]. More attention has also been paid in recent years to Mg-

related defects whose appearance correlates with sudden decreases in hole concentrations when the atomic concentration of Mg passes a critical level [24,25]. The main lesson taken so far from this latter issue is that very careful control of the Mg concentration must be maintained to avoid the decreased doping that will occur if Mg-related crystal begins to form in grown layers.

B. Polarity

Non-polar growth is typically regarded as a possible solution to the problem of piezoelectric fields reducing emission efficiency. However, recent papers imply that non-polar growth might hold some promise for improving p-doping of GaN-related compounds. One piece of evidence supporting this comes from ELO growths in which parts of the film grown with a non [0001] growth facet show no evidence of extended Mg-related defects, even though pl associated with the presence of Mg atoms implies no decrease in Mg concentration [26]. Another piece of evidence comes from recent results showing higher doping levels achieved when growing a-plane GaN instead of c-plane GaN. It is worth mentioning here that both of these results would be consistent with such surface-sensitive processes as the requirement of supersaturation observed by Stephan Figge et. al in their study of pyramidal defect formation in Mg-doped GaN layers [27].

2.2. Crystallography of Gallium Nitride

First of all, GaN is a direct bandgap material (see Fig 2.1), which means that electron-hole pairs will combine radiatively, i.e. through photon emission. This is in contrast to indirect bandgap materials, in which recombination tends to be non-radiative.

Another positive aspect of GaN is that it can be alloyed with related compounds aluminum nitride and/or indium nitride to form ternary compounds AlGaN and InGaN, or the quaternary compound AlInGaN. Starting with the binary GaN ($E_g = 3.4$ eV), one can theoretically alloy InN

(or AlN) into GaN, and decrease (or increase) the bandgap in a controlled fashion. As shown in Figure 1.3, The GaN material system can thus be used to cover a very broad range of bandgap values (0.7~6.1 eV), and thus a wide span of emission wavelengths (200~1378 nm) that covers nearly of the visible spectrum. Use of the quaternary material, AlInGaN, has the added advantage of giving one the ability to independently control both bandgap and lattice parameter.

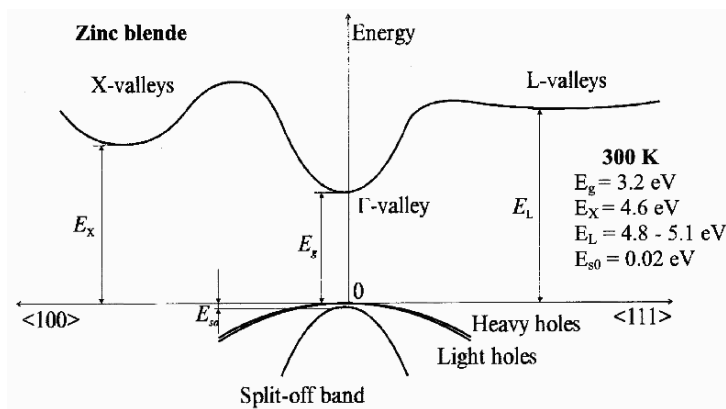


Fig.2.1 E-k diagram of gallium nitride

There are two allotropes of gallium nitride: cubic and hexagonal. The vast majority of research in the GaN field focuses on the stable hexagonal form, including the work presented herein. However, there has been a significant amount of attention paid to the metastable cubic phase. The atoms in cubic GaN (c-GaN) are arranged into a zinc blende (also known as sphalerite) structure. This arrangement is achieved by the juxtaposition of two FCC unit cells (one with Ga atoms and one with N atoms), with a displacement $\frac{1}{4}$ length along the cubic diagonal, as shown in Fig. 2.2.

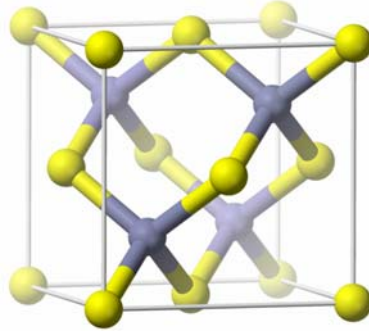


Fig.2.2 The unit cell of Zinc blende ($a = 4.52$ @300K)

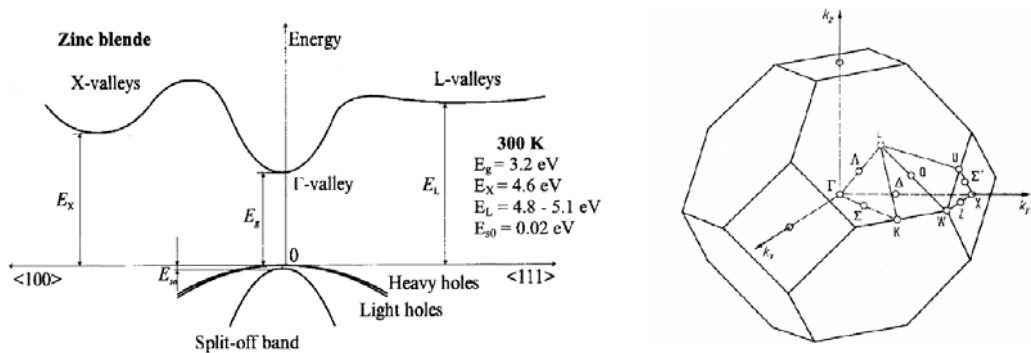


Fig.2.3 Band structure of zinc blende(cubic) GaN.

The lattice parameter of this allotrope gallium nitride is 4.52 \AA ; its bandgap is 3.28 eV [28]. As is the case with hexagonal gallium nitride (h-GaN), c-GaN is normally grown using MOCVD [29,30] or molecular beam epitaxy (MBE) [31,32]. There are several intriguing aspects of cubic GaN that make it a potentially useful material. First of all, due to its inversion symmetry, there is no

spontaneous polarization present in the material [33]. The higher symmetry of the cubic crystal, as compared to its hexagonal counterpart, should also lead to lower phonon scattering and thus higher mobilities [29, 34]. Additionally, it is believed that cubic GaN may be more amenable to p-type doping [35]. Synthesis of ternary alloys does not appear to be prohibitively problematic, as successful growth of cubic AlGaN [36] and InGaN [37] has been reported. However, there are also many difficulties inherent in the growth of c-GaN.

As mentioned earlier, there is a large lattice mismatch between c-GaN and GaAs which makes epitaxy challenging. Also, due to the metastability of c-GaN, it is very difficult to grow material that is purely cubic; appreciable amounts of the stable hexagonal subdomains tend to form during growth [34, 38, 39].

The hexagonal form of GaN is by far the more commonly studied allotrope. Its atoms assume the wurtzite structure (space group $P6_3mc$) [40], which is shown in Fig.2.4. All samples in this study were grown under conditions conducive to wurtzite GaN, thus the remainder of the dissertation will focus exclusively on this crystal structure. Fig.2.3 shows Brillouin zone of the face centered cubic lattice, the Bravais lattice of the diamond and zincblende structures. And Wurtzite (Brillouin zone of the hexagonal lattice) Band structure (see Fig.2.5) which have important minima of the conduction band and maxima of the valence band. Its valence band has 3 splitted bands. This splitting results from spin-orbit interaction and from crystal symmetry.

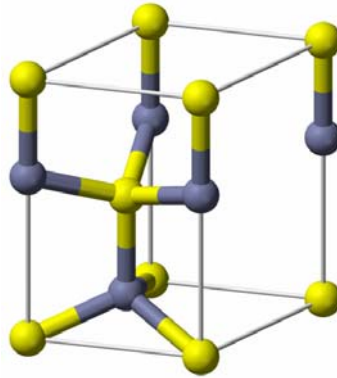


Fig.2.4 The unit cell of wurtzite ($a = 3.19 \text{ \AA}$, $c = 5.18 \text{ \AA}$ @ 300K)

Qien, et al. (1996)

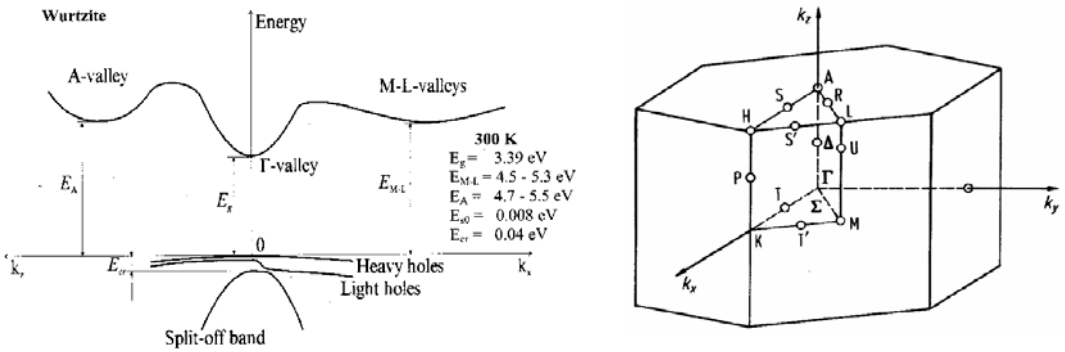


Fig.2.5 Band structure of zinc wurtzite GaN

The band discontinuities (see Fig.2.6) of nitride semiconductors in valence and conduction bands are the key parameters governing the behavior of heterojunctions; these junctions are essential for the device properties of optoelectronic devices. The large lattice mismatch between the nitride semiconductors (AlN, GaN, InN) complicates determination of these offsets, which are

strongly affected by strain [41].

The nitride semiconductors crystallize in the wurtzite structure but the zinc-blende structure is only slightly higher in energy (see Fig.2.7). These two structures differ from each other in the stacking sequence along the [0001] (or [111]) direction. Stacking faults can form relatively easily [42];

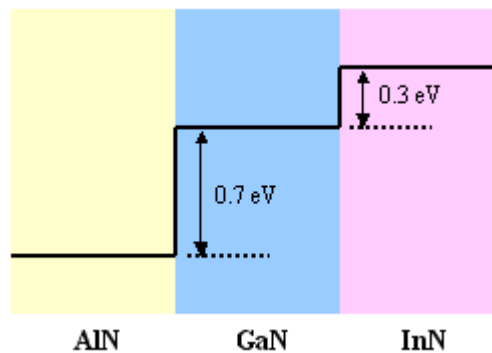


Fig.2.6 Band offsets at nitride semiconductors

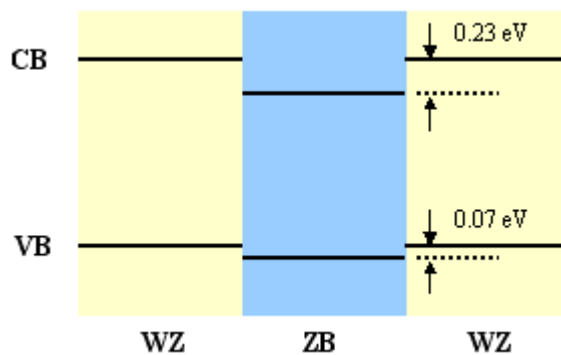


Fig.2.7 Zinc-blende/wurtzite band offsets

2.3. Characteristics of Gallium Nitride

GaN crystallizes both in the hexagonal wurtzite and zincblende forms [43-46]. However, wurtzite polytype appears to be more common than the zincblende polytype. This semiconductor has been most extensively studied [47-50] among all the few III-V nitrides. Similar to AlN, chemical stability at elevated temperatures combined with its wide bandgap has made GaN an attractive material for device operation in high temperatures and caustic environments. While the thermal stability of GaN allows high temperature processing steps to be performed, the chemical stability of GaN requires that dry etching methods be used for processing. Many different growth techniques have been employed to obtain high-quality single-crystal GaN films. As a result, it can now be grown with background concentrations as low as mid-E16. In order to produce GaN, large kinetic barriers of crystal formation have been overcome by employing high temperatures, activated nitrogen species and/or high nitrogen pressures.

For example, for MOCVD growth of GaN, typical pressures are of the order of 0.1~1.0 atmosphere, and typical temperatures are of the order of 600~700 °C in reactive ion beam assisted vacuum deposition. In order to minimize ion impact damage and decomposition during MBE growth, a source (such as Kauffman ion source) which can produce a high flux of activated species with a small but well-defined kinetic energy has been adopted [51-53]. Several groups have reported p-type GaN using electron cyclotron resonance (ECR) and radio frequency (RF) plasma activated nitrogen, and light emitting diodes with p-n junctions have been fabricated. The growths of zincblende GaN using several substrates have also been reported [47-50]. All these zincblende polytypes grown so far have high densities of planar defects, mostly {1 1 1} microtwins and stacking faults, resulting from large lattice mismatches. Structural, electrical, and optical properties of GaN have been critically reviewed in previous articles. Thus only a brief outline of these properties is presented in the following.

2.3.1. Doping of Gallium Nitride

Nitride semiconductors are easy to dope n-type; in fact they often exhibit unintentional n-type conductivity. Nitrogen vacancies were long thought to be the source of this unintended doping; I know that nitrogen vacancies are unlikely to form in n-type nitrides. Unintentional impurities, such as oxygen or silicon, are a more consistent explanation for the observed n-type conductivity.

Oxygen exhibits a very interesting behavior in nitrides. In GaN, it behaves as a shallow acceptor, but when the band gap is increased (either under hydrostatic pressure, or by alloying with AlN), the oxygen undergoes a transition to a deep center (a so-called DX center). In this new configuration, which is illustrated at right, oxygen actually behaves as a deep acceptor, i.e., it becomes a compensating center. Note that the oxygen atom (the red ball) moves away from its normal, substitutional site by almost 1 angstrom. (see Fig.2.8)

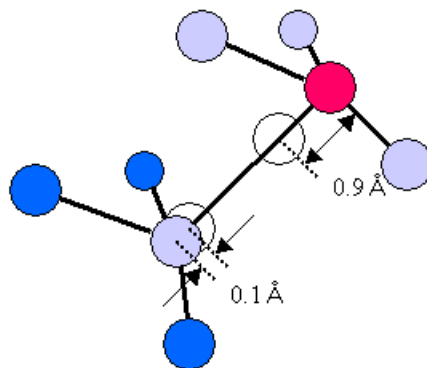


Fig.2.8 Moving away of oxygen atom

Oxygen becomes a deep level in AlGaN when the Al concentration exceeds about 30 %. Our calculations have shown that silicon does not undergo the DX transition. Silicon should therefore act as a shallow donor in AlGaN up to very high Al concentrations. Note, however, that oxygen

tends to be unintentionally incorporated in compound semiconductors with high Al content; and any oxygen that is present in AlGaIn with more than 30 % Al will act as a compensating center [54-56]. Magnesium is the most common p-type dopant. I have found that the limits in the hole concentration are mainly due to Mg solubility, not to incorporation of Mg on other sites [57,58].

A. n-Type Doping

In order to utilize the n-GaN for device fabrication, the unintentional doping, attributed by some to background nitrogen vacancies must be minimized. The level of such unintentional doping in some cases is as high as $2 \times 10^{20} \text{ cm}^{-3}$. Following the reduction in background doping, intentionally doped n-GaN was realized, among others, by Nakamura et al. who used Si and Ge as n dopant atoms for the GaN growth by MOVPE [59]. The electron concentrations of GaN doped with Si were in the range of 1×10^{17} ~ $2 \times 10^{19} \text{ cm}^{-3}$. On the other hand, the electron concentrations of GaN doped with Ge were in the range of 7×10^{16} ~ $2 \times 10^{19} \text{ cm}^{-3}$. Goldenberg observed that n-type GaN conductivities can be increased significantly if NH_3 flow is increased during the growth [60]. This might have been due to hydrogen passivation of acceptors in the material during the growth. In this paper, I tried to introduce Te as n dopant of GaN and In(Al)GaN growth by MS-HVPE. It was the first trial to make white LED ever not reported till now either.

B. p-Type Doping

As many device applications of GaN depend on the formation of p-n junctions, concerted efforts were made to dope GaN p-type. Various types of acceptor atoms including Mg and C were tried for this doping. However, these efforts led only to compensate high resistivity material until Akasaki et al. demonstrated that compensated Mg-doped GaN could be converted into conductive p-type material by low energy electron beam irradiation (LEEBI) [61,62]. Due to large binding

energy of Mg (150~200 meV), until recently, acceptor activation ratios of only $10^{-2}\sim 10^{-3}$ was achieved in Mg doped p-GaN. Thus very large Mg incorporation was necessary in order to obtain high p-doping levels. These results were later improved upon by Nakamura *et al.* who achieved p-GaN with hole concentration as high as $3 \times 10^{18} \text{ cm}^{-3}$ and resistivity $0.2 \text{ } \Omega\text{-cm}$ [63-65]. Subsequently it was discovered that thermal annealing at $700 \text{ } ^\circ\text{C}$ under an N_2 ambient can serve the same purpose as LEEBI process. However, as the GaN reverts to insulating and compensated material when annealed under NH_3 , the process appeared to be reversible. The main compensating agent responsible for the reversibility was thought to be hydrogen. So, when growth techniques were modified to minimize the effect of hydrogen, such as MBE with ECR, p-type conductivity in as-grown wurtzite GaN was readily achieved [66].

2.3.2. Optical Properties of Gallium Nitride

As reported earlier, GaN is a direct wide bandgap semiconductor crystallizing usually in the wurtzite structure. The value of the energy bandgap E_g and its gradient with respect to the temperature, dE_g/dT are determined from measurements of absorption edge position and its temperature evolution. Optical absorption studies indicate that, for GaN with negligible contribution due to free electrons, the temperature dependence of E_g is linear with a temperature coefficient of $-4.5 \times 10^{-4} \text{ eV /K}$ at 300 K [67]. Based on photoluminescence excitation measurements the temperature dependence of the energy bandgap may empirically be modeled as [68]

$$E_g = E_{00} - \frac{a_g T^2}{T + T_g} \text{ eV} \dots\dots\dots (1)$$

Ground State Energy @ 2K

When $E_{00} = 3.503$ eV, $T_g = -996$ K, and $\alpha_g = 5.08E-4$ according to Monemar [54], (1) is valid for $T < 295^\circ\text{K}$. Recent experimental data by Tiesseyre et al. suggest that when $T_g = 745$ K for the bulk crystals, and $T_g = 772$ K for layers, (1) becomes valid for T as high as 600 K [69]. Measurements in high quality samples in laboratory indicate that $E_{00} = 3.489$ eV, $\alpha_g = 7.32E-4$, and $T_g = 700$ K, respectively [70]. To obtain the bandgap accurately, however, one must add the exciton binding energy to E_{00} figure that brings its bandgap value to 3.509 eV in films grown in laboratory.

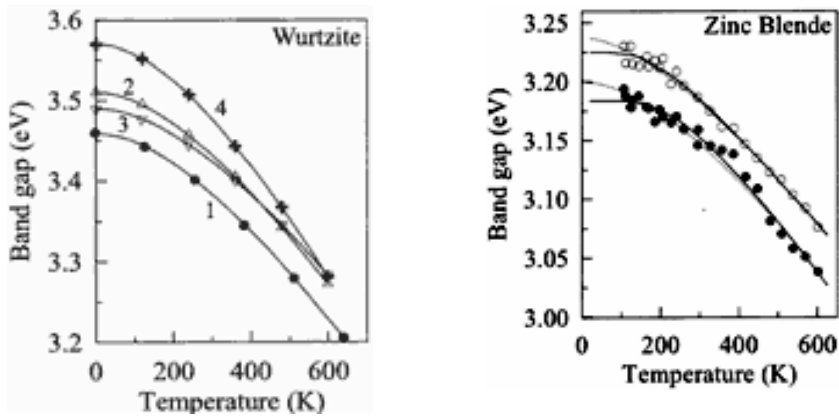


Fig.2.9 (a) GaN, Wurtzite. Band gap energy versus temperature.

GaN samples were grown on different substrates using different techniques. Experimental data are taken from four different works.... Bougrov et al. (2001)

(b) GaN, Zinc Blende(cubic). The Band gap energy versus temperature.

GaN films were grown on Si (100) substrates. The dependences were extracted from pseudodielectric-function spectrum using two different theoretical models...Petalas et al. (1995)

Owing to intense activity in light emitters and detectors, there has been also an activity into the transition energies of optical processes in GaN and AlGaIn. The available data up to a few years ago

were recently reviewed by Akasaki and Amano [71]. Pioneering work in this area was performed by Pankove et al. who reported on the low temperature (1.6 K) photoluminescence spectrum of wurtzite GaN [72]. Strong near gap emission was observed at 3.477 eV and a weaker peak was noted at 3.37 eV, which split into a -10 meV spaced doublet when the temperature was increased to 35 K. Again, recent investigations in collaboration with D. C. Reynolds of Wright Laboratory and Profs. Jiang and Lin at Kansas State University, identified all three excitonic transitions, A, B, and C associated with the three closely spaced valence bands [73]. (In wurtzitic structures, such as that for GaN, the valence band is degenerate with light and heavy hole bands closely spaced and the spin orbit splitting is very small which allow observation of excitonic transitions associated with all three bands in high quality samples.) In addition, neutral donor bound excitons I2, was also identified.

In brief, the 2 K energies of I2 (donor bound exciton), A, B, C related excitonic transitions are 3.477, 3.4831, 3.4896, and 3.525 eV, respectively (see Table 2.1).

Table.2.1 GaN Parameters

Parameters	Values
A-Exciton	
Ground State Energy @ 2K	3.4831 eV
$n = 2$ Energy @ 2K	3.4982
Exciton Binding Energy	0.02
Bandgap Energy @ 2K	3.5031
Effective Mass	0.129 m_0
Bohr Radius	36 Å
B Exciton	
Ground State Energy @ 2K	3.4896 eV
$n = 2$ Energy @ 2K	3.5067 eV
$n = 3$ Energy @ 2K	3.5093
Bandgap Energy @ 2K	3.5116
Effective Mass	0.413 m_0
Bohr Radius	32.5 Å
C Exciton	
Ground State Energy @ 2K	3.525 eV
$E_{AB}, \Gamma_9 - \Gamma_7$	0.0085
$E_{BC}, \Gamma_9 - \Gamma_7$	0.025
Dielectric Constant	$\epsilon = 9.3$
Spin Orbit Parameter	0.0173 eV
Crystal Field Parameter	0.0247 eV

A number of studies of optical properties have been performed on the zincblende GaN grown on MgO, Si, GaAs, and 3C-SiC, respectively. Employing these measurements at 300 K Lei et al. determined the refractive index below the absorption edge to be $n = 2.5$ [74]. The low temperature CL spectrum of GaN obtained by Strite et al. tentatively identified the free electron to acceptor and D-A transitions, and a phonon mode at 403 cm^{-1} [75].

A temperature coefficient of $-3.5 \times 10^{-4} \text{ eV/K}$ was measured for the free electron to acceptor peak in the linear region above 180 K. Notably, the phonon mode at 740 cm^{-1} obtained from Raman spectroscopy measurement on zincblende GaN by Humphreys et al. E621 and by Pankove [76] is about twice that value obtained by Strite et al. [75].

2.3.3. Polarity in Gallium Nitride

Another way in which the highly directional bonds in nitrides manifest themselves is through the presence of polarity in the as-grown films. Epitaxial growth of wurtzite GaN almost always results in films growth with the [0001] or [000-1] direction perpendicular to the substrate. Since this is the polar axis of the material, the resultant films will exhibit strong polarity.

It is important to be able to distinguish between the two different polarities (Ga-face and N-face) possible in gallium nitride. In the interest of clarity, I will adhere to the polarity designations set forth in the “standard framework” suggested by Hellman [77]. These designations will be explained henceforth.

Fig.2.10 shows both polar orientations of GaN. In Fig.2.10(a), the gallium atoms (depicted as white spheres) are shown to have a single bond pointing upwards away from the substrate. This is indicative of growth in the [0001] direction, which is defined as Ga-face. On the other hand, the configuration in Fig.2.10(b) shows the nitrogen atoms (blue spheres) with a single bond pointing

away from substrate. This is an example of growth the $[000-1]$ direction, which is defined as N-face.

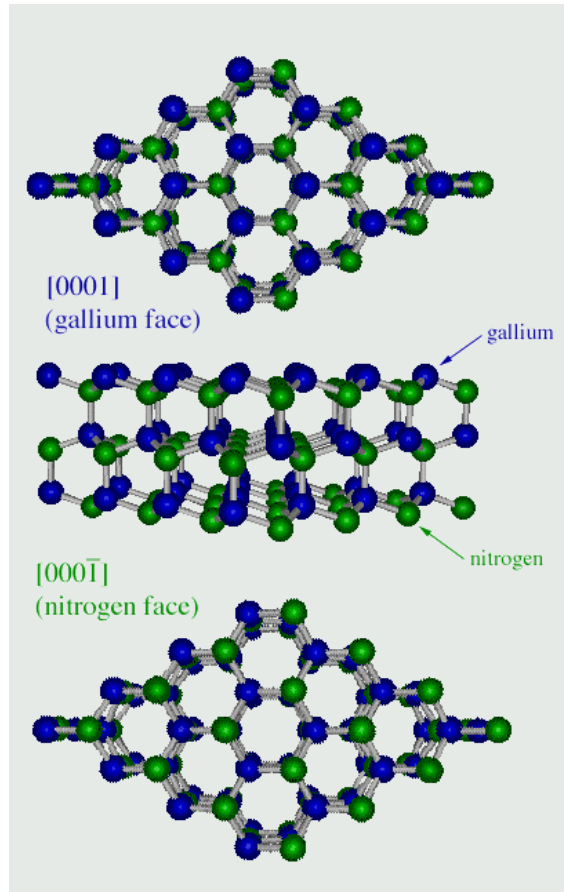


Fig.2.10 the wurtzite-GaN crystal structure showing inequivalent faces

It is important to bear in mind that polarity is a bulk property, not a surface property. For that reason, the often-used terms “Ga-terminated” and “N-terminated” can be misleading. For example, the structure shown in Fig.2.10 can conceptually be capped with a layer of N, P atoms (ie, be N, P-terminated). However, the proper polarity designation of the structure remains Ga-face. The terms “Ga-terminated” and “N-terminated”, when used correctly, refer to a surface property only.

There are several ways to measure the polarity of as-grown GaN films, including convergent

beam electron diffraction [78], Rutherford backscattering ion channeling [79], and chemical etching in KOH [80]. Characterization results have consistently shown that high quality MOCVD-grown films grown with a low temperature buffer layer and having a smooth surface morphology is almost exclusively Ga-face [77]. The GaN samples grown in this study have shown no reason why they should be anomalous, and therefore will be assumed to be Ga-face as well.

One of the consequences of the polarity in GaN is the presence of a spontaneous polarization field, \mathbf{P}_{sp} , within the material. The value of this field has been found to be -0.029 C/m^2 [81]. The negative sign indicates that the field is pointed towards the substrate (Ga-polar material is assumed).

2.4. Substrates for GaN Epitaxial Growth

2.4.1 Substrate Issues

One of the early problems with the growth of gallium nitride was lack of suitable substrates for homoepitaxy. Due to its high melting temperature and high pressure, GaN crystals cannot be made by typical techniques like Czochralski or Bridgeman. Instead, GaN was grown heteroepitaxially, most commonly on c-plane (0001) sapphire. However, due to the large lattice parameter and thermal conductivity mismatch ($\Delta\alpha_0 = 16.1 \%$, $\Delta\alpha_T = 25.5 \%$) [82], the resultant films were of poor crystal quality.

A major breakthrough occurred in 1986 when Akasaki and Amano reported that a low-temperature “buffer layer” of AlN, when grown under the right set of conditions, drastically improved the quality of GaN-on-sapphire [83]. A low-temperature buffer layer of GaN was found by Nakamura to have similar beneficial effects [84].

C-plane sapphire is by no means the only substrate upon which high-quality GaN can be grown. Silicon carbide is a very common (albeit costly) alternative [85-86]; and reports of GaN grown successfully on (111) silicon [87], zinc oxide [88], and spinel (MgAl_2O_4) [89] have been published.

The use of alternate crystallographic orientations of sapphire, such as a-plane, r-plane, and m-plane [90-92], has been studied as well. In all cases, some form of buffer layer was required to compensate for the lattice parameter and thermal conductivity mismatches between film and substrate.

2.4.2. Sapphire

Sapphire semiconductor substrates are manufactured from high quality optical grade Czochralski sapphire. As shown in Fig.2.11, Sapphire semiconductor substrates are available in all orientations including r-axis (10-12), c-axis (0001), a-axis (11-20), and m-axis (11-10). Fig.2.11 also shows orientations of sapphire semiconductor substrates.

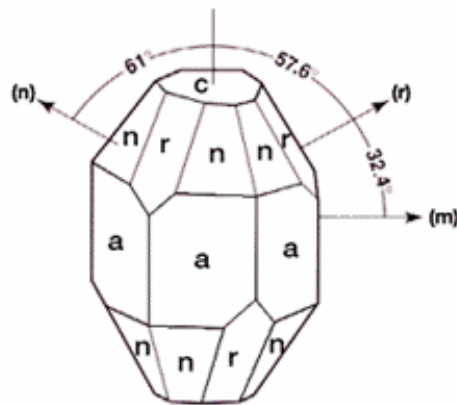


Fig.2.11 Orientations of sapphire semiconductor substrates

Sapphire is also an anisotropic crystal these are average values. Sapphire (single crystal of Al_2O_3) is being used extensively as a substrate for III-V nitrides and for many other epitaxial films. Synthetic single-crystal sapphire is a single crystal form of corundum, Al_2O_3 , also known as alpha-alumina, alumina, and single crystal Al_2O_3 . Sapphire is aluminium oxide in purest form with no

porosity or grain boundaries, making it theoretically dense. The combination of favourable chemical, electrical, mechanical, optical, surface, thermal, and durability properties make sapphire preferred material for high performance system and component designs. For various semiconductor applications sapphire is the best choice in the comparison with other synthetic single-crystals.

Sapphire is highly inert and resistant to attack in most process environments including hydrofluoric acid and the fluorine plasma applications commonly found in semiconductor wafer processing. Sapphire also provides a high, stable dielectric constant with the electrical insulation required for electronic substrates, RF and microwave transmitting windows and tubes. A selection of crystallographic orientation ensures consistent electrical properties. Sapphire is characterized by high toughness and solidity, and demonstrates excellent resistance in different environments ranging from cryogenic to over 1500 °C. Due to the transmission range from below 0.2 μm , to over 4 μm , combined with the favourable chemical durability, wear resistance, toughness, and the ability to withstand high temperatures sapphire may be used in windows and sensor optics in high performance vacuum systems, furnaces, and for other optical applications.

Thermal properties with a melting point over 2000 °C, and high thermal conductivity are often used in many harsh process environments for a combination of its thermal, chemical, mechanical, and optical properties. Thanks to its unique properties sapphire is the preferred material for a number of substrate applications that require dielectric isolation, uniform dielectric constant, and a favourable lattice match.

Table.2.2 Physical property of sapphire

Parameter	Physical property
Crystal structure	Hexagonal a=4.758 Å c=12.992 Å
Crystallographic spacing	(11-20) - a plane ; 4.758 Å (1102) - r plane ; 1.740 Å
	(1010) - m plane ; 1.375 Å (1123) - n plane ; 1.147 Å
	(0001) - c plane ; 2.165 Å (1011) - s plane ; 1.961 Å
Melt point	2040 °C
Density	3.98 g/cm ³
Hardness	9 (mohs)
Thermal expansion	7.5 (E-6/°C)
Specific heat	0.10 (cal/°C)
Thermal conductivity	46.06@0 °C 25.12@100 °C 12.56@400 °C (W/m.K)
Dielectric constant	~9.4@300K, A axis ~11.58@300K, C axis
Loss tangent at 10GHz	<2E-5 @A axis, <2E-5 @C axis

Sapphire has high intrinsic crystalline quality and can be processed to achieve very smooth surface finishes without residual stress or work damage. Sapphire is the substrate for the growth of III-V and II-VI compounds such as GaN for LED's. It also provides the substrate for the growth of mercury cadmium tellurium (HgCdTe).

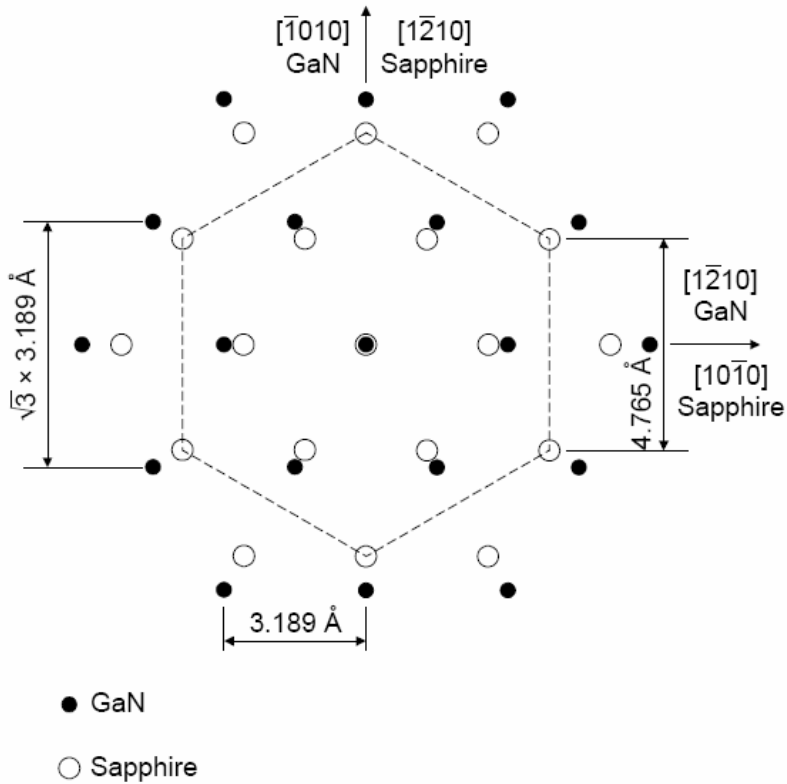


Fig.2.12 Schematic illustration of GaN growth on sapphire (0001) surface

Sapphire is used for its durability and erosion/corrosion resistance, often in combination with the ability to withstand high heat while having a very broad transmission range. Sapphire is used for short and long wavelength applications (UV and IR) beyond the range where conventional optics performs adequately. High temperatures and hostile environments also necessitate the use of sapphire optics. Sapphire lightguides are used in high temperature thermometry beyond the range of quartz optics. Optical components such as lenses, prisms and other laser and infrared optics are fabricated from high optical quality sapphire.

2.4.3. SiC

Silicon carbide exists in at least 70 crystalline forms. Alpha silicon carbide (α -SiC) is the most commonly encountered polymorph; it is formed at temperatures greater than 2000 °C and has a hexagonal crystal structure (similar to Wurtzite). The beta modification (β -SiC), with a face-centered cubic crystal structure (similar to diamond and zincblende or sphalerite), is formed at temperatures below 2000 °C. Until recently, the beta form has had relatively few commercial uses, although there is now increasing interest in its use as a support for heterogeneous catalysts, owing to its higher surface area compared to the alpha form.

Silicon carbide has a specific gravity of 3.2, and its high sublimation temperature (approximately 2700 °C) makes it useful for bearings and furnace parts. Silicon carbide does not melt at any known pressure. It is also highly inert chemically. There is currently much interest in its use as a semiconductor material in electronics, where its high thermal conductivity, high electric field breakdown strength and high maximum current density make it more promising than silicon for high-powered devices. In addition, it has strong coupling to microwave radiation, which together with its high melting point, permits practical use in heating and casting metals. SiC also has a very low coefficient of thermal expansion and experiences no phase transitions that would cause discontinuities in thermal expansion. Table 2.3 shows several physical properties of SiC comparing GaAs and Si.

Pure SiC is clear. The brown to black color of industrial product results from iron impurities. The rainbow-like luster the crystals are caused by a passivation layer of silicon dioxide that forms on the surface. Pure α -SiC is an intrinsic semiconductor with band gaps of 3.26 eV (4H) and 3.03 eV (6H) respectively.

Table.2.3 Physical property of SiC

Parameter	Physical property	
Energy Bandgap	4H-SiC ~ 3.26 (eV)	GaAs~1.43eV, Si~1.12eV
	6H-SiC ~ 3.03 (eV)	
Breakdown Electric Field	4H-SiC ~ 2.2E6 (V/cm)	GaAs~3E5 (V/cm) , Si~2.5E5 (V/cm)
	6H-SiC ~ 2.4E6 (V/cm)	
Thermal conductivity (@RT)	4H-SiC ; 3.0~3.8 (W/cm.K)	GaAs~0.5(W/cm.K), Si~1.5(W/cm.K)
	6H-SiC ; 3.0~3.8 (W/cm.K)	
Electron drift velocity (@E≥2E5)	4H-SiC ~2E7 (V/cm)	GaAs, Si~1.0(V/cm)
	6H-SiC ~2E7 (V/cm)	

Silicon carbide is used for blue LEDs, ultrafast, high-voltage Schottky diodes, MESFETs and high temperature thyristors for high power switching. A famous paper by Jayan Baliga shows enormous potential of SiC as a power device material [93]. However, some problems with the interface of SiC with silicon dioxide have hampered the development of SiC based power MOSFET and IGBTs. Extensive research is going on to solve the problem. Due to its high thermal conductivity, SiC is also used as substrate for other semiconductor materials such as gallium nitride [94]. Due to its wide band gap, SiC-based parts are capable of operating at high temperature (over 350 °C), which together with good thermal conductivity of SiC reduces problems with cooling of power parts. They also possess increased tolerance to radiation damage, making it a material desired for defense and aerospace applications. Its main competitor is gallium nitride. Although diamond has an even higher band gap, SiC-based devices are easier to manufacture due to the fact that it is more convenient to grow an insulating layer of silicon dioxide on the surface of a silicon carbide wafer than it is with diamond.

Pure SiC is a poor electrical conductor. Addition of suitable dopants significantly enhances its conductivity. Typically, such material has a negative temperature coefficient between room temperature and about 900 °C, and positive temperature coefficient at higher temperatures, making

it suitable material for high temperature heating elements.

Silicon carbide is also used as an ultraviolet detector. Nikola Tesla, around the turn of the 20th century, performed a variety of experiments with carborundum. Electroluminescence of silicon carbide was observed by Captain Henry Joseph Round in 1907 and by O. V. Losev in the Soviet Union in 1923 [95].

References

- [1] Isamu Akasaki and Hiroshi Amano, "Crystal Growth and Conductivity Control of Group III Nitride Semiconductors and Their Application to Short Wavelength Light Emitters", *Jpn. J. Appl. Phys. Vol.36 Pages 5393-5408 2003*
- [2] J.Leitner, "High temperature enthalpy and heat capacity of GaN", *Thermochimica Acta, Volume 401, Issue 2, 19 May 2003, Pages 169-173*
- [3] Hiroshi Amano, Masahiro Kito, Kazumasa Hiramatsu and Isamu Akasaki, "P-Type Conduction in Mg-Doped GaN Treated with Low-Energy Electron Beam Irradiation (LEEBI)", *Jpn. J. Appl. Phys. Vol. 28 (1989) L2112-L2114, DOI:10.1143/JJAP.28.L2112*
- [4] Shinji Terao, Motoaki Iwaya, Ryo Nakamura, Satoshi Kamiyama, Hiroshi Amano and Isamu Akasaki, "Fracture of $\text{Al}_x\text{Ga}_{1-x}\text{N}/\text{GaN}$ Heterostructure —Compositional and Impurity Dependence—", *Jpn. J. Appl. Phys. Vol. 40 (2001) L195-L197, DOI:10.1143/JJAP.40.L195*
- [5] lbl.gov, blue-light-diodes
- [6] Hajime Okumura, "Present Status and Future Prospect of Widegap Semiconductor High-Power Devices", *Jpn. J. Appl. Phys. Vol. 45 (2006) 7565-7586, DOI:10.1143/JJAP.45.7565*
- [7] *Applied Physics Letters, Volume 48, Issue 5, pp. 353-355*
- [8] Hiroshi Amano, Tsunemori Asahi and Isamu Akasaki, "Stimulated Emission Near Ultraviolet at Room Temperature from a GaN Film Grown on Sapphire by MOVPE Using an AlN Buffer Layer", *Jpn. J. Appl. Phys. Vol. 29 (1990) L205-L206 DOI:10.1143/JJAP.29.L205*
- [9] Isamu Akasaki, Hiroshi Amano, Shigetoshi Sota, Hiromitsu Sakai, Toshiyuki Tanaka and Masayoshi Koike, "Stimulated Emission by Current Injection from an AlGaIn/GaN/GaInN Quantum Well Device", *Jpn. J. Appl. Phys. Vol.34(1995) L1517-L1519 DOI:10.1143/JJAP.34.L1517*
- [10] Goldberger et al, *Nature* 422, 599-602 (10 April 2003)

- [11] *Journal of Crystal Growth* (2004); DOI:doi:10.1016/j.jcrysgr.2004.09.007
- [12] Nakamura S, Senoh M, Nagahama S-I, Iwasa N, Yamada T, Matsushita T, Kiyoku H, Sugimoto Y, Kozaki T, Umemoto H, Sano M, Chocho K. *Japanese Journal of Applied Physics Part 2-Letters*, vol.36, no.12A, 1 Dec. 1997, pp.1568-71.
- [13]. Lang T, Odnoblyudov M, Bougrov V, Sopanen M. *Journal of Crystal Growth*, vol.277, no.1-4, 15 April 2005, pp. 64-71.
- [14] Obnobyudov M, Lang T, Bougrov V. Presented at Fall MRS Meeting, Boston, MA (2004) FF2.4
- [15] Zhang JP, Asif Khan M, Sun WH, Wang HM, Chen CQ, Fareed Q, Kuokstis E, Yang JW. *Applied Physics Letters*, vol.81, no.23, 2 Dec. 2002, pp. 4392-4.
- [16] Bykhovski AD, Gelmont BL, Shur MS. *Journal of Applied Physics*, vol.81, no.9, 1 May 1997, pp. 6332-8.
- [17] Romanov AE, Pompe W, Beltz GE, Speck JS. *Applied Physics Letters*, vol.69, no.22, 25 Nov. 1996, pp. 3342-4.
- [18] Zhang JP, Wang HM, Gaevski ME, Chen CQ, Fareed Q, Yang JW, Simin G, Khan MA. *Applied Physics Letters*, vol.80, no.19, 13 May 2002, pp. 3542-4.
- [19] Hiramatsu K, Nishiyama K, Onishi M, Mizutani H, Narukawa M, Motogaito A, Miyake H, Iyechika Y, Maeda T. Elsevier. *Journal of Crystal Growth*, vol.221, Dec. 2000, pp. 316-26.
- [20] Heikman S, Keller S, Newman S, Wu Y, Moe C, Moran B, Schmidt M, Mishra UK, Speck JS, DenBaars SP. *Japanese Journal of Applied Physics, Part 2 (Letters)*, vol.44, no.12-15, 2005, pp. L405-7.
- [21] 44. Fujito K, Hashimoto T, Samonji K, Speck JS, Nakamura S. Elsevier. *Journal of Crystal Growth*, vol.272, no.1-4, 10 Dec. 2004, pp. 370-6.
- [22] Collins CJ, Sampath AV, Garrett GA, Sarney WL, Shen H, Wraback M, Nikiforov AY, Cargill

- GS, Dierolf V. *Applied Physics Letters*, vol.86, no.3, 17 Jan. 2005, pp. 31916-1-3.
- [23] Jeon S.-R, Ren Z, Cui G, Su J, Gherasimova M, Han J, Cho H-K, and Zhou L.
- [24] Romano LT, Kneissl M, Northrup JE, Van de Walle CG, Treat DW. *Applied Physics Letters*, vol.79, no.17, 22 Oct. 2001, pp.2734-6
- [25] Vennegues P, Leroux M, Dalmaso S, Benaissa M, De Mierry P, Lorenzini P, Damilano B, Beaumont B, Massies J, Gibart P. *Physical Review B (Condensed Matter and Materials Physics)*, vol.68, no.23, 15 Dec. 2003, pp. 235214-1-8.
- [26] Bell A, Liu R, Ponce FA, Amano H, Akasaki I, Cherns D. *Applied Physics Letters*, vol.82, no.3, 20 Jan. 2003, pp. 349-51.
- [27] Figge S, Kroger R, Bottcher T, Ryder PL, Hommel D. *Applied Physics Letters*, vol.81, no.25, 16 Dec. 2002, pp.4748-50
- [28] C.A. Daul. University of Fribourgh. Found online at <http://www-chem.unifr.ch/cd/cdaul/CD/cours/geometry/#1.5>
- [29]. V. Bougrov, M.E. Levinshtein, S.L. Rumyantsev, and A. Zubrilov. in *Properties of Advanced Semiconductor Materials GaN, AlN, InN, BN, SiC, SiG*, p1. M.E. Levinshtein, S.L. Rumyantsev, and M.S. Shur, eds. John Wiley & Sons, Inc., New York (2001).
- [30] J. Wu, H. Yaguchi, K. Onabe, Y. Shiraki, and R. Ito. "Metalorganic vapor phase epitaxy Growth of High Quality Cubic GaN on GaAs (100) Substrates." *Jpn. J. Appl. Phys.* 37, 1440 (1998).
- [31] Z.H. Feng, H. Yang, Y. Fu, Y.P. Sun, X.M. Shen, and Y.T. Wang. "Optimization of cubic GaN growth by metalorganic chemical vapor deposition based on residual strain relaxation." *Appl. Phys. Lett.* 82, 206 (2002).
- [32] K. Amimer, A. Georgakilas, K. Tsagaraki, M Androulidaki, D. Cengher, L. Toth, and B. Pecz. "Single crystal hexagonal and cubic GaN growth directly on vicinal (001) GaAs substrates by molecular-beam epitaxy." *Appl. Phys. Lett.* 76, 2580 (2000).

- [33] A. Tabata, A.P. Lima, J.R. Leite, V. Lemos, D. Schikora, B. Schöttker, U. Köhler, D.J. As, and K. Lischka. "Micro-Raman analysis of cubic GaN layers grown by MBE on (001) GaAs substrate." *Semicond. Sci. Technol.* 14, 318 (1999).
- [34] E.T. Yu. "Spontaneous and piezoelectric polarization in nitride heterostructures." in *III-V Nitride Semiconductors: Applications and Devices*, Ch. 4. E.T. Yu and O. Manasreh, eds. Taylor & Francis, New York (2003).
- [35] H. Okumura, K. Ohta, G. Feuillet, K. Balakrishnan, S. Chichibu, H. Hamaguchi, P. Hacke, and S. Yoshida. "Growth and characterization of cubic GaN." *J. Crys. Gr.* 178, 113 (1997).
- [36] S. Strite and H. Morkoç. "GaN, AlN, and InN: a review." *J. Vac. Sci. Tech. B* 10, 1237 (1992).
11. Nakadaira and H. Tanaka. "Metalorganic Vapor-Phase Epitaxial Growth and Characterization of Cubic $\text{Al}_x\text{Ga}_{1-x}\text{N}$ Alloy." *Jpn. J. Appl. Phys.* 37, 1449 (1998).
- [37] J.R. Müllhäuser, B. Jenichen, M. Wassermeier, O. Brandt, and K.H. Ploog. "Characterization of zinc blende $\text{In}_x\text{Ga}_{1-x}\text{N}$ grown by radio frequency plasma assisted molecular beam epitaxy on GaAs (001)." *Appl. Phys. Lett.* 71, 909 (1997).
- [38] M. Katsikini, E.C. Paloura, and T.D. Moustakas. "Application of near-edge x-ray absorption fine structure for the identification of hexagonal and cubic polytypes in epitaxial GaN." *Appl. Phys. Lett.* 69, 4206 (1996).
- [39] D. Xu, H. Yang, S.M. Zhang, L.X. Zheng, D.G. Zhao, S.F. Li, Y.T. Wang, R.H. Wu. "Investigation into the origin of wurtzite domains in thick cubic GaN using reactive ion etching." *Thin Solid Films* 372, 25 (1999).
- [40] H. Morkoç. *Nitride Semiconductors and Devices. Chapter 2.1.* Springer, Berlin (1999).
- [41] "Small valence-band offsets at GaN/InGaN heterojunctions", Chris G. Van de Walle and J. Neugebauer, *Appl. Phys. Lett.* 70, 2577 (1997).
- [42] "Energetics and electronic structure of stacking faults in AlN, GaN, and InN", C. Stampfl and

Chris G. Van de Walle, *Phys. Rev. B.* 57, R15052 (1998).

[43] I. Gorczyca and N. E. Christensen, "Band structure and highpressure phase transition in GaN," *Solid State Commun.*, vol. 80, p. 335, 1991

[44] M. Mizuta, S. Fujieda, Y. Matsumoto, and T. Kawamura, "Low temperature growth of GaN and AlN on GaAs utilizing metal organics and hydrazine," *Jpn. J. Appl. Phys.*, vol. 25, p. L-945, 1986.

[45] M. J. Paisley, Z. Sitar, J. B. Posthill, and R. F. Davis, "Growth of cubic phase gallium nitride by modified molecular beam epitaxy," *J. Vac. Sci. Technol. A*, vol. 7, pp. 701-705, 1989.

[46] M. E. Sherwin and T. J. Drummond, "Predicted elastic constants and critical layer thicknesses for cubic phase AlN, GaN, and InN on-SiC," *J. Appl. Phys.*, vol. 69, pp. 8423-8425, 1991

[47] H. Morkoc et al.. "A review of large bandgap SiC, III-V nitrides, and ZnSe based III-VI semiconductors and devices," *J. Appl. Phys. Rev.*, vol. 76, no. 3, pp. 1363-1398, Aug. 1994.

[48] H. Morkoc, "GaN and silicon carbide as optoelectronic materials," *CRC Handbook on Optoelectronics*, M. Gupta, Ed.

[49] S. Strite, M. E. Lin, and H. Morkoc, "Progress and prospects for GaN and the III-V nitride semiconductors," *Thin Solid Films*,

[50] R. F. Davis, "III-V nitrides for electronic and optoelectronic applications," *IEEE Proc.*, vol. 80, pp. 702-712, 1991.

[51] R. C. Powell, N.-E. Lee, Y.-W. Kim, and J. E. Greene, "Heteroepitaxial wurtzite and zinc blende structure GaN grown by reactive-ion molecular beam epitaxy: Growth kinetics, microstructure, and properties," *J. Appl. Phys.*, vol. 73, pp.

[52] K. Matsubara and T. Takagi, *Jpn. J. Appl. Phys.*, vol. 22, p. 511, 1982;

[53] H. Gotoh, T. Suga, H. Suzuki, and M. Kimata, *Jpn. J. Appl. Phys.*, vol. 20, p. L545, 1981.

[54] "DX center formation in wurtzite and zinc-blende AlGaInN", Chris G. Van de Walle, *Phys. Rev.*

B 57, 2033 (1998).

[55] "Doping of $\text{Al}_x\text{Ga}_{1-x}\text{N}$ ", C. Stampfl and Chris G. Van de Walle, *Appl. Phys. Lett.* 72, 459 (1998).

[56] "Metastability of oxygen donors in AlGaN ", M. D. McCluskey, N. M. Johnson, Chris G. Van de Walle, D. P. Bour, M. Kneissl, and W. Walukiewicz, *Phys. Rev. Lett.* 80, 4008 (1998).

[57] "Defects and doping in GaN ", J. Neugebauer and C. G. Van de Walle, in *Proceedings of the 22th International Conference on the Physics of Semiconductors, Vancouver, 1994*, edited by D. J. Lockwood (World Scientific Publishing Co Pte Ltd., Singapore), p. 2327.

[58] "Chemical trends for acceptor impurities in GaN ", J. Neugebauer and Chris G. Van de Walle, *J. Appl. Phys.* 85, 3003 (1999).

[59] S. Nakamura, T. Mukai, and M. Seno, "Si and Ge-doped GaN films grown with GaN buffer layers," *Jpn. J. Appl. Phys.*,

[60] Goldenberg, *APS Mar. Meet.*, Seattle, WA, 1993.

[61] H. Amano, M. Kito, K. Hiramatsu, and I. Akasaki, "p-type conduction in Mg-doped GaN treated with low-energy electron beam irradiation (LEEBI)," *Jpn. J. Appl. Phys.*, vol. 28, pp.

[62] -, "Photoluminescence of Mg doped p-type GaN and electroluminescence of GaN p-n junction LED," *J. Lumin.*, vol. 48/49, pp. 666-670, 1991.

[63] S. Nakamura, N. Isawa, M. Seno, and T. Mukai, "Hole compensation mechanism of p-type GaN films," *Jpn. J. Appl. Phys.* vol. 231, pp. 197-210, 1993. 189-204, 1993. vol. 31, pp. 2883-2888, 1992 L2112-2114, 1989. - 1. *J. Appl. Phys.* 31, pp. 1258, 1992- 1-491.

[64] "Thermal annealing effects on D-tvDe ME-doped GaN films," *Jpn. J. Appl. Phys.*; vol. 31, p. 1101, 1992

[65] -, "Highly p-typed Mg-doped GaN films grown on GaN buffer layers," *Jpn. J. Appl. Phys.* vol. 30, p. L1708, 1991.

- [66] M. E. Lin, C. Xue, G. L. Zhou, and H. Morkq, "p-type zincblende GaN on GaAs substrates," *Appl. Phys. Lett.*, vol. 63, pp. 932-933, 1993
- [67] H. Tiesseyre et al., "Temperature dependence of the energy gap in GaN bulk single crystals and epitaxial layer," *J. Appl. Phys.*,
- [68] B. Monemar, "Fundamental energy gap of GaN from photoluminescence excitation spectra," *Phys. Rev.*, vol. B10, p. 676, 1974.
- [69] H. Tiesseyre et al., "Temperature dependence of the energy gap in GaN bulk single crystals and epitaxial layer," *J. Appl. Phys.* vol. 15, pp. 327-329, 1996. vol. 76, pp. 2429-2434, 1994.
- [70] A. Salvador and H. Morkoq, unpublished.
- [71] I. Akasaki and H. Amano, "Basic optical properties, photoluminescence and cathodoluminescence of GaN and AlGa_N," in *Properties of Group III Nitrides*, J. H. Edgar, Ed. London, UK: INSPEC, IEE, 1994, pp. 222-230.
- [72] J. I. Pankove, E. A. Miller, and J. E. Berkeyheiser, "GaN electroluminescent diodes," *RCA Rev.*, vol. 32, pp. 383, 1971.
- [73] D. C. Reynolds et al., "Ground and excited state exciton spectra from GaN grown by molecular beam epitaxy," unpublished.
- [74] T. Lei et al., "Epitaxial growth and characterization of zincblende gallium nitride on (011) silicon," *J. Appl. Phys.*, vol. 71, pp. 4933-4943, 1992.
- [75] S. Strite et al., "Structural properties of InN films grown on GaAs substrates: observation of zinc blende polytypes," *J. Crystal Growth*, vol. 127, pp. 204-208, 1993.
- [76] J. I. Pankove, private communications.
- [77] E.S. Hellman. "The polarity of GaN: a critical review." *MRS Internet J. Nitride Semicond. Res.* 3, 11 (1998). 77
- [78] F.A. Ponce, D.P. Bour, W.T. Young, M. Saunders, J.W. Steeds. "Determination of lattice

polarity for growth of GaN bulk single crystals and epitaxial layers.” *Appl. Phys. Lett.* 69, 337 (1996).

[79] B. Daudin, J.L. Rouvière, M. Arlery. “Polarity determination of GaN films by ion channeling and convergent beam electron diffraction.” *Appl. Phys. Lett.* 69, 2480 (1996).

[80] J.L. Weyher, S. Müller, I.Grzegory, and S. Porowski. “Chemical polishing of bulk and epitaxial GaN.” *J. Crys. Gr.* 182, 17 (1997).

[81] F. Bernardini, V.Fiorentini, and D. Vanderbilt. “Spontaneous polarization and piezoelectric constants of III-V nitrides.” *Phys. Rev. B* 56, R10024 (1997).

[82] S. Nakamura, S. Pearton, and G. Fasol. *The Blue Laser Diode: The Complete Story*, Chapter 3.2.2. Springer, Berlin (2000).

[83] H. Amano, N. Sawaki, I. Kasaki, and Y. Toyoda. “Metalorganic vapor phase epitaxial growth of a high quality GaN film using an AlN buffer layer.” *Appl. Phys. Lett.* 48, 353 (1986).

[84] S. Nakamura. “GaN growth using GaN buffer layer.” *Jpn. J. Appl. Phys.* 30, L1705 (1991).

[85] S. Fischer, C. Wetzel, W.L. Hansen, E.D. Bourret-Courchesne, B.K. Meyer, and E.E. Haller. “Properties of GaN grown at high rates on sapphire and on 6H-SiC.” *Appl. Phys. Lett.* 69, 2716 (1996).

[86] L. Lu, H. Yan, C.L. Yang, M. Xie, Z. Wang, J. Wang, and W. Ge. “Study of GaN thin films grown on vicinal SiC (0001) substrates by molecular beam epitaxy.” *Semicond. Sci. Tech.* 17, 957 (2002).

[87] P. Rajagopal, T. Gehrke, J.C. Roberts, J.D. Brown, T.W. Weeks, E. Piner, and K. Linthicum. “Large-area, device quality GaN on Si using a novel transition layer scheme.” *Materials Research Society Symposium Proceedings Vol. 743: GaN and Related Alloys—2002*, p. L.1.2.1 (2003).

[88] X. Gu, M.A. Reshchikov, L. He, A. Teke, F. Yun, D.K. Johnstone, B. Nemeth, J. Nause, and H.

Morkoç. "Epitaxy of highly optical efficient GaN on O and Zn face ZnO." *Materials Research Society Symposium Proceedings Vol. 798: GaN and Related Alloys—2003*, p. Y.9.1.1 (2004).

[89] C. J. Sun, J. W. Yang, Q. Chen, M. Asif Khan, T. George, P. Chang-Chien, S. Mahajan. "Deposition of high quality wurtzite GaN films over cubic (111) MgAl₂O₄ substrates using low pressure metalorganic chemical vapor deposition." *Appl. Phys. Lett.* 68, 1129 (1996).

[90] K. Doverspike, L.B. Rowland, D.K. Gaskill, and J.A. Freitas, Jr. "The effect of GaN and AlN buffer layers on GaN film properties grown on both c-plane and a-plane sapphire." *J. Elec Mat.* 24, 269 (1995).

[91] D. Doppalapudi, E. Iliopoulos, S.N. Basu, and T.D. Moustakas. "Epitaxial growth of gallium nitride thin films on A-plane sapphire by molecular beam epitaxy." *J. Appl. Phys.* 85, 3582 (1999).

[92] S. Tripathy, R. K. Soni, H. Asahi, K. Iwata, R. Kuroiwa, K. Asami, and S. Gonda. "Optical properties of GaN layers grown on C-, A-, R-, and M-plane sapphire substrates by gas source molecular beam epitaxy." *J. Appl. Phys.* 85, 8386 (1999).

[93] Comparison of 6H-SiC, 3C-SiC, and Si for power devices, Bhatnagar, M., Baliga, B.J., *IEEE Transactions on Electron Devices*, March 1993

[94] http://www.qinetiq.com/home/commercial/information_communication_and_electronics/Electronics/optronics/quantum_electronics.html

[95] <http://www.indiana.edu/~hightech/fpd/papers/ELDs.html>

Chapter 3.

Overview of Epitaxial Growth Experimental

3.1. Hydride Vapor Phase Epitaxy

3.1.1. Introduction to HVPE

Although we have seen a tremendous development of short wavelength optoelectronic and electronic devices based on GaN and related materials for the recent years, the further improvement of such devices is still limited by the fact that epitaxial structures have to be grown on foreign substrates like sapphire, SiC, or Si, because high quality bulk GaN wafers are not yet really available. Therefore, the heteroepitaxial growth of thick GaN layers by hydride vapor phase epitaxy (HVPE) has been developed in many R&D groups that can be used as substrates for subsequent device epitaxy. As we have observed on thin GaN layers grown by MOVPE (metalorganic vapor phase epitaxy), the residual strain depends strongly on the nucleation method. When an AlN nucleation layer is used, the GaN layer exhibits large compressive strain whereas samples with a low temperature GaN nucleation layer show much lower strain at room temperature. GaN layers of these types are often used as templates for the deposition of thicker GaN layers by HVPE. Thus, it is interesting to evaluate whether the strain state of these templates may influence the final strain or other properties of the HVPE layers.

Therefore, we have investigated the HVPE growth of thick GaN layers on different GaN templates. Besides the cracking behavior, our studies focus also on the surface morphology problem and its relation to the template properties. Such studies require an optimization of all growth parameters to achieve an excellent surface morphology.

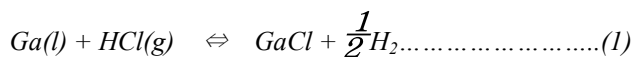
The hydride vapor phase epitaxy (HVPE) process is straightforward chemistry. When producing gallium nitride (GaN), hydrochloric acid gas is passed over a bowl of molten gallium,

which reacts with the gas to form gallium chloride gas. The gallium chloride flows into a chamber where it meets the sapphire substrates and ammonia gas. The ammonia reacts with the gallium chloride forming the GaN, which condenses on the substrate.

HVPE is cheaper, faster, and simpler than metal organic chemical-vapor deposition (MOCVD) because the HVPE reactor does not require a vacuum. HVPE uses less expensive and dangerous chemical precursors, and it deposits material faster than MOCVD. MOCVD deposits between 1 and 2 microns of wide-bandgap semiconductor material per hour and HVPE deposits the material up to 100 times faster. HVPE is capable of producing much thicker layers with lower defects.

The HVPE method is the most popular technique for the development of bulk GaN substrates. This process is still in a rather early stage, but the produced material is of interest for studies of the HVPE process as well as the physical properties of bulk GaN. The HVPE growth of GaN in different laboratories is so far essentially done on homemade growth equipment, meaning that growth conditions in different laboratories cannot be directly compared. We shall give some materials characteristics related to the growth conditions in our growth systems, related to structural defects but mainly optical properties. The residual impurities and their corresponding optical signatures will be also discussed.

For HVPE, gallium metal is used as group III precursor. At a temperature between 800 °C and 900 °C the liquid gallium reacts with hydrogen chloride (HCl) and forms gallium chloride (1). On the wafer gallium chloride and the group V precursor ammonia (NH₃) react to gallium nitride (2).



GaN has been grown on several substrates, the most popular and widely used being Sapphire

and SiC. Both of these substrates have relatively large lattice mismatches with GaN and require the use of a Nucleation layer (or Buffer layer) made up of AlN or GaN. This Nucleation layer is usually grown at low temperature, while this layer is necessary for the growth of GaN, it is also one of the most likely sources of Threading Dislocations in the material [1].

For the production of GaN substrates the Hydride Vapor Phase Epitaxy (HVPE) is the most promising technique due to its capability to grow high-quality GaN layers with a growth rate of up to 100 $\mu\text{m/h}$.

3.1.2. Mixed-source HVPE System

To study the growth of GaN by HVPE [2-4], a horizontal hot-wall reactor was made with quartz tubes and the substrate was mounted horizontally with respect to the oncoming gas streams. The mixed-source hydride vapor phase epitaxy (HVPE) system was designed to be able to grow InN, AlN, GaN and their ternary/Quaternary compounds by using metallic materials and ammonia as preliminary sources. It is alternative growth method against conventional HVPE growth.

The metallic In (Ga) mixed with Ga (In) and Al is loaded in the HVPE chamber as a source material. In order to obtain the In(Al)GaN layer by mixed-source HVPE, the source zone temperatures of the metallic In mixed with Ga are varied from around 750 °C to 1000 °C. The InGaN layers are grown from chemical reaction between a NH_3 and an In-Ga chloride formed by HCl flown over metallic In mixed with Ga at 990 °C. The growth of InGaN layer is generally performed on a sapphire (0001) substrate with templated GaN. The system is homemade growth equipment in laboratory to perform experiment of GaN related materials. It is exclusive fusion system of liquid phase epitaxy (LPE) and vapor phase epitaxy (VPE).

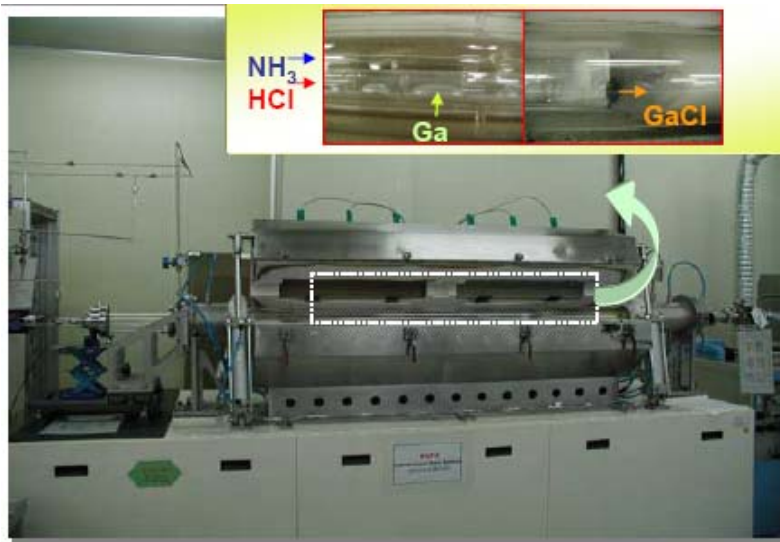


Fig.3.1(a) Mixed Source HVPE system.

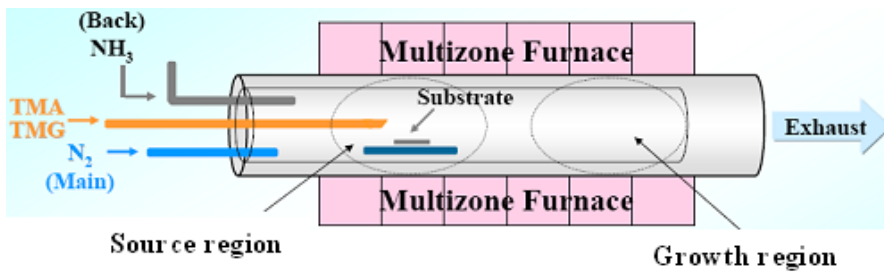


Fig.3.1 (b) Schematic diagram of the MS-HVPE reactor.

Normally, the experiments were carried out in a atmospheric horizontal HVPE system (see Fig.3.1) by using N_2 as the carrier gas. The GaN layers were grown on GaN buffer/ Al_2O_3 substrates. The reactor is divided into six separate temperature zones to create the definite temperature profile. The NH_3 flow rates and HCl flow rates were kept by mass flow controller (MFC) respectively.

Either a mixture including nitrogen or only nitrogen was used as the carrier gas. The growth temperature and the Ga source temperature were maintained at the difference of 200 °C (see Fig.3.2). The GaN layers were grown by the use of metallic Ga and ammonia (NH₃). High purity NH₃ gas and Ga ingot were employed as nitrogen and gallium sources, respectively. The mixed-source HVPE method is simple and economic for III-V semiconductors (see Fig.3.3).

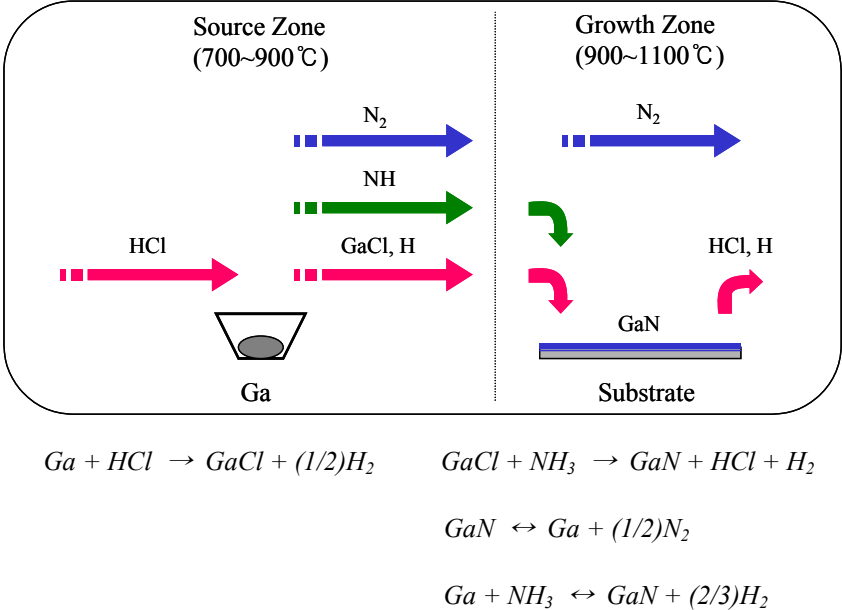


Fig.3.2 GaN growth by HVPE

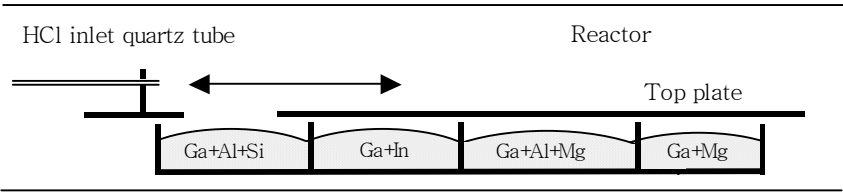


Fig.3.3 Multi-sliding boat system of the mixed-source HVPE

3.1.3. Some parameters for optimized GaN Growth

The development of substrates for GaN based devices is a topic of increasing importance as the lifetime and performance of recent devices like laser diodes, UV emitting LEDs or FETs require high-quality substrates. Usual GaN layers grown on foreign substrates have a high dislocation density in the order of $10^8\sim 10^{10}$ cm^{-2} thus reducing the carrier mobility, the efficiency in optoelectronic devices and the homogeneity of the grown structures.

A big improvement can be achieved by applying methods to reduce the dislocation density like the epitaxial growth on structured substrates. However, the perfect solution is the homoepitaxial growth on GaN substrates. For MOVPE nitrogen and hydrogen are used as carrier gas and it is a well-known fact that the choice of the carrier gas affects the properties of the grown layer. For HVPE hydrogen must not be regarded, as an inert carrier gas because hydrogen is directly involved in the growth reactions as Chlorine is removed from the crystal surface by a reaction to HCl. Therefore a strong impact of the carrier gas composition must be expected.

With pure nitrogen a severe cracking of the GaN layer occurs. Cracking can be reduced by adding hydrogen. Another effect on the sample morphology is that the number and size of hexagonal pyramids on the surface is reduced with increasing hydrogen concentration. The growth rate on the other hand was reduced. After the optimization of the carrier gas composition, the V-III ratio was re-adjusted. A sample series with V-III ratios by varying the ammonia flow. This parameter has a significant impact on the growth rate. For the higher V-III values the surface morphology remained almost constant, whereas for the lowest value an upcoming coarse pattern replaced the typical fine structure. The effect of the reactor pressure was also important. Again a decrease in the growth rate was found. A roughening of the surface was found for decreasing reactor pressure. Based on the described experiment, Because of the mismatch in the thermal expansion coefficients a bowing of the structure was also found.

3.2. Wafer fabrication process

3.2.1. Selective area growth

In this paper, I report the selective area growth (SAG) of GaN directly on patterned (0001) sapphire and Si substrates by the MS-HVPE technique, thus eliminating an entire GaN growth sequence. The selective area growth leads to epitaxial lateral overgrowth (ELO) of the GaN on the patterned substrate. Bare sapphire substrates were coated with a silicon dioxide layer. The SiO_2 was photolithographically patterned and etched to make selective area patterns on the sapphire substrate. These substrates were used for the ELO-GaN growth. The pattern was chosen in such a manner that coalescence between the individual GaN islands nucleated in the openings was not possible in the growth times employed for these samples. This allowed for the growth of segregated GaN structures, in the form of hexagonal pyramids, on these patterned substrates. These structures were studied by optical and scanning electron microscopy. Photoluminescence and optical pumping studies were also performed to characterize the ELO-GaN layers. In this paper, most of device had processed as selective area growth (SAG) method.

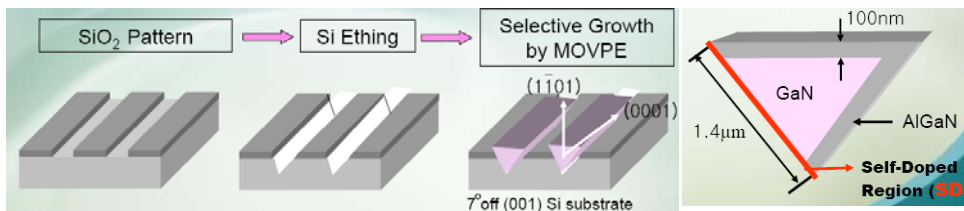


Fig.3.4 (a) SAG Growth process on Si substrate

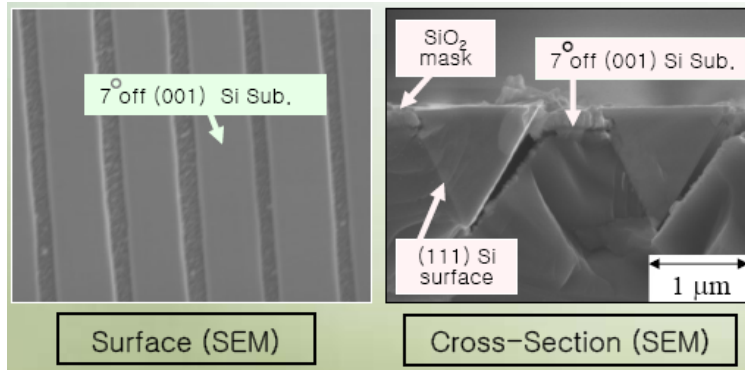


Fig.3.4 (b) SEM of SAG on Si substrate

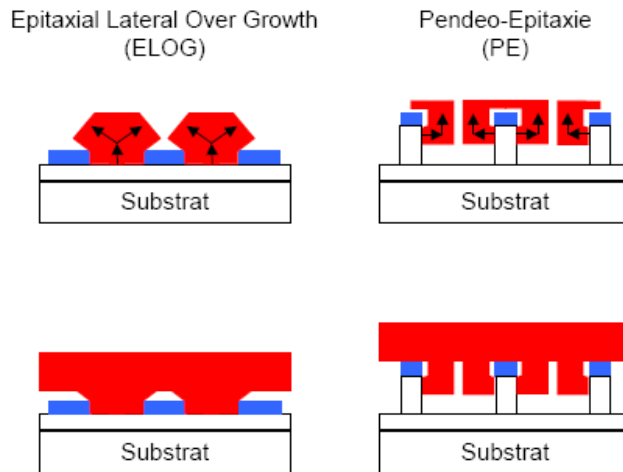


Fig 3.4 (c) GaN SAG types by HVPE

3.2.2. Metallization of GaN

Ohmic contacts to GaN related materials are an essential part of the production of all optical and electronic devices from the GaN system, but the requirements are particularly stringent for high power microwave devices, and the contacts are still not well understood or optimized. To

understand such contacts, and hence establish the major factors influencing electrical behaviour, studies of the microstructure of various contacts are required. Nitrides are wide band gap semiconductors that are supposed to exhibit reduced interface Fermi level pinning with respect to lower gap III-V's and large dependence of Schottky barrier heights on the metal work function. Yet, these issues are still largely undecided. This rather surprising situation, given the technological importance of the materials, is due in most part to the lack of a "standard" starting nitride surface, which in turn results from the difficulties of preparing clean, stoichiometric, and ordered surfaces by conventional techniques. It is well known that parasitic resistances, in the form of contact resistance, substantially reduce the overall performance of these electronic and optical devices [5]. Often the major loss of performance is due to high resistance metal-semiconductor "ohmic" contacts. Therefore, in order to attain optimum device performance, minimization of the contact resistance is absolutely necessary. Low resistance ohmic contacts for GaN are particularly challenging, as compared to the other well studied III-V compounds (GaAs and InP), because of its large band gap (3.4 eV). Although the nitrides, GaN, AlN, and InN, show great potential for use as ultraviolet and blue optical devices as well as high temperature/high power electrical devices, there still remains much more work to be done in obtaining ohmic contacts with small specific resistivities. In an earlier attempt to achieve ohmic contacts on GaN epilayers, Foresi et al used Al and Au contacts with 575 °C anneal cycle [6]. However, the specific contact resistivity of these contacts was relatively poor ($10^{-3} \Omega\text{-cm}^2$). In this dissertation, we report the process of an ohmic contact of device metallization schemes is Ti/Al for n-GaN, Ni/Au for p-GaN. We also introduced RTA (rapid thermal annealing) process.

3.3. Measurements

3.3.1. Photoluminescence

Photoluminescence (PL) spectroscopy is a contact-less, nondestructive method to probe the structure and composition of materials. PL is a process in which a chemical compound absorbs photons thus transitioning to a higher electronic energy state, and then radiates photons back out, returning to a lower energy state. The intensity and spectral content of the emitted photoluminescence is a direct measurement of various important material properties. The spectral distribution of PL from a semiconductor can be analyzed to nondestructively determine the electronic band-gap. This provides a means to quantify the elemental composition of compound semiconductor. The PL spectrum at low temperatures often reveals spectral peaks associated with impurities contained within the host material. The high sensitivity of this technique provides the potential to identify extremely low concentrations of intentional and unintentional impurities that can strongly affect material quality and device performance. The quantity of PL emitted from a material is directly related to the relative amount of radiative and nonradiative recombination rates. Nonradiative rates are typically associated with impurities and thus, this technique can qualitatively monitor changes in material quality as a function of growth and processing conditions. Ultimately, available chemical energy states and allowed transitions between states are determined by the rules of quantum mechanics. A basic understanding of the principles involved can be gained by studying the electron configurations and molecular orbitals of simple atoms and molecules.

The PL set up used in this work is shown schematically in fig. Basically, it consists of excitation light sources, a spectrometer, a lock-in amplifier and computer system. As excitation sources, the 325 nm line of a He-Cd laser was used. Its optical power was around 100 mW. For the detector, PM tube was used. For the low-temperature cryostate, Helium compressor was used, which is necessary to obtain the fullest spectroscopic information by minimizing thermally

activated non-radiative recombination processes and thermal line broadening. PL measurements in this work were carried out at 10 K.

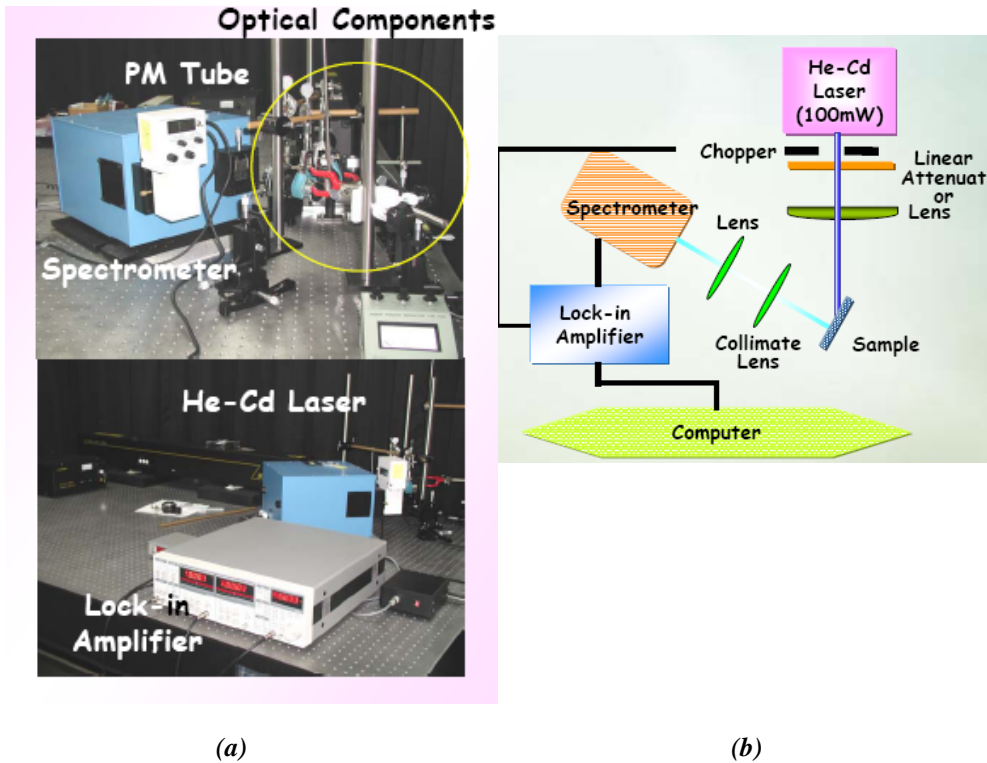


Fig.3.5. (a) Schematic diagram of the PL measurement (b) Experimental setup of PL system in Lab.

3.3.2. DXRD

X-ray diffraction techniques are based on the elastic scattering of x-rays from structures that have long range order. High-resolution x-ray diffraction is used to characterize thickness, crystallographic structure, and strain in thin epitaxial films. It employs parallel-beam optics. X-ray pole figure analysis enables one to analyze and determine the distribution of crystalline orientations within a crystalline thin-film sample. X-ray rocking curve analysis is used to quantify grain size and mosaic spread in crystalline materials.

X-rays are electromagnetic radiation with typical photon energies in the range of 100 eV - 100

keV. For diffraction applications, only short wavelength x-rays in the range of a few angstroms to 0.1 angstrom (1 keV ~ 120 keV) are used. Because the wavelength of x-rays is comparable to the size of atoms, they are ideally suited for probing the structural arrangement of atoms and molecules in a wide range of materials. The energetic x-rays can penetrate deep into the materials and provide information about the bulk structure.

X-rays are produced generally by either x-ray tubes or synchrotron radiation. In a x-ray tube, which is the primary x-ray source used in laboratory x-ray instruments, x-rays are generated when a focused electron beam accelerated across a high voltage field bombards a stationary or rotating solid target. As electrons collide with atoms in the target and slow down, a continuous spectrum of x-rays are emitted, which are termed Bremsstrahlung radiation. The high-energy electrons also eject inner shell electrons in atoms through the ionization process. When a free electron fills the shell, a x-ray photon with energy characteristic of the target material is emitted. Common targets used in x-ray tubes include Cu and Mo, which emit 8 keV and 14 keV x-rays with corresponding wavelengths of 1.54 Å and 0.8 Å, respectively. (The energy E of a x-ray photon and its wavelength is related by the equation $E = hc/\lambda$, where h is Planck's constant and c the speed of light)

X-rays primarily interact with electrons in atoms. When x-ray photons collide with electrons, some photons from the incident beam will be deflected away from the direction where they original travel, much like billiard balls bouncing off one another. If the wavelength of these scattered x-rays did not change (meaning that x-ray photons did not lose any energy), the process is called elastic scattering (Thompson Scattering) in that only momentum has been transferred in the scattering process. These are the x-rays that we measure in diffraction experiments, as the scattered x-rays carry information about the electron distribution in materials. On the other hand, in the inelastic scattering process (Compton Scattering), x-rays transfer some of their energy to the electrons and the scattered x-rays will have different wavelength than the incident x-rays. Diffracted waves from

different atoms can interfere with each other and the resultant intensity distribution is strongly modulated by this interaction. If the atoms are arranged in a periodic fashion, as in crystals, the diffracted waves will consist of sharp interference maxima (peaks) with the same symmetry as in the distribution of atoms.

Measuring the diffraction pattern therefore allows us to deduce the distribution of atoms in a material. The peaks in a x-ray diffraction pattern are directly related to the atomic distances. Let us consider an incident x-ray beam interacting with the atoms arranged in a periodic manner. For a given set of lattice plane with an inter-plane distance of d , the condition for a diffraction (peak) to occur can be simply written as

$$2d\sin\theta = n\lambda \dots\dots\dots(3)$$

Which is known as the Bragg's law, after W.L. Bragg, who first proposed it. In the equation, λ is the wavelength of the x-ray, θ the scattering angle, and n an integer representing the order of the diffraction peak. The Bragg's Law is one of most important laws used for interpreting x-ray diffraction data.

It is important to point out that although we have used atoms as scattering points in this example, Bragg's Law applies to scattering centers consisting of any periodic distribution of electron density. In other words, the law holds true if molecules or collections of molecules, such as colloids, polymers, proteins and virus particles, replace the atoms. Generally speaking thin film diffraction refers not to a specific technique but rather a collection of XRD techniques used to characterize thin film samples grown on substrates. These materials have important technological applications in microelectronic and optoelectronic devices, where high quality epitaxial films are critical for device performance. Thin film diffraction methods are used as important process development and control tools, as hard x-rays can penetrate through the epitaxial layers and measure the properties of both the film and the substrate.

There are several special considerations for using XRD to characterize thin film samples. First, reflection geometry is used for these measurements, as the substrates are generally too thick for transmission. Second, high angular resolution is required because the peaks from semiconductor materials are sharp due to very low defect densities in the material. Consequently, multiple bounce crystal monochromators are used to provide a highly collimated x-ray beam for these measurements. For example, a 4-crystal monochromator made from Ge is used to produce an incident beam with less than 5 arc seconds of angular divergence. Basic XRD measurements made on thin film samples include precise lattice constants measurements derived from 2θ scans, which provide information about lattice mismatch between the film and the substrate and therefore is indicative of strain & stress. Rocking curve measurements made by doing a scan at a fixed 2θ angle, the width of which is inversely proportionally to the dislocation density in the film and is therefore used as a gauge of the quality of the film. Superlattice measurement in multilayered heteroepitaxial structures manifests as satellite peaks surrounding the main diffraction peak from the film. Film thickness and quality can be deduced from the data. Reflectivity measurements of incidence x-ray can determine the thickness, roughness, and density of the film. This technique does not require crystalline film and works even with amorphous materials.

3.3.3. SEM/CL

The scanning electron microscope (SEM) is a type of electron microscope capable of producing high-resolution images of a sample surface. Due to the manner in which the image is created, SEM images have a characteristic three-dimensional appearance and are useful for judging the surface structure of the sample.

In a typical SEM, electrons are thermionically emitted from a tungsten or lanthanum hexaboride (LaB₆) cathode and are accelerated towards an anode; alternatively, electrons can be

emitted via field emission (FE). Tungsten is used because it has the highest melting point and lowest vapour pressure of all metals, thereby allowing it to be heated for electron emission. The electron beam, which typically has an energy ranging from a few hundred eV to 100 keV, is focused by one or two condenser lenses into a beam with a very fine focal spot sized 1 nm to 5 nm. The beam passes through pairs of scanning coils in the objective lens, which deflect the beam horizontally and vertically so that it scans the sample surface.



Fig.3.6 SEM/CL system

When the primary electron beam interacts with the sample, the electrons lose energy by repeated scattering and absorption within a teardrop-shaped volume of the specimen known as the interaction volume, which extends from less than 100 nm to around 5 μm into the surface. The size of the interaction volume depends on the beam accelerating voltage, the atomic number of the specimen and the specimen's density. The energy exchanges between the electron beam and the sample results in the emission of electrons and electromagnetic radiation which can be detected to produce an image. The most common imaging mode monitors low energy secondary electrons. Due

to their low energy, these electrons originate within a few nanometers from the surface. The electrons are detected by a scintillator-photomultiplier device and the resulting signal is rendered into a two-dimensional intensity distribution that can be viewed and saved as a digital image. This process relies on a raster-scanned primary beam. The brightness of the signal depends on the number of secondary electrons reaching the detector. If the beam enters the sample perpendicular to the surface, then the activated region is uniform about the axis of the beam and a certain number of electrons "escape" from within the sample. As the angle of incidence increases, the "escape" distance of one side of the beam will decrease, and more secondary electrons will be emitted. Thus steep surfaces and edges tend to be brighter than flat surfaces, which results in images with a well-defined, three-dimensional appearance. Using this technique, resolutions less than 1 nm are possible [7].

The spatial resolution of the SEM depends on the size of the electron spot which in turn depends on the magnetic electron-optical system which produces the scanning beam. The resolution is also limited by the size of the interaction volume, or the extent to which the material interacts with the electron beam. The spot size and the interaction volume are both very large compared to the distances between atoms, so the resolution of the SEM is not high enough to image down to the atomic scale, as is possible in the transmission electron microscope (TEM). The SEM has compensating advantages, though, including the ability to image a comparatively large area of the specimen; the ability to image bulk materials; and the variety of analytical modes available for measuring the composition and nature of the specimen. Depending on the instrument, the resolution can fall somewhere between less than 1 nm and 20 nm. In general, SEM images are much easier to interpret than TEM images.

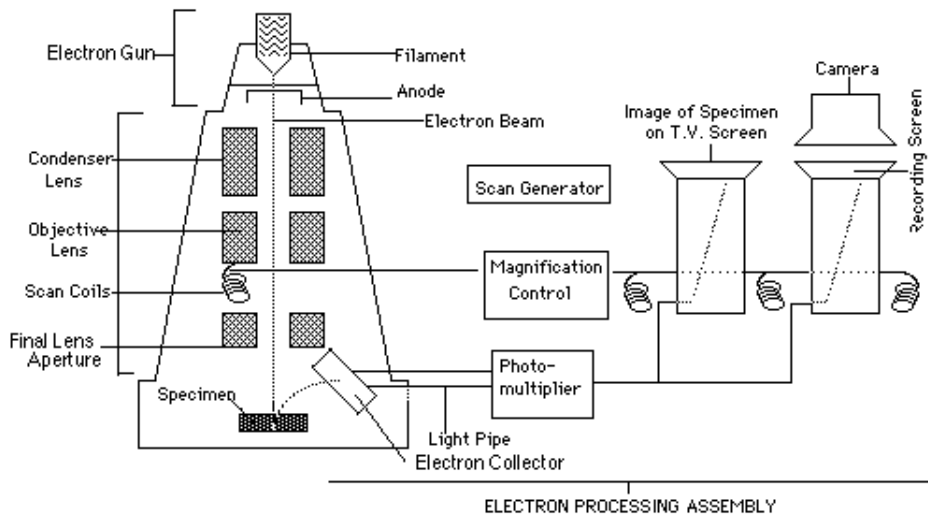


Fig.3.7 Schematic diagram of SEM system

Cathodoluminescence, the emission of light when atoms excited by high-energy electrons return to their ground state, is analogous to UV-induced fluorescence, and some materials such as zinc sulphide and some fluorescent dyes, exhibit both phenomena. Cathodoluminescence is most commonly experienced in everyday life as the light emission from the inner surface of the cathode ray tube in television sets and computer CRT monitors. In the SEM, CL detectors either collect all light emitted by the specimen, or can analyse the wavelengths emitted by the specimen and display a spectrum or an image of the cathodoluminescence in real colour.

Cathodoluminescence is an optical and electrical phenomenon whereby a beam of electrons is generated by an electron gun (e.g. cathode ray tube) and then impacts on a luminescent material such as a phosphor, causing the material to emit visible light. The most common example is the

screen of a television. In geology, mineralogy and materials science a scanning electron microscope with specialized optical detectors, or an optical cathodoluminescence microscope, is used to examine internal structures of semiconductors, rocks, ceramic, glass etc. in order to get information on the composition, growth and quality of the material.

Cathodoluminescence occurs because the impingement of a high energy electron beam onto a semiconductor will result in the promotion of electrons from the valence band into the conduction band, leaving behind a hole. When an electron and a hole recombine, it is possible for a photon to be emitted. The energy (color) of the photon, and the probability that a photon and not a phonon will be emitted, depends on the material, its purity, and its defect state. In this case, the "semiconductor" examined can,

In materials science and semiconductor engineering, cathodoluminescence will mostly be performed in either a scanning electron microscope or a scanning transmission electron microscope. In these cases, the highly focused beam of electrons impinges on a sample and induces it to emit light from a localized area. This light will be collected by an optical system, such as an elliptical mirror. From there, a fiber optic will transfer the light out of the microscope where it will be separated by a monochromator and then detected with a photomultiplier tube. By scanning the microscope's beam in an X-Y pattern and measuring the light emitted with the beam at each point, a map of the optical activity of the specimen can be obtained. The primary advantages to the electron microscope based technique is the ability to resolve features down to 10-20 nanometers, the ability to measure an entire spectrum at each point if the photomultiplier tube is replaced with a CCD camera, and the ability to perform nanosecond- to picosecond-level time-resolved measurements if the electron beam can be "chopped" into nano- or pico-second pulses. However, as the abilities are improved, the cost of the electron-microscope based techniques becomes very high. These advanced techniques are useful for examining low-dimensional semiconductor structures, such a

quantum wells or quantum dots.

Although direct bandgap semiconductors such as GaAs or GaN are most easily examined by these techniques, indirect semiconductors such as silicon also emit weak levels of light, and can be examined as well. In particular, the luminescence of dislocated silicon is different from intrinsic silicon, and can be used to map defects in integrated circuits. Cathodoluminescence is a technique that can be implemented in an optical or electron microscope with the proper accessories, and allows the optical properties of non-metallic materials to be examined.

3.3.4. E-CV

The study of capacitance associated with the depletion region of a schottky junction diode provides extensive information on the characteristics of electrically active centers in the near surface region of semiconductors. The contact of two materials with different workfunctions results in the diffusion of free carriers at the interface, until equilibrium state is obtained. Then, the transition regions at the interface of the two materials that free carrier are diffused out and depleted is composed of space charges. Consequently, the transition region is called as the space charge region or the depletion region. The absence of free carriers in the space charge region causes it to act as an insulator. Therefore, the represents a parallel plate capacitor having a space between two conducting materials, which is considered as

$$C = \epsilon(A/x) \dots \dots \dots (4)$$

Where C is the capacitance due to space charges, ϵ is permittivity, A is the junction area, and x is the width of the space charge region. We note that the capacitance, determined by the width of the space charge region, is dependent on applied bias voltage. Capacitive-voltage (C-V) measurement relies on the space charge region of the Schottky junction diode. Using the voltage

dependence of the space charge region, the information about net doping density can be obtained. When reverse bias voltage is applied to Schottky junction diode for the instance of an n-type semiconductor, the width of the space charge region is increased. In Schottky junction diode, there is no ambiguity of the width of the space charge region. Since it does not almost spread into a metal electrode but only spreads into a semiconductor. Moreover, it terminates at the breakdown voltage and cannot be extended further. Then, capacitance is determined by superimposing a small amplitude ac voltage on a DC voltage, which is defined as

$$C=dQ/dV.....(5)$$

Where dQ is the increased charge and dV is the incremental voltage.

Increasing from zero to small positive voltage adds an equal amount of charge increment to a metal electrode and s semiconductor. The charge increment in the semiconductor (dQs) is given by

$$dQs=qANd(x)dx.....(6)$$

Where Nd(x) is the net-doping density and dx is the increment of space charge region. We note that the net-doping density, which is due to shallow levels, is more or less different from the free carrier concentration obtained by Hall measurements. In the ideal case without defects and dislocations, the two would be the same.

From (5),(6), we find

$$C= qANd(x)(dx/dV).....(7)$$

Differentiating with respect to V and substituting dx/dV into (5), the net doping density is derived as

$$Nd(x) = 2 / \{q \epsilon A^2 (dC^2/dV)\} \dots \dots \dots (8)$$

Which can also be written as

$$C^{-2} = 2(V_{meas} - V_{bi}) / q \epsilon A^2 Nd(x) \dots \dots \dots (9)$$

In the derivation of the C-V relationship, we used the depletion approximation that completely neglects minority carriers and assumes the total depletion of majority carriers in the space charge region and perfect charge neutrality beyond the space charge region. This is generally a reasonably good approximation when a sample is uniformly doped. Furthermore we used the incremental charge variation of ionized donor concentration at the edge of the space charge region. However, the charges that actually move in response to ac voltage are mobile electrons, not ionized donors. From that point of view, the carrier profiling obtained from C-V measurements determines the majority carrier concentration, not the net doping density.

3.3.5. Hall measurement

The Hall effect was discovered by Hall in 1879 when he investigated the nature of the force acting on a conductor carrying current in a magnetic field. In particular, he measured the transverse voltage on gold foils. Later, K.R. Sopka gave A nice discussion of the discovery of the Hall effect, including the excerpt from Hall’s unpublished notebook. The Hall effect can be achieved by inducing a magnetic field perpendicular to the current flow direction in a semiconductor. Under such conditions, a voltage is developed perpendicular to both the current and magnetic field. This voltage is known as the Hall voltage. The origin of the Hall voltage can be seen by considering the forces on a charged carrier in the presence of a magnetic field (see figure 3.8):

$$F = qE + (qV \times B) \dots \dots \dots (10)$$

The first term is due to the total electric field driving the current through the sample. The second term is due to the Lorentz force on the charged carriers, and tends to deflect the carrier toward the side of the sample.

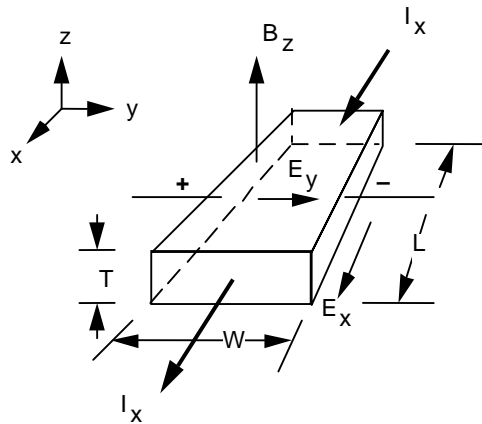


Fig.3.8 Hall effect device.

(Current flows in the positive x-direction. The applied magnetic field is in the positive z-direction. For a p-type sample an internal electric field develops in the positive y-direction.)

The direction of the deflection depends on the sign of the carrier's charge. Consider the example illustrated in Fig.3.8 Let's assume that we have a p-type semiconductor bar. The applied electric field and the current are in the positive x-direction, the applied magnetic field is in the positive z-direction. The y-component of the force is:

$$F_y = qE_y + (qV_x \times B_z) \dots\dots\dots (11)$$

This equation implies that unless something happens, all carriers moving in the sample will experience a force that will drive them toward one side of the sample. In this case, the holes would

move in the negative y-direction. If a number of holes were to collect at the right side of the sample, that side would take on a positive charge relative to the left side. This sets up an internal electric field in the +y-direction. Note that the only applied electric field is in the +x-direction. The force due to the internal electric field opposes the Lorentz force. To maintain a steady flow of current through the sample, we must have a balance of forces:

$$E_y = V_x \times B_z \dots\dots\dots (12)$$

Resulting in no net force on the carriers in the y-direction. The internal field can be set up by moving the holes only slightly to the right. The presence of the internal field can be detected by measuring the voltage developed across the sample:

$$E_y = V_y / w \dots\dots\dots (13)$$

Where w is the width of the sample. This is known as the Hall voltage. Carriers subject to an electric field move with a velocity called the drift velocity. The hole current in our sample can be written as

$$I_p = q p V_d A \dots\dots\dots (14)$$

Where +q is the hole charge, p is the hole density in #/cm³, v_d is the drift velocity, and A is the cross sectional area of the sample. If we convert this to an equation for the current density vector, where the magnitude J = I/A and the direction is parallel to the drift velocity, we have

$$J_p = q p V_d \dots\dots\dots (15)$$

The drift velocity is related to the electric field driving it through a proportionality constant known as the mobility:

$$V_d = \mu_p E \text{ for holes, } V_d = -\mu_n E \text{ for electrons, } \dots\dots\dots(16)$$

Substituting this into the current density equation, we get

$$J_p = q p \mu_p E \text{ for holes, } J_n = q p \mu_n E \text{ for electrons, } \dots\dots\dots (17)$$

Using this relationship in our equation for the field E_y , we get:

$$E_y = V_x B_z = (J_x/q p) B_z = R_H J_x B_z \dots\dots\dots (18)$$

Where $R_H = 1/qp$ is called the Hall coefficient. You can also show that $R_H = -1/qn$ for n-doped samples. We can also extend this model to consider the Hall effect when both electrons and holes are present, resulting in the following equation (for small fields):

$$R_H = \frac{1}{q} \frac{(P \mu_p^2 - n \mu_n^2)}{(P \mu_p^2 + n \mu_n^2)} \dots\dots\dots (19)$$



Fig.3.9 Hall Measurement System.

References

- [1] V. Narayanan, K. Lorenz, W. Kim, S. Mahajan, *Applied Physics Letters* 78, 1544 (2001)
- [2] E. Aujol, A. Trassoudaine, D. Castelluci and R. Cadoret, *Mater. Sci. Eng. B* 82, 65 (2001).
- [3] P. R. Tavernier, E. V. Etzkorn, Y. Wang and D. R. Clarke, *Appl. Phys. Lett.* 77, 1804 (2000).
- [4] T. Paskova, E. M. Goldys, R. Yakimova, E. B. Svedberg, A. Henry and B. Monemar, *J. Crystal Growth* 208, 18 (2000).
- [5] "T. C. Shen, G. B. Gao, and H. Morkoq, *J. Vat. Sci. Technol. B* 10, 2113 (1992).
- [6] J. S. Foresi and T. D. Moustakas, *Appl. Phys. Lett.* 82, 2859 (1993).
- [7] Danilatos, G.D (1988). "Foundations of environmental scanning electron microscopy" (in English). *Advances in Electronics and Electron Physics* 71: 109-250.

Chapter 4.

Mixed source HVPE growth experiment for Bulk Characteristics

The uniqueness of HVPE in growing thick layers arises due to its near-equilibrium nature of the process. In such a process, the growth rate is proportional to the input amount of the active gases. Near equilibrium nature arises due to the reversible processes occurring at the interface due to the volatility of chlorides of group III (e.g., InCl) at the operating temperatures [1]. In this report, we have tried to indicate the strength of MS-HVPE. This technique of MS-HVPE's specific phenomenon enables to make new white LED competitive.

4.1. GaN growth

GaN crystallizes both in the hexagonal wurtzite and zincblende forms [2-5]. However, wurtzite polytype appears to be more common than the zincblende polytype. This semiconductor has been most extensively studied [6-8] among all the III-V nitrides. Similar to AlN, chemical stability at elevated temperatures combined with its wide bandgap has made GaN an attractive material for device operation in high temperatures and caustic environments. While the thermal stability of GaN allows high temperature processing steps to be performed, the chemical stability of GaN requires that dry etching methods be used for processing. Many different growth techniques have been employed to obtain high-quality single-crystal GaN films. As a result, it can now be grown with background concentrations as low as mid-E16 cm⁻³. In order to produce GaN, large kinetic barriers of crystal formation have been overcome by employing high temperatures, activated nitrogen species and/or high nitrogen pressures.

To study the growth of GaN by HVPE [9-11], a horizontal hot-wall reactor was made with

quartz tubes and the substrate was mounted horizontally with respect to the oncoming gas streams. The HVPE system was designed to be able to grow AlN, GaN and/or their ternary compounds by using metalorganic materials and ammonia as preliminary sources. GaN and AlN buffer layers were each formed by HVPE on sapphire substrate to test growth condition. In this paper, we studied about the surface morphology problems to get optimized crystal quality.

The growth temperature during buffer growth is an important parameter to improve crystal quality of devices, which need step growth. It also unavoidably occurs in the specific fabrication method. Thus, we need to examine the influence of the growth temperature to develop hetero-structures with high -quality GaN. The GaN samples were analyzed by PL measurements at 300 K and RMS roughness. Here, we keep the following problems in mind during the epitaxial growth. As mentioned, surface morphology is basic issue of GaN growth technology.

4.1.1 Buffer growth of GaN layer

The experiments were carried out in a conventional atmospheric horizontal HVPE system by using N₂ as the carrier gas. The GaN layers were grown on GaN buffer/Al₂O₃ substrates. The AlN layers were also grown on AlN buffer/Al₂O₃ substrates. The reactor is divided into six separate temperature zones to create the definite temperature profile. The NH₃ flow rates and HCl flow rates were kept at 300 sccm and 12 sccm, respectively [12]. Either a mixture including nitrogen or only nitrogen was used as the carrier gas. The GaN layers were grown by the use of metallic Ga and ammonia (NH₃). High purity NH₃ gas and Ga ingot were employed as nitrogen and gallium sources, respectively. The samples were measured by PL system and atomic force microscope (AFM) and compared with each other.

A. GaN Buffer

Fig.4.1 shows the 3D AFM images of GaN epitaxial layer by mixed source HVPE method. And Fig.4.1 presents the RMS roughness of each sample. We could get smallest RMS roughness at 800 °C. And FWHM (Full Wave Half Maximum) of CL also was sharper than others at 800 °C.

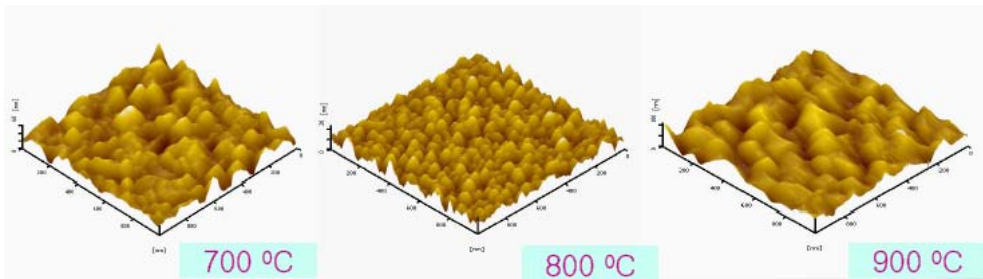


Fig.4.1 the 3D AFM images of GaN buffer layer by mixed source HVPE method

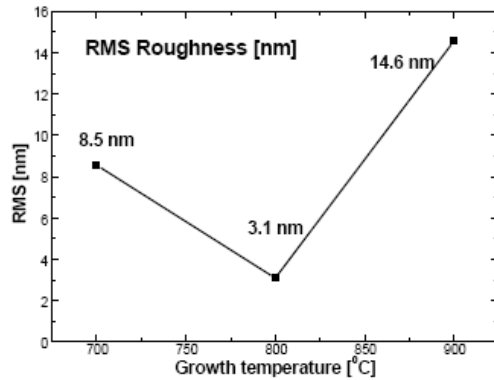


Fig.4.2 the RMS roughness of each samples of GaN buffer layer by mixed source HVPE method

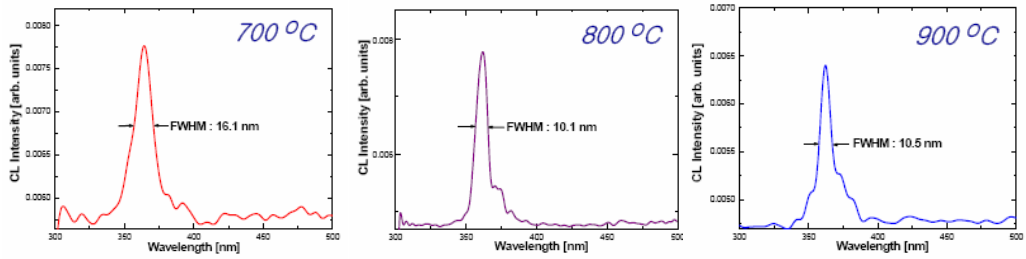


Fig.4.3 CL measurement of each GaN buffer layer

B. AlN Buffer

Fig.4.4 shows the 3D AFM images of AlN epitaxial layer by mixed source HVPE method. And Fig.4.4 presents the RMS roughness of each sample. RMS of AlN buffer is proportional to growth temperature different from GaN layer. But FWHM(Full Wave Half Maximum) of CL was narrowest at 1000 °C.

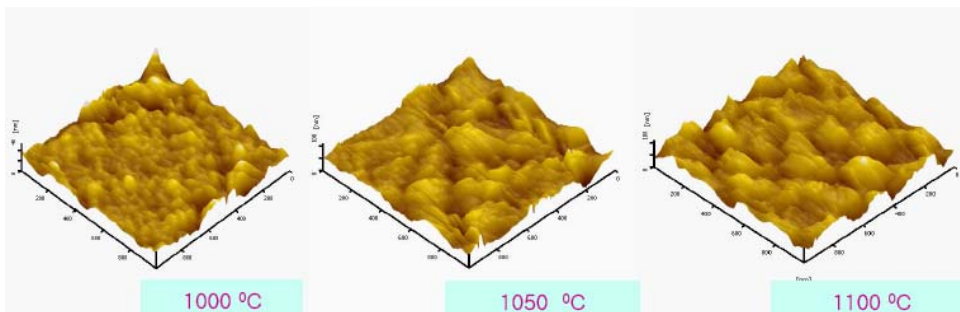


Fig.4.4 the 3D AFM images of AlN buffer layer by mixed source HVPE method

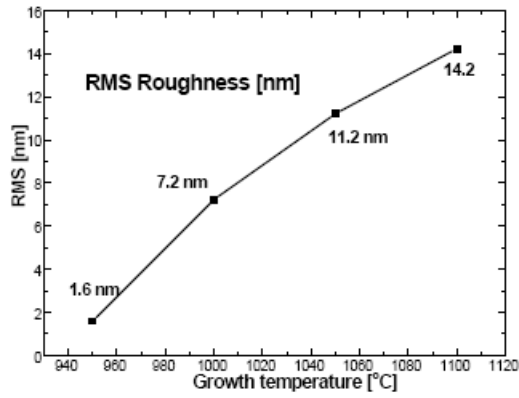


Fig.4.5 the RMS roughness of each samples of AlN buffer layer by mixed source HVPE method

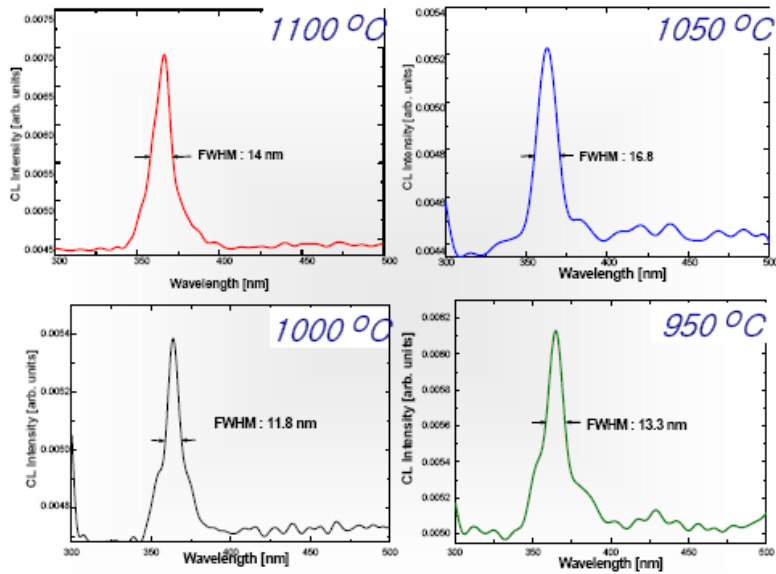


Fig.4.6 CL measurement of each GaN buffer layer

4.1.2. Mg-doped GaN layer

One of the most important issues for GaN-based devices is the control of p-type doping. Various types of acceptor atoms including Mg and C were tried for p-doping. The device performance of GaN-based material strongly depends on doping concentration and activation. We studied the growth of Mg-doped GaN layers by the mixed source HVPE method. These experiments led to compensate high resistivity of GaN material. Fig.4.7 shows the optical microscopic images of GaN epitaxial layer by mixed source HVPE method.

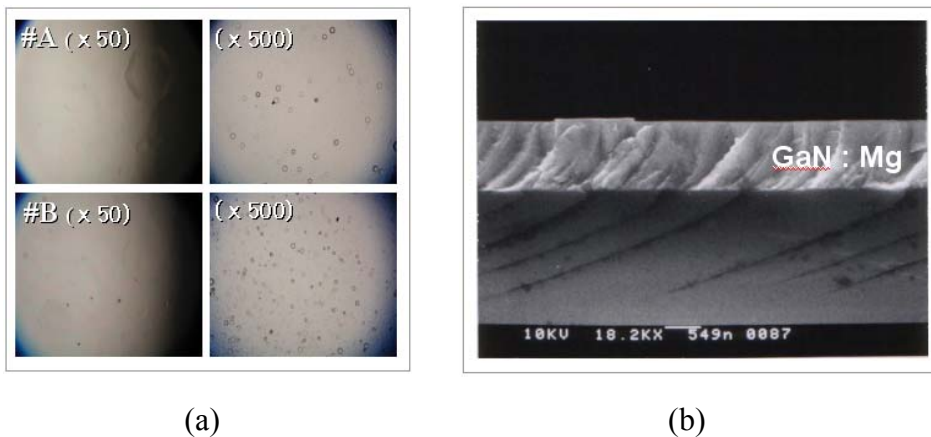


Fig.4.7 (a) The surface of GaN film by MS-HVPE (the Mg atomic fraction ; sample A ~0.026, sample B~0.057) (b) SEM image of cleaved facet of Mg-doped GaN film

The carrier concentration at room temperature increased with Mg atomic fraction. We also found that the activation energy of grown sample was 378 meV at 250 K~300 K. The optimized Mg-doped GaN layer was applied to the fabrication of DH LED structure.

Fig.4.8 shows XRD spectrum of Mg-doped GaN by mixed source HVPE method. It presents that Mg-doping in mixed-source HVPE does not have a great effect on the GaN crystalline structure.

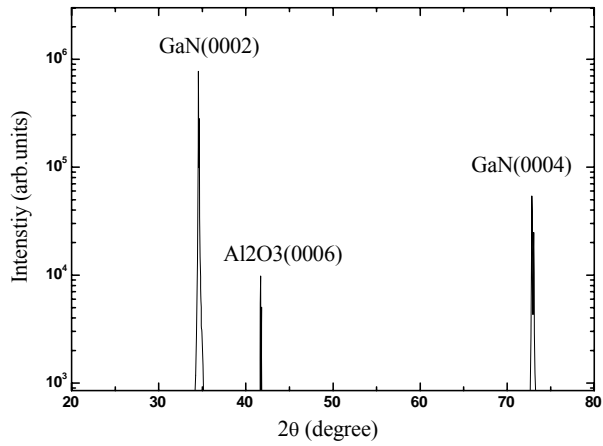


Fig.4.8 XRD spectrum of Mg-doped GaN On sapphire by mixed source HVPE

Fig.4.9 shows AFM Images of Mg-doped GaN. The RMS roughness of the Mg-doped GaN films is about 2.0 nm and 9.5 nm, respectively.

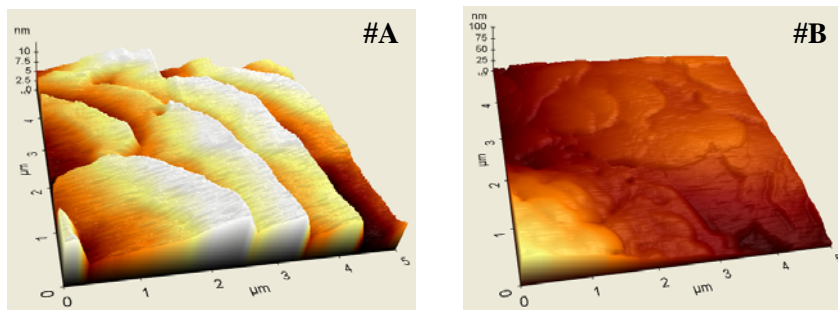


Fig.4.9 AFM Images of Mg-doped GaN (scan area: $5 \times 5 \mu\text{m}^2$)

Fig.4.10 shows hole concentration and Mobility dependence on atomic fraction of Mg. The hole concentration increase linearly, As Mg atomic fraction in $[\text{Ga}+\text{Mg}]$ solution increases. But

mobility decreases because the ionized impurity scattering increase

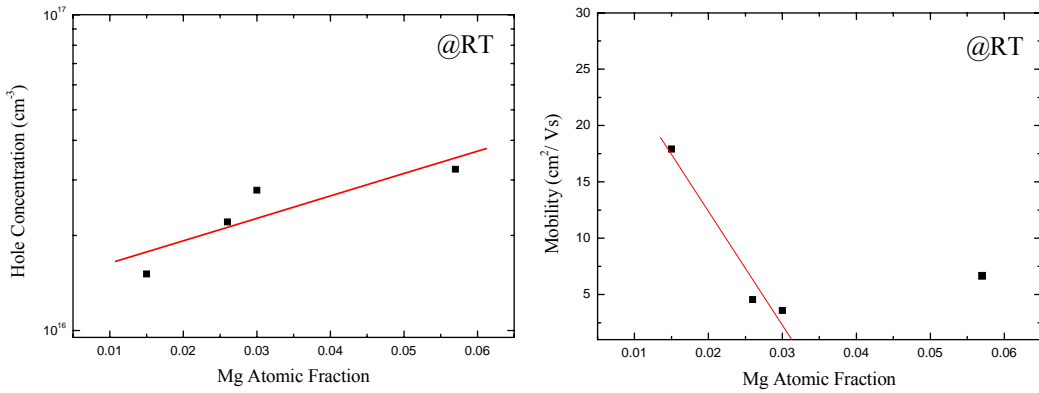


Fig.4.10 Hole Concentration and Mobility vs. atomic fraction of Mg

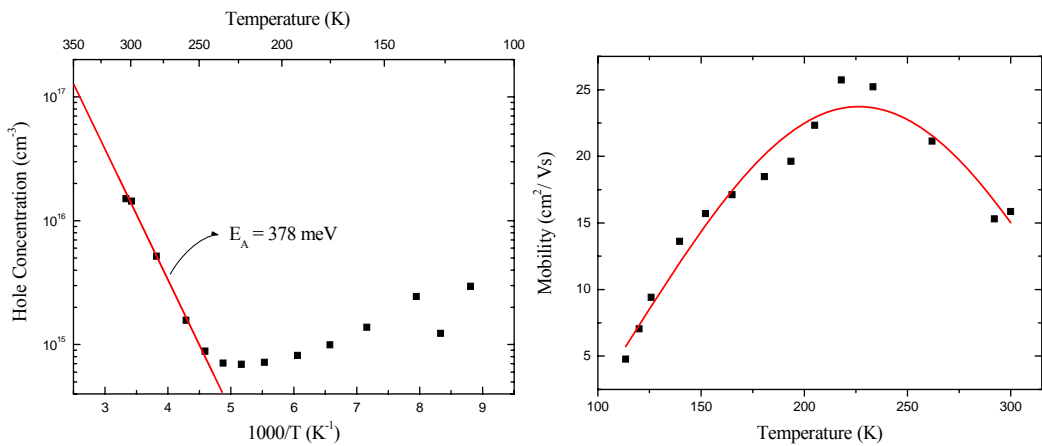


Fig.4.11 Temperature dependence of Hall measurement

We also got activation energy by Hall measurement. The activation energy was 378 meV for Mg-doped GaN (250~300 K). In general, an activation energy of Mg-doped GaN grown by MOCVD is about 110~215 meV. Fig.4.11 shows the hole concentration increases at $T > 250$ K. It

means the ionization of acceptors increases. But hole concentration decreases at $100\text{ K} < T < 150\text{ K}$ because hopping conduction occurs due to the high acceptor concentration. The mobility decreases at $T > 250\text{ K}$ because of phonon scattering. But it increases at $T < 250\text{ K}$ due to ionized impurity scattering.

4.2. AlGaN Growth

A. Introduction

Currently there is some controversy in the choice of method for determining Al mole fraction in AlGaN. One of the key properties of an alloy is the compositional dependence of the energy bandgap. This dependence appears to be controversial in the case of AlGaN. Yoshida et al. [13] observed that the energy bandgap of $\text{Al}_x\text{Ga}_{1-x}\text{N}$ deviates upwards with increase in AlN mole fraction. However, Hagen et al. [14] and Koide et al. [15] observed that energy bandgap deviates downward with increase in AlN mole fraction. They noted that the energy bandgap of $\text{Al}_x\text{Ga}_{1-x}\text{N}$ might be given by

$$E_g(x) = xE_g(\text{AlN}) + (1 - x)E_g(\text{GaN}) - bx(1 - x) \dots\dots\dots(1)$$

where $E_g(\text{GaN}) = 3.39\text{ eV}$, $E_g(\text{AlN}) = 6.20\text{ eV}$, $b = 1.0 \pm 0.3\text{ eV}$.

However, recent studies [16,17] suggest that a linear relationship (e.g., $b = 0$) between the energy bandgap of this ternary and the AlN mole fraction can be attained. According to Yoshida et al. [13] the energy bandgap E_g of AlGaN is a nonlinear function of the Al mole fraction. AlGaN is reasonably linear with respect to the AlN mole fraction.

While according to Koide et al. the bowing parameter $b \sim 1.0\text{ eV}$, according to Yoshida et al. $b \sim 0.80\text{ eV}$ [13]. The optical energy bandgap of AlGaN with Al mole fraction is rather a linear

function of x . A recent Hall measurement for n-Al_{0.09}Ga_{0.91}N at 300 K yielded a mobility of 35 cm²/V.s corresponding to a carrier concentration of 5×10^{18} cm⁻³ [18].

Other Hall measurements on Mg-doped p-Al_{0.08}Ga_{0.92}N grown by MOVPE indicated that the hole mobility decreases with increase in temperature, and that it is about 9 cm²/V.s for a doping density of 1.48×10^{19} cm⁻³ [19]. Given the fact that the carrier concentration is high, and that the inter grain scattering is present even in the best samples, such a low mobility is expected. Until recently it was noted that the resistivity of unintentionally doped AlGa_xN however increases rapidly with increasing AlN mole fraction, and AlGa_xN becomes insulating for AlN mole fraction exceeding 20 %.

For example, the n-type carrier concentration dropped 10^{20} to 10^{17} cm⁻³ and mobility increased from 10 to 0.4 cm²/V.s as the AlN mole fraction was increased from 0.0 to 0.3. This is probably due to an increase in the native defect ionization energies with increasing AlN. Although it was not known how the doping characteristics of AlGa_xN with dopant atoms such as Si and Mg react to the variation of AlN mole fraction, it was anticipated that, as the AlN mole fraction increases, the dopant atoms would move deeper into the forbidden energy bandgap. The scenario has lately changed, and AlGa_xN with Al mole fraction as high as 50~60 % and up to 30 % is dopable by n-type and p-type impurity atoms, respectively. More however, lattice constant dependency of promising results should soon be expected as AlN can be doped both n- and p-type. The ability to dope high mole fraction AlGa_xN, especially when low resistivity p-type material is required, is important, because it may otherwise restrict the overall structure of devices such as laser diodes. Despite the fact that good optical field confinement may be obtained with low Al mole fraction in AlGa_xN, this is an important issue, as devices operating in UV will surely be investigated.

Generally, for the HVPE growth of GaN epitaxial layers, a Ga and a NH₃ are used as a volatile chlorine compound and a nitrogen precursor, respectively. In case of the AlGa_xN growth, Al

metallic source is also usually loaded in the HVPE chamber and HCl is passed over the metals to form aluminum chloride. The AlGa_xN cladding layer with an arbitrary carrier concentration can be employed on high power light emitting diode (LED) structures with an InGa_xN/GaN MQWs [20]. Generally, silane (SiH₄) is commonly used as a source for n-type doping [21].

In this paper, I got the Al_xGa_{1-x}N layers on GaN/Al₂O₃ substrates for various source zone temperatures of the metallic Ga mixed with Al. The Al_xGa_{1-x}N layers are characterized by x-ray diffraction (XRD) measurements. I report the new results from the growth of Te-doped by a new attempt and Si-doped AlGa_xN layers using mixed-source HVPE, respectively. The n-type doping of AlGa_xN layers were attempted on a (0001) sapphire substrate using Al-Ga-Te (or Si), HCl and NH₃. The n-type AlGa_xN cladding layers was achieved successfully, and the InGa_xN/GaN MQWs are grown on SAG-Te (or Si)-doped AlGa_xN cladding layers by MOCVD, respectively. And p-n diodes are fabricated, the optical properties are investigated. I experiment the EL properties of SAG-LEDs for two cladding layers, respectively. The highlight of the present study is on the successful growth of Te-doped AlGa_xN layers by our mixed source HVPE method.

B. Experiment

The Al_xGa_{1-x}N layers are grown on GaN templated (0001) sapphire substrates. The metallic Ga mixed with Al as a source material is loaded in the HVPE chamber. NH₃ and Al-Ga chloride formed by HCl that is flown over Ga mixed with Al are used. In order to change the composition x of Al_xGa_{1-x}N layer by mixed-source HVPE, the source zone temperatures of the metallic Ga mixed with Al are varied from 700 °C to 1000 °C. The Al_xGa_{1-x}N layers are grown at 1090 °C. The SiO₂ mask with the approximately 2500 Å thickness formed by sputter for SAG is used. The SAG window is formed by conventional photolithography and wet chemical etching. The SAG diameter is 250 μm. The Te and Si-doped Al_xGa_{1-x}N (x = 0.16) are achieved by putting small amount of Te

(or Si) into the Al-Ga source, respectively. The thickness of the sample is typically 20 μm and shows n-type conduction with mirror-like surface morphology. For the growth of n-type AlGa_N, we use metallic Te and undoped single crystalline Si as an n-type source. To change the carrier concentration of n-type AlGa_N layers, the X_{Te}^{ℓ} (where X_{Te}^{ℓ} is atomic fraction of Te in the Ga-Al-Te solution) is varied from 0.003 to 0.042, and the X_{Si}^{ℓ} (where X_{Si}^{ℓ} is the atomic fraction of Si in the Ga-Al-Si solution) is varied from 0.102 to 0.218. InGa_N/Ga_N MQWs are grown on SAG-Te-doped and SAG-Si-doped AlGa_N cladding layers by MOCVD, respectively. The InGa_N/Ga_N MQWs consist of 7 wells and 6 barriers. The thicknesses of InGa_N well and Ga_N barrier are 2.5 nm and 6 nm, respectively.

C. Results

Fig.4.12(a) shows the typical XRD result of the undoped Al_xGa_{1-x}N layers grown by mixed-source HVPE using the ω -mode scan of (0002) reflecting planes. In case of the Al_xGa_{1-x}N layer grown at source zone temperature of 900 °C, the rocking curve shows two peaks. One of the two peaks is the (0002) peak of Ga_N; the other is that of AlGa_N. The Al mole fraction of the AlGa_N is determined by calculating the difference of peak positions between AlGa_N and Ga_N peaks assuming that the (0002) peak of Ga_N is constant at $2\theta = 34.53$ degree and Vegard's law is valid.

Fig.4.12 1(b) shows the source zone temperature dependence of the Al composition of the Al_xGa_{1-x}N layer. The sample with Al composition of 80 % shows large compositional fluctuation with non-uniformity of Al in sample due to hillocks and islands [22]. From these results, we find that the range of the source zone temperature for the composition x of Al_xGa_{1-x}N layer limits the application scope of the mixed-source HVPE.

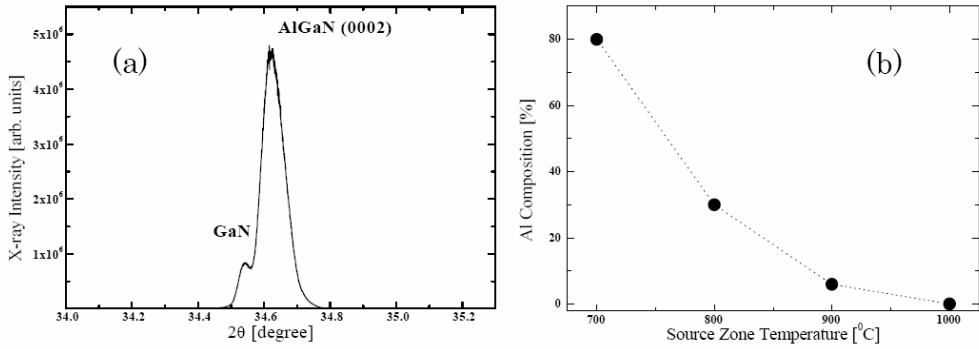


Fig.4.12 (a) Typical XRD results of the $Al_xGa_{1-x}N$ layers grown at source zone temperature of 900 °C. (b) Dependence of the Al composition of the $Al_xGa_{1-x}N$ layer on source zone temperature.

Fig.4.13 shows the typical cross-section SEM images of Te (or Si)-doped AlGaIn layers grown by mixed-source HVPE. The thicknesses of the Te (or Si)-doped AlGaIn layers are 30 μm and 20 μm, respectively.

The carrier concentrations of Te (or Si)-doped $Al_{0.16}Ga_{0.84}N$ layers are measured at 300 K by Hall effect measurement using the van der Pauw technique. The n-ohmic of the n- $Al_{0.16}Ga_{0.84}N$ layers is formed by e-beam deposited Ti(500 Å)/Al(1000 Å) as shown in inset Fig. 3(a). Annealing is performed at 600 °C under N₂ for 60 s.

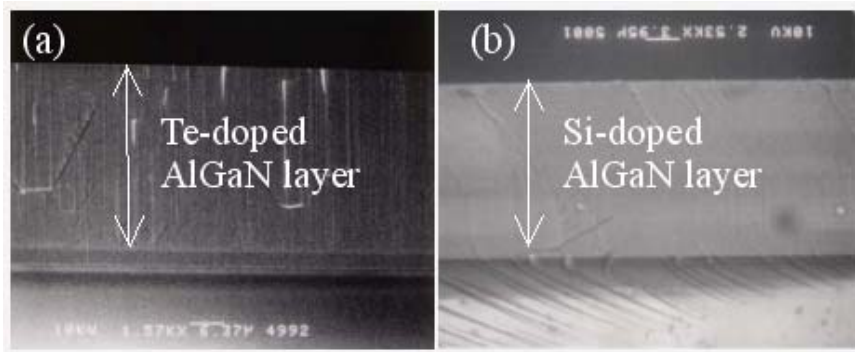


Fig.4.13 Typical SEM images of n-type $Al_{0.16}Ga_{0.84}N$ layers grown by mixed-source HVPE.

(a) Te-doped $Al_{0.16}Ga_{0.84}N$ layer (b) Si-doped $Al_{0.16}Ga_{0.84}N$ layer

Fig.4.14 shows the dependence of the carrier concentration of n-type AlGaIn layers on the atomic fraction of Te and Si in the Ga-Al source. In case of Te-doped $Al_xGa_{1-x}N$ ($x = 0.16$), the carrier concentration is varied from 1.1×10^{18} to $8.0 \times 10^{18}/\text{cm}^3$ while in case of Si-doped one, it is varied from 2.0×10^{16} to $1.1 \times 10^{17}/\text{cm}^3$. The carrier concentration did not increase linearly with the atomic fraction of Te in the source. The Te and Si activation energies are not estimated yet, but the successful growth of a Te-doped AlGaIn layer shows that our novel method provides the possibility of a high n-type concentration of the Te-doped AlGaIn layer. This shows that Te doping is more suitable to get a high n-type concentration by mixed-source HVPE.

The InGaIn/GaN MQWs structures are grown on SAG-Te-doped and SAG-Si-doped AlGaIn cladding layer by MOCVD, respectively, and p-n diodes are fabricated. EL characteristics of these fabricated LED structure at room temperature are evaluated by injecting DC current into these LED structures.

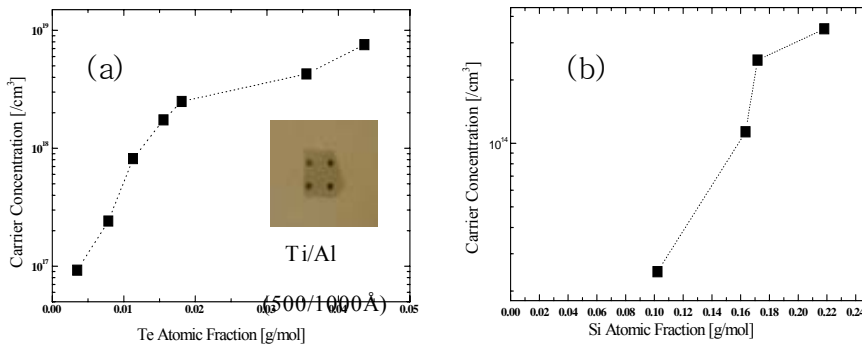


Fig.4.14 Dependence of the carrier concentrations of the n - $Al_{0.16}Ga_{0.84}N$ layers on the atomic fraction of Te (or Si). (a) Te-doped $Al_{0.16}Ga_{0.84}N$ layer (b) Si-doped $Al_{0.16}Ga_{0.84}N$ layer

Fig.4.15 shows the EL spectra of LEDs of the two different cladding layers at room temperature. The typical EL spectrum of SAG-InGaN/GaN MQWs LED structure on SAG-Te-doped $Al_xGa_{1-x}N$ ($x = 0.38$) cladding layer is shown in Fig.4.15 (a). The wavelength of emission peak is observed at nearly 488 nm (2.5 eV) and the full width at half maximum (FWHM) is 355 meV. Fig.4.15 (b) shows the EL spectrum of SAG-InGaN/GaN MQWs LED structure on SAG-Si-doped $Al_xGa_{1-x}N$ ($x = 0.38$) cladding layer. The wavelength of emission peak is about 520 nm (2.4 eV) and the FWHM is 420 meV. The difference between two wavelengths may be because the flatness of SAG-Si-doped AlGa_N cladding layer is not uniform. The thicknesses of InGa_N well and barrier might be varied along the distance from the center to the edge of the SAG window. This will be the reason why we have got the large FWHM values of the LEDs.

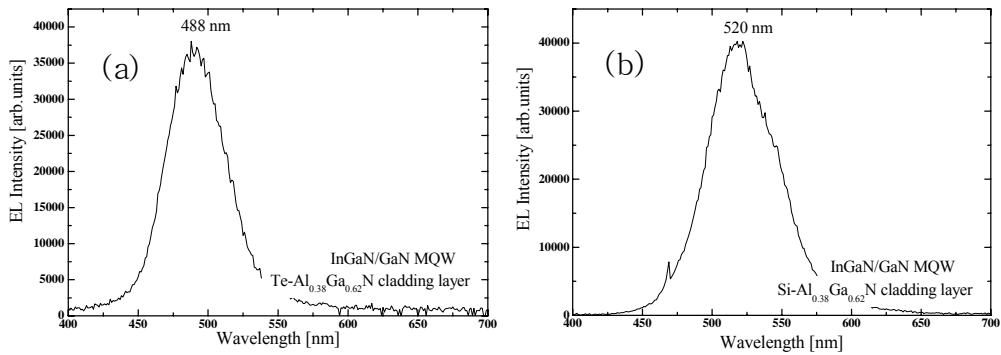


Fig.4.15 EL spectra of LEDs of the two different cladding layers at room temperature.

(a) SAG-Te-doped $Al_{0.38}Ga_{0.62}N$ cladding layer (b) SAG-Si-doped $Al_{0.38}Ga_{0.62}N$ cladding layer

4.3. InGaN growth

A. Introduction

InGaN can be a promising strained QW material having use for the fabrication of electrical and optical devices, such as LED's and lasers which can emit in the violet or blue wavelengths. During last several years there has been significant progress in the growth and characterization of this material. Osamura et al. [23] measured the bandgap across the entire compositional range and found a smooth variation with some bowing represented by

$$E_g(x) = (1 - z)E_g(InN) + zE_g(GaN) - bx(1 - x) \dots \dots \dots (2)$$

Where $E_g(GaN) = 3.40$ eV, $E_g(InN) = 2.07$ eV, and $b = 1.0$ eV. The bandgap dependence of $In_zGa_{(1-z)}N$ (z is the In mole fraction) on In mole fraction has also been deduced by a number of researchers [23-26]. The observed and calculated dependencies of InGaN energy bandgap with InN

mole fraction are shown in Fig. 2. From this figure one may note that, despite variations in the growth conditions, the experimental dependence of energy bandgap on In mole fraction tends to follow a regular trend, and that the calculated results from (4) agree well with experiments. Nagatomo et al. [27] have observed that the InN lattice constant is 11% larger than GaN that places strict limits on the InN content and thickness of InGaN layers on GaN. They have also noted that the $\text{In}_z\text{Ga}_{(1-z)}\text{N}$ lattice constant varies linearly with InN mole fraction up to at least $z = 0.42$, thus violating Vegard's law for $x > 0.42$. Yoshimoto et al. [25] observed that for a particular alloy composition ($x = 0.2$) grown on sapphire a reduction in carrier concentration from 10^{20} to 10^{18} cm^{-3} and an increase in the carrier mobility from less than $10 \text{ cm}^2/\text{Vs}$ to $100 \text{ cm}^2/\text{Vs}$ can be possible if the deposition temperature is increased from $500 \text{ }^\circ\text{C}$ to $900 \text{ }^\circ\text{C}$. Similar results were observed by them [28] again in 1992 for films grown onto ZnO substrates. InN mole fractions as large as 23 % were achieved by these workers. Nakamura and Mukai [29] discovered that if InGaN films are grown on high-quality GaN films, they could exhibit significantly improved quality.

Thus, from the reports cited above it may be concluded that the major challenge of obtaining high mobility InGaN is to find a compromise in the growth temperature, since InN is unstable at typical GaN deposition temperatures. Nakamura et al. have since expanded the study of InGaN employing Si and Cd [30] as dopant atoms. Note that In incorporation at these elevated temperatures is very inefficient because of In desorption and flow rates for In precursor larger than those used for GaN must be employed just to get 20~30 % in the solid. In addition the ammonia flow rate must be increased well above that used for GaN growth only. A review of various transport properties of GaInN and AlInN is given by Bryden and Kistenmacher [31], and the growth and mobility of p-GaInN is presented by Yamasalu et al. [32].

B. Growth temperature vs. Phase shape of InGaN Crystal

We investigated phase shape of InGaN layers which are grown by MS-HVPE. Growth temperature was varied from 650 °C to 800 °C at same temperature source zone of 900 °C. And we increased indium composition purposely to study various crystal formation of MS-HVPE. As known, high indium composition in InGaN on GaN makes indium segregation and accelerates nano phase such as nano-rod. Table 4.1 shows growth condition for each sample.

Table 4.1 Growth conditions of samples

	Temperature of source zone	Temperature of growth zone	HCl flow	Growth time	Phase shape	In composition (XPS)
1	900°C	800°C	20sccm	60min	Tetrapod	80%
2	900°C	750°C	20sccm	60min	Symmetric cluster	27%
3	900°C	700°C	20sccm	60min	Asymmetric cluster	37%
4	900°C	650°C	20sccm	60min	Maple Leaf	44%

We got various phase shape on each substrate according to growth temperature. We also got various Indium compositions in InGaN nano phase crystal as Fig.4.17~4.49. It was important physical phenomenon that was a clue of multi spectrum emission.

Fig.4.16 shows room temperature CL spectrum of sample grown at 750 °C on silicon substrate. Three peaks of 400 nm, 440 nm and 520 nm were observed at localized region. It presents extraordinary state being seen in mixed source HVPE growth mechanism. In this experiment, typical surface images of the InGaN layer grown on each substrate taken by scanning electron

microscope (SEM) were similar. But growth temperature had a strongly effect on phase shape.

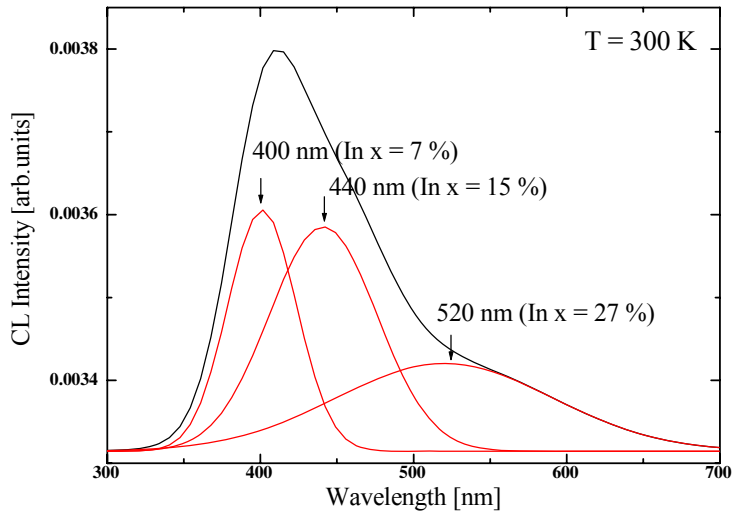


Fig.4.16 CL spectrum of sample grown at 750 °C

Fig.4.17 shows InGa_N phase shape on c-plane sapphire. At low temperature growth, mapole leaves were seen all over surface of substrate. As growth temperature increasing, Indium composition reduces gradually. But it increased at 800 °C, tetrapod shape. I think it needs supplementary experiment to verify a cause. In this experiment, we confirmed MS-HVPE technology had specific chemical and physical phenomenon dislike other crystal growth system. Especially, for indium related Ga_N, multi spectrum emission can be possible. We targeted its phenomenon for making white emission LED.

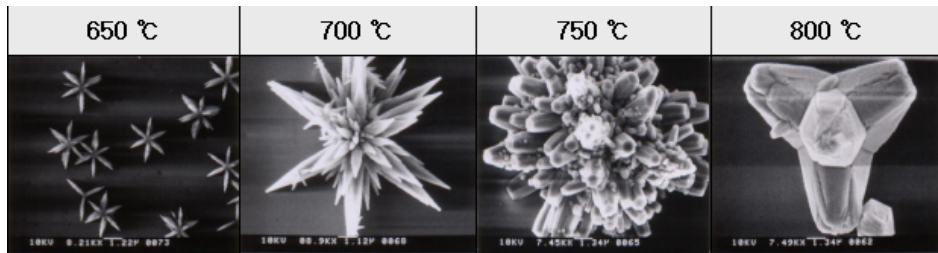


Fig.4.17 InGaN phase shape on c-plane sapphire

Fig.4.18 shows InGaN phase shape on silicon substrate. And Fig.4.19 also shows InGaN phase shape on r-plane sapphire. We think there are different compositions in each hexagonal rod of nano phase shape.

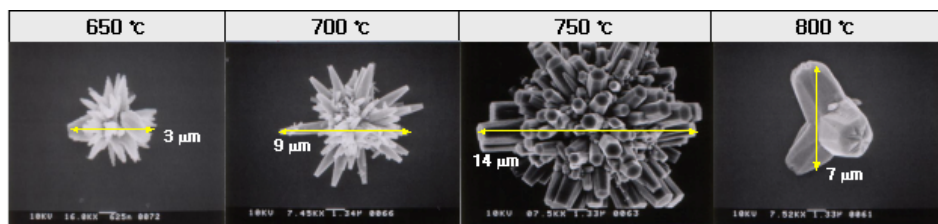


Fig.4.18 InGaN phase shape on silicon substrate

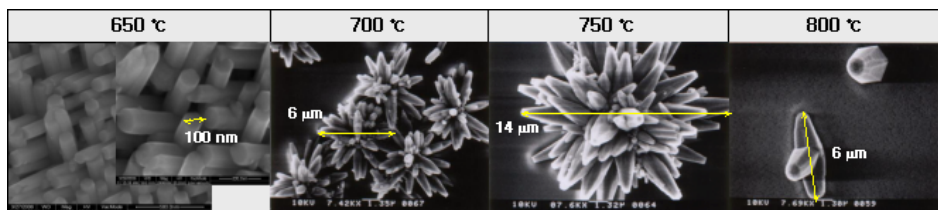


Fig.4.19 InGaN phase shape on r-plane sapphire

Fig.4.20 shows 5 μm x 5 μm AFM images of InGaN surfaces grown by mixed-source HVPE.

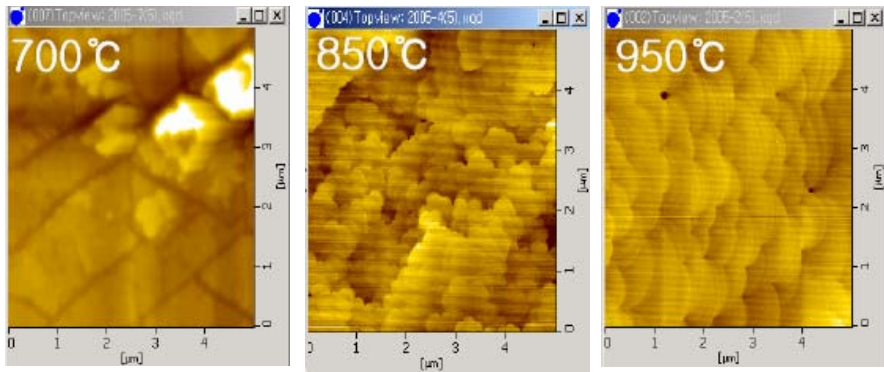


Fig.4.20 AFM images of InGaN surfaces grown by mixed-source HVPE.

Fig.4.21 shows RMS roughness change of InGaN grown by mixed source HVPE. At source zone temperature of 800 $^{\circ}\text{C}$, RMS roughness was minimum.

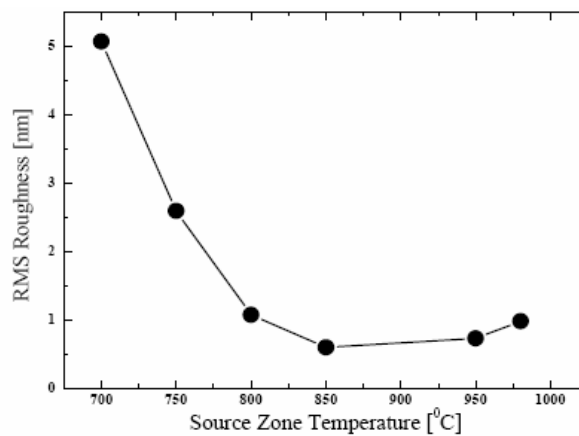


Fig.4.21 RMS roughness of InGaN source zone temperature

C. InGaN layer grown on the GaN templated (111) Si substrates

HVPE growth method is necessary to obtain freestanding substrates even though it is difficult to grow high quality GaN layer directly on the Si substrates. Recently, the epitaxial lateral overgrowth (ELO)-GaN layer was grown using AlGaIn as an intermediate layer on Si (111) substrates [33]. The problems in the growth process of GaN layer on Si substrates by HVPE are melt-back etching of substrates caused by Ga droplet and chemical reactions between substrates and source gas (HCl) [34]. So, Si substrates should be covered with a GaN or AlN buffer layers. In order to obtain the thick GaN layer on Si substrates, another severe problem should be solved is cracking of the buffer layers.

In this paper, we solved the problem of the melt-back etching of substrates caused by Ga droplet by the growth of a GaN on a GaN templated Si (111) substrates using an InGaIn intermediate layer grown by mixed-source HVPE method.

Even in the case of using GaN templated Si substrates for the growth of thick GaN layer by HVPE, the templated GaN layer on Si can be easily cracked in the growth process of thick GaN at relatively high temperature. In order to grow an InGaIn intermediate layer, the metallic In mixed with Ga is loaded in the HVPE chamber as a source material. The temperature of the metallic Indium mixed with Ga zone was 900 °C, and the InGaIn layer was grown at 990 °C. The 400 nm-thick InGaIn as an intermediate layer was grown by mixed-source HVPE method. The growth rate was about 0.1 μm/h. To perform selective area growth (SAG) process, dot-patterned and stripe windows were formed by conventional photolithography and wet chemical etching. The SiO₂ mask formed by sputter for SAG was used. The InGaIn surface was slightly etched by HCl gas for 5 min before the GaN growth, and the thick GaN layer was grown at 1050 °C. For the growth of GaN layer, the gas flow rate of HCl and NH₃ were maintained at 10 sccm and 500 sccm, respectively. The temperature of the source zone was 850 °C. The thickness of the GaN layer was about 12 μm.

The growth was 25 $\mu\text{m}/\text{h}$. The 500 nm-thick templated GaN layer on Si (111) was grown by MOCVD.

Typical surface images of the InGaN layer grown on the GaN templated (111) Si substrates taken by scanning electron microscope (SEM) are shown in Fig.4.22. The SEM image shows the fine surface morphology as shown in Fig.4.22 (b). We found that the ratio between the vertical and the lateral growth rate for the InGaN grown on the GaN templated Si (111) substrates is 5.5.

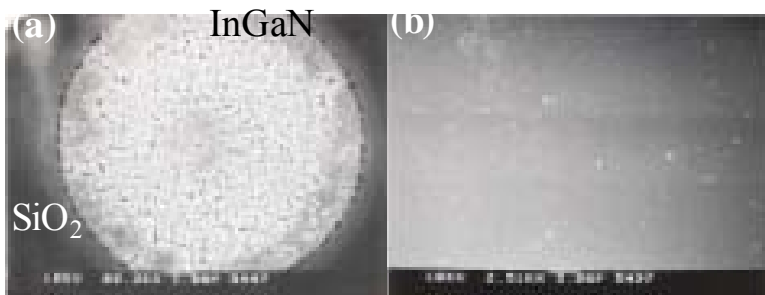


Fig.4.22 Typical surface images of the InGaN layer grown on the GaN templated (111) Si substrates by mixed-source HVPE method

Fig.4.23(a) and (b) show typical PL spectra of the InGaN layer and the GaN templated Si (111) substrates at 300 K, respectively. There is an intensive edge peak wavelength attributed to the band edge emission of the InGaN layer at 492 nm (2.50 eV, labeled as A_2). The FWHM of the peak is 0.64 eV. The In composition is estimated to be about 23 %. The two peaks (labeled as A_1 and A_3) at 443 nm (2.79 eV) and 561 nm (2.20 eV) in PL spectrum might be due to the optical property of the GaN templated (111) Si substrates. The PL spectrum of the GaN templated Si (111) substrates is shown in Fig.4.23 (b). In Fig.4.23 (b), the band-edge peak is observed at 365 nm (3.39eV, labeled as B_1). The strong peak at 373 nm (3.32eV, labeled as B_2) corresponds to the impurity related peak.

The two peaks (labeled as B₃ and B₅) at 432 nm (2.86 eV) and 554 nm (2.23 eV) in PL spectrum might be related to oxygen and yellow band emission, respectively. Although the origin of a broad peak (labeled as B₄) at 478 nm (2.59 eV) has not been identified yet, this might be considered due to unintentional impurities.

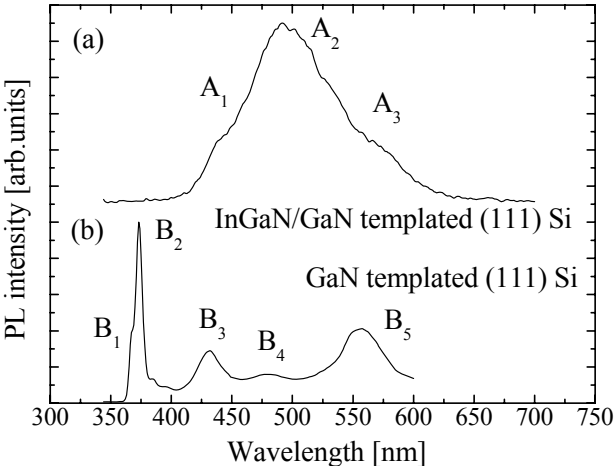


Fig.4.23 (a) Typical PL spectrum of the InGaN layer at 300 K. (b) PL spectrum of GaN templated Si (111) substrates at 300 K.

Fig.4.24 shows typical SEM images of the GaN layer grown on the InGaN intermediate layer on GaN templated Si (111) substrates. As shown in Fig.4.24 (a), the uniform GaN layer is achieved successfully. The c-axis is along the <111> axis of the Si and the <1101> axis is parallel to the <112> axis [34]. The GaN surface is flat as shown in Fig.4.24 (b). The thickness of GaN layer is 3.5 μm. At the longer growth time, the thickness of GaN layer is 12 μm and we can see the lateral overgrowth of GaN layer as shown in Figs.4.24 (c) and (d), respectively. But in this particular sample, the surface morphology is poor. We might expect better results by improving the growth

method.

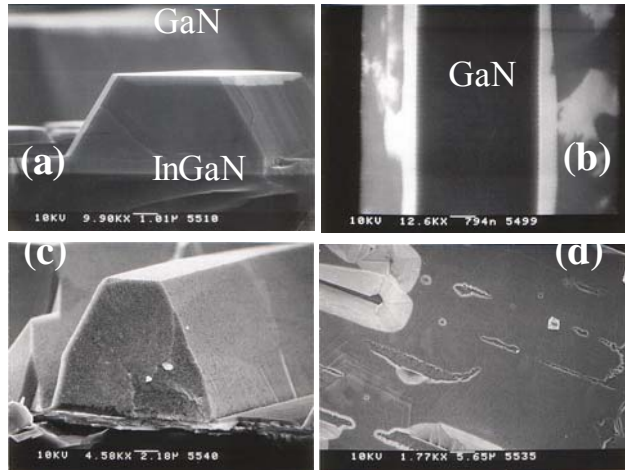


Fig.4.24 (a) Cross-sectional SEM image, (b) Surface (the sample thickness of the GaN layers in (a) and (b) is 3.5 μm). (c) Cross-sectional SEM image, (d) Surface (the sample thickness of the GaN layer in (c) and (d) is 12 μm).

Fig.4.25 shows the SEM and the CL images of the thick GaN layer at 230 K. The CL intensity image is measured at peak wavelength of 0 and 362 nm, respectively. The corresponding monochromatic CL image taken at 362 nm is shown in Fig.4 (c). The SEM image shows the fine surface morphology whereas the CL image shows spatially the bright/dark region for 362 nm emission. A strong emission due to oxygen impurity is observed at 390 nm (not shown). However, we successfully grow a GaN layer on the GaN templated Si (111) substrates using an InGaN intermediate layer grown by mixed-source HVPE.

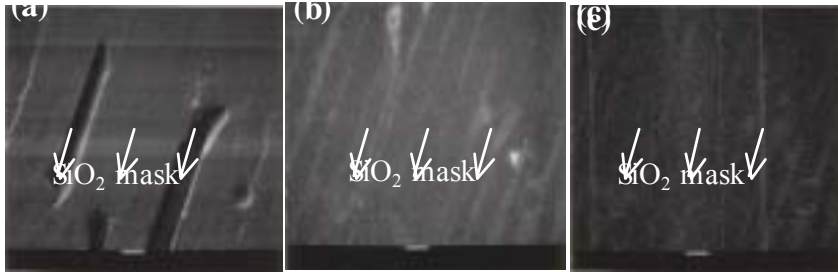


Fig.4.25 (a) SEM image. The CL images measured at the peak wavelength of (b) 0 and (c) 362 nm at 230 K. Figs. (a), (b), and (c) are images of the GaN layer with 12 μm thickness.

D. SAG-InGaN grown by mixed-source HVPE

The growth of the thick InGaN layer results in the low crystalline quality and the inhomogeneous distributions of the In composition in the InGaN layer [36].

In this experiment, we showed the SAG of thick InGaN layers on a GaN templated sapphire (0001) substrates by mixed-source HVPE method as a new method to investigate growth performance. The mixed-source HVPE growth technique could be also used to obtain the AlGaIn layer with an arbitrary composition [37]. The grown InGaIn layers were characterized by XPS, PL and CL measurements to verify its properties. We got the new results of the SAG growth of the InGaIn layers by mixed-source HVPE method.

The metallic In (99.9999 %) mixed with Ga (99.9999 %) was loaded in the HVPE chamber as a source material. The source zone temperature of the metallic In mixed with Ga is 900 $^{\circ}\text{C}$, and the InGaIn layer was grown at 990 $^{\circ}\text{C}$. The atomic fractions of Ga (X_{Ga}) in the solution used for the growth of InGaIn layers were 0.25 and 0.18, respectively. The gas flow rates of HCl that enabled to make In-Ga chloride and NH_3 were maintained at 10 sccm and 500 sccm, respectively. The HVPE

method had maintained the atmospheric pressure during processing. To perform the SAG process, the dot-patterned and the stripe-patterned windows were formed by conventional photolithography and wet chemical etching [38]. The dot pattern had the array of $3\ \mu\text{m}$ diameter with a $7\ \mu\text{m}$ period. The stripe patterns had the array of $3\ \mu\text{m}$ and the $5\ \mu\text{m}$ windows with $10\ \mu\text{m}$ period, respectively. The SiO_2 mask with the approximately $2500\ \text{\AA}$ thickness formed by sputter for was used.

Figure 4.26 shows the scanning electron microscopy (SEM) images of the SAG-InGaN. As shown in Fig. 1, a good selectivity of the SiO_2 mask was achieved. The height of the hexagonal pyramid InGaN layer was $5\ \mu\text{m}$ at dot-patterned area. We found that the pyramidal InGaN with narrow top c -plane is formed.

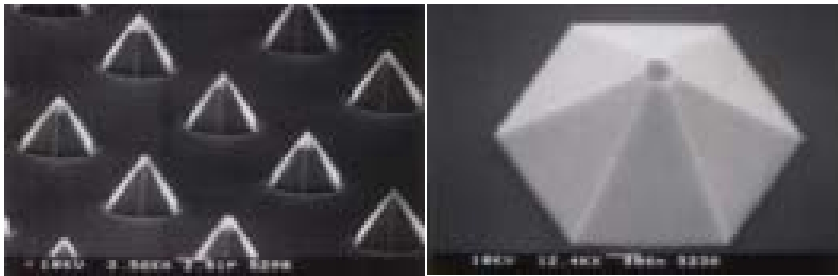


Fig.4.26 SEM images of hexagonal pyramid with height $5\ \mu\text{m}$ obtained by 30 min growth.

Fig.4.27 shows the SEM image of SAG-InGaN with stripe windows. The vertical growth thickness of InGaN grown by the selective mixed-source HVPE method was $12\ \mu\text{m}$ and the lateral growth thickness was $6\ \mu\text{m}$. We found that the ratio between the vertical growth rate and the lateral growth rate for the InGaN grown on GaN templated substrates was 2.

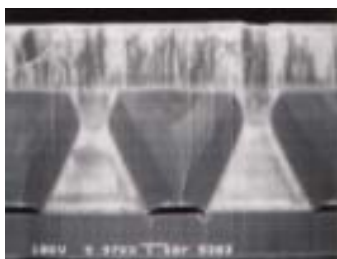


Fig.4.27 SEM image of thick InGaN alloy with thickness 12 μm obtained by 60 min growth.

Figs.4.28 (a) and (b) show XPS narrow-scan of each element and the PL spectrum of the InGaN layer ($X_{\text{Ga}}^{\text{c}} = 0.25$), respectively. The binding energy of the In3d peak shown in Fig.4.28 (a) was 445 eV. The strong peak of 530 eV was due to the oxide. In the HVPE growth, the indium metal often interacted with O_2 and/or H_2O as unintentional impurities caused by the metal source, the source gases and the quartz ware. Thus, more refinement of the growth conditions was desirable to improve the crystal quality. As shown in Fig.4.28 (b), there were two peaks at 362 nm and 382 nm, which correspond to the band edge emission of GaN templated layer and InGaN layer, respectively. The In composition was estimated to be about 3 %.

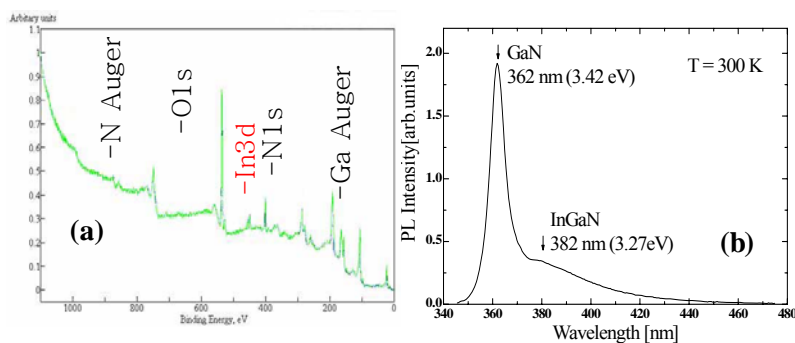


Fig.4.28 (a) XPS spectrum for the SAG-InGaN grown by mixed-source HVPE method. (b)

Typical PL spectrum of InGaN.

Fig.4.29 shows the SEM and the CL images of the cross-section of the SAG-InGaN layer ($X_{\text{Ga}}^{\ell} = 0.25$) at 230 K. The corresponding monochromatic CL image taken at 380 nm is shown in Fig.4.29 (d). In case of the InGaN layer grown at $X_{\text{Ga}}^{\ell} = 0.25$, the In composition is about 3 %. In case of $X_{\text{Ga}}^{\ell} = 0.18$, the In composition of the InGaN layer was about 10 % (not shown). The SEM image shows the fine surface morphology of cross-section whereas the CL image shows spatially inhomogeneous optical properties due to the non-uniform growth of InGaN SAG area. It was considered as the variation of the indium composition along the crystal direction. However, we demonstrated that the thick InGaN alloys were successfully grown using our new novel method.

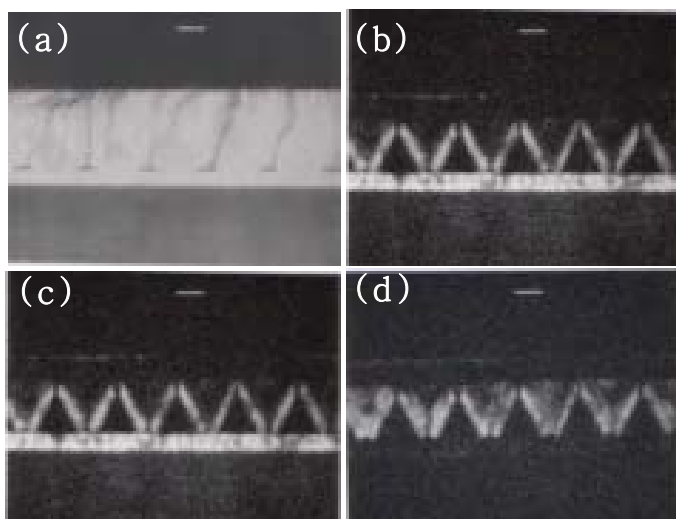


Fig.4.29 (a) SEM image. The CL intensity images of InGaN grown ($X_{\text{Ga}}^{\ell} = 0.25$) by mixed-source HVPE method measured at the peak wavelength of (b) 0 nm, (c) 360 nm, and (d) 380 nm at 230 K.

References

- [1] G.B. Stringfellow, "Fundamental aspects of vapor growth and epitaxy," *J. Crystal Growth*, vol. 115, pp. 1-11, 1991.
- [2] I. Gorczyca and N. E. Christensen, "Band structure and highpressure- phase transition in GaN," *Solid State Commun.*, vol. 80. v. 335, 1991
- [3] M. Mizuta, S. Fujieda, Y. Matsumoto, and T. Kawamura, "Low temperature growth of GaN and AlN on GaAs utilizing metal organics and hydrazine," *Jpn. J. Appl. Phys.*, vol. 25, p. L-945, 1986.
- [4] M. J. Paisley, Z. Sitar, J. B. Posthill, and R. F. Davis, "Growth of cubic phase gallium nitride by modified molecular beam epitaxy," *J. Vac. Sci. Technol. A*, vol. 7, pp. 701-705, 1989.
- [5] M. E. Sherwin and T. J. Drummond, "Predicted elastic constants and critical layer thicknesses for cubic phase AlN, GaN, and InN on-Sic," *J. Appl. Phys.*, vol. 69, pp. 8423-8425, 1991
- [6] H. Morkq, "GaN and silicon carbide as optoelectronicmaterials," *CRC Handbook on Optoelectronics*, M. Gupta, Ed.
- [7] S. Strite, M. E. Lin, and H. Morkoq, "Progress and prospects for GaN and the 111-V nitride semiconductors," *Thin Solid Films*, vol. 231, Issues 1-2, pp. 197-210, 1993
- [8] R. F. Davis, "111-V nitrides for electronic and optoelectronic applications," *IEEE Proc.*, vol. 80, pp. 702-712, 1991.
- [9] E. Aujol, A. Trassoudaine, D. Castelluci and R. Cadoret, *Mater. Sci. Eng. B* 82, 65 (2001).
- [10] P. R. Tavernier, E. V. Etzkorn, Y. Wang and D. R. Clarke, *Appl. Phys. Lett.* 77, 1804 (2000).
- [11] T. Paskova, E. M. Goldys, R. Yakimova, E. B. Svedberg, A. Henry and B. Monemar, *J. Crystal Growth* 208, 18 (2000).
- [12] S. A. Safvi, N. R. Perkins, M. N. Horton, R. Matyi and T. F. Kuech, *J. Crystal growth* 182, 233 (1997).

- [13] S. Yoshida, S. Misawa, and S. Gonda, "Properties of Al, Ga, N films prepared by reactive molecular beam epitaxy," *J. Appl. Phys.*, vol. 53, pp. 6844-6846, 1982.
- [14] J. Hagen, R. D. Metcalfe, D. Wickenden, and W. Clark, "Growth and properties of $Ga_xAl_{1-x}N$ compounds," *J. Appl. Phys.*
- [15] Y. Koide et al., "Energy band-gap bowing parameter in an AlGaN alloy," *J. Appl. Phys.*, vol. 61, pp. 454W543, 1987.
- [16] M. A. Khan, R. A. Scogman, R. G. Schulze, and M. Gershenson, "Properties and ion implantation of Al,Ga,N epitaxial single crystal films prepared by low pressure metal organic chemical vapor deposition," *Appl. Phys. Lett.*, vol. 43, pp. 492494, 1983.
- [17] D. K. Wickenden, C. B. Barger, W. A. Bryden, and J. Miragliotta, "High-quality self-nucleated Al, Ga - N layers on (001) sapphire by low-pressure metal organic chemical vapor deposition," *Appl. Phys. Lett.*, vol. 65, pp. 2024-2026, 1994.
- [18] M. A. Khan, J. M. Van Hove, J. N. Kuznia, and D. T. Olson, "High electron mobility GaN/Al, Ga, N hetero structure grown by low-pressure metal organic chemical vapor deposition," *Appl. Phys. Lett.*, vol. 58, pp. 2408-2410, 1991. 1994, pp. 231-238. *Appl. Phys. Lett.*, vol. 66, pp. 1112-1114, 1995. *Appl. Phys. Lett.*, vol. 11, pp. L143-L146, 1978
- [19] T. Tanaka et al., "p-type conduction in Mg-doped GaN and Al_{0.05}Ga_{0.95}N grown by metalorganic vapor phase epitaxy," *Appl. Phys. Lett.*, vol. 65, pp. 593-595, 1994
- [20] M. Koide, S. Yamasaki, S. Nagai, N. Koide, S. Asami, H. Amani, and I. Akasaki, *Appl. Phys. Lett.* 68, 1403 (1996).
- [21] S. Nakamura, T. Mykai, and M. Shenon, *J. Appl. Phys.* 31, 2883 (1992).
- [22] H. S. Ahn, K. H. Kim, M. Yang, J. Y. Yi, H. J. Lee, J. H. Chang, H. S. Kim, S.W. Kim, S. C. Lee, Y. Honda, M. Yamaguchi, and N. Sawaki, *phys. stat. sol. (a)* 202, 1048 (2005).
- [23] K. Osamura, K. Nakajima, and Y. Murakami, "Fundamental absorption edge in GaN, InN, and

their alloys," *Solid State Commun.*, vol. 11, pp. 617-621, 1972.

[24] K. Osamura, S. Naka, and Y. Murakami, "Preparation and optical properties of Gal-,In,N thin films," *J. Appl. Phys.*,

[25] T. Nagatomo, K. Kuboyama, H. Minamino, and O. Omoto, "Properties of Gal - In, N films prepared by MOVPE," *Jpn. J. Appl. Phys.*, vol. 28, pp. L1334-L1336, 1989.

[26] N. Yoshimoto, T. Matsuoka, and A. Katsui, "Photoluminescence of InGaN films grown at high temperature by metalorganic vapor phase epitaxy," *Appl. Phys. Lett.*, vol. 59, pp. 2251-2253, 1991.

[27] T. Nagatomo, T. Kuboyama, H. Minamino, and O. Omoto, "Properties of Gal-,In,N films prepared by MOVPE," *Jpn. J. Appl. Phys.*, vol. 28, pp. L133LL336, 1989

[28] T. Matsuoka, N. Yoshimoto, T. Sasaki, and A. Katsui, "Wideband gap semiconductor InGaN and InGaAlN grown by MOVPE," *J. Electron. Mater.*, vol. 21, pp. 157-163, 1992.

[29] S. Nakamura and T. Mukai, "High quality InGaN films grown on GaN films," *Jpn. J. Appl. Phys.*, vol. 31, p. L1457-L1459, 1992.

[30] S. Nakamura, T. Mukai, and M. Seno, "Si-doped InGaN films grown on GaN films," *Jpn. J. Appl. Phys.* vol. 31, pp. L1CL19, 1993; S. Nakamura, N. Iwasa, and S. Nagahama, "Cd-doped InGaN films grown on GaN films," *Jun. J. Amd. Phys.* vol. 32. *Appl. Phys. Lett.*, vol. 65, pp. 593-595, 1994. vol. 46, pp. 3432-3437, 1975. 1 1 , , pp. L338-341, 1993. 1~9- 31

[31] W. A. Brvden and T. J. Kistenmacher. "Electrical transuort properties bf InN, GaInN and AlInN," in *Properties of Group II Nitrides*, J. H. Edgar, Ed. London, UK INSPEC, IEE, 1994, pp. 117-124.

[32] S. Yamasaki et al., "p-type conduction in Mg-doped Ga_{0.91}In_{0.09}N grown by metal organic vapor-phase epitaxy," *A&. Phy~L. ett.*, vol. 66, pp. 1112-1114, 1995.

[33] S. Tanaka, Y. Honda, and N. Sawaki, *Appl. Phys. Lett.* 79, (2001), p.955.

[34] H. Ishikawa, G. Y. Zhao, N. Nakada, T. Egawa, T. Jimbo and M. Umeno, *Jpn. J. Appl. Phys.* 38,

L492 (1999).

[35] Y. Honda, T. Ishikawa, Y. Nishimura, M. Yamaguchi, and N. Sawaki, *phys. stat. Sol. (c)* 0, (2002), p. 107.

[36] M. Shimizu, Y. Kawaguchi, K. Hiramatsu, and N. Sawaki, *Jpn. J. Appl. Phys.* 36, 6A, (1997), p. 3381.

[37] H. S. Ahn, K. H. Kim, M. Yang, J. Y. Yi, H. J. Lee, C. R. Cho, H. K. Cho, S. W. Kim, T. Narita, Y. Honda, M. Yamaguchi, and N. Sawaki, *Appl. Surf. Sci.* 243, (2005), p. 178.

[38] Y. Honda, Y. Kawakuchi, Y. Ohtaka, S. Tanaka, M. Yamaguchi, and N. Sawaki, *J. Crystal Growth* 230, (2001), p. 346.

Chapter 5.

Fabrication of AlInGaN-Based LED for White Emission

5.1. AlInGaN SAG-DH structure growth

The InAlGaN quaternary system have been shown to be practical interest in the realization of a wide variety of devices such as light emitting diodes, injection lasers, transistors, photodiodes etc [1,2]. Nitride semiconductors of AlGaInN are also suitable for light emitting diodes (LEDs) covering colors from violet to amber because of their wide bandgap and direct-transition band structure. HVPE has been elucidated the high quality nitride devices than other technology and was informed of having high performance about thick layers [3,4].

I report the growth of AlGaN and InAlGaN alloys by mixed-source hydride vapor phase epitaxy (HVPE) method. The metallic In (99.9999%) mixed with Ga (99.9999%) and Al(99.9999%) are loaded in the HVPE chamber as a source material [5-7]. In order to obtain the AlGaN layer by mixed-source HVPE, the source zone temperatures of the metallic Al mixed with Ga are varied from 900 °C to 1090 °C. The AlGaN layers are grown from chemical reaction between a NH_3 and an Al-Ga chloride formed by HCl that enabled to make Al-Ga chloride flown over metallic In mixed with Ga at 1090 °C. The growth of AlGaN cladding layer is performed on a GaN templated sapphire (0001) substrate. GaN/AlN buffer layer and undoped GaN of $\sim 2 \mu\text{m}$ is grown on 2 inch Al_2O_3 by MOCVD method. The mobility and carrier concentration of undoped GaN is $230 \text{ cm}^2/\text{V}\cdot\text{S}$ and $5\text{E}18 /\text{cm}^3$, respectively.

Table.5.1 SAG-DH Growth parameters

	n-cladding layer	active layer	p-cladding layer	p-cap layer
Source/growth temperature	900 °C /1090 °C	900 °C/1090 °C	900 °C/1090 °C	900 °C/1090 °C
Growth time	10 min	10 min 210 sec (GaN)	10 min	30 sec ~ 210 sec
Growth thickness	~5 μ m	< 0.2 μ m	~ 5 μ m	~ 1 μ m
Growth rate	5 μ m/h	0.01 μ m/min	3 μ m/h	5 μ m/h
Al composition	10 ~ 15 %	Al(x) In(y)	10 ~ 15 %	
In composition		0 ~ 10 %		
Carrier concentration	~ 5 x 10 ¹⁷ /cm ³		~ 1 x 10 ¹⁷ /cm ³	~ 1 x 10 ¹⁷ /cm ³
V/III ratio	40	40	40	40
HCl (sccm)	20	20	20	20
NH ₃ (sccm)	800	800	800	800
Main N ₂ (sccm)	800	800	800	800
Back N ₂ (sccm)	600	600	600	600
HCl N ₂ (sccm)	200	200	200	200
NH ₃ N ₂ (sccm)	200	200	200	200

Wafer cleaning and etching process was performed to eliminate native oxide layer before growing. Aceton and methanol were used for cleaning and HF was used for etching. I used optimized SiO₂ as SAG mask. Aluminum react easily with SiO₂, it cause Al-poly deposit on SiO₂

Mask. Therefore SiO₂ film quality is critical parameter to make device, successfully. I introduced RF-sputter system with 6 inch target to deposit SiO₂. Base pressure of sputter system was ~5E-6 torr and working pressure was 9E-4~1E-5 torr at Ar gas flowing of 65 sccm. Film deposition was performed at RF power of 210 W after 30 min pre deposition. I got optimized thickness of 5000 Å through thickness dependence experiment. I used quarter size wafer of 2 inch. HMDS was coated by spin coater on condition of 3000 RPM-30 sec to improve PR adhesion on wafer surface. After 30 sec, PR coating was performed. Soft baking condition was 90 °C-10 min and exposure time was 10 sec. After 30 sec~1 min developing with MIF500 developer, hard baking was performed on condition of 120 °C-10 min.

After developing process, etching process was performed to remove patterned SiO₂. Etching condition was around 3 min in BOE etchant. I also introduced ultrasonic system to improve etching uniformity. I observed wavelength change according as active material was GaN, AlGaN, InAlGaN. First mixed source of Ga(20 g), Al(0.6 g) and Te(0.2 g) at multi sliding boat was used for n-cladding layer. Second mixed source of Ga(20 g, fixed), Al(0.1~0.6 g, varied) and In(0.1~0.5 g, varied) at multi sliding boat was used for active layer. Third mixed source of Ga(20 g), Al(0.6 g) and Mg(0.09 g) at multi sliding boat was used for p-cladding layer. Metal source was etched on condition of 50%-HCl to remove native oxide layer before loading in boat. All loaded source was soaked for 3 hours at 920 °C to mix. During growth, source temperature was 900 °C and growth temperature was 1090 °C, respectively. Stable temperature control was needed to get high quality crystal. To reduce environment effect, quartz reactor and boat was pre-baked before loading sources. Table.5.2 shows all experimental conditions and results of DH growth. I also processed 3 times as same condition to verify reproducibility.

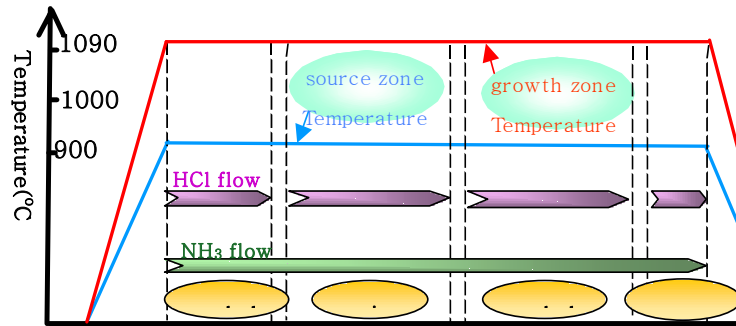


Fig.5.1 Temperature profile of MS-HVPE

Table.5.2 Experimental conditions and results of SAG-DH growth.

Date	NUM	N2 NH3	N2 HCl	N2 Back	N2 Main	NH3	Temp	Flow (HCl)	Growth Time	Substrate	Growth Material	Result	Remark
	135	200	200	600	800	800	900-1090	20	10' 2'30" 10' 2'30"	LED Pattern n-GaN (2007.3.21)	Te-AlGaN GaN Mg-AlGaN Mg-GaN	Grow	Active:GaN
	136	200	200	600	800	800	900-1090	20	10' 2'30" 10' 2'30"	LED Pattern n-GaN (2007.4.6)	Te-AlGaN GaN Mg-AlGaN Mg-GaN	Grow	Active:GaN
	137	200	200	600	800	800	900-1090	20	10' 2'30" 10' 2'30"	LED Pattern n-GaN (2007.4.6)	Te-AlGaN GaN Mg-AlGaN Mg-GaN	Grow	Active:GaN
	138	200	200	600	800	800	900-1090	20	10' 2'30" 10' 2'30"	LED Pattern n-GaN (2007.4.6)	Te-AlGaN GaN Mg-AlGaN Mg-GaN	Grow	Active:GaN
	139	200	200	600	800	800	900-1090	20	5'	U-GaN (2007.4.6)	GaN	Grow	Active:GaN
070426	140	200	200	600	800	800	900-1090	20	10' 10' 10' 2'30"	LED Pattern n-GaN (2007.4.6)	Te-AlGaN AlGaN Mg-AlGaN Mg-GaN	Grow	Active:AlGaN (0.1)
	141	200	200	600	800	800	900-1090	20	10' 10' 10' 2'30"	LED Pattern n-GaN (2007.4.6)	Te-AlGaN AlGaN Mg-AlGaN Mg-GaN	Grow	Active:AlGaN (0.1)
	142	200	200	600	800	800	900-1090	20	10' 10' 10' 2'30"	LED Pattern n-GaN (2007.4.6)	Te-AlGaN AlGaN Mg-AlGaN Mg-GaN	Grow	Active:AlGaN (0.1)
	143	200	200	600	800	800	900-1090	20	10'	U-GaN (2007.4.6)	AlGaN	Grow	Active:AlGaN (0.1)
	144	200	200	600	800	800	900-1090	20	10' 10' 10' 2'30"	LED Pattern n-GaN (2007.3.21)	Te-AlGaN AlGaN Mg-AlGaN Mg-GaN	Grow	Active:AlGaN (0.3)
	145	200	200	600	800	800	900-1090	20	10' 10' 10' 2'30"	LED Pattern n-GaN (2007.3.21)	Te-AlGaN AlGaN Mg-AlGaN Mg-GaN	Grow	Active:AlGaN (0.3)
	146	200	200	600	800	800	900-1090	20	10' 10' 10' 2'30"	LED Pattern n-GaN (2007.3.21)	Te-AlGaN AlGaN Mg-AlGaN Mg-GaN	Grow	Active:AlGaN (0.3)
	147	200	200	600	800	800	900-1090	20	10'	U-GaN (2007.4.6)	AlGaN	Grow	Active:AlGaN (0.3)
	148	200	200	600	800	800	900-1090	20	10' 10' 10' 2'30"	LED Pattern n-GaN (2007.3.21)	Te-AlGaN AlGaN Mg-AlGaN Mg-GaN	Etching	Active:AlGaN (0.4)
070427	149	200	200	600	800	800	900-1090	20	10' 10' 10' 1'	LED Pattern n-GaN (2007.3.21)	Te-AlGaN AlGaN Mg-AlGaN Mg-GaN	Etching	Active:AlGaN (0.4)
	150	200	200	600	800	800	900-1090	20	10' 10' 10' 20"	LED Pattern n-GaN (2007.3.21)	Te-AlGaN AlGaN Mg-AlGaN Mg-GaN	Grow	Active:AlGaN (0.4)
	151	200	200	600	800	800	900-1090	20	10' 10' 10' 1'	LED Pattern n-GaN (2007.3.21)	Te-AlGaN AlGaN Mg-AlGaN Mg-GaN	Grow	Active:AlGaN (0.4)
	152	200	200	600	800	800	900-1090	20	10' 10' 10' 40"	LED Pattern n-GaN (2007.4.6)	Te-AlGaN AlGaN Mg-AlGaN Mg-GaN	Grow	Active:AlGaN (0.4)

	153	200	200	600	800	800	900-1090	20	10'	U-GaN (2007.4.6)	AlGa _N	Grow	Active AlGa _N (0.4)
	154	200	200	600	800	800	900-1090	20	10' 10' 10' 40''	LED Pattern n-GaN (2007.4.6)	Te-AlGa _N AlGa _N Mg-AlGa _N Mg-GaN	Grow	Active AlGa _N (0.5)
070428	155	200	200	600	800	800	900-1090	20	10' 10' 10' 40''	LED Pattern n-GaN (2007.4.6)	Te-AlGa _N AlGa _N Mg-AlGa _N Mg-GaN	Grow	Active AlGa _N (0.5)
	156	200	200	600	800	800	900-1090	20	10' 10' 10' 40''	LED Pattern n-GaN (2007.4.6)	Te-AlGa _N AlGa _N Mg-AlGa _N Mg-GaN	Grow	Active AlGa _N (0.5)
	157	200	200	600	800	800	900-1090	20	10'	U-GaN (2007.4.6)	AlGa _N	Grow	Active AlGa _N (0.5)
	158	200	200	600	800	800	900-1090	20	10' 10' 10' 40''	LED Pattern n-GaN (2007.4.6)	Te-AlGa _N AlGa _N Mg-AlGa _N Mg-GaN	Grow	Active AlGa _N (0.6)
	159	200	200	600	800	800	900-1090	20	10' 10' 10' 40''	LED Pattern n-GaN (2007.4.6)	Te-AlGa _N AlGa _N Mg-AlGa _N Mg-GaN	Grow	Active AlGa _N (0.6)
	160	200	200	600	800	800	900-1090	20	10' 10' 10' 40''	LED Pattern n-GaN (2007.4.6)	Te-AlGa _N AlGa _N Mg-AlGa _N Mg-GaN	Grow	Active AlGa _N (0.6)
	161	200	200	600	800	800	900-1090	20	10'	U-GaN (2007.4.6)	AlGa _N	Grow	Active AlGa _N (0.6)
	162	200	200	600	800	800	900-1090	20	10' 10' 10' 40''	(1)(2)(3) U-GaN (2007.4.6) (4)LED Pattern n-GaN (2007.4.6)	Te-AlGa _N InAlGa _N Mg-AlGa _N Mg-GaN	Etching	Active:InAlGa _N (0.1)
		163	200	200	600	800	800	900-1090	20	10' 10' 10' 40''	LED Pattern n-GaN (2007.4.6)	Te-AlGa _N InAlGa _N Mg-AlGa _N Mg-GaN	Grow
070429	164	200	200	600	800	800	900-1090	20	10' 10' 10' 40''	LED Pattern n-GaN (2007.4.6)	Te-AlGa _N InAlGa _N Mg-AlGa _N Mg-GaN	Grow	Active:InAlGa _N (0.1)
	165	200	200	600	800	800	900-1090	20	10' 10' 10' 20''	LED Pattern n-GaN (2007.4.6)	Te-AlGa _N InAlGa _N Mg-AlGa _N Mg-GaN	Grow	Active:InAlGa _N (0.1)
	166	200	200	600	800	800	900-1090	20	10'	U-GaN (2007.4.6)	InAlGa _N	Etching	Active:InAlGa _N (0.1)
	167	200	200	600	800	800	900-1090	20	10' 10' 10' 30''	LED Pattern n-GaN (2007.4.6)	Te-AlGa _N InAlGa _N Mg-AlGa _N Mg-GaN	Etching	Active:InAlGa _N (0.2)
	168	200	200	600	800	800	900-1090	20	10' 10' 10' 40''	LED Pattern n-GaN (2007.4.6)	Te-AlGa _N InAlGa _N Mg-AlGa _N Mg-GaN	Grow	Active:InAlGa _N (0.2)
	169	200	200	600	800	800	900-1090	20	10' 10' 10' 40''	(1)(2) LED Pattern n-GaN (2007.4.6)	Te-AlGa _N InAlGa _N Mg-AlGa _N Mg-GaN	Grow	Active:InAlGa _N (0.2)
	170	200	200	600	800	800	900-1090	20	10'	U-GaN (2007.4.6)	InAlGa _N	?	Active:InAlGa _N (0.2)
		171	200	200	600	800	800	900-1090	20	10' 10' 10' 40''	(1)LED Pattern n-GaN (2007.4.6) (2)U-GaN (2007.4.6)	Te-AlGa _N InAlGa _N Mg-AlGa _N Mg-GaN	Grow
	172	200	200	600	800	800	900-1090	20	10' 10' 10' 20''	(1)(2) LED Pattern n-GaN (2007.4.6)	Te-AlGa _N InAlGa _N Mg-AlGa _N Mg-GaN	Grow	Active:InAlGa _N (0.3)
	173	200	200	600	800	800	900-1090	20	10'	U-GaN (2007.4.6)	InAlGa _N	Grow	Active:InAlGa _N (0.3)

070430	174	200	200	600	800	800	900-1090	20	10' 10' 10' 40''	(1)(3)U-GaN (2007.4.6) (2)LED Pattern n-GaN (2007.4.6)	Te-AlGaIn InAlGaIn Mg-AlGaIn Mg-GaN	(1)(3)Etching (2)Grow	Active:InAlGaIn (0.4)
	175	200	200	600	800	800	900-1090	20	10' 10' 10' 40''	LED Pattern n-GaN (2007.4.6)	Te-AlGaIn InAlGaIn Mg-AlGaIn Mg-GaN	Grow	Active:InAlGaIn (0.4)
	176	200	200	600	800	800	900-1090	20	10' 10' 10' 30''	(1)(2) LED Pattern n-GaN (2007.4.6)	Te-AlGaIn InAlGaIn Mg-AlGaIn Mg-GaN	Grow	Active:InAlGaIn (0.4)
	177	200	200	600	800	800	900-1090	20	10'	U-GaN (2007.4.6)	InAlGaIn	Local Grow	Active:InAlGaIn (0.4)
070501	178	200	200	600	800	800	900-1090	20	10' 10' 10' 30''	LED Pattern n-GaN (2007.4.30)	Te-AlGaIn InAlGaIn Mg-AlGaIn Mg-GaN	Etching	Active:InAlGaIn (0.5)
	179	200	200	600	800	800	900-1090	20	10' 10' 10' 30''	LED Pattern n-GaN (2007.4.30)	Te-AlGaIn InAlGaIn Mg-AlGaIn Mg-GaN	Grow	Active:InAlGaIn (0.5)
	180	200	200	600	800	800	900-1090	20	10' 10' 10' 30''	LED Pattern n-GaN (2007.4.30)	Te-AlGaIn InAlGaIn Mg-AlGaIn Mg-GaN	Grow	Active:InAlGaIn (0.5)
	181	200	200	600	800	800	900-1090	20	10'	U-GaN (2007.4.6)	InAlGaIn	Center Grow	Active:InAlGaIn (0.5)
070502	182	200	200	600	800	800	900-1090	20	10' 10' 10' 30''	n-GaN(호춘) 2 inch	Te-AlGaIn InAlGaIn(0.4) Mg-AlGaIn Mg-GaN	Center Grow	Tray 앞쪽 챔 Furnace 42- 5mm
	183	200	200	600	800	800	900-1090	20	10' 10' 10' 30''	(1)LED Pattern n-GaN (2007.4.30) (2)LED Pattern Si (2007.4.29)	Te-AlGaIn InAlGaIn(0.4) Mg-AlGaIn Mg-GaN	(1)Grow (2)Center Grow	
	184	200	200	600	800	800	900-1090	20	10' 10' 10' 30''	(1)LED Pattern n-GaN (2007.4.30) (2)(3)(4) U-GaN (2007.4.6)	Te-AlGaIn InAlGaIn(0.4) Mg-AlGaIn Mg-GaN	(1)Grow (2)(3)(4)Cir cle Grow	
	185	200	200	800	800	800	900-1090	30	10' 10' 10' 30''	(1)n-GaN(호춘) 2 inch (2)U-GaN(호춘) 2 inch	Te-AlGaIn InAlGaIn(0.4) Mg-AlGaIn Mg-GaN	(1)(2)Grow	Growth Zone Tray 65-115mm
	186	200	200	800	800	800	900-1090	30	7' 5' 7' 30''	(1)LED Pattern n-GaN (2007.4.30) (2)LED Pattern Si (2007.4.29)	Te-AlGaIn InAlGaIn(0.4) Mg-AlGaIn Mg-GaN	(1)Grow (2)Etching (3-4 pattern grow) CRACK	
	187	200	200	800	800	800	900-1090	30	7' 5' 7' 30''	THELEDs Pattern	Te-AlGaIn InAlGaIn(0.4) Mg-AlGaIn Mg-GaN	Grow	
070503	188	200	200	800	800	800	900-1090	20	7' 5' 7' 10'	U-GaN(HL-241) (2006.12.26) Te-GaN 900-1090 10cc 10'	Te-AlGaIn InAlGaIn(0.4) Mg-AlGaIn Mg-GaN	Grow	큰 패턴 Etching
	189	200	200	800	800	800	900-1090	20	7' 5' 7' 10'	U-GaN(호춘) 2inch	Te-AlGaIn InAlGaIn(0.4) Mg-AlGaIn Mg-GaN	Grow	위 아래 가장자리 Etching
	190	200	200	800	800	800	900-1090	20	7' 5' 7' 10'	n-GaN(호춘) 2inch	Te-AlGaIn InAlGaIn(0.4) Mg-AlGaIn Mg-GaN	Grow	위 아래 가장자리 Etching

070504	191	200	200	800	800	800	900-1090	20	7' 5' 7' 10''	(1)U-GaN (HL-245) (2006.12.27) (2)LED Pattern Si (2007.4.29)	Te-AlGaN InAlGaN(0.4) Mg-AlGaN Mg-GaN	Grow	(1)두꺼운 성장 SAG 잘 안됨 (2)중간부분 pattern 3개정도 성장
	192	200	200	800	800	800	900-1090	20	4' 5' 4' 10''	(1)LED Pattern Si (2007.4.29) (2)U-GaN (HL-247) (2006.12.27)	Te-AlGaN InAlGaN(0.4) Mg-AlGaN Mg-GaN	Etching	
	193	200	200	800	800	800	900-1090	20	4' 5' 4' 10''	(1)U-GaN(호준) (2007.4.6) (2)LED Pattern Si (2007.4.29)	Te-AlGaN InAlGaN(0.4) Mg-AlGaN Mg-GaN	(1)Grow (2)Etching	(1)성장하였으나 지저분하고 상태가 좋지 않음

The epilayers are analyzed by X-ray photoelectron spectroscopy (XPS) to characterize the Al(In)GaN ternary and quaternary alloys. To improve SAG selectivity of SiO₂ mask, we enhanced the velocity of carrier gas. It shorten mean free path of atom and reduce the probability of GaN nucleation existence on SiO₂ mask. The optimized flow rate was 800 sccm. The growth rate of AlGaN is slow than GaN, so growth time was 10min. N-cladding AlGaN is the first layer of DH-structure and effect on total crystal quality. The thickness of active layer was targeted under 2 μm. But we couldn't measure exactly by SEM. Expected intrinsic carrier concentration of active layer was 1E17 cm⁻³. The key parameter of this experiment was material combination of active layer. As mentioned, we tried to use GaN, AlGaN and AlInGaN as active layer. Growth time of GaN active layer was 2 min 30 sec. But growth time of AlGaN and AlInGaN active layer was 10min because of slow growth rate. P-cladding AlGaN still has some issues. All over the nitride related material system, P-doping was very difficult. Mg activation was also needed. It was performed during cooling temperature after p-GaN cap layer. The gas flow rates of HCl and NH₃ are maintained at 20 sccm and 800 sccm, respectively. To perform the SAG process, the mesa-patterned windows are formed by conventional photolithography and wet chemical etching. The pattern has the array of 250 μm diameter with a 500 μm period. The SiO₂ mask with the approximately 5000 Å thickness formed by sputter for SAG is used. Figure 5.2 shows the p-i-n- double heterostructure.

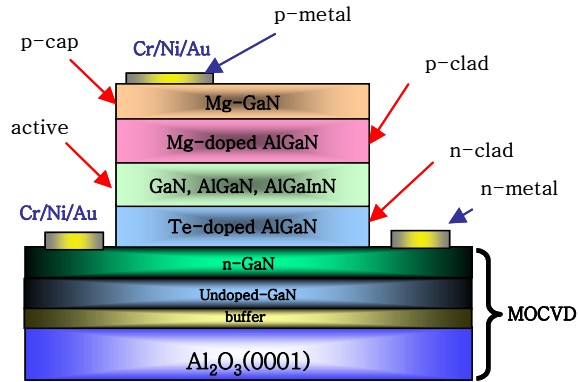


Fig. 5.2 The schematic structure of the AlInGaN/AlGaN DH Structure

5.2. Characterization of AlInGaN SAG-DH epitaxial structure

We also prepared some samples to test the trend of optical performance. The atomic fractions of Al (X_{Al}^l) in the solution used for the AlGaInN cladding layers were from 0.1 to 0.6 respectively. The atomic fractions of In (X_{In}^l) in the solution used for the AlInGaInN cladding layers were also from 0.1 to 0.6 at Al_{0.6}InGaInN respectively.

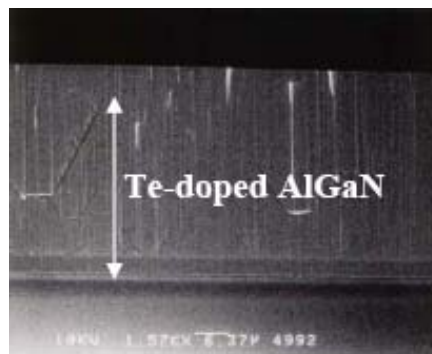
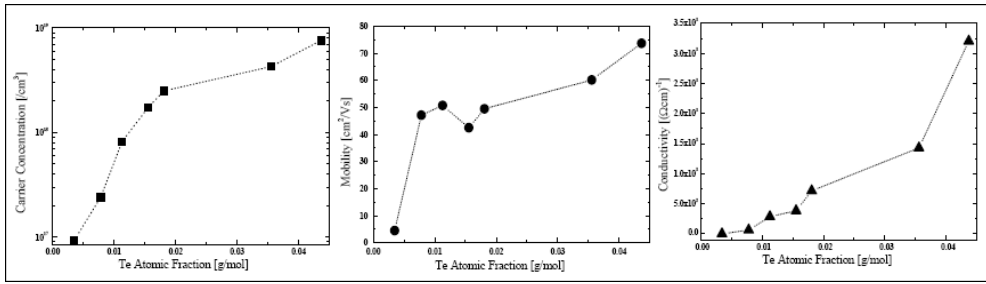


Fig. 5.3 Te-doped Bulk Al_{0.16}GaInN of ~30 μm



(a)

(b)

(c)

Fig. 5.4 Characterization of $\text{Al}_{0.16}\text{GaN}$ (a) Te Atomic fraction vs. Carrier concentration (b) Te Atomic fraction vs. Carrier mobility (c) Te Atomic fraction vs. Conductivity

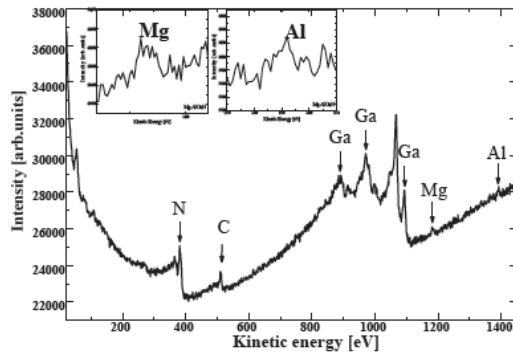


Fig. 5.5 AES of Mg-doped Bulk $\text{Al}_{0.16}\text{GaN}$

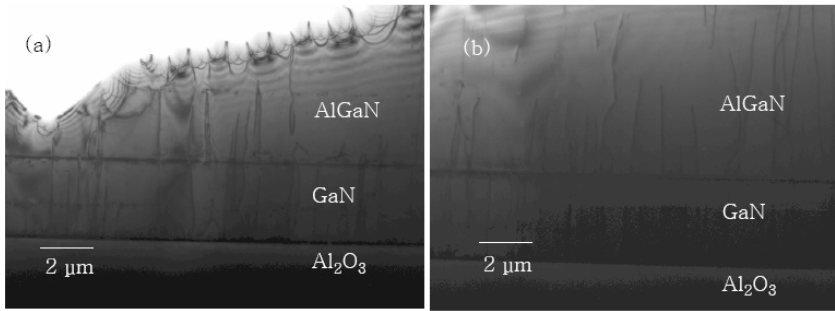


Fig.5.6 TEM of Si-doped Bulk AlGaN (a) Non-optimized growth condition (b) Optimized growth condition

Generally, Al atom reacts faster than Ga atom with NH_4 when AlGaN is grown by HVPE. It occurs v-shape at surface due to high sticking coefficient of Al atom as Fig. 5.6(a). And the difference of thermal expansion coefficient of sapphire substrate and GaN crystal generates much dislocation at interface. But Fig 5.6(b) shows the facet of optimized growth condition. We verified that it is possible by selective area growth and optimized growth of GaN buffer layer.

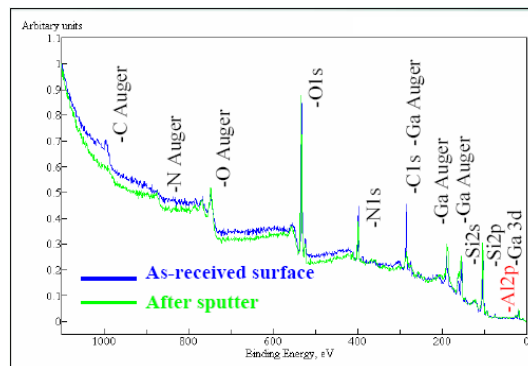


Fig.5.7 XPS spectrum of the InAlGaN alloy

Fig.5.7 shows the XPS narrow-scan of each element of InAlGaN layer. The binding energies of the In 3d and Al 2p peaks are 74 eV and 445 eV, respectively. The In and Al compositions are estimated to be about 3 % and 14 %, respectively. Fig.5.9 shows AFM image of InAlGaN layer grown by the mixed-source HVPE. We also found surface morphology depends on buffer layer growth condition.

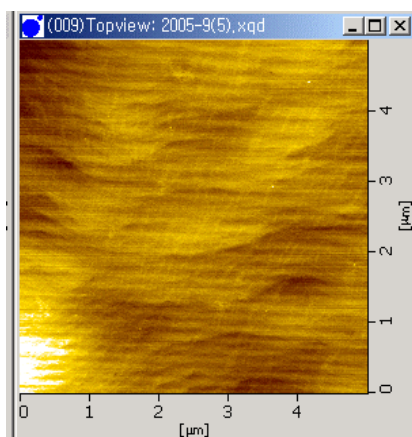
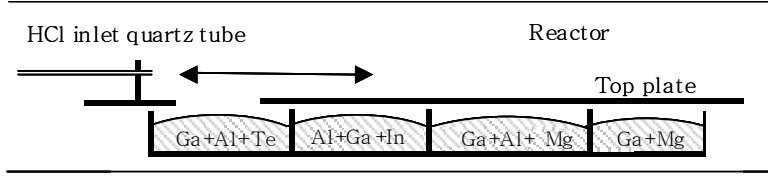


Fig.5.8 5μm x 5μm AFM image of InAlGaN layer grown by the mixed-source HVPE

The SAG-AlInGaN/AlGaN LEDs were performed by the mixed-source HVPE method with multi-sliding boat system. Moreover, as a new attempt in obtaining an InAlGaN layers, the growth of the thick InAlGaN layer is performed by putting small amount of Ga and Al into the In source. We found the new results that the metallic In mixed with Ga (and Al) as a group III source material could be used in the growth process of the In(Al)GaN layer by mixed-source HVPE method.



*Fig.5.9 Multi sliding boat system and mixed metal source in MS-HVPE
for AlGaN/AlInGaN LED*

Each well is separated by compartments and contained with mixed metallic source, (Ga+Al+Te) for n-AlGaN, (Al+Ga+In) for AlInGaN, (Ga+Al+Mg) for p-AlGaN and (Ga+Mg) for p-GaN layer, respectively. The HCl inlet quartz tube is moved to a position over the melt source by moving the top plate. The upper top plate has a window for the chemical reaction of HCl and metallic source. The top cover plate can protect vaporization of volatile doping sources in other wells during the growth of one layer.

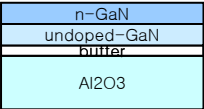
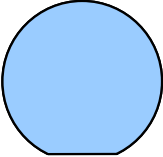
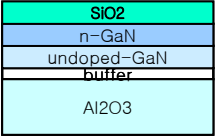
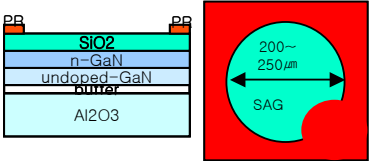
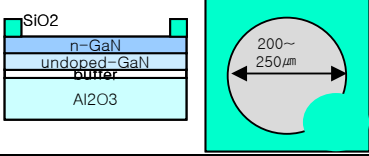
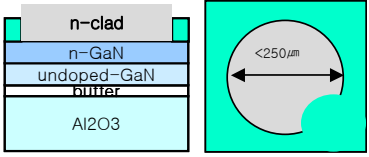
The layer structure of the SAG-LED consists of a 0.5 μm -thick Te-doped AlGaN cladding layer, a 0.5 μm -thick AlInGaN, a 0.5 μm -thick Mg-doped AlGaN cladding layer and a 0.5 μm -thick Mg-doped GaN cap layer. The carrier concentration of the n-AlGaN cladding layer depends on the atomic fraction of the Te in the Al-Ga source. In case of the Si-doped one, it is varied from $9.0\text{E}16 / \text{cm}^3$ to $7.5\text{E}18 / \text{cm}^3$, while in case of the Si-doped one; it was varied from $2.0\text{E}16 / \text{cm}^3$ to $1.1\text{E}17 / \text{cm}^3$. This shows that the Te doping is more suitable to get a high n-type concentration by MS-HVPE method.

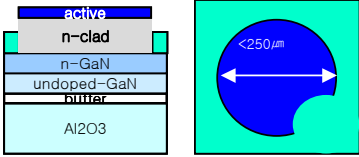
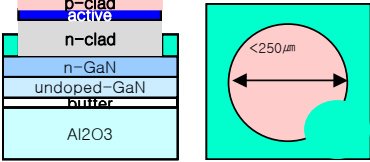
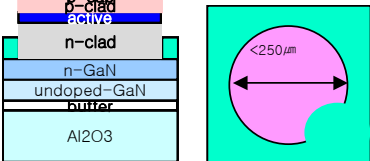
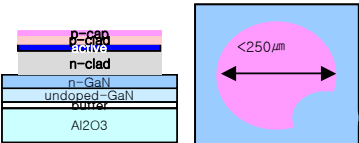
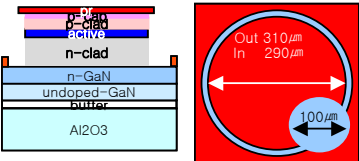
5.3. Device fabrication

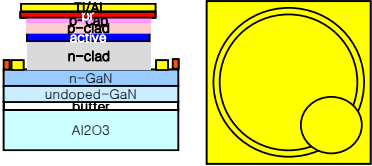
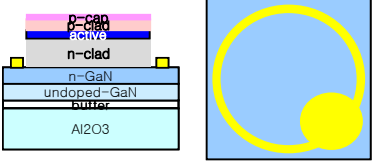
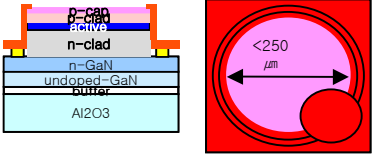
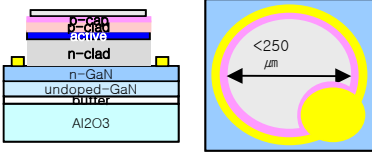
In this chapter, we will describe the all-over process to make SAG-LED. Having defined the epitaxial layer stack and the device layout, the next step is to process technology needed to fabricate

AlInGaN/AlGaN LED. As previously stated, Cr/Ni/Au(150/150/500 Å) layer is deposited on the p-GaN and n-GaN layers as electrode, respectively after removal of the SiO₂ film surfaces. We will describe key process steps of the fabrication process in the order of their appearance in the process flow. Detailed descriptions of the different process steps can be found in table 5.3.

Table. 5.3 AlInGaN/AlGaIn SAG-LED making process

	Process Step	Geometry of Processed Device	Raw Material	Process Condition
1	n-GaN/Al ₂ O ₃ template wafer		n-GaN/Al ₂ O ₃ template wafer (MOCVD) TMGa NH ₃ , Silane	n-GaN Thick: : 2~3μm Mobility ; 200~300 C/C ~ 5x10 ¹⁸ /cm ³ u-GaN Thickness: 1~2μm Crack free (2inch)
2	Wafer cleaning (Wet station ultrasonic)		Aceton Methanol HF DI Water	Aceton ~ 5 min Methanol ~ 5 min HF etching time ~ 5min DI Water cleaning ~ 10min
3	SiO ₂ deposition (PECVD)		Silane N ₂ O	pressure ~ 800 mTorr temperature ~300°C Silane ~150 sccm / N ₂ O ~400 sccm deposition time ; 30~60min, 2000~3000Årf Power ~25 W
4	Photolithography SAG pattern(Mask Aligner PR coater)		Developer PR DI Water	PR AZ 5214 ; 3500rpm, 30sec soft baking ; 90°C, 10min exposure ; 8W/cm ² , 10 sec developing ; MIF500, 40~60sec hard baking ~ 120°C, 10min
5	SiO ₂ etching (Wet station)		BOE	Time ; 1~3 min
6 6-1	SAG DH growth n-cladding layer (Mixed-source HVPE)		n-GaN/Al ₂ O ₃ template wafer Ga(6N) NH ₃ , HCl, N ₂ , Te(5N), Al(5N)	Al composition : 20~30% carrier concentration ; ~1x10 ¹⁸ /cm ³ growth rate ~40μm/h, Thickness ~40μm growth temperature ; ~1090 °C dislocation density ; 1x10 ⁸ ~8x10 ⁸ /cm ² crack free Dia.300 μm SAG

	Process Step	Process Outline	Raw Material	Process Condition
6 6-2	SAG DH growth Active layer (Mixed-source HVPE)		In(6N) Ga(6N) NH3 N2 HCl	In composition : 0~45% (Cd doped?) growth rate ~0.2μm/min growth temperature ~ 990 °C Thickness : <0.2μm
6 6-3	SAG DH growth p-cladding layer (Mixed-source HVPE)		Ga(6N) NH3 HCl N2Mg(4N) Al(5N)	Al composition: 20~30% carrier concentration ~ 1~5x10 ¹⁷ /cm ³ growth rate ~20μm/h, Thickness ~20μm growth temperature ~ 1090 °C dislocation density ; 5x10 ⁸ ~1x10 ⁹ /cm ² crack free Dia.300 μm SAG
6 6-4	SAG DH growth p-GaN (Mixed-source HVPE)		Ga(6N) NH3, N2HCl Mg(4N)	growth rate ~ 30μm/h growth temperature ~ 1050 °C Thickness ~ 0.2μm
7	Mg-activation (Mixed-source HVPE)		N2	Temperature ~ 600 °C Time ~10 min
8	SiO ₂ lift-off (Wet station ultrasonic)		HF DI Water	Ultrasonic time : all lift-off DI Water cleaning ~10min
9	Photolithography Lift-off (Mask Aligner PR coater)		Developer PR DI Water	PR AZ 4620 ; 3000rpm, 30sec soft baking ; 90 °C, 10min exposure ; 8W/cm ² , 10 sec developing ; MIF500, 40~60sec hard baking ; 120 °C, 10min

	Process Step	Process Outline	Raw Material	Process Condition
10	n-metal (e-Beam)		Ti Al	Vacuum <math><5 \times 10^{-6}</math> Torr temperature <math><60^\circ\text{C}</math> Ti/Al thickness 500/1000 Å ~3 RPM
11	Lift-off (Acetone spray N ₂ Dry Ultrasonic)		Acetone Methanol N ₂	Acetone spray 2~3 kg/cm ² , 50 cc Ultrasonic time : all lift-off Methanol ~100 °C, 5min. N ₂ 5min
12	n-Metal Alloy (RTA)		N ₂	RTP temperature ~ 600 °C Time ~ 30sec N ₂ gas 500±10 sccm
13	Photolithography Lift-off (Mask Aligner PR coater)		Developer PR DI Water	PR AZ 4620.; 3000rpm, 30sec soft baking ; 90 °C, 10min exposure ; 8W/cm ² , 10 sec developing ; MIF500, 40~60sec hard baking ; 120 °C, 10min
14	TM metal		Ni Au	Vacuum <math><5 \times 10^{-6}</math> Torr Ni/Au thickness 50/50 Å Rotation Speed ~3 RPM
15	Lift-off (Acetone spray N ₂ Dry Ultrasonic)		Acetone Methanol N ₂	Acetone spray ; 2~3 kg/cm ² , 50 cc Ultrasonic time : all lift-off Methanol ~100 °C, 5min. N ₂ 5min
16	TM metal alloy (RTA)		N ₂ O ₂	RTP temperature ~ 500 °C Time ~ 1min O ₂ gas /N ₂ gas 5%

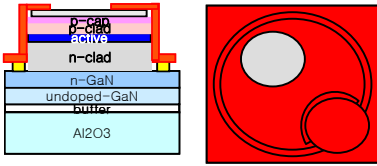
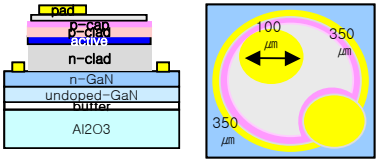
	Process Step	Process Outline	Raw Material	Process Condition
17	Photolithography Lift-off (Mask Aligner PR coater)		Developer PR DI Water	PR AZ 4620 ; 3000rpm, 30sec soft baking ; 90 °C, 10min exposure ; 8W/cm ² , 10 sec developing ; MIF500, 40~60sec hard baking ; 120 °C, 10min
18	p-pad metal (e-beam)		Au	Vacuum <5x10 ⁻⁶ Torr temperature <60 °C Au thickness < 2000 Å Rotation Speed ~3 RPM
19	Lapping (Lapping machine)		Wax Mount Hot Plate DI	Lapping rpm ; 50~60RPM time ; 80~100min Wafer thickness ~100 μm
20	Lapping (Lapping machine)		Wax Mount Hot Plate DI	Polishing rpm ; 50~60RPM time ~ 60min Wafer thickness ~100 μm
21	Test & etc			<p><Measurement Parameter></p> <p>Forward Voltage V_f (V) Reverse current I_r (μA) Radiant Power P_o (mW) Peak Wavelength λ_p (nm) Dominant Wavelength λ_d (nm)</p>

Fig.5.10 shows SEM image of the SAG-LED grown by mixed-source HVPE with multi-sliding boat system. as shown in it, die size is $350\ \mu\text{m} \times 350\ \mu\text{m}$ and a circular n- metal and p-metal pad is about $100\ \mu\text{m}$. Most samples are processed in laboratory equipped with all fabrication system. But only wafer level test was possible because there was't any system of making dice.

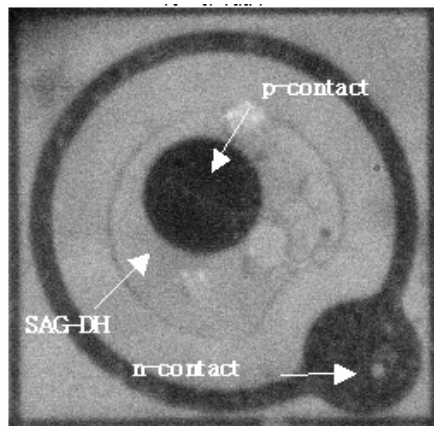


Fig.5.10 Top-view image of the SAG-LED chip grown by mixed-source HVPE

References

- [1] S. Nakamura and G. Fasol, *The Blue Laser Diode*, Springer, New York, 1997.
- [2] S. Strite and H. Morkoc, *J. Vac. Sci. Technol. B*10, 1237 (1992).
- [3] M. A. Mastro, D. Tsvetkov, V. Soukhoveev, A. Usikov, V. Dmitriev, B. Luo, F. Ren, K. H. Baik, and S. J. Pearton, *Solid State Electronic*. 47, 1075 (2003).
- [4] J. LaRoche, B. Luo, F. Ren, K.H. Baik, D. Stodilka, B. Gila, C. R. Abernathy, S. J. Pearton, A. Usikov, D. Tsvetkov, V. Soukhoveev, G. Gainer, A. Rechnikov, V. Dimitriev, G.T. Chen, C. C. Pan, and J. I. Chyi, *Solid State Electronic*. 48, 193 (2003).
- [5] S. L. Hwang, K. H. Kim, K. S. Jang, H. S. Jeon, W. J. Choi, J. H. Chang, H. S. Kim, M. Yang, H.S. Ahn, J.S. Bae and S.W. Kim, *Journal od the Korean Crystal Growth and Crystal Technology* Vol.16, No. 4 (2006) 157-161
- [6] K. H. Kim, H. S. Ahn, M. Yang, K.S. Jang, S. L. Hwang, W. j. Choi, C. R. Cho, S.W. Kim, Y. Honda, M.Yamaguchi, and N. Sawaki, J. Yoo. S. M. Lee, and M. Koike, *phys. stat. sol. (c)* 3, No.6, 1461~1465 (2006).
- [7] H. S. Ahn, K. H. Kim, M. Yang, J. Y. Yi, H. J. Lee, J. H. Chang, H. S. Kim, S.W. Kim, S. C. Lee, Y. Honda, M.Yamaguchi, and N. Sawaki, *phys. stat. sol. (a)* 202, 1048 (2005).

Chapter 6.

Experimental results for Active layer's Condition

By utilizing the GaN-based double hetero structure with broad wavelengths, Si and Te doped white-light or near-white-light generation without using phosphor have been demonstrated. However, their output electroluminescence (EL) spectra are dependent on the bias current.

In this chapter, I will summarize test result of Al(In)GaN base white LED grown by MS-HVPE. Optical spectra (410 nm ~ 610 nm) of the near whitelight emitted by the device are almost invariable, from low to high levels of bias current. The bias independent performance of the optical spectra of the demonstrated device can be attributed to the uniform distribution of the injected carriers in Al(In)GaN active with different center wavelengths. The active layers are composed of Al(In)GaN, sandwiched between upper p-type AlGaN and lower n-type AlGaN layers. The top p-metal (Cr-Ni-Au) circle has a diameter of 100 μm and is surrounded by ring pattern of n-metal contacts on the same plane.

The total active area of our device is around 350 μm circle. In order to perform the on-wafer probing and measurement of the fabricated device, a circular n-type metal contact, with an Cr/Ni/Au thickness of 150/150/500 \AA in diameter was deposited.

Details of the geometry and size of the fabricated device are shown in chapter 5. The overall fabrication-processes are similar to fundamental LED production process. Under a forward bias, strong near-white-light emission can be observed between the two circles in the p-metal region and the p-pad; there is no output light from the trench region making the total effective light-emitting region ring-shaped. The output power and EL spectral performance of devices fabricated with different active composition are studied.

The major difference between the traditional LEDs or super-luminescence-diodes and our demonstrated device, is that in our structure the p-n junction is made by SAG MS-HVPE process and that nano-phase In-rich localized crystal will result in a wavelength distribution of injected carriers. The problems of nonuniform gain spectrum and carrier distribution can be optimized in the devices by developing more experiment.

All devices perform similarly in terms of the output EL spectra. The slight difference in the center wavelengths may be attributed to the nonuniformity of the HVPE-grown epi-layers. The performance of the EL spectra achieved is superior to that reported for phosphor-free whitelight GaN LEDs [3-8].

According to the measured bias-insensitive EL spectra and CIE chromaticity diagram, the calculated color coordinates will be close to that of the white-light region of the CIE diagram. I can, thus, conclude that in order to achieve the desired color temperature and color coordinates, Indium composition of Al(In)GaN active layer must be optimized.

6.1. Performance of AlInGaN White LED

I demonstrated that the conventional AlGaN/Al(In)GaN DH structure are successfully grown using our MS-HVPE method. Normally Bandgap of Al(In)GaN quaternary composition in phase diagram is UV area. To emit white spectrum, In-rich localized nano phase crystal such as quantum dot coexist with intrinsic Al(In)GaN UV band. We could exactly observe EL emission through microscope. When electron is injected into device, LED surface emit red and green light with intrinsic UV~blue. I thought it was novel physics ever not seen before.

Figure 6.1 shows the PL spectrum of the SAG-Al(In)GaN/InGaN DH structure ($X_{Ga}^l = 0.25$) at room temperature. The Epi wafer grown Al(In)GaN quaternary active emitted broad spectrum from UV to red area. Sharp peak of the left is GaN buffer peak. And broad peak of the right is expected

Al(Ga)InN active layer's peak. Relative intensity depends on surface morphology and composition uniformity. It is considered as the variation of the indium composition along the crystal direction.

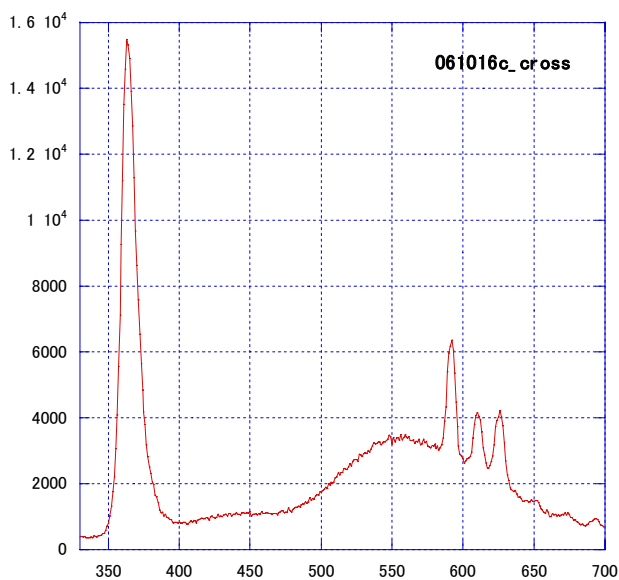


Fig. 6.1 PL spectrum of the SAG-Al(In)GaN/InGaN DH structure

Fig.6.2 shows temperature dependence of PL peak for AlGaN/Al(In)GaN DH structure. I found the peak position of wavelength nearly change as temperature. But the peak intensity of UV (~400 nm) range strongly depends on temperature comparing other spectrum range. Its spectrum shape was changeable as indium mole fraction of MS-HVPE source. It means that it is controllable.

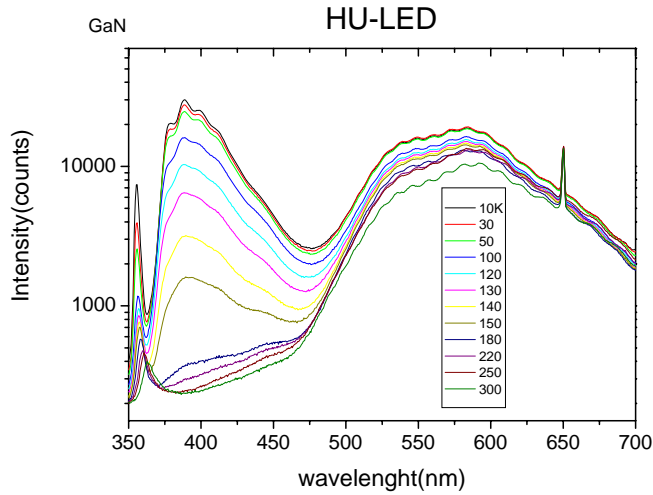


Fig.6.2 temperature dependence of PL peak for AlGaN/Al(In)GaN DH structure

Fig.6.3(a) shows PL peak at low temperature (10 K) of AlGaN/Al(In)GaN DH layers. And Fig.6.3(b) shows peak change as temperature increase. I found that spectrum of 550~600 nm range changed a little but UV range changed steeply under 150 K. We guess that localized In-rich nano phase crystal is little sensitive about temperature.

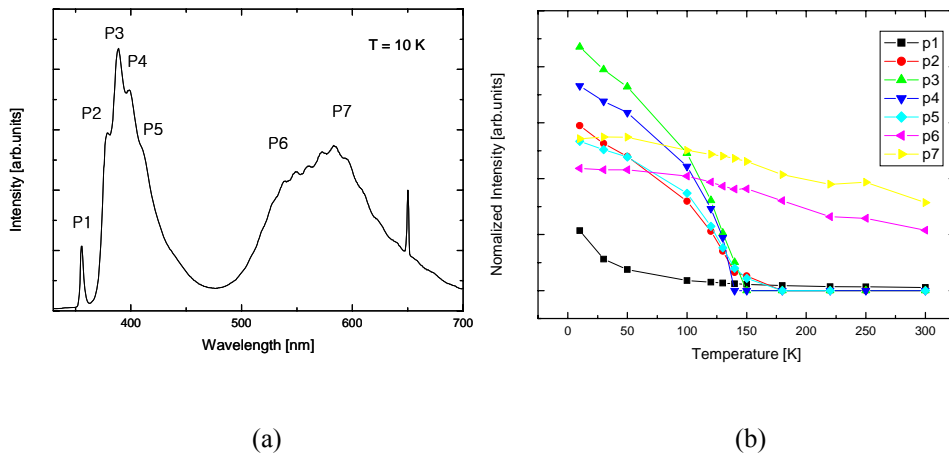


Fig.6.3 (a) PL peak at low temperature at 10 K (b) temperature dependence of PL peak for AlGaN/Al(In)GaN DH layers

6.2 EL characteristics of AlGaIn and AlInGa active

6.2.1 GaN active layer

At first, LED structure with GaN active was grown for reference purpose. N-GaN grown by MOCVD on sapphire was used for substrate. N-cladding layer was Te-doped AlGaIn and P-cladding layer was Mg-doped AlGaIn. P-cap layer was Mg-GaN. All DH-structures was grown by SAG-HVPE. Cr(150 Å)/Ni(150 Å)/Au(500 Å) deposition by e-beam evaporator was used as n-metal and p-metal at once. After formation of metal, alloy process was followed. As expected, blue light emitted and its spectrum was around 430 nm as shown Fig 6.4.

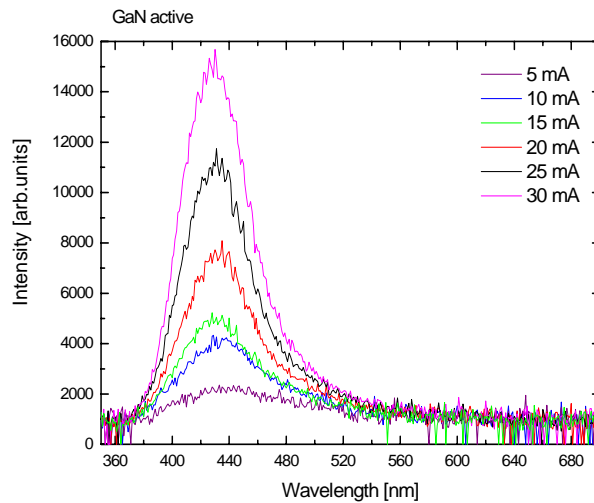


Fig.6.4. Injection current dependance of EL spectrum for DH structure with GaN active layer

Table 6.1. shows EL measurement results of wavelength, intensity and FWHM as injected current.

Table.6.1. Injection current dependence of GaN EL spectrum

GaN (#137)	Wavelength [nm]	Intensity [arb.units]	FWHM [nm]
5mA	433	2352	77.863
10mA	433	3862	64.479
15mA	433	4887	58.243
20mA	431	7566	52.463
25mA	431	11746	49.987
30mA	430	15681	49.068

Injection current was varied from 5 mA to 30 mA. Main peak was observed at 433 nm. There was not any peak at region over 520 nm. At all over wafer, spectrum was similar. Fig 6.5 shows blue light emits clearly at 20 mA.

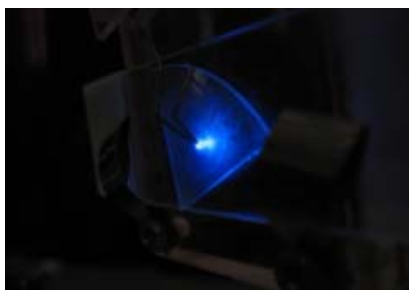


Fig.6.5 Emitting light of DH structure with GaN active layer

Reproducibility was also confirmed through consecutive three samples grown by MS-HVPE. Fig 6.6 shows that there was no change of EL peak intensity from 15 mA to 30 mA of forward injection current. At 20 mA, EL peak FWHM was 52 nm and device performance was good.

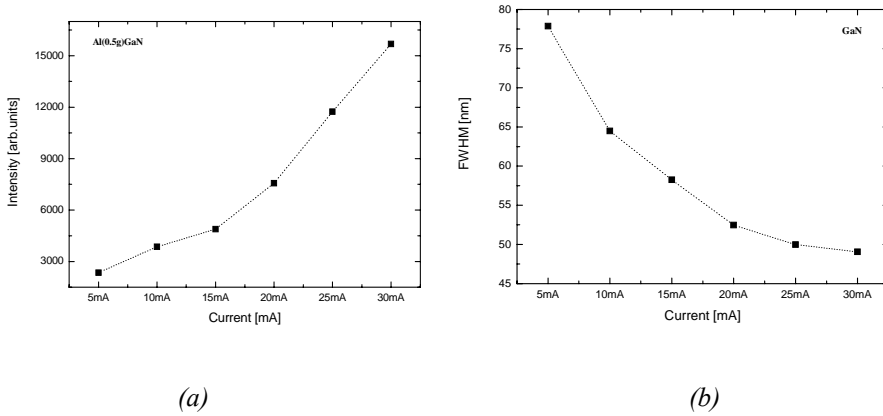


Fig.6.6 Injection current dependence of EL (a) intensity and (b) FWHM

6.2.2 Al(0.1 g)GaN active layer

LED structure with AlGa_N(Al~0.1 g) active was grown and growth time of active layer was 10 min. Fig 6.7 shows EL characteristics as injection current. We could find spectrum peak near 480 nm, 550 nm and 610 nm. It was certainly different from GaN active layer's spectrum.

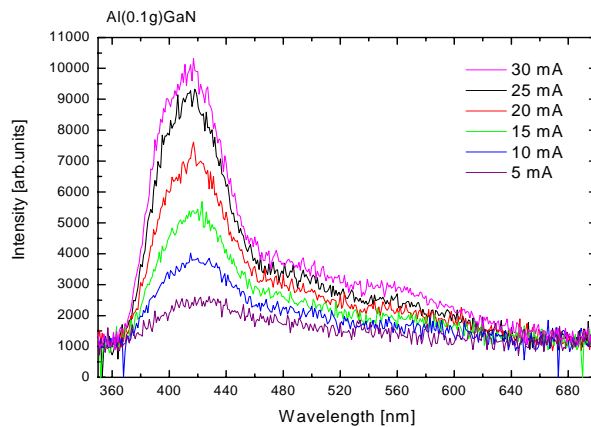


Fig.6.7 Injection current dependence of EL spectrum for DH structure with Al(0.1g)GaN active layer

I could also observe white color emitted and understood it was caused by Al material. Table 6.2 shows EL measurement results of wavelength, intensity and FWHM as injected current of Al(0.1g)GaN active.

Table.6.2. Injection current dependance of Al(0.1 g)GaN EL spectrum

AlGaN 0.1g (#141)	Wavelength [nm]	Intensity [arb.units]	FWHM [nm]
5mA	420	2420	68.979
10mA	420	3859	56.236
15mA	417	5386	51.536
20mA	418	7328	48.322
25mA	415	9281	46.511
30mA	415	10119	46.902

I found the position of main peak shifted forward long wavelength about 10nm comparing with GaN active layer's spectrum. In addition, we could observe difference between GaN active and AlGaN active in over 500 nm region. It means Al material in AlGaN layer effects on growth mechanism and causes yellow band spectrum strongly. Fig 6.8 shows device photography emitting at 20 mA injection current. We checked reproducibility from consecutive experimental result. In conclusion, Al material in AlGaN active dramatically effected on device spectrum and caused white emitting.



Fig. 6.8 Emitting light of DH structure with Al(0.1 g)Ga_N active layer

Fig 6.9 shows spectrum intensity and FWHM characteristics of each injection current. We found it had linear relation with injection current and FWHM of main peak was under 50 nm.

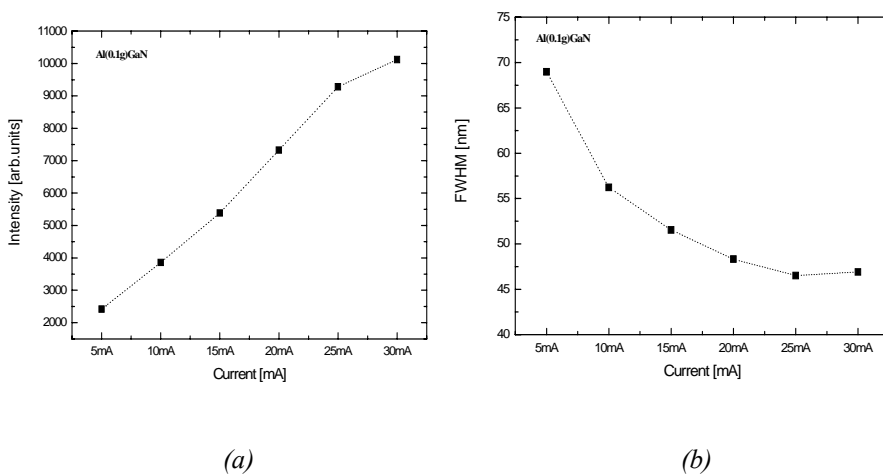


Fig. 6.9 Injection current dependance of EL (a) intensity and (b) FWHM

6.2.3 Al(0.3 g)GaN active layer

LED structure with AlGaN(Al~0.3 g) active was grown. I could also observe white color emitted but couldn't measure EL spectrum because fabrication process had some trouble after crystal growth and formation of electrode was unstable.

6.2.4 Al(0.4 g)GaN active layer

LED structure with AlGaN(Al~0.4 g) active was grown and growth time of active layer was 10 min. Fig 6.10 shows EL characteristics of each injection current. We could find spectrum emitting white color. Blue and white spectrums coexisted in a device.

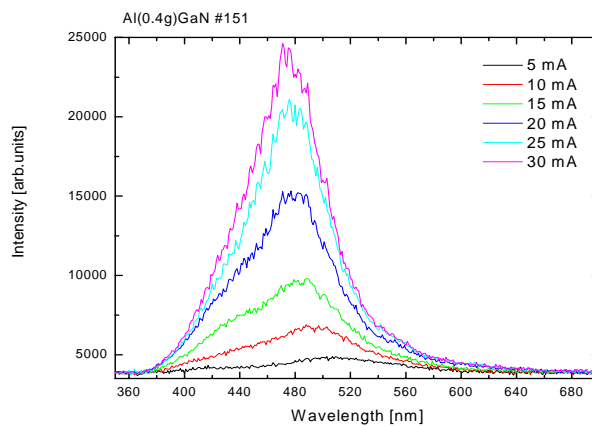


Fig.6.10 Injection current dependance of EL spectrum for DH structure with Al(0.4 g)GaN active layer

In general, Main peak appeared near 480 nm~490 nm comparing with AlGaN(Al~0.1 g) active. It meant that Al amount affected on spectrum distribution. Table 6.3 shows intensity and FWHM of AlGaN(Al~0.4 g) active and Fig 6.11 shows device emitting white color with green color.

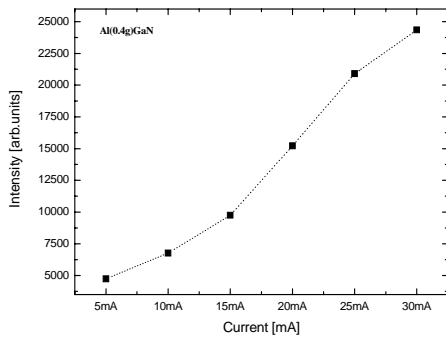
Table.6.3. Injection current dependence of Al(0.4 g)GaN EL spectrum

AlGaN 0.4g (#151)	Wavelength [nm]	Intensity [arb.units]	FWHM [nm]
5mA	496	4742	92.702
10mA	489	6770	88.696
15mA	487	9751	82.451
20mA	482	15213	73.989
25mA	475	20905	65.922
30mA	472	24348	64.241

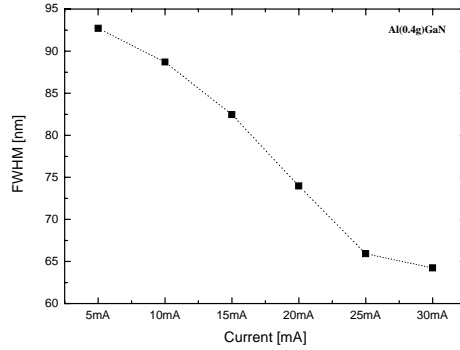


Fig.6.11 Emitting light of DH structure with Al(0.4 g)GaN active layer

I found it had linear relation with injection current and intensity of main peak was higher than expected. Main peak's FWHM of 480 nm was 64 nm~92 nm and was changed in proportion to injection current. A peak of 420 nm tends to red shift. On the other hand, a peak of 500 nm tends to blue shift. When injection current increases, the intensity of 500 nm peak increases more than other peak relatively. It means that it is not impurities effect but stable crystal formation of AlGaN active layer. We thought it needed more study to verify this phenomenon.



(a)



(b)

Fig.6.12 Injection current dependance of EL (a) intensity and (b) FWHM

6.2.5 Al(0.5 g)GaN active layer

LED structure with AlGa_N(Al~0.5 g) active was grown and growth time of active layer was 10 min. Fig 6.13 shows EL characteristics about each injection current. We could find spectrum emitting white color. Blue and white spectrum also coexisted in a device. Main peak appeared near 447 nm~431 nm and was changed in proportion to injection current. There were not other peak such as 550 nm and 610 nm in EL spectrum. But FWHM of 57 nm~150 nm range was more broad than other samples. We could observe white light with blue light and it was definitely different from GaN active.

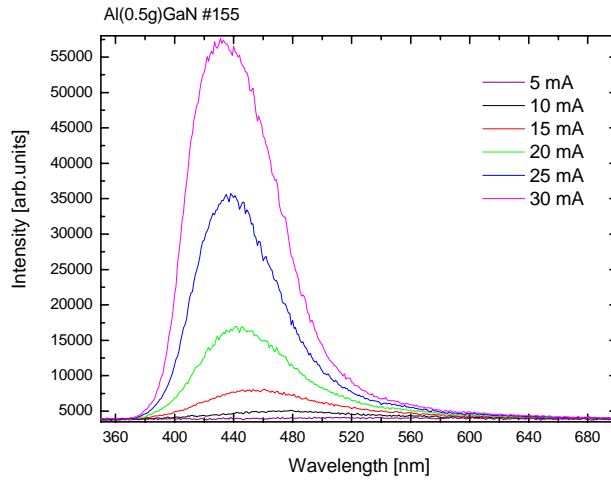


Fig.6.13 Injection current dependence of EL spectrum for DH structure with Al(0.5 g)GaN active layer

Table.6.4. Injection current dependence of Al(0.5g)GaN EL spectrum

AlGaN 0.5g (#155)	Wavelength [nm]	Intensity [arb.units]	FWHM [nm]
5mA	447	3826	150.5
10mA	447	4681	95.293
15mA	446	8011	75.581
20mA	442	16937	61.791
25mA	438	35720	55.105
30mA	431	57647	57.05

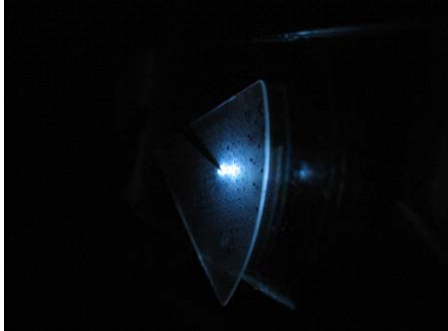


Fig.6.14 Emitting light of DH structure with Al(0.5)GaN active layer

As Table 6.4 shows, intensity increases dramatically over 15 mA injection current and increases linearly in proportion to injection current. We thought it was caused by metallization process.

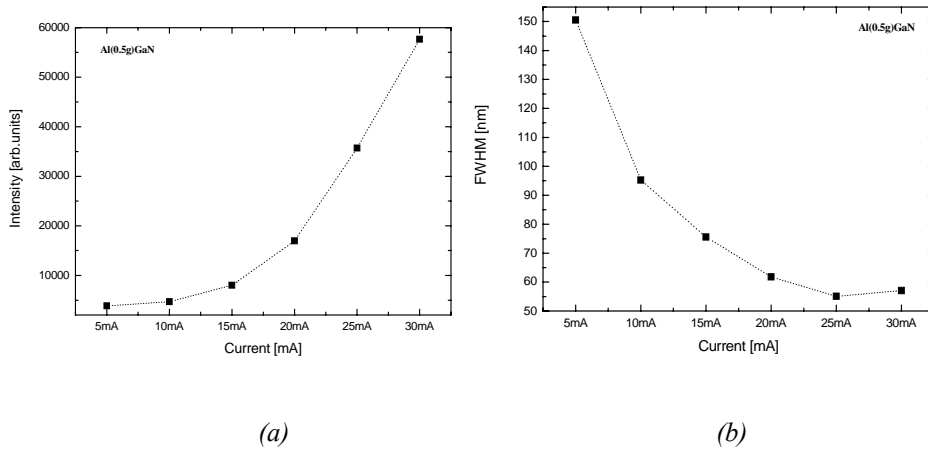


Fig.6.15 Injection current dependance of EL (a) intensity and (b) FWHM

As Al amount increases, the intensity of long wavelength peak tends to be strong. We thought it meant change of growth mechanism and device characteristics as Al amount increased in AlGa_{1-x}N.

active layer.

6.2.6 Al(0.6 g)GaN active layer

LED structure with AlGaN(Al~0.6 g) active was grown and growth time of active layer was 10 min. Fig 6.16 shows EL characteristics as injection current. I could find spectrum emitting white color. Main peak appeared near 396 nm, we could find spectrum peaks near 550 nm and 610 nm. Fig 6.16 shows EL FWHM of AlGaN(Al~0.6 g) active is about 100 nm, it is more broad than other samples.

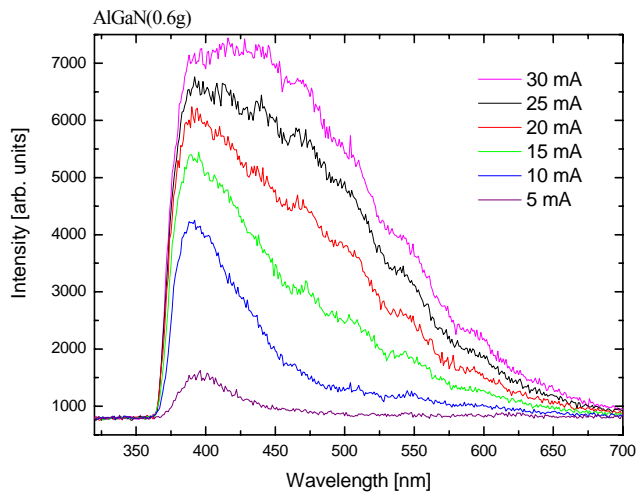


Fig.6.16 Injection current dependance of EL spectrum for DH structure with Al(0.6 g)GaN active layer

Table.6.5. Injection current dependence of Al(0.6g)GaN EL spectrum

AlGa _N 0.6g (#159)	Wavelength [nm]	Intensity [arb.units]	FWHM [nm]
5mA	396	1622	36.349
10mA	392	4253	48.383
15mA	390	5396	77.69
20mA	390	6239	114.07
25mA	392	6762	122.89
30mA	392	7177	123.97

I couldn't measure each peak over 500 nm because of mixed spectrum peak. The EL intensity was linear over 10 mA and was higher than other samples.

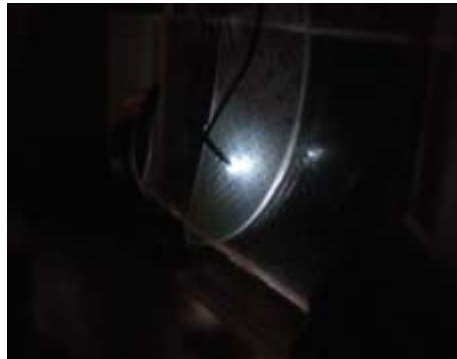


Fig.6.17 Emitting light of DH structure with Al(0.6 g)GaN active layer

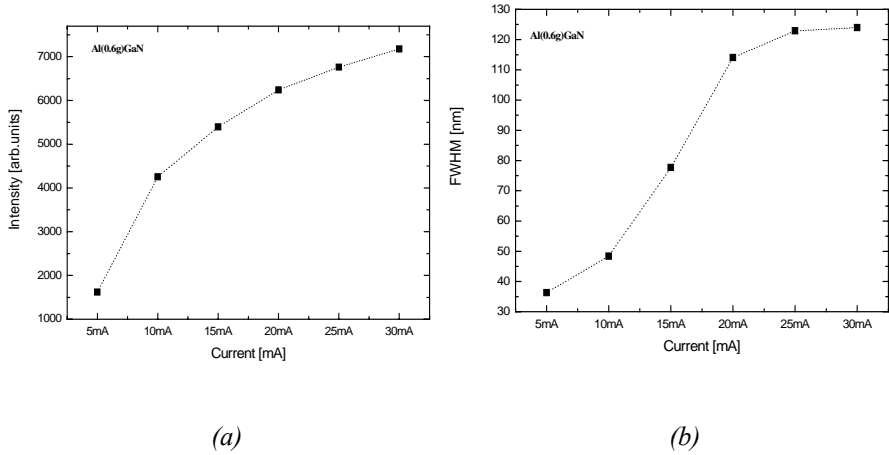


Fig. 6.18 Injection current dependence of EL (a) intensity and (b) FWHM

In case of Al~0.6 g in AlGa_N active layer, white emission intensity was highest. I tried to add In at AlGa_N(Al~0.6 g) active to check spectrum of AlInGa_N quaternary active. It let us know spectrum trend as In mole fraction increase. Other layers are fixed to compare performance exactly.

6.2.7 In(0.1 g) Al(0.6 g) Ga_N active layer

LED structure with In(0.1 g)Al(0.6 g)Ga_N active was grown and growth time of active layer was 10min. Fig 6.19 shows EL characteristics for each injection current. Main peak appeared near 403 nm~410 nm according to injection current. We could find spectrum peaks near 550 nm and 610 nm definitely. Table 6.6 shows EL spectrum's FWHM of main peak is about 80 nm.

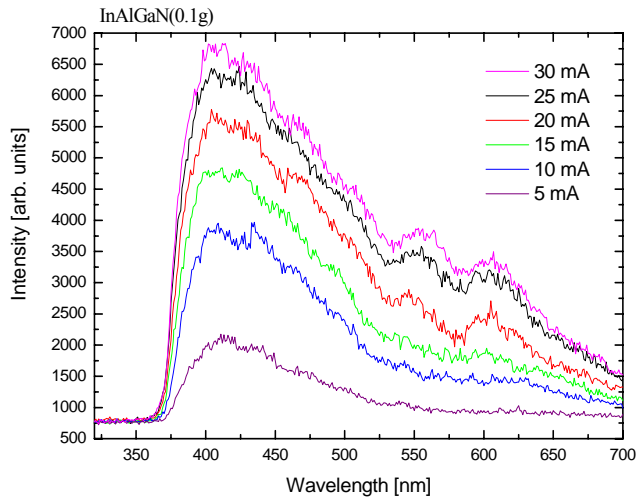


Fig.6.19 Injection current dependance of EL spectrum for DH structure with In(0.1 g)Al(0.6 g)GaN active layer

Table.6.6. Injection current dependance of In(0.1 g)Al(0.6 g)GaN EL spectrum

InAlGaN 0.1g (#165)	Wavelength [nm]	Intensity [arb.units]	FWHM [nm]
5mA	410	2086	72.322
10mA	408	3924	80.671
15mA	405	4767	82.314
20mA	405	5699	91.374
25mA	403	6358	89.256
30mA	403	6808	93.136

Peaks of 550 nm and 610 nm appeared from 10 mA and they separated clearly at 20 mA. I found Al and In material in InAlGaN active effected on two peaks. Especially, 610 nm peak was strongly caused by In material. I thought it was also caused by MS-HVPE growth mechanism.



Fig.6.20 Emitting light of DH structure with In(0.1 g)Al(0.6 g)GaN active layer

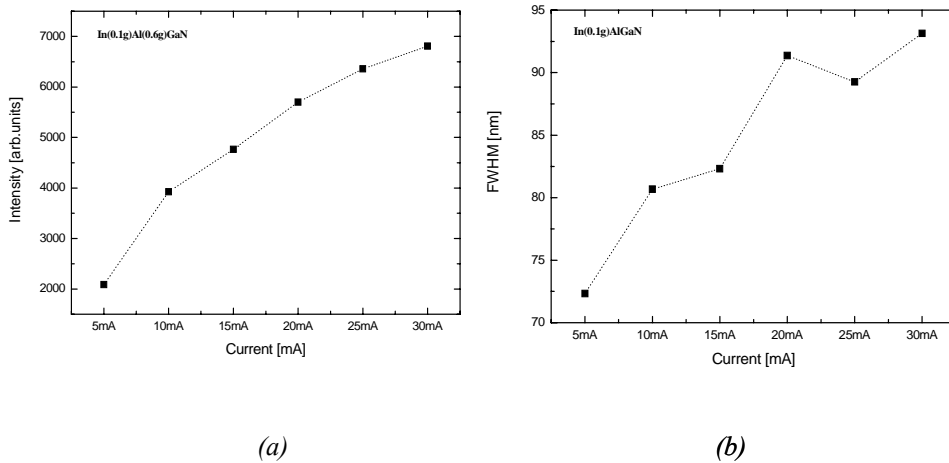


Fig.6.21 Injection current dependance of EL (a) intensity and (b) FWHM

Peak intensity was changed in proportion to injection current and FWHM was very broad because of several mixed peak effect.

6.2.8 In(0.2 g)Al(0.6 g)GaN active layer

LED structure with In(0.2 g)Al(0.6 g)GaN active was grown and growth time of active layer was 10 min. Fig 6.22 shows EL characteristics for each injection current. Main peak appeared near

405 nm~413 nm according to injection current. It increased slightly comparing with In~0.1 g of InAlGa_N active. I could find spectrum peaks near 550 nm and 610 nm definitely. Table 6.7 shows EL FWHM of main peak is about 75~100 nm.

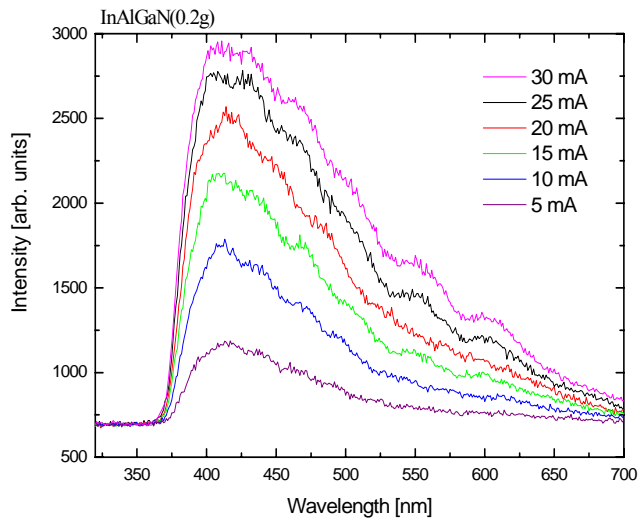


Fig.6.22 Injection current dependence of EL spectrum for DH structure with In(0.2 g)Al(0.6 g)Ga_N active layer

Table.6.7. Injection current dependence of In(0.2 g)Al(0.6 g)Ga_N EL spectrum

InAlGa _N 0.2g (#169)	Wavelength [nm]	Intensity [arb.units]	FWHM [nm]
5mA	413	1186	75.918
10mA	409	1753	80.117
15mA	408	2173	83.623
20mA	412	2537	87.165
25mA	406	2753	94.287
30mA	405	2917	103.74

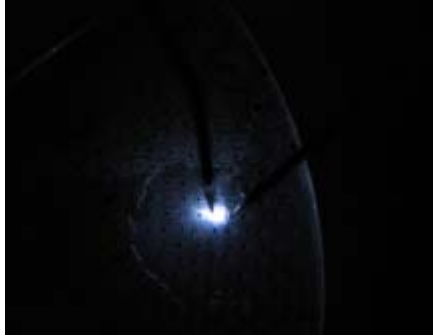


Fig.6.23 Emitting light of DH structure with In(0.2 g)Al(0.6 g)GaN active layer

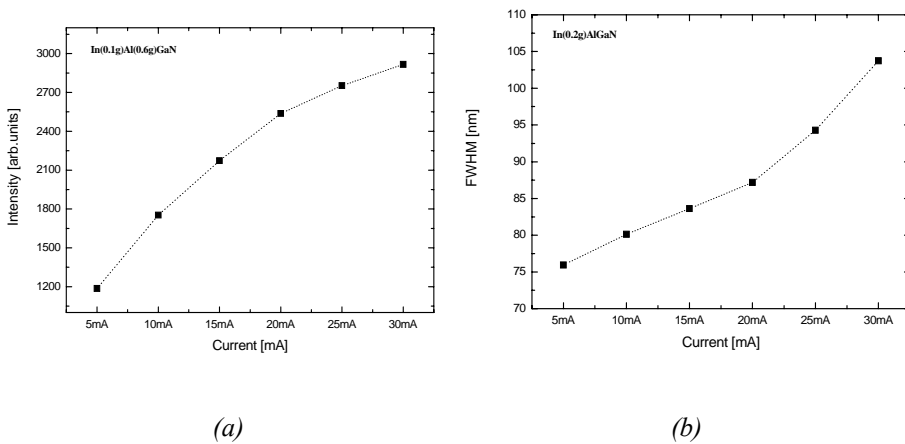


Fig.6.24 Injection current dependance of EL (a) intensity and (b) FWHM

Peak intensity was linearly changed in proportion to injection current but it was saturated over 20 mA. I thought it was caused by metallization process effecting on joule heating.

6.2.9 In(0.3 g)Al(0.6 g)GaN active layer

LED structure with In(0.3 g)Al(0.6 g)GaN active was grown and growth time of active layer was 10 min. Fig 6.25 shows EL characteristics for each injection current. Main peak appeared near

415 nm. It increased slightly comparing with In~0.2 g of InAlGaN active. I could find spectrum peaks near 550 nm and 610 nm definitely. Table 6.8 shows EL FWHM of main peak is about 92~156 nm.

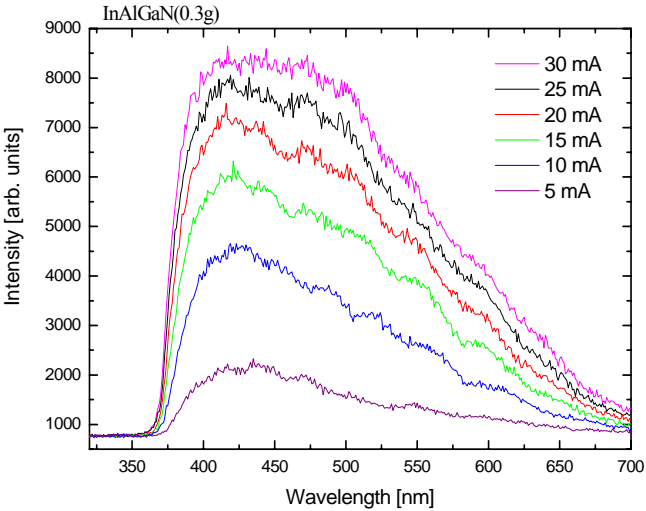


Fig.6.25 Injection current dependance of EL spectrum for DH structure with In(0.3 g)Al(0.6 g)GaN active layer

Table.6.8. Injection current dependance of In(0.3 g)Al(0.6 g)GaN EL spectrum

InAlGaN 0.3g (# 72)	Wavelength [nm]	Intensity [arb.units]	FWHM [nm]
5mA	417	2223	92.591
10mA	418	4613	127.06
15mA	417	6031	146.75
20mA	415	7254	149.58
25mA	417	7979	152.64
30mA	415	8368	156.47

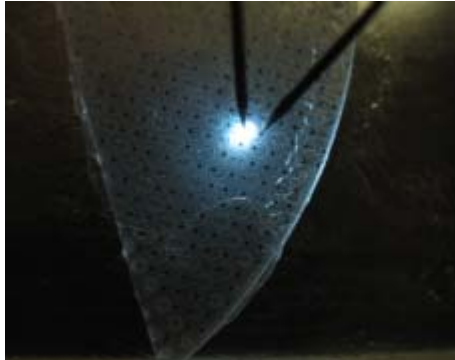


Fig.6.26 Emitting light of DH structure with In(0.3 g)Al(0.6 g)GaN active layer

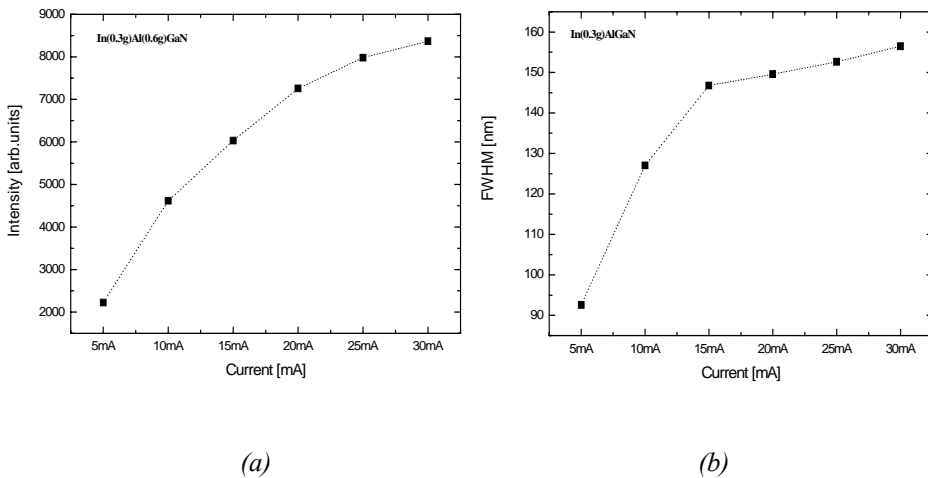


Fig.6.27 Injection current dependance of EL (a) intensity and (b) FWHM

Peak intensity was linearly changed in proportion to injection current and FWHM was unchanged from 15 mA. I had got same experimental result of three times continuously. It meant reproducibility was no problem.

6.2.10 In(0.4 g)Al(0.6 g)GaN active layer

LED structure with In(0.4 g)Al(0.6 g)GaN active was grown and growth time of active layer was 10min. Fig 6.28 shows EL characteristics as injection current. Main peak appeared near 410nm~415nm according to injection current. It was the same as In(0.3 g)Al(0.6 g)GaN sample. I could find spectrum peaks near 550 nm and 610 nm definitely. Table 6.9 shows EL FWHM of main peak is about 96~136 nm.

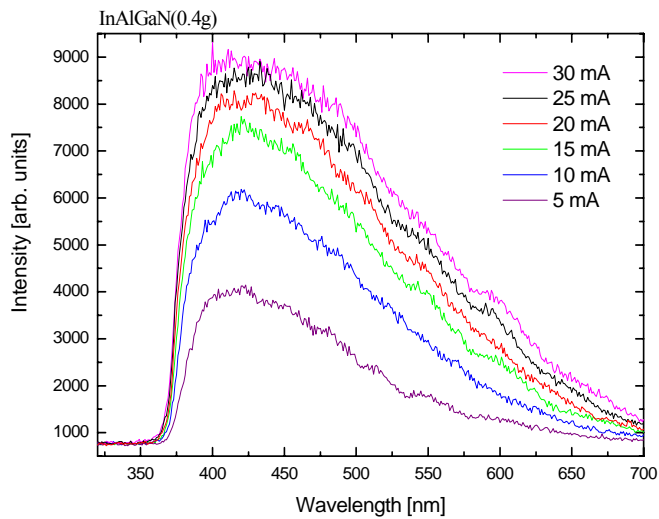


Fig.6.28 Injection current dependance of EL spectrum for DH structure with In(0.4 g)Al(0.6 g)GaN active layer

Table.6.9. Injection current dependence of In(0.4 g)Al(0.6 g)GaN EL spectrum

InAlGaN 0.4g (#176)	Wavelength [nm]	Intensity [arb.units]	FWHM [nm]
5mA	415	4075	97.145
10mA	417	6101	116.56
15mA	413	7539	121.25
20mA	415	8282	126.52
25mA	411	8548	131.96
30mA	410	9007	136.95

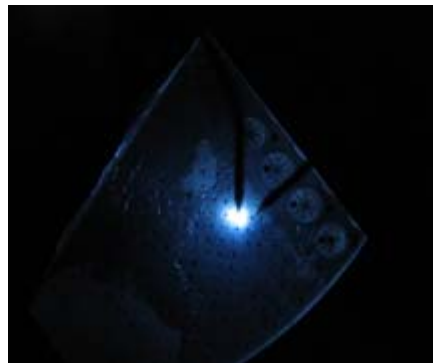


Fig.6.29 Emitting light of DH structure with In(0.4 g)Al(0.6 g)GaN active layer

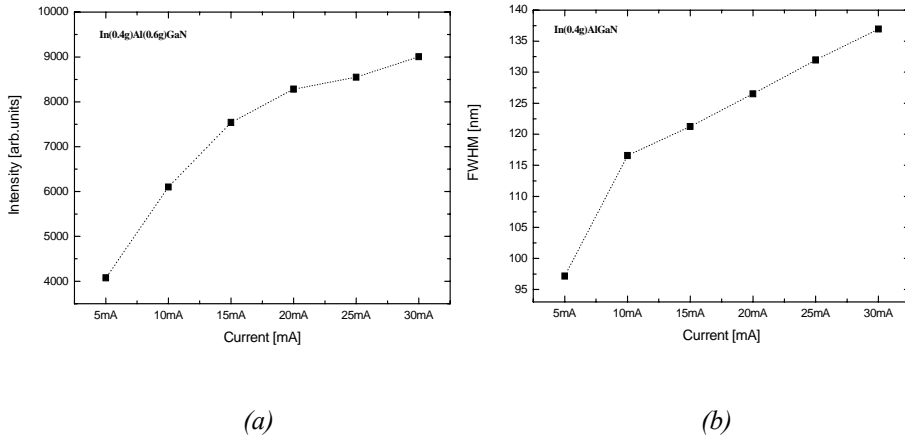


Fig.6.30 Injection current dependence of EL (a) intensity and (b) FWHM

Peak intensity was linearly changed in proportion to injection current and I could observe bluish white color. I had got same experimental result of three times continuously

6.2.11 In(0.5 g)Al(0.6 g)GaN active layer

LED structure with In(0.5 g)Al(0.6 g)GaN active was grown and growth time of active layer was 10 min. Fig 6.31 shows EL characteristics as injection current. Main peak appeared near 407 nm~423 nm according to injection current. I could find spectrum peaks near 550 nm and 610 nm definitely. Table 6.10 shows EL spectrum's FWHM of main peak is about 85~150 nm.

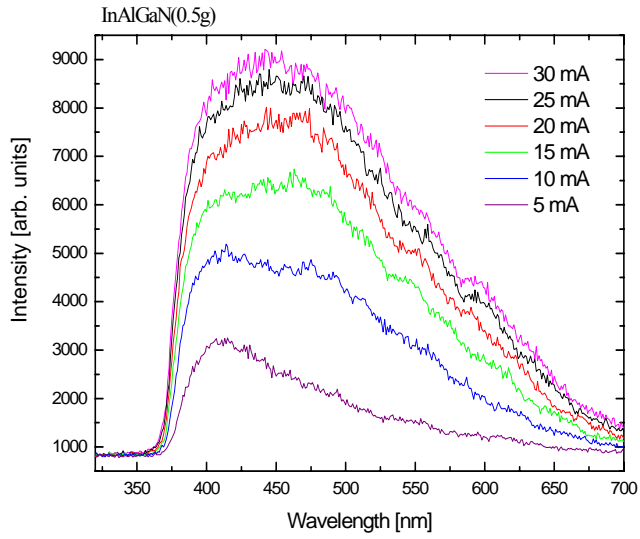


Fig.6.31 Injection current dependance of EL spectrum for DH structure with $In(0.5\text{ g})Al(0.6\text{ g})GaN$ active layer

Table.6.10 Injection current dependance of $In(0.5\text{ g})Al(0.6\text{ g})GaN$ EL spectrum

InAlGaN 0.5g (#180)	Wavelength [nm]	Intensity [arb.units]	FWHM [nm]
5mA	407	3234	85.397
10mA	414	5186	137.87
15mA	416	6256	143.13
20mA	419	7584	142.25
25mA	424	8610	145.74
30mA	423	9040	150.78



Fig.6.32 Emitting light of DH structure with $In(0.5)Al(0.6)GaN$ active layer

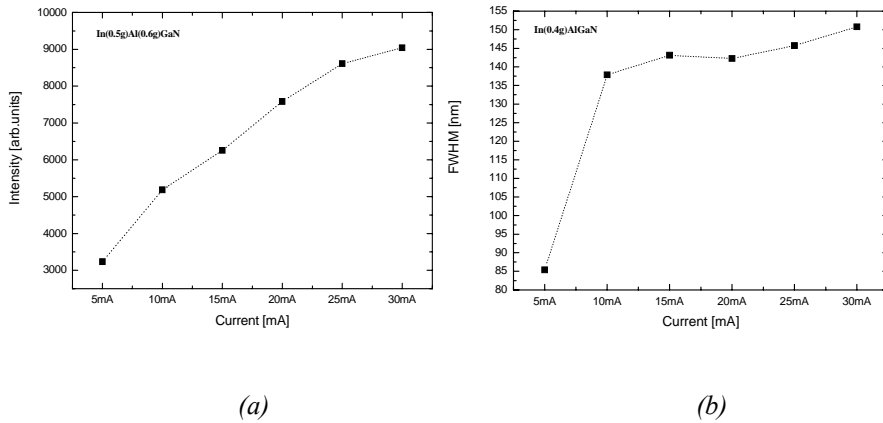


Fig.6.33 Injection current dependance of EL (a) intensity and (b) FWHM

Peak intensity was linearly changed in proportion to injection current and I could observe bluish white color like other samples. FWHM increased dramatically over 10 mA. I thought it was caused by new generated peak near 500 nm. I had got same experimental result of three times continuously

6.3 XRD characteristics

The atomic planes of a crystal cause an incident beam of X-rays to interfere with one another as they leave the crystal. The phenomenon is called X-ray diffraction. XRD technique is used to identify crystalline phases and orientation. It is also used to determine structural properties of lattice parameters such as strain, grain size, epitaxy, phase composition, preferred orientation (Laue) order-disorder transformation, and thermal expansion. Thickness measurement of thin films and multi-layers can be done through determination of atomic arrangement. I changed Al atomic fraction in Ga melt to adjust Al composition of crystal. I inserted Al amount from 0.1g to 0.6g in Ga amount of 20 g. Each Al atomic fraction was 0.0127 at 0.1 g, 0.0373 at 0.3 g, 0.0495 at 0.4 g, 0.0607 at 0.5 g and 0.072 at 0.6 g. Temperature was 900 °C at source region and 1090 °C at growth region. The flow rate of HCl and NH₃ was 20 sccm and 800 sccm. Growth rate was 20um/hr and thickness of AlGa_{1-x}N was 2~5 um. Sample size for XRD measurement was 1/4". 2θ-ω scan was processed about (0002) face to find a lattice constant. To find c lattice constant, the measurement of (0004) and (0006) face should be done. But we found c lattice constant through formula (2) instead of it. We also processed XRD mapping in case of low Al composition causing vague peak near GaN buffer peak.

$$\frac{l}{d^2} = \frac{4}{3} \cdot \frac{h^2 + hk^2 + k^2}{a^2} + \frac{l^2}{c^2} \dots\dots\dots (1)$$

$$a = \frac{c \times 3.189}{5.185} \dots\dots\dots (2)$$

I could find ‘a’ and ‘c’ lattice constant using formula (1) and (2). The ratio of two values is

called poisson's ratio and it shape logarithmic function. Poisson's ratio means varied amount of material by elastic metamorphosis and is determined by material. For example, if a sample lengthens forward one direction by pulling force, it shrinks relatively for its perpendicular direction.

I can express changing ratio ($\Delta\omega/\omega$) as following formula

$$\frac{c\text{-axis variation}}{a\text{-axis variation}} = \frac{\Delta\omega/\omega}{\Delta l/l} = \sigma \text{ (poisson's ratio)}$$

for hexagonal structure

$$\sigma = \frac{C_{12}C_{33} - C_{13}^2}{C_{11}C_{33} - C_{13}^2}$$

$$\frac{c' - \{5.185(1-x) + 4.982x\}}{5.185(1-x) + 4.872x} = \frac{a' - \{3.189(1-x) - 0.077x\}}{3.189(1-x) + 3.112x}$$

$$\frac{[\{c_{12AlN}x + c_{12GaN}(1-x)\} \{c_{33AlN}x + c_{33GaN}(1-x)\} - \{c_{13AlN}x + c_{13GaN}(1-x)\}]^2}{[\{c_{11AlN}x + c_{11GaN}(1-x)\} \{c_{33AlN}x + c_{33GaN}(1-x)\} - \{c_{13AlN}x + c_{13GaN}(1-x)\}]^2} \dots\dots\dots(3)$$

Fig.6.34 shows experimental result of K. Tsubouchi, N. Mikoshiba and theoretical result of V. A. Savastenko, A. U. Sheleg that is first-principles molecular dynamics method, of A. F. Wright that is pseudopotential local density approximation method, and of K. Shimada, T. Sota, K. Suzuki. It expresses relation of Al composition and Poisson's ratio. In Fig 6.34, red line is the results of K. Shimada, blue and green lines are the results of V. A. Savastenko and A. F. Wright. We found Poisson's value from 'a' and 'c' lattice constant by XRD measurement and formula (3). There is much error in low Al composition region relatively. In this paper, I used the results of V. A. Savastenko to estimate Al composition. For example, For example, Fig.6.35 shows simulated results of Al composition and poisson ratio. Atomic fraction of Al~0.0496(Al~0.4 g) AlGaN layer agree to mole fraction of 0.315~0.308 range and is estimated to 31 % according to V. A. Savastenko's result.

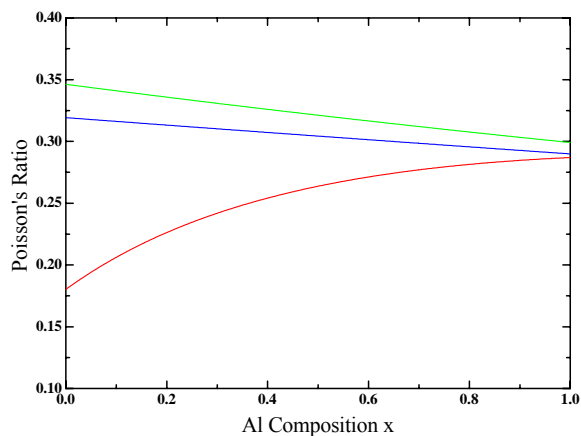


Fig.6.34 the relation between Al atomic fraction and Poisson's ratio

#143(Al:0.1g)

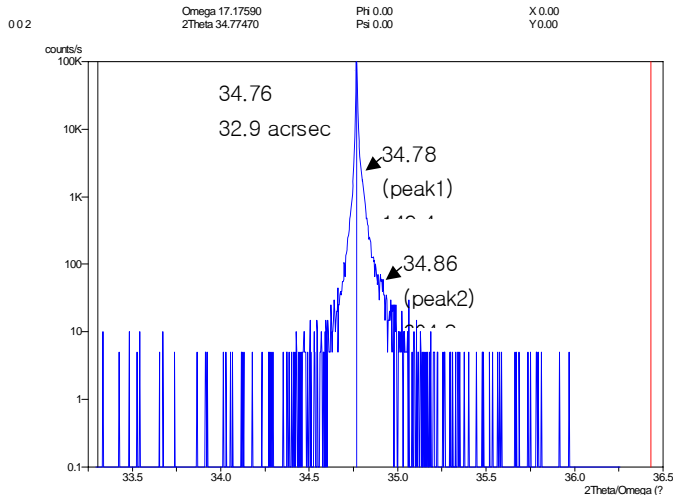


Fig.6.35 XRD measurement of AlGaN layer at Al~0.0127(0.1 g)

In case of Al~0.0127(0.1 g) in AlGaN layer, Fig 6.35 shows two peaks in XRD measurement. c lattice constants of peak 1 and peak 2 were 5.154 and 5.153 respectively using equation (1) of (0002) face and a lattice constants of peak 1 and peak 2 were 3.17 and 3.163 respectively using equation (2). I could estimate Al mole fraction of peak 1 and peak2 were 16.5 % and 22.7 % through the relation graph of Al composition and poisson ratio.

#147(Al:0.3g)

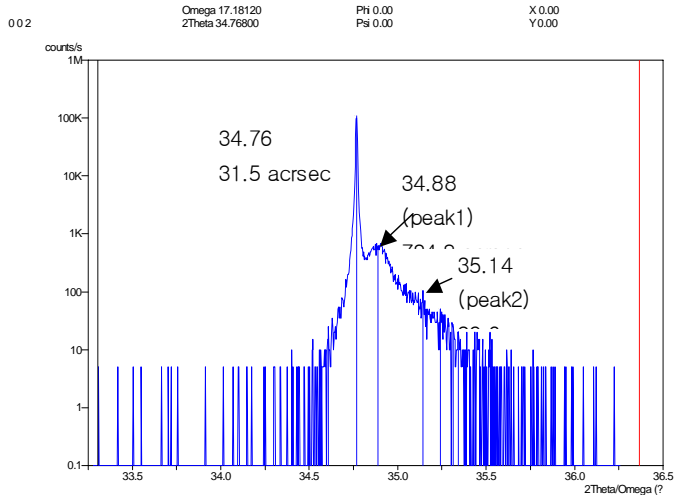


Fig.6.36 XRD measurement of AlGaIn layer at Al~0.0373(0.3 g)

In case of Al~0.0373(0.3 g) in AlGaIn layer, Fig 6.36 also shows two peaks in XRD measurement. c lattice constants of peak 1 and peak 2 were 5.14 and 5.103 respectively using equation (1) of (0002) face and a lattice constants of peak 1 and peak 2 were 3.161 and 3.139 respectively using equation (2). I could estimate Al mole fraction of peak 1 and peak2 were 24.2 % and 44.1 % through the relation graph of Al composition and poisson ratio.

#153(Al:0.4g)

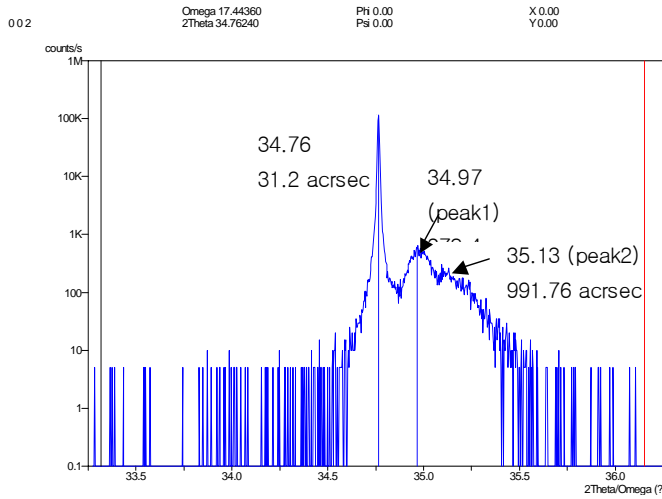


Fig.6.37 XRD measurement of AlGaIn layer at Al~0.0495(0.4 g)

In case of Al~0.0495(0.4 g) in AlGaIn layer, Fig 6.37 also shows two peaks in XRD measurement. c lattice constants of peak 1 and peak 2 were 5.127 and 5.105 respectively using equation (1) of (0002) face and a lattice constants of peak 1 and peak 2 were 3.153 and 3.140 respectively using equation (2). I could estimate Al mole fraction of peak 1 and peak2 were 31.1 % and 43.3 % through the relation graph of Al composition and poisson ratio.

#157(Al:0.5g)

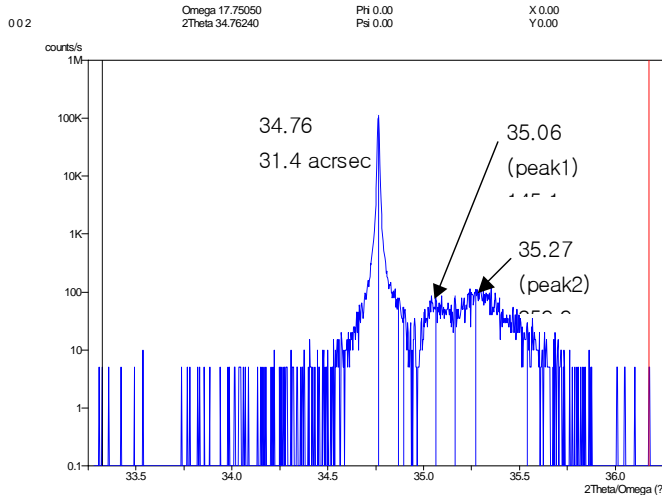


Fig.6.38 XRD measurement of AlGaIn layer at Al=0.0607(0.5 g)

In case of Al=0.0607(0.5 g) in AlGaIn layer, Fig 6.38 also shows two peaks in XRD measurement. c lattice constants of peak 1 and peak 2 were 5.114 and 5.085 respectively using equation (1) of (0002) face and a lattice constants of peak 1 and peak 2 were 3.146 and 3.127 respectively using equation (2). I could estimate Al mole fraction of peak 1 and peak2 were 38 % and 53.9 % through the relation graph of Al composition and poisson ratio.

#161 (Al:0.6g)

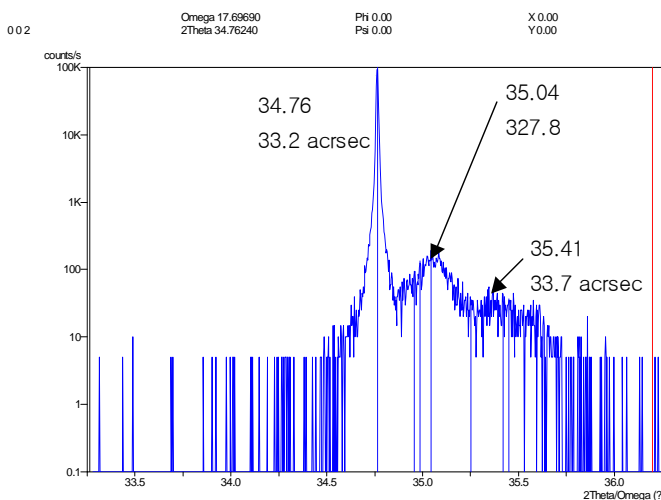


Fig. 6.39 XRD measurement of AlGaN layer at Al~0.0072(0.6 g)

In case of Al~0.072(0.6 g) in AlGaN layer, Fig 6.39 also shows two peaks in XRD measurement. c lattice constants of peak 1 and peak 2 were 5.117 and 5.065 respectively using equation (1) of (0002) face and a lattice constants of peak 1 and peak 2 were 3.147 and 3.115 respectively using equation (2). I could estimate Al mole fraction of peak 1 and peak2 were 36.5 % and 64.5 % through the relation graph of Al composition and poisson ratio.

Table 6.11 shows the relation of Al atomic fraction and Al mole fraction in AlGaN layer. I could find it changed linearly in proportion to Al atomic fraction. Two peaks in XRD mean difference of reaction time of Al and Ga source in NH₃ gas. It effects on surface morphology

Table.6.11 The relation of Al atomic fraction and Al mole fraction in AlGaN layer:

GaN			
2 θ	c	a	d1
34.76	5.157	3.172	2.579

AlGaN							
Atomic fraction	peak	Estimated Al (%) composition	Diffraction angle (0002) (degree)	Lattice constant c (Å) ± 0.001	Lattice constant a (Å) ± 0.001	d2	d1-d2
0.0127 (Al 0.1 g)	peak1	16.5	17.39	5.154	3.170	2.577	0.001
	peak2	22.7	17.43	5.143	3.163	2.571	0.007
0.0373 (Al 0.3 g)	peak1	24.2	17.44	5.140	3.161	2.570	0.009
	peak2	44.1	17.57	5.103	3.139	2.552	0.027
0.0495 (Al 0.4 g)	peak1	31.1	17.485	5.127	3.153	2.564	0.015
	peak2	43.3	17.565	5.105	3.140	2.552	0.026
0.0607 (Al 0.5 g)	peak1	38	17.53	5.114	3.146	2.557	0.021
	peak2	53.9	17.635	5.085	3.127	2.542	0.036
0.072 (Al 0.6 g)	peak1	36.5	17.52	5.117	3.147	2.559	0.020
	peak2	64.5	17.705	5.065	3.116	2.533	0.046

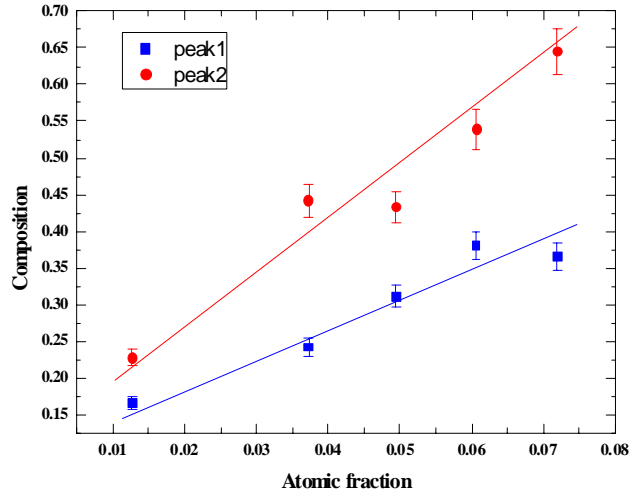


Fig.6.40 The relation of Al atomic fraction and Al mole fraction in AlGaIn layer:

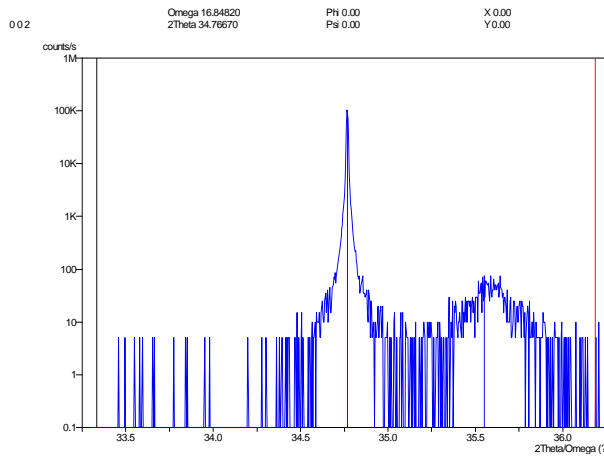


Fig.6.41 XRD measurement of AlInGaIn layer at Al~0.0072(0.6 g)

Fig.6.41 shows DXRD measurement results of AlInGaIn layers. The strain increased when In was added as I expected. It also means AlInGaIn can be successfully grown by MS-HVPE.

Fig.6.42 shows EL peak at room temperature 20 mA of AlGaN/AlInGaN DH layers. As In composition in AlInGaN active layer increase, spectrum gradually tends to be broadened. White balance of LED device is also possible because it can be controlable by MS-HVPE. Fig.6.43 shows EL peak as injection current of AlGaN/AlInGaN DH layers. I could find green and red peak over 20 mA. It means carrier injection is unfavorable to In-rich nano phase crystal relatively. But more research will be needed as it depends on versatile parameter such as growth condition and ohmic contact.

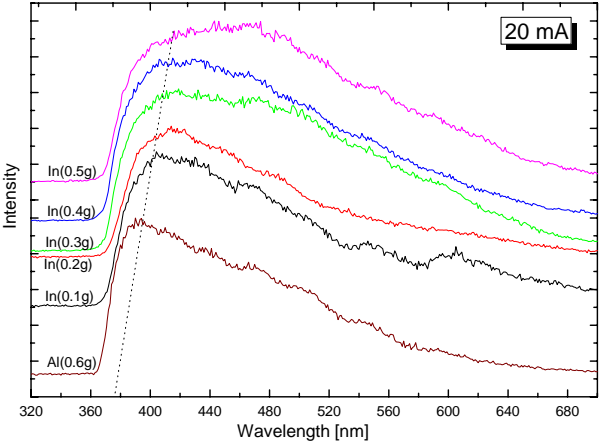


Fig. 6.42 EL peak at room temperature 20 mA of AlGaN/AlInGaN DH layers.

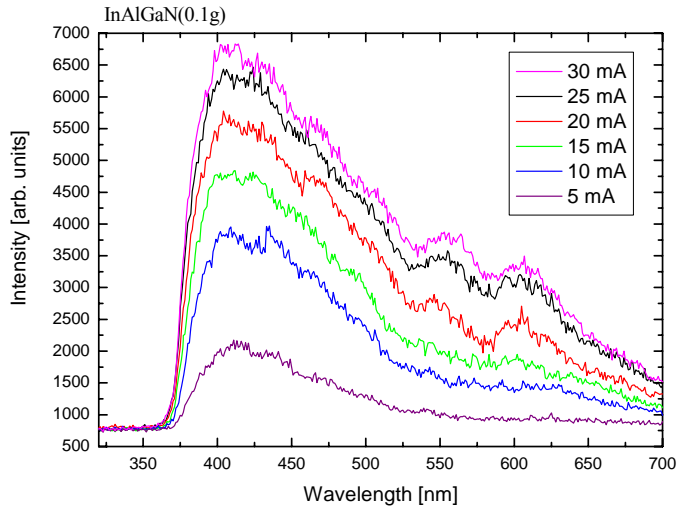


Fig.6.43 EL peak as injection current of AlGaN/AlInGaN DH layers

Fig.6.44 shows emitting images at room temperature, 20 mA of AlGaN/AlInGaN DH structures. The wafer fabrication of all samples was processed simultaneously, after crystal growth. As In composition in AlInGaN active layer increases, its color changes near white. It means wavelength broadens gradually and long wavelength region increases relatively.



(a) $Al_{(0.6g)}In_{(0.1g)}GaN$

(b) $Al_{(0.6g)}In_{(0.3g)}GaN$

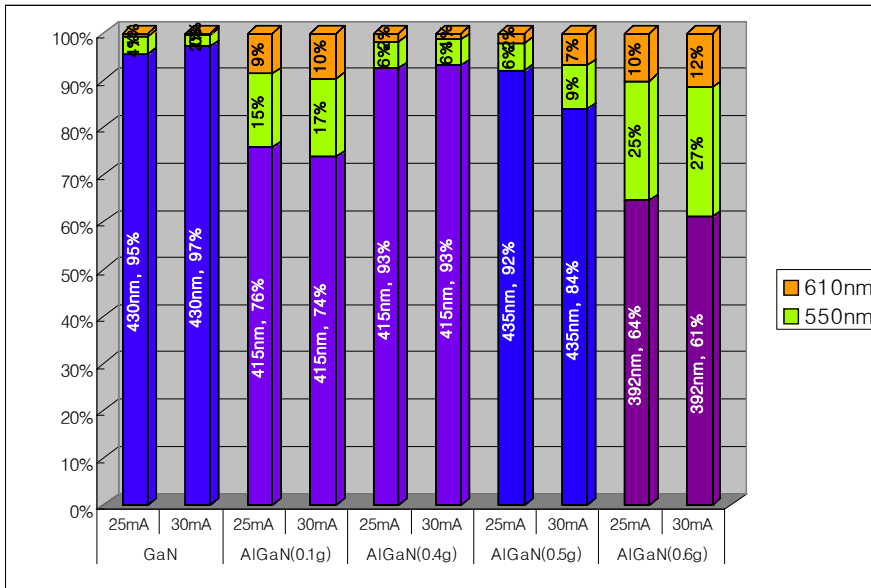
(c) $Al_{(0.6g)}In_{(0.5g)}GaN$

Fig. 6.44. Emitting images at room temperature, 20 mA of AlGaN/AlInGaN DH

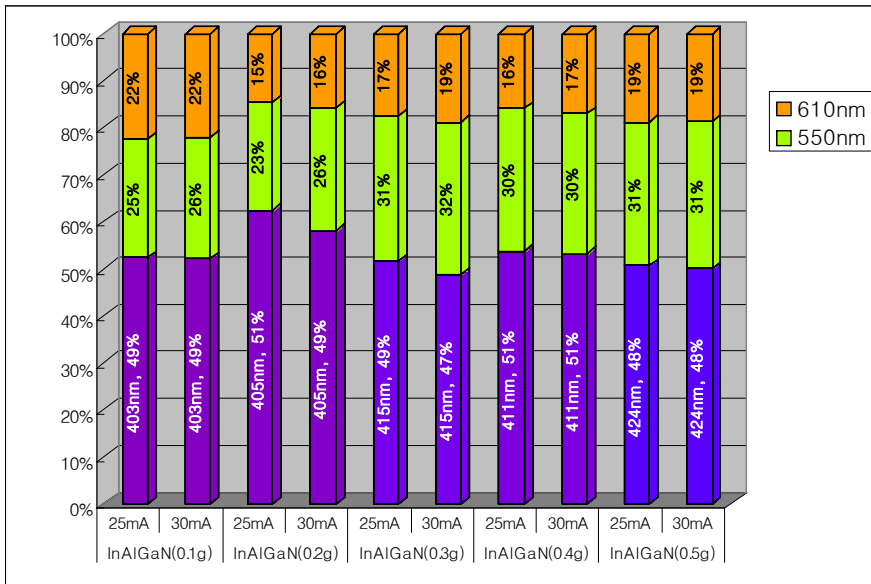
I reported the growth of InGaN and InAlGaN alloys by mixed-source hydride vapor phase epitaxy (HVPE) method. Most of experiment process was similar to conventional HVPE. But we found that there were some different phenomena in mixed-source hydride vapor phase epitaxy. The devices grown AlInGaN quaternary active emitted broad spectrum from UV to red area as Fig.6.43. Its spectrum was changeable as In amount. I confirmed that it could be controllable.

The growth layer was performed on GaN templated sapphire (0001) substrates. The device structure was consisted of conventional double-hetero structure (DH). I prepared some samples that most of layers were same except AlInGaN active layer. And I processed same fabrication to escape external variable factors. I have been successful in developing white LEDs emitting wide spectrum in active layer using a conventional DH structure. MS-HVPE enhanced localized composition of AlGaIn and makes many other energy levels in same layer. I could make sure various wavelengths emitted at the surface of chip simultaneously when biased forward.

I measured wavelength distribution of each active layer to check active layer's composition dependance. Fig.6.45 shows that InAlGaIn active samples are closer to white color than AlGaIn active samples. We already found aluminum composition could be controllable, and confirmed it was reproducible. When active layer was Al(0.6 g)GaIn, intensity ratio of main peak was 61 %. 550 nm was 27 % and 610 nm was 21 %. Fig.6.45 (b) shows Indium also affect color change. I can adjust emitting color that strongly depends on aluminum composition. Fig.6.46 shows EL peak ratio change is related to injection carrier. Most of samples are similar trend.



(a) AlGaIn active layer



(b) InAlGaIn active layer

Fig. 6.45 Wavelength distribution of each samples at $I_f=25\text{ mA}$ and $I_f=30\text{ mA}$

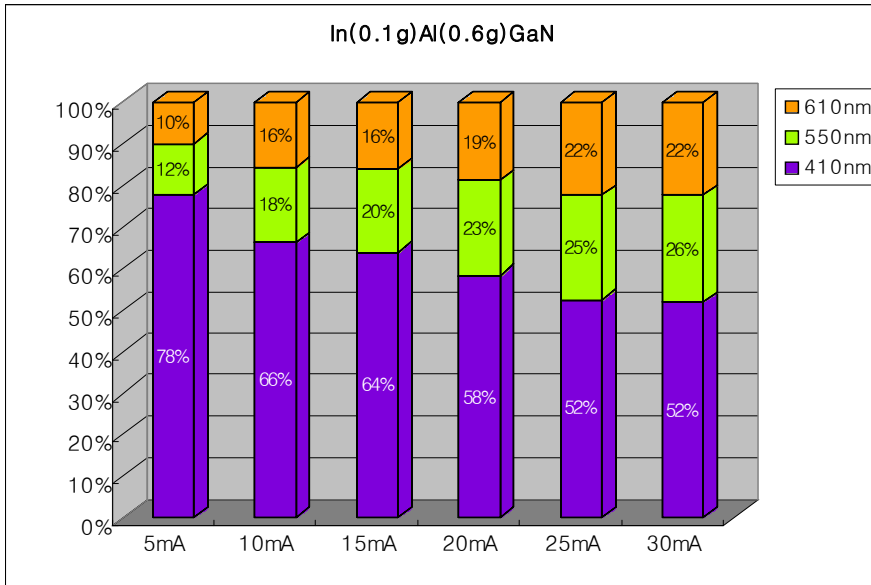


Fig. 6.46 Wavelength distribution of InAlGaN active layer Vs. forward current from 5 mA to 30 mA

Fig.6.47 shows growth formation about HVPE system. As shown in Fig.6.47(a), conventional HVPE systems have each source flows in gas phase region and precursor decomposition take place on wafer surface through mass transport to the surface by diffusion. Most of atoms are placed along crystal direction from atomic step. But MS-HVPE system delivers mixed source in source zone to gas phase. It has big different chemical and physical phenomenon. As shown in Fig.6.47(b), Mixed sources have mixed metal precursor-chloride formation, they are decomposed simultaneously on wafer surface and make localized different molecular composition. I think it is micro (or nano) size multi composition formation and makes multi spectrum when current is biased. I also think quaternary mixed materials are more various than ternary.

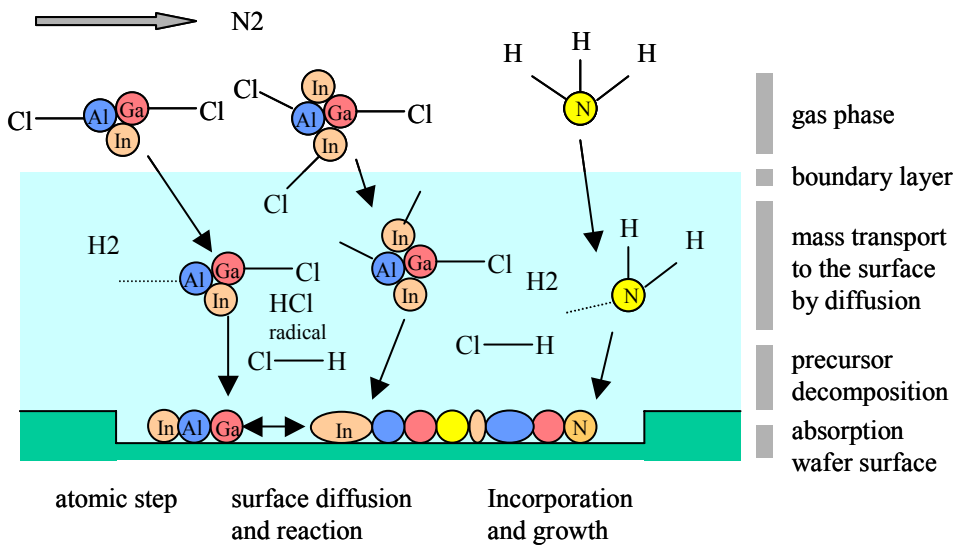
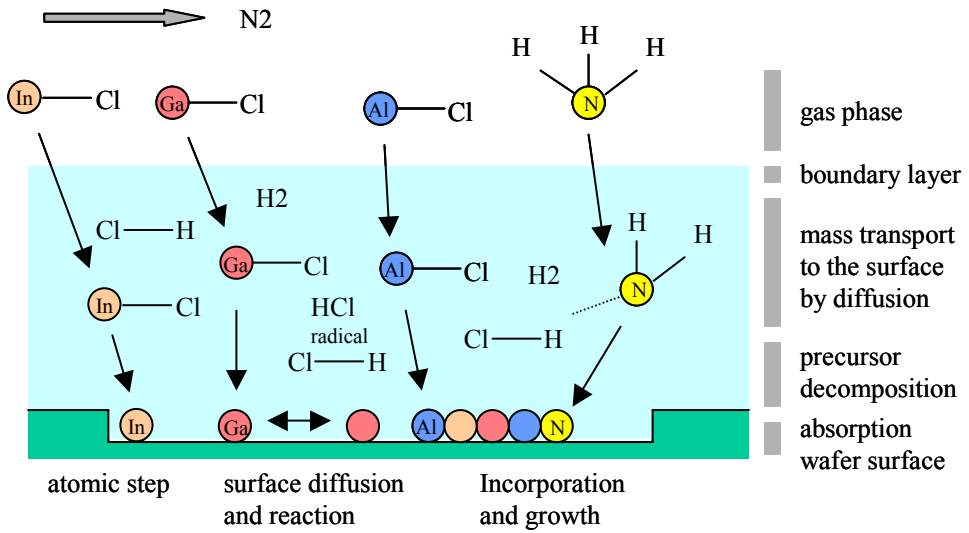


Fig. 6.47 Growth formation of conventional HVPE(a) and MS-HVPE(b)

Fig.6.48 shows CL measurement results of cross section of AlInGaN DH. I could observe luminescence not only short wavelength region but also long wavelength. I think such multi wavelength is originated from localized multi structure of AlInGaN active layer.

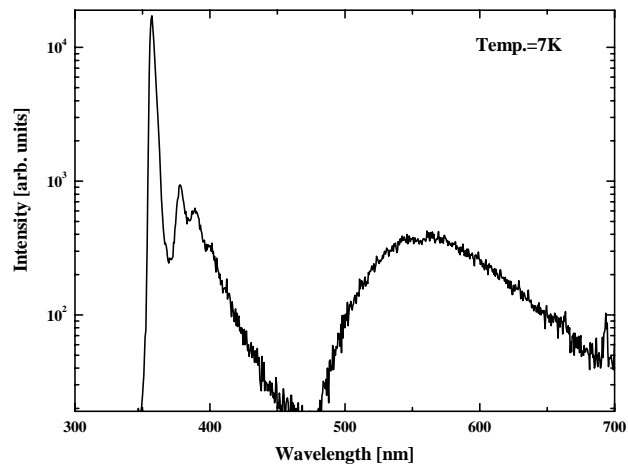
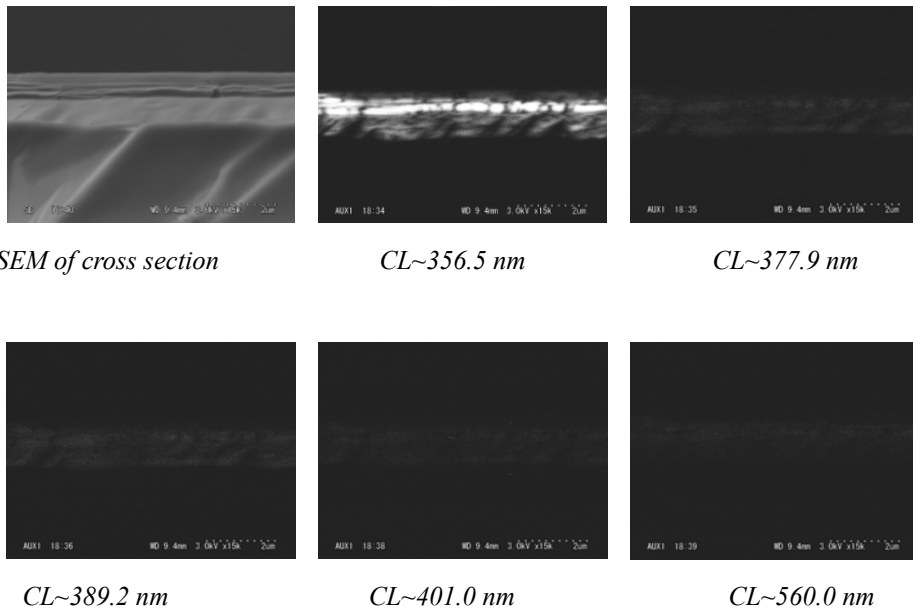


Fig. 6.48 CL measurement results of cross section of AlInGaN DH

Chapter 7.

Phosphor-Free White LED Lamp

7.1. Manufacturing of White LED Lamp

The development of MS-HVPE crystal growth techniques enabled the introduction of a new material system of white emitting, Al(In)GaN on GaN. It resulted in the fabrication of materials from ultra violet to red. As already reported, there are currently three general approaches to generating white lights from LEDs. The first method directly mixes light from three monochromatic sources, which are red, green and blue (RGB), to produce a white source matching with the RGB sensors in the human eye. The second technique uses a blue LED to pump one or more visible light-emitting phosphors integrated into the phosphor-converted LED package. The third technique uses an ultraviolet LED to pump a combination of red, green and blue phosphors in such a way that none of the pump LED light is allowed to escape. By far the most common LED-based white light source is the phosphor-converted-LED used in a configuration with a blue LED and a yellow phosphor. The blue LED is used to pump a yellow emitting phosphor integrated into the LED package. Inherently less efficient than an RGB source, simple white sources are made.

I made LED lamp to check performance of GaN base LED devices grown by MS-HVPE system. By varying the active composition, I fabricated devices layer by layer. It was our first trial of manufacturing LEDs grown by MS-HVPE system. It was consist of conventional 5 mm Φ transparent epoxy mold package and aluminum lead frame. It was the first practical white LED Lamp, which was made without any fluorescent material. Finally lighting sources are predominantly white with CIE color coordinates very near the Planckian curve, producing good to excellent color rendering.

7.2. Analysis of White LED Spectra and Color Rendering

The energy efficiency of a white light source is evaluated by luminous efficacy of a source, which is the ratio of luminous flux (lumen) emitted by the source to the input electrical power (watt).

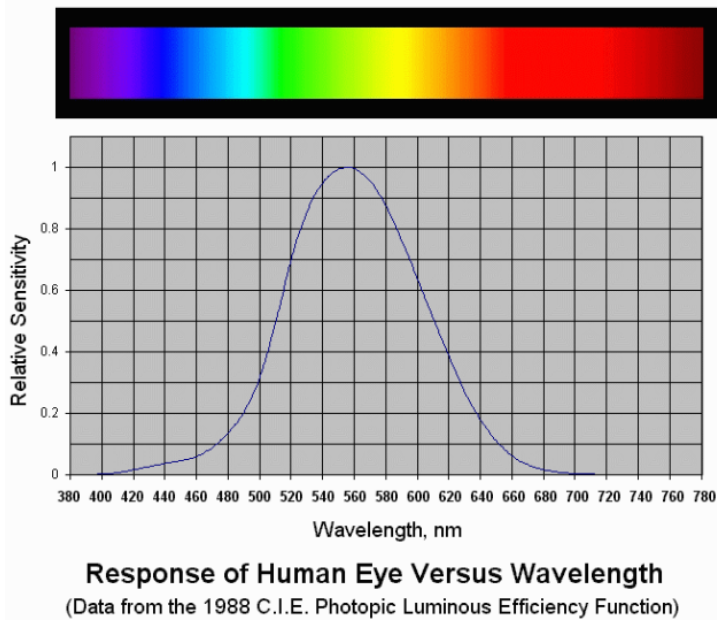


Fig. 7.1 Photopic vision of visual spectrum

As shown in Fig.7.1, Photopic visual efficacy is ‘1’ at 555 nm and it is ‘0.1’ at 470 nm. It means that luminous efficiency of 555 nm is ten times higher than 470 nm even if they are same radiant power.

The luminous efficacy of a source, $\eta_v(\text{lm/W})$, is determined by two factors:

$$\eta_v = \eta_e \cdot K \dots\dots\dots(1)$$

where η_e is the radiant efficiency of the source. K is the luminous efficacy of radiation and is determined by the spectral distribution $S(\lambda)$ of the source as given by

$$K = \frac{\text{luminous flux}}{\text{radiant flux}} = \frac{K_m \int_{\lambda} S(\lambda)V(\lambda)d\lambda}{\int_{\lambda} S(\lambda)d\lambda} \dots\dots\dots(2)$$

Where, $K_m=638(\text{lm/W})$.

When considering spectra of light sources for general illumination, another important aspect to consider is luminous efficacy of radiation. Which is the conversion factor from optical power (watt) to luminous flux (lumen) and is determined solely by the spectrum of the source. The luminous efficacy and color rendering are both critical parameters for light sources used for general lighting, and these two are generally in trade-off relationship. Based on the CRI, color rendering is best achieved by broadband spectra distributed throughout the visible region, while luminous efficacy is best achieved by monochromatic radiation at 555 nm. The challenge in creating LEDs for use as illumination sources is to provide the highest possible luminous efficacy while achieving sufficiently good color rendering.

Chromaticity coordinates is determined by 1931 CIE color matching function. Fig.7.2 shows standard spectrum of blue, green, and purple, which are integrated along wavelength. (x,y) chromaticity coordinates can be calculated by each spectrum portion as Fig.7.2.

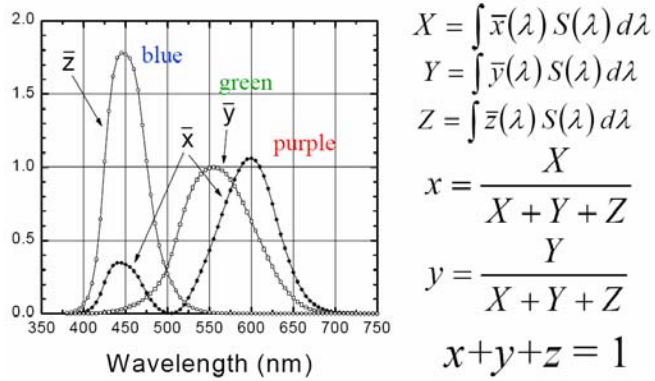
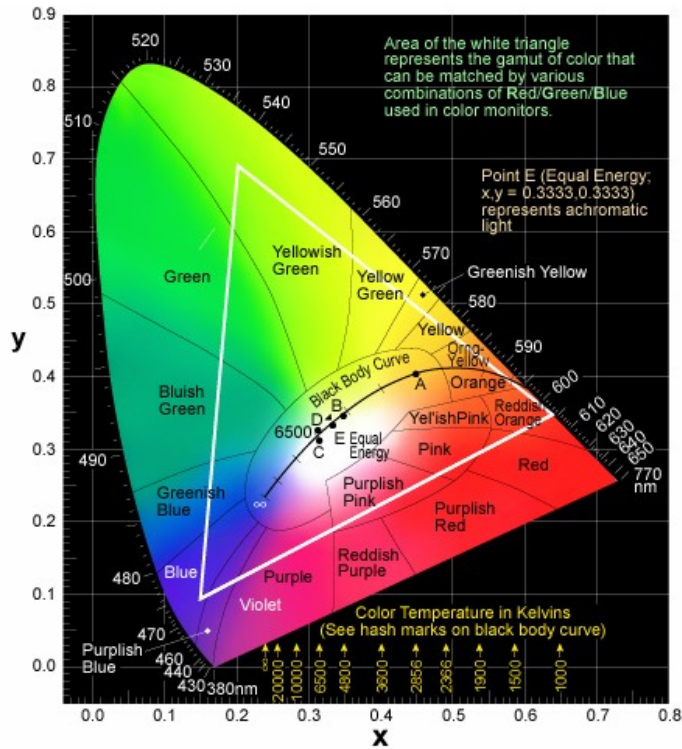


Fig.7.2 Standard spectrum of blue, green, and purple and calculation of chromaticity coordinates

Fig.7.3 show chromaticity coordinates and CCT (Correlated Color Temperature) of black body for standard light source. It is called plankian locus of black body radiation.



- Source A ; $x = 0.4476, y = 0.4075$ (tungsten 2856 K)
 Source B ; $x = 0.3485, y = 0.3517$ (direct sunlight, approximately 4870 K)
 Source C ; $x = 0.3101, y = 0.3163$ (overcast sunlight 6770 K)
 Source D ; $x = 0.3127, y = 0.3291$ (daylight 6504 K)
 Source E ; $x = 0.3333, y = 0.3333$

From Introduction to Solid State Lighting A. Zukauskas, M. S. Shur, and R. Gaska, 27

Copyright © Wiley (2002). Used by permission of John Wiley and Sons, Inc.

Fig.7.3 1931 CIE chromaticity coodinates and Black body curve

In the calculation of the CRI, the color appearance of 14 reflective samples is simulated when illuminated by 8 specified reference source and six additional test source. This gives an evaluation of color rendering for each particular color. The reference source is a Planckian radiator (if below 5000 K) or a CIE Daylight source (if at or above 5000 K), matched to the correlated color temperature (CCT) of the test source. After accounting for chromatic adaptation with a Von Kries correction, the difference in color appearance ΔE_i for each sample between the test and reference light sources is computed in CIE 1964 W*U*V* uniform color space. The special color-rendering index (R_i) is calculated for each reflective sample by:

$$R_i = 100 - 4.6\Delta E_i \dots\dots\dots(3)$$

The general color-rendering index (R_a) is simply the average of R_i for the first eight samples, all of which have low to moderate chromatic saturation:

$$R_a = \frac{1}{8} \sum_{i=1}^8 R_i \dots\dots\dots(4)$$

Where $R_i = 100 - 4.60\{[W_{ki} - W_{ri}]^2 + 13^2[W_{ki}(u'_{ki} - u_r) - W_{ri}(u_{ri} - u_r)]^2 + 13^2[W_{ki}(v'_{ki} - v_r) - W_{ri}(v_{ri} - v_r)]^2\}^{1/2} \dots\dots\dots(5)$

$$W = 25Y^{1/3} - 17$$

$$c = (4 - u - 10v)/v$$

$$d = (1.708v + 0.404 - 1.481u)/v$$

$$u'_{ki} = \frac{10.872 + 0.404c_r c_{ki}/c_k - 4d_r d_{ki}/d_k}{16.518 + 1.481c_r c_{ki}/c_k - d_r d_{ki}/d_k}$$

$$v'_{ki} = \frac{5.520}{16.518 + 1.481c_r c_{ki}/c_k - d_r d_{ki}/d_k}$$

A perfect score of 100 represents no color differences in any of the eight samples under the test and reference sources.

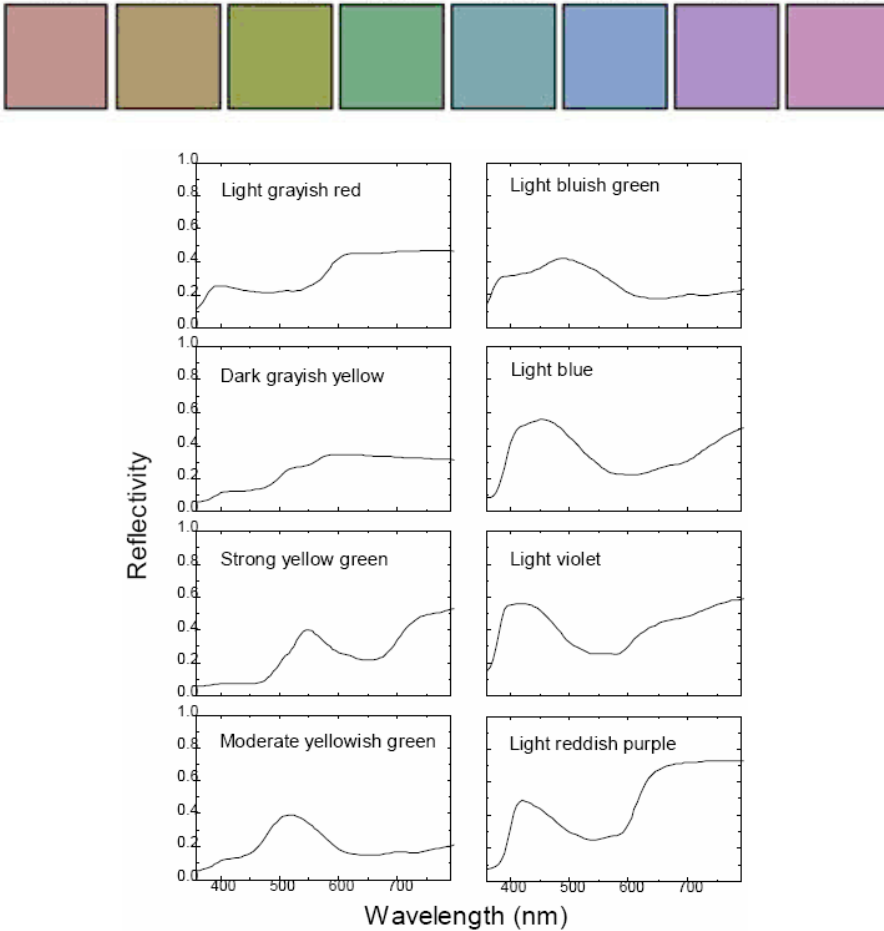


Fig.7.4 The eight specified reference source used in the calculation of R_a .

“CRI” is often used to refer to R_a , but the CRI actually consists of 15 numbers; R_a and R_i ($i=1$ to 14). The CRI has a number of problems, particularly when applied to LEDs or when used as an indicator of color quality. The uniform color space used to calculate color differences is outdated and no longer recommended for use. The red region of this color space is particularly non-uniform. Instead, the CIE currently recommends CIE 1976 $L^*a^*b^*$ (CIE LAB) and CIE 1976 $L^*u^*v^*$ (CIE LUV) [1] for calculating color differences. Additionally, the chromatic adaptation transform is considered inadequate. The Von Kries chromatic adaptation correction used in the CRI has been

shown to perform poorer than other available models, such as the CMC CAT2000 (the Colour Measurement Committee's chromatic adaptation transform) and the CIE CAT02 (the CIE's chromatic adaptation transform) [2].

The CRI method specifies that the CCT of the reference source be matched to that of the test source, which assumes complete chromatic adaptation to the chromaticity of the light source. This assumption fails at extreme CCTs, however. For example, a 2000 K (very reddish) blackbody source achieves $R_a = 100$, as does a daylight spectrum of 20,000 K (very bluish). However, neither of these sources renders colors well.

None of the eight reflective samples used in the computation of R_a are highly saturated. This is problematic, especially for the peaked spectra of white LEDs. Color rendering of saturated colors can be very poor even when the R_a value is good. Further, by optimization of lamps' spectra to the CRI, R_a values can be made very high while actual color rendering is much poorer. This problem exists because too few samples are used in the calculation of R_a , and they are of too low chromatic saturation.

The eight special color-rendering indices are simply averaged to obtain the general color-rendering index. This makes it possible for a lamp to score quite well, even when it renders one or two colors very poorly. LEDs are at an increased risk of being affected by this problem, as their peaked spectra are more vulnerable to poor rendering in only certain areas of color space.

Finally, the very definition of color rendering is flawed for use when one is interested in the overall color quality of a light source. Color rendering is a measure of only the fidelity of object colors under the illuminant of interest and any deviations of object color appearance from under a blackbody source is considered bad. Due to this constraint, all shifts in perceived object hue and saturation result in equal decrements in CRI score. In practical application, however, increases in chromatic saturation, observed when certain sources illuminate certain surfaces, is considered

desirable. Increases in saturation yield better visual clarity and enhance perceived brightness [3]. It is proposed that the absolute focus on color fidelity of the CRI is flawed and a more general metric of color quality be considered. Further details on the analyses of CRI for solid-state sources are found in references [4-6].

7.3. Measurement of Phosphor free white LED

Normally, Phosphor-converted-LED is designed to leak some of the blue light beyond the phosphor to generate the blue portion of the spectrum, while phosphor converts the remainder of the blue light into the red and green portions of the spectrum. The phosphor density and thickness are chosen to leak a predetermined fraction of the blue light. Striking the correct blue/yellow ratio depends upon having the correct amount, density, and particle size of phosphor, distributed evenly around the blue-emitting chip. Variations in any of these parameters will give rise to color or CCT variations at different viewing angles from a single lamp, or between adjacent LED lamps. Table 7.1 shows chromaticity measurement results of phosphor free white LED lamp grown by MS-HVPE at $I_f=30$ mA. We got the result of CCT 8900~10500 K and CRI 76~87 for each samples. Generally, Color-rendering index (**CRI**) is reported 80 for warm-white, 75 for neutral-white, and 70 for cool-white. Fig.7.6~Fig.7.11 show spectrum and CCT variation from $I_f=10$ mA to $I_f=100$ mA for each samples.

Table.7.1. Chromaticity measurement (1931 Coordinates) results of phosphor free white LED lamp grown by MS-HVPE at $I_f=30\text{ mA}$

Sample No.	Chrom x	Chrom y	Color Temp(K)	Purity	General CRI
1-1	0.28	0.31	9098	0.20	86.78
1-2	0.28	0.32	8885	0.19	84.62
1-3	0.28	0.31	9139	0.20	85.85
2-1	0.29	0.37	7123	0.13	76.25
2-2	0.26	0.32	10500	0.27	75.82

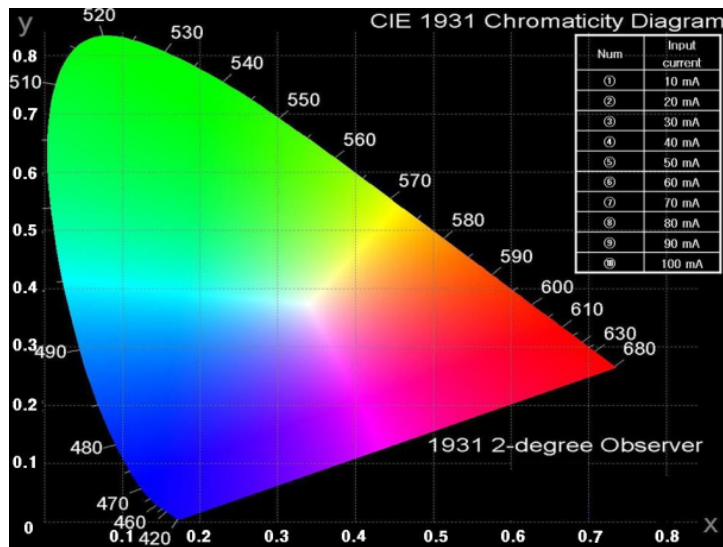


Fig.7.5 CIE 1931 Chromaticity Diagram

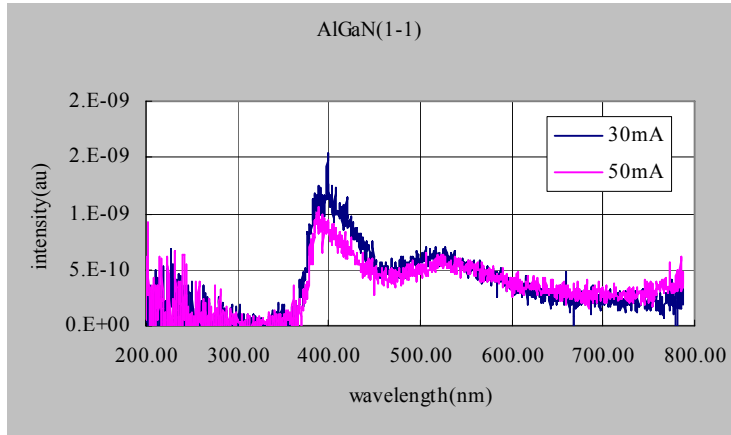


Fig.7.6 Spectrum measurement results of phosphor free white LED lamp grown by MS-HVPE at $I_f=30\text{ mA}$ and $I_f=50\text{ mA}$

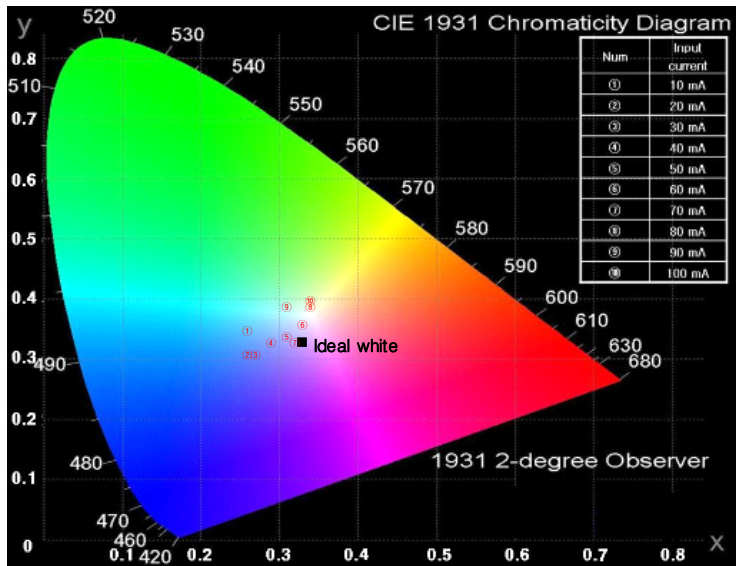


Fig.7.7 Chromaticity coordinates variation of sample No. 1-1 from $I_f=10\text{ mA}$ to $I_f=100\text{ mA}$

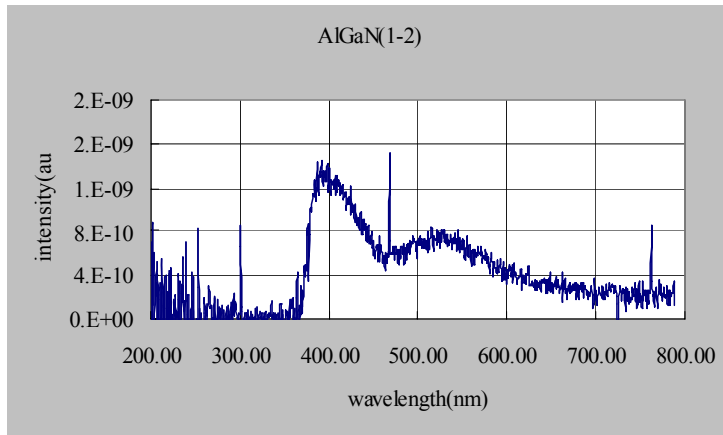


Fig.7.8 Spectrum measurement results of phosphor free white LED lamp grown by MS-HVPE at $I_f=30\text{ mA}$

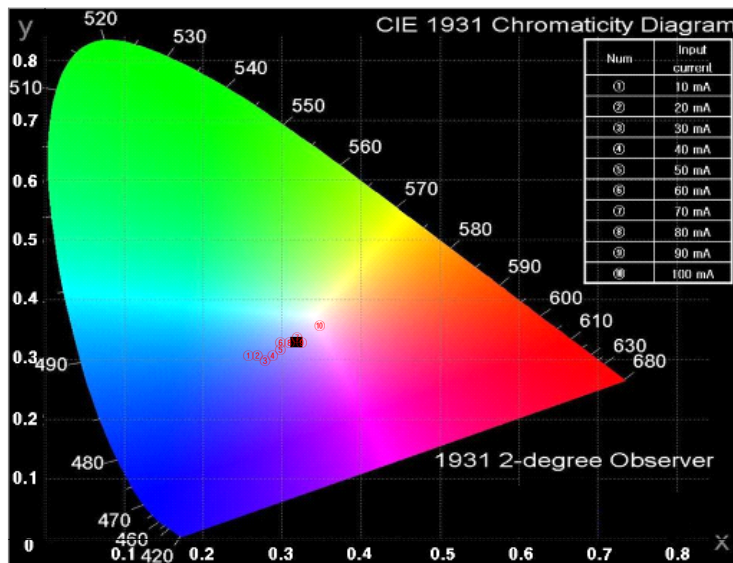


Fig.7.9 Chromaticity coordinates variation of sample(No. 1-2) from $I_f=10\text{ mA}$ to $I_f=100\text{ mA}$

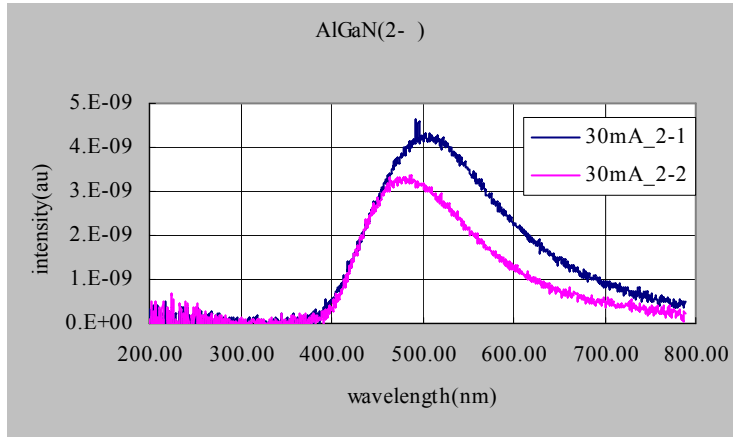


Fig.7.10 Spectrum measurement results of phosphor free white LED lamp grown by MS-HVPE at $I_f=30\text{ mA}$

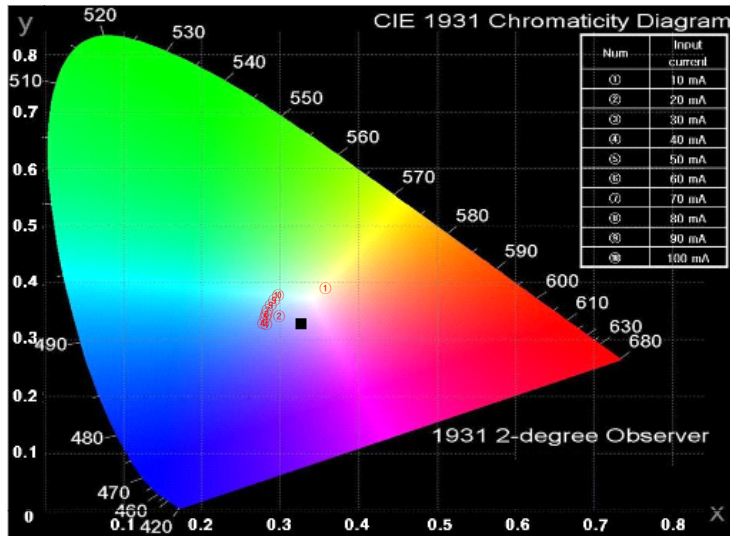


Fig.7.11 Chromaticity coordinates variation of sample(No. 2-1) from $I_f=10\text{ mA}$ to $I_f=100\text{ mA}$

The quantum deficit between the pump LED and the phosphors, especially the low-energy red phosphor, dissipates significant energy and makes this approach inherently less efficient than RGB LED combination. Scattering and absorption losses in the package are also considered. But our new trial can overcome several demerits such as quantum deficit and scattering and absorption losses in the package comparing with Phosphor-converted-LED. In order to achieve the emission of other desired colors, including UV and blue, we adjusted aluminum composition of AlGaIn active. Fig 7.6~7.11 show spectrum measurement results and chromaticity coordinates variation of phosphor-free LED lamp. As shown, spectrum distribution is similar to conventional phosphor-converted-LED. But we found there was a different phenomenon.

Chromaticity coordinates of phosphor-free LED varies forward yellow region when forward current increase, while chromaticity coordinates of Phosphor-converted LED varies forward blue region. [see Fig.7.12~7.13] It means red and green spectrums are dominated than blue spectrum relatively. We think there is so many complicated energy levels' shift of LED structure grown by MS-HVPE. It means LED made by MS-HVPE have localized multi wavelength structure. At previous chapter, we verified multi spectrum of various active condition of LED structure grown by MS-HVPE.

In all its aspects, series resistance was much higher than commercialized lamp. But, if ohmic condition is improved by manufacturing process, it can be reduced normally. Most of all, the basic problem with GaN is how to reduce heat produced. Because materials other than GaN are used as substrates, there is inevitably some mismatch where the crystalline lattices of the substrate and the semiconductor meet. This mismatch produces imperfections called dislocations, which are a prime culprit in the conversion of photons to heat in the devices. The much bigger problem, though, is internal quantum efficiency, which at least for the moment is too low. For reasons researchers do not completely understand, when some electrons and holes meet, their combination creates not

photons but rather heat-producing vibrations in the semiconductor crystal's lattice. In this experiment, Mesa etching was not necessary because device was structured as SAG, which considerably simplified the processing step and eradicated any complication arising from the dry etching process. The p- and n-contact metal systems were Cr/Ni/Au. Spectrum characteristics of optical devices were almost close to conventional white LED. However, surface morphology was not good and fabrication process facilities stability in lab was the main obstacles that still need to be resolved to improve ohmic contact. Eventhough it was lab results at present, we were convinced that it could be good candidate of low cost white LED products in the near future.

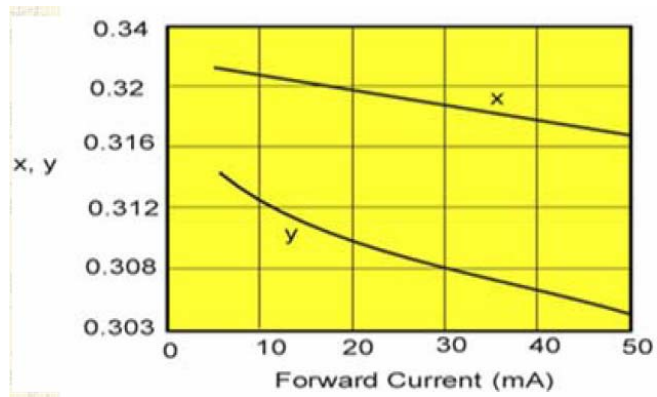


Fig.7.12 Chromaticity coordinates variation of Phosphor-converted LED

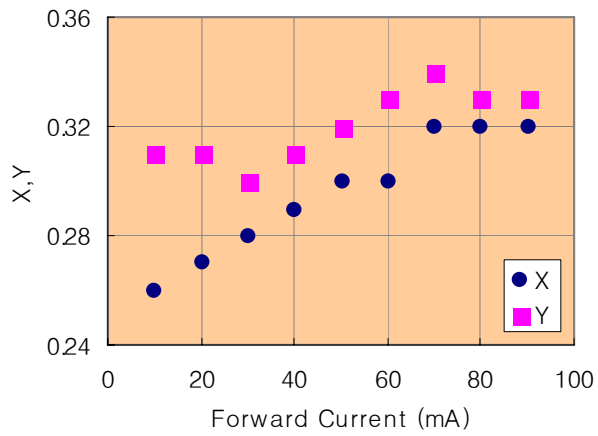


Fig.7.13 Chromaticity coordinates variation of Phosphor-free LED

(Experimental results)



Fig.7.14 White emission of Phosphor-free LED Lamp

7.4. Future research

In our lab, the project was in a very promising state. Now that the basic parameters of the system are established, we have carried some very exciting work. Obviously, one of our main goals was emission white wavelengths with RGB spectrum it means phosphorus free white LED. When thinking about the future research, I see each of my ideas falling into one of two categories: short term projects that can be accomplished in our lab; or longer-term efforts that the scientific community as whole can undertake in an effort to advance the study of GaN in general and GaN-based lighting in particular.

The research reported in this dissertation may provide some new technology of GaN-based crystal growth. There was an observation that SAG-DH structures exhibited poor emission characteristics. This seems to indicate that the crystal quality of SAG is critical in achieving good emission. Therefore it needs some steps to improve crystal quality. The first is growth condition optimization. Recently, most of crystal growth system was well known to researcher widely. But MS-HVPE system was new crystal growth technology. Epitaxial wafer grown by MS-HVPE have

new material characteristics and it need more research to reveal new phenomenon. I also expect its more desirable properties. Especially, I would be interested to see some more research into non-polar-GaN grown by MS-HVPE discussed briefly in Chapter 2.

The second is the device aspect of this project has versatile application. I would be curious to research from violet to red spectrum emission in fabricated device from this growth system. To commercialize, it needs increment of device efficiency and understanding of reliability for this technology. It needs not only optical property but also electrical property to improve performance. Ohmic contact of electrode of device and p-doping issues should be studied thoroughly. Finally, more analysis of chromaticity coordinates of phosphor-free LED is needed. We think it helps for understanding of localized multi wavelength phenomenon.

Such research could help us gain a better overall understanding of the GaN material system.

References

- [1]. *Commission Internationale de l'Eclairage. Colorimetry, CIE 15 (2004).*
- [2]. *Commission Internationale de l'Eclairage. A Review of Chromatic Adaptation Transforms, CIE 160 (2004).*
- [3]. *Visual Clarity and Feeling of Contrast, Hashimoto, K. & Nayatani, Y. Color Res. Appl., 19(3), 171-185 (1994).*
- [4]. *Simulation Analysis of White LED Spectra and Color Rendering, Y. Ohno, Proc., CIE Symposium '04, LED Light Sources: Physical Measurement and Visual and Photobiological Assessment, 7-8 June 2004, Tokyo Japan, 28-32 (2004).*
- [5]. *Color Rendering and Luminous Efficacy of White LED Spectra, Proc., Y. Ohno, SPIE Fourth International Conference on Solid State lighting, Denver, CO, August 2004, 5530, 88-98 (2004).*
- [6]. *Spectral Design Considerations for Color Rendering of White LED Light Sources, Y. Ohno, Opt. Eng. 44, 111302 (2005).*

Chapter 8.

Conclusions

As discussed in this paper, the GaN material system has been shown to be excellent candidate for solid-state lighting. And rapid progress has been made recently in the area of III-nitride emitters. I studied gallium nitride Based LED and tried to explore the possibility of phosphor-free white LED.

The structures were to be grown using mixed source hydride vapor phase epitaxy (MS-HVPE). MS-HVPE is of great advantage to thick-film growth process, which involves the flow of heated mixed metal source of Al, In, Ga (usually, as the name implies, mixed source) into a reaction chamber, which contains a heated substrate. It was unique technology different from conventional HVPE and MOCVD system. I observed peculiar phenomenon through manifold experiment by its system. I found multiband spectrum emission for AlGaInN and InAlGaInN active layer and it was easily controllable through composition change so phosphor-free white-emitting LED could be performed. For this particularly study, mixed source hydride vapor phase epitaxy (MS-HVPE) has been chosen. An extensive binary, ternary and quaternary of AlGaInN growth study was carried out continuously.

This work included wafer fabrication and test of white device structure. I also made LED lamps for some samples grown by MS-HVPE to test characteristics. I got good CCT and CRI results comparing to conventional phosphor converted white LED and multi spectrum emission results. I found chromaticity coordinates changed according to forward current. It also means there is localized multi wavelength in active layer grown by MS-HVPE.

Eventhough it is immature technology at present, experimental results clearly explain future R&D direction for low cost white light source. The research reported in this dissertation may provide some insight. On a larger scale, I tried to fabricate and characterize structures grown using

MS-HVPE. I found that it could be candidate of new device technology.

Lastly, I think further studies into novel substrates will revolutionize this field. Exactly the time of innovative research can bring GaN-based white-emitting solid-state lighting technology to the next level. In our lab, the project is in a very promising state. Now that the experimental results of the system are established, we are primed to start carrying some very exciting work. One of our main goals will verify details of the origin of multiband wavelengths emission in the far yellow, amber and red. It is sufficiently competitive than normal white LED and it can be commercialized if next step research is following. They can be used for many applications for full color display and LCD backlight, solid-state lighting and so on. Commercial demands of white LED will tend to increase tremendously because the future of household lighting will soon be the wide spread adoption and use of white LED light bulbs. Though the present market for finished white LED products is geared mainly towards enthusiasts and early-adopters, the efficiency and cost effectiveness of LED lighting systems will drive demand for more affordable LED lights. Opto-electronics is an exciting area and we predict, that in the near future, white LED lighting applications will be powerful and cheap enough to replace incandescent lighting for everyday use in our homes, in street lights, outdoor signs, and offices. In the near future, it will be expected that, the phosphor free white LEDs will take some part in illumination market as one of primary light sources.

I've certainly enjoyed working on this project, and the experience I've gained has been invaluable and unforgettable. As I continue on my career, I will always keep an eye on the newest advances in GaN-based phosphor-free white-emitting LED and be proud that I was once part of that drive. I also hope many researcher will perform advanced experiment and contribute to optoelectric field. We also expect that it can be commercially available and new trial for illumination field.

Publications

	Title	Author	Journal
1	Growth and doping of AlGa _N and electroluminescence of SAG-InGa _N /AlGa _N heterostructure by mixed-source HVPE	K. H. Kim, H. S. Ahn, M. Yang, K. S. Jang, S. L. Hwang , W. J. Choi, C. R. Cho, S. W. Kim, Y. Honda, M. Yamaguchi, N. Sawaki, J. Yoo, S. M. Lee, M. Koike	<i>physica status solidi (c)</i> , 3, 6, 1461 (2006)
2	Growth of InGa _N /AlGa _N heterostructure by mixed-source HVPE with multi-sliding boat system	K.S.Jang, K.H.Kim, S.L.Hwang , H.S.Jeon, W.J.Choi, M.Yang, H.S.Ahn, S.W.kim, J.Yoo, S.M.Lee, and M.Koike	<i>Journal of Korean Crystal Growth and Crystal Technology</i> , 16, 4, 162-165 (2006).
3	Characterization of In(Al)Ga _N layer grown by mixed-source hydride vapor phase epitaxy	S.L.Hwang , K.H.Kim, K.S.Jang, H.S.Jeon, W.J.Choi, J.H.Chang, H.S.Kim, M.Yang, H.S.Ahn, J.S.Bae, and S.W.Kim	<i>Journal of Korean Crystal Growth and Crystal Technology</i> , 16, 4 (2006) 157-161.
4	Characterization of AlGa _N , Te-doped Ga _N and Mg-doped Ga _N grown by hydride vapor phase epitaxy	K. S. Jang, K. H. Kim*, S. L. Hwang , H. S. Jeon, H. S. Ahn, M. Yang, W. J. Choi, S. W. Kim, Y. Honda, M. Yamaguchi, N. Sawaki, J. Yoo, S. M. Lee, and M. Koike	<i>physica status solidi (c)</i> , 4, 1, 133-136 (2007)
5	Growth of InGa _N layer on a Ga _N templated Al ₂ O ₃ (0001) and Si (111) substrates by mixed-source HVPE	S. L. Hwang , K. S. Jang, K. H. Kim, H. S. Jeon, H. S. Ahn, M. Yang, S. W. Kim, Y. Honda, M. Yamaguchi, N. Sawaki, J. Yoo, S. M. Lee, and M. Koike	<i>physica status solidi (c)</i> , 4, 1, 125-128 (2007)
6	Fabrication of SAG-AlGa _N /InGa _N /AlGa _N LEDs by mixed-source HVPE with multi-sliding boat system	K. H. Kim, K. S. Jang, S. L. Hwang , H. S. Jeon, W. J. Choi, M. Yang, H. S. Ahn, S. W. Kim, Y. Honda, M. Yamaguchi, N. Sawaki, J. Yoo, S. M. Lee, and M. Koike	<i>physica status solidi (c)</i> , 4, 1, 29-32 (2007)
7	GROWTH CHARACTERISTICS OF HVPE THICK A-PLANE Ga _N LAYER	C. H. Lee, H. S. Jeon, S. L. Hwang , K. H. Kim, K. S. Jang, H. S. Ahn, M. Yang, J. S. Bae, S. W. Kim, S. H. Jang, S. M. Lee, G. H. Park, and M. Koike	<i>Journal of Korean Crystal Growth and Crystal Technology</i> , 17, 1 1-5 (2007).
8	HVPE GROWTH OF Ga _N /InGa _N HETEROSTRUCTURE ON R-PLANE SAPPHIRE SUBSTRATE	H. S. Jeon, S. L. Hwang , K. H. Kim, K. S. Jang, C. H. Lee, M. Yang, H. S. Ahn, S. W. Kim, S. H.	<i>Journal of Korean Crystal Growth and Crystal Technology</i> , 17,

		<i>Jang, S. M. Lee, G. H. Park, and M. Koike</i>	<i>1 6-10 (2007).</i>
9	<i>Characterization of heterostructure and a-plane GaN layer grown by hydride vapor phase epitaxy</i>	S. L. Hwang , M. Yang, H. S. Jeon, C. H. Lee, K. H. Kim, H. S. Ahn, S. W. Kim, Y. S. Jin, W. T. Lim, J. H. Lee, S. K. Shee	<i>Saemulli, 54, 3, 244-248 (2007).</i>
10	<i>Characterization of AlGaN/InGaN/AlGaN heterostructure with selective area growth of Te-doped AlGaN cladding layer grown by mixed-source HVPE</i>	K. S. Jang, K. H. Kim, S. L. Hwang , H. S. Jeon, M. Yang, H. S. Ahn, S. W. Kim, Y. Honda, M. Yamaguchi, N. Sawaki, S. H. Jang, S. M. Lee, and M. Koike	<i>physica status solidi, (c) 4, No. 7, 2240– 2243 (2007)</i>
11	<i>Growth of HVPE-GaN/InGaN Heterostructure on r-Plane Sapphire Substrate</i>	S. L. Hwang , M. Yang, K. H. Kim, H. S. Jeon, C. H. Lee, H. S. Ahn*, S. W. Kim, S. H. Jang, S. M. Lee, G. H. Park, and M. Koike	<i>J. Korean Phys. Soc. (2007), 51, 216-219</i>
12	<i>Characterization of SAG-InGaN/AlGaN LED by Mixed-Source HVPE with Multi-Sliding Boat System</i>	S. L. Hwang , H. K. Kim, H. S. Jeon, C. H. Lee, S. H. Hong, I. H. Heo, M. Yang, and H. S. Ahn, S. W. Kim, S. H. Jang, S. M. Lee, G. H. Park, and M. Koike	<i>Journal of the Society for Information Display, April 2008 Volume 16, Issue 4, pp. 541-544</i>
13	<i>Structural Phase Variation of InGaN Micro-structures Grown by Mixed-source HVPE</i>	M. Yang, S. L. Hwang , C. H. Lee, H. S. Jeon, K. H. Kim, S. H. Hong, I. H. Heo and H. S. Ahn, J. H. Shim, S. W. Kim, I. S. Cho, J. H. Lee and S. K. Shee	<i>Saemulli, 56, 3, 238–243 (2008)</i>
14	<i>Doping of Nitride Semiconductors by Using Mixed-source HVPE</i>	I. H. Heo, S. L. Hwang , H. S. Jeon, C. H. Lee, S. H. Hong, Y. H. Han, E. J. Kim, M. Yang and H. S. Ahn, J. H. Shim, S. W. Kim, I. S. Cho, J. H. Lee and S. K. Shee	<i>Saemulli, 56, 3, 272–277 (2008)</i>
15	<i>Fabrication and Characteristics of HVPE-SAG-LED Grown on the r-plane Sapphire Substrate</i>	S. H. Hong, S. L. Hwang , H. S. Jeon, C. H. Lee, I. H. Heo, E. J. Kim, Y. H. Han, M. Yang and H. S. Ahn, J. H. Shim, S. W. Kim, I. S. Cho, W. T. Lim, J. H. Lee and S. K. Shee	<i>Saemulli, 56, 3, 231–237 (2008)</i>

Conference

	Title	Author	Journal
1	혼합소스 HVPE에 의한 후막 InGaN 층의 성장과 특성	전현수, 장근숙, 황선령 , 김경화, 안형수, 양민, 김홍승, 장지호, 조채룡, 김석환, 유재은, 이수민, M. Koike	한국물리학회, 전주, 전북대학교, 2005.10.21-22
2	후막 Te-doped AlGaIn cladding layer를 갖는 SAG-LED의 특성	장근숙, 황선령 , 전현수, 김경화, 안형수, 양민, 김홍승, 장지호, 조채룡, 김석환, 유재은, 이수민, M. Koike	한국물리학회, 전주, 전북대학교, 2005.10.21-22
3	Selective Area Growth of InGaIn/AlGaIn Light-Emitting Diodes Grown by Mixed-Source HVPE with Multi-Sliding Boat System	K. S. Jang, K. H. Kim, S. L. Hwang , H. S. Jeon, J. H. Chang, H. S. Kim, M. Yang, H. S. Ahn, S. W. Kim, S. C. Lee, J. Yoo, S. M. Lee, and M. Koike	한국반도체학술대회, 제주, 라마다프라자 제주호텔, 2006.2.23-24
4	p-type GaN 성장을 위한 Mixed-Source HVPE 성장방법	김경화, 장근숙, 황선령 , 전현수, 이충현, 최원진, 안형수, 양민, 조채룡, 김석환, 유재은, 이수민, Koike Masayoshi	한국물리학회, 휘닉스파크, 2006. 4. 20-21
5	HVPE-InGaIn 결정의 성장온도에 따른 상(phase)의 변화	황선령 , 이충현, 김경화, 장근숙, 전현수, 최원진, 안형수, 양민, 조채룡, 배종성, 김석환, 유재은, 이수민, Koike Masayoshi	한국물리학회, 휘닉스파크, 2006. 4. 20-21
6	AlN 버퍼층을 이용한 r-plane GaIn 결정의 HVPE 성장	전현수, 김경화, 장근숙, 이충현, 황선령 , 양민, 안형수, 최원진, 조채룡, 김석환, 유재은, 이수민, Koike Masayoshi	한국물리학회, 휘닉스파크, 2006. 4. 20-21
7	Characterization of AlGaIn, Te-doped GaIn and Mg-doped GaIn grown by hydride vapor phase epitaxy	Jang Keunsuk, Kim Kyunghwa, Hwang Sunlyeong , Jeon Hunsoo, Choi Wonjin, Yang Min, Kim Sukwhan, Yoshio Honda Masahito Yamaguchi, Nobuhiko Sawaki, Yoo Jaeun, Soomin Lee, Masayoshi Koike	The 6th International Symposium on Blue Laser and Light Emitting Diodes, Montpellier, France, 2006. 5. 14-19
8	Growth of InGaIn Layer on a GaIn	Hwang Sunlyeong , Jang Keunsuk,	The 6th International

	<i>Templated Al₂O₃ (0001) and Si (111) Substrates by mixed-source HVPE</i>	<i>Kim Kyunghwa, Jeon Hunsoo, Choi Wonjin, Yang Min, Cho Chaeryong, Kim Sukwhan, Yoshio Honda Masahito Yamaguchi, Nobuhiko Sawaki</i>	<i>Symposium on Blue Laser and Light Emitting Diodes, Montpellier, France, 2006. 5. 14-19</i>
9	<i>Fabrication of SAG-AlGa_N/InGa_N/AlGa_N LEDs by mixed-source HVPE with multi-sliding boat system</i>	<i>Kim Kyunghwa, Jang Keunsuk, Hwang Sunlyeong, Jeon Hunsoo, Choi Wonjin, Yang Min, Ahn Hyungsoo, Kim Sukwhan, Yoshio Honda Masahito Yamaguchi, Nobuhiko Sawaki, Yoo Jaeun, Soomin Lee, Masayoshi Koike</i>	<i>The 6th International Symposium on Blue Laser and Light Emitting Diodes, Montpellier, France, 2006. 5. 14-19</i>
10	<i>Growth of InGa_N/AlGa_N heterostructure by mixed-source HVPE with multi-sliding boat system</i>	<i>K.S.Jang, K.H.Kim, S.L.Hwang, H.S.Jeon, W.J.Choi, M.Yang, H.S.Ahn, S.W.kim, J.Yoo, S.M.Lee, and M.Koike</i>	<i>International Conference on Crystal Technology and KACG Spring Meeting & 2nd Interantional Symposium for Nano and Advanced Materials, 창원대학교, 2006. 6. 8-10</i>
11	<i>Characterization of In(Al)Ga_N layer grown by mixed-source hydride vapor phase epitaxy</i>	<i>S.L.Hwang, K.H.Kim, K.S.Jang, H.S.Jeon, W.J.Choi, J.H.Chang, H.S.Kim, M.Yang, H.S.Ahn, J.S.Bae, and S.W.Kim,</i>	<i>International Conference on Crystal Technology and KACG Spring Meeting & 2nd Interantional Symposium for Nano and Advanced Materials, 창원대학교, 2006. 6. 8-10</i>
12	<i>Grwoth and Characterization of InGa_N and InAlGa_N Alloys using by Mixed-Source HVPE</i>	<i>S.L.Hwang, K.H.Kim, K.S.Jang, H.S.Jeon, C.H.Lee, M.Yang, H.S.Ahn, J.S.Bae, S.W.Kim, Y.Honda, M.Yamaguchi, N.Sawaki</i>	<i>International Symposium on the Physics of Semiconductors and Applications, 제주, 라마다프라자 제주호텔, 2006. 8. 22-25</i>
13	<i>Characterization of InGa_N nanostructures Grown by HVPE</i>	<i>K. H.Kim, K. S.Jang, S. L.Hwang, H. S.Jeon, C. H.Lee, H. S. Ahn, M.Yang, J.S.Bae, S.W.Kim, Y.Honda, M.Yamaguchi, N.Sawaki</i>	<i>International Symposium on the Physics of Semiconductors and Applications, 제주, 라마다프라자</i>

			제주호텔, 2006. 8. 22-25
14	Growth and Characterization of InGaN and InAlGaN Alloys using Mixed-Source HVPE	<u>S. L. Hwang</u> , K. H. Kim, K. S. Jang, H. S. Jeon, C. H. Lee, M. Yang, H. S. Ahn, J. S. Bae, S. W. Kim, Y. Honda, M. Yamaguchi, N. Sawaki	International Symposium on Physics of Semiconductors and Applications, 제주, 라마다프라자호텔, 2006. 8. 22-25
15	HVPE 후막 a-plane GaN 결정의 성장과 물리적 특성에 관한 연구	이충현, 김경화, 장근숙, 전현수, <u>황선령</u> , 안형수, 양민, 배종성, 김석환	한국물리학회, 대구 경북대학교, 2006. 10. 19-20
16	넓은 EL 스펙트럼 반치폭을 갖는 HVPE-LED 제작	전현수, 김경화, 장근숙, 이충현, <u>황선령</u> , 안형수, 양민, 김석환, 장성환, 이수민, 박길한, M. Koike	한국물리학회, 대구 경북대학교, 2006. 10. 19-20
17	Characterization of AlGaIn/InGaIn/AlGaIn Heterostructure with Selective Area Growth of Te-doped AlGaIn Cladding Layer Grown by Mixed-Source HVPE	K. S. Jang, K. H. Kim, <u>S. L. Hwang</u> , H. S. Jeon, M. Yang, H. S. Ahn, S. W. Kim, Y. Honda, M. Yamaguchi, N. Sawaki, J. Yoo, S. M. Lee, and M. Koike	International Workshop on Nitride Semiconductor 2006, Kyoto, Japan, 2006. 10. 22-27
18	GROWTH CHARACTERISTICS OF HVPE THICK A-PLANE GaN LAYER	C. H. Lee, H. S. Jeon, <u>S. L. Hwang</u> , K. H. Kim, K. S. Jang, H. S. Ahn, M. Yang, J. S. Bae, S. W. Kim, S. H. Jang, S. M. Lee, G. H. Park, and M. Koike	International Conference on Crystal Technology and KACG Spring Meeting & 2nd Interantional Symposium for Nano and Advanced Materials, 인천대학교, 2006. 11. 2-4
19	HVPE GROWTH OF GaN/InGaN HETEROSTRUCTURE ON R-PLANE SAPPHIRE SUBSTRATE	H. S. Jeon, <u>S. L. Hwang</u> , K. H. Kim, K. S. Jang, C. H. Lee, M. Yang, H. S. Ahn, S. W. Kim, S. H. Jang, S. M. Lee, G. H. Park, and M. Koike	International Conference on Crystal Technology and KACG Spring Meeting & 2nd Interantional Symposium for Nano and Advanced Materials, 인천대학교, 2006. 11. 2-4
20	Characterization of SAG-InGaIn/AlGaIn LED by Mixed-Source HVPE with Multi-Sliding	K. H. Kim, <u>S. L. Hwang</u> , K. S. Jang, H. S. Jeon, C. H. Lee, M. Yang, H. S. Ahn, S. W. Kim, S. H.	The 1st International Conference on Display LEDs - ICDL 2007,

	Boat System	Jang, S. M. Lee, G. H. Park, and M. Koike	서울, COEX, 2007.1.30-2.2
21	Fabrication of InGaN LED with Selective Area Growth of HVPE-AlGaN Cladding Layer	<u>S. L. Hwang</u> , K. H. Kim, K. S. Jang, H. S. Jeon, C. H. Lee, W. J. Choi, M. Yang, H. S. Ahn, S. W. Kim, J. S. Kim, Y. Honda, M. Yamaguchi, and N. Sawaki	The 1st International Conference on Display LEDs - ICDL 2007, 서울, COEX, 2007.1.30-2.2
22	Structural Phase Variation of InGaN Quantum Sized Structures Grown by Mixed Source HVPE	<u>S. L. Hwang</u> , K. H. Kim, K. S. Jang, H. S. Jeon, C. H. Lee, H. S. Ahn, M. Yang, J. S. Bae, S. W. Kim, Y. Honda, M. Yamaguchi, N. Sawaki	International Symposium on Physics of Semiconductors and Applications, 제주, 롯데호텔, 2007. 2. 8-9.
23	Growth of HVPE-GaN/InGaN Heterostructure on r-Plane Sapphire Substrate	<u>S. L. Hwang</u> , M. Yang, K. H. Kim, K. S. Jang, H. S. Jeon, C. H. Lee, S. H. Hong, H. S. Ahn, S. W. Kim, S. H. Jang, S. M. Lee, G. H. Park, and M. Koike	International Symposium on Physics of Semiconductors and Applications, 제주, 롯데호텔, 2007. 2. 8-9.
24	R-plane 사파이어 기판에 형성된 GaN/InGaN 이중접합구조 형성	전현수, <u>황선령</u> , 김경화, 이충현, 허인혜, 홍상현, 양민, 안형수, 김석환, 진용성, 조인성, 이재학, 시상기	한국물리학회, 평창, 휘닉스파크, 2007. 4. 19-20
25	HVPE 방법에 의해 선택성장된 Si(111) 기판 위의 Lighting Emitting Diode	이충현, <u>황선령</u> , 김경화, 전현수, 허인혜, 홍상현, 안형수, 양민, 김석환, 진용성, 조인성, 이재학, 시상기	한국물리학회, 평창, 휘닉스파크, 2007. 4. 19-20
26	혼합소스 HVPE 방법에 있어 성장시간과 소스량의 변화에 따른 에피특성	허인혜, <u>황선령</u> , 김경화, 전현수, 이충현, 홍상현, 양민, 안형수, 김석환, 진용성, 조인성, 이재학, 시상기	한국물리학회, 평창, 휘닉스파크, 2007. 4. 19-20
27	The Growth of n-, p-type GaN by Mixed-Source HVPE	<u>S. L. Hwang</u> , I. H. Heo, H. S. Jeon, C. H. Lee, S. H. Hong, M. Yang, H. S. Ahn, S. W. Kim, Y. S. Jin, I. S. Cho, W. T. Lim, J. H. Lee, S. K. Shee	한국물리학회, 제주 ICC, 2007. 10. 18-19
28	Wide EL Spectrum Characteristics of White-LED grown By Mixed-Source HVPE	<u>S. L. Hwang</u> , C. H. Lee, H. S. Jeon, S. H. Hong, I. H. Heo, M. Yang, H. S. Ahn, S. W. Kim, Y. S. Jin, I. S. Cho, W. T. Lim, J. H. Lee, S. K. Shee	한국물리학회, 제주ICC, 2007. 10. 18-19
29	HVPE 방법에 의해 성장된 a-	한영훈, 홍상현, <u>황선령</u>	한국물리학회,

	<i>plane GaN 에피층을 이용한 SAG-GaN/AlGaN LED의 특성</i>	전현수, 이충현, 허인혜, 김은주, 양민, 안형수, 김석환, 조인성, 이재학, 시상기	대전컨벤션센터, 2008. 4... 17-18
30	저휘도 구현을 위한 CCFL+LED 액정표시소자	이아름, 정효진, <u>황선령</u> , 전현수, 이충현, 홍상현, 허인혜, 한영훈, 김은주, 양민, 안형수, 김석환, 송장훈, 문근수, 신흥근, 하홍주	한국물리학회, 대전컨벤션센터, 2008. 4... 17-18
31	HVPE Array LED의 성장과 특성	김은주, 전현수, <u>황선령</u> , 이충현, 홍상현, 허인혜, 한영훈, 양민, 안형수, 김석환, 조인성, 임원택, 이재학, 시상기	한국물리학회, 대전컨벤션센터, 2008. 4... 17-18

BIOGRAPHY

Sun-Lyeong Hwang was born on October 31st, in 1964, in Daegu, Korea. In 1983 he began studying physics at Kyungpook National University in Daegu, Korea. On Feb in 1987, he received a Bachelor's degree in physics from Kyungpook National University. After graduating, Hwang joined the army and served as a telecommunication officer for three years. After discharging from military service, he continued to study the compound semiconductor and performed research at the Optoelectronics Lab under the direction of Dr. S. Y. Lee. He received his Master's degree in physics from Kyungpook National University and began working for the industry project.

In 1992, he joined R&D Division of LG Electronics Inc. During his research career as a process engineering of compound semiconductor in LG, he worked on advanced process development for LED and LD technology and performed many projects for multi media applications and industrial applications. In 2000, he moved into Samsung Electronics Inc. In Samsung Telecommunication R&D center, he performed many of optoelectronics project for ultra high-speed network and local area network application. He worked for Samsung to perform project from crystal growth technology over semiconductor package technology as a senior engineer. He had studied overall compound semiconductors such as GaAs, InP and GaN since he was in master's degree course in 1990. He had also worked advanced display project for mobile applications, which were already commercialized. He had many experiences not only in optoelectronics but also telecommunication fields. He was also awarded as high performance researcher from Samsung Electronics. He began his doctoral course in applied sciences at Korea Maritime University in 2005 under the direction of professor H.S Ahn.

Currently, He is working for advanced telecommunication R&D center as a principal engineer in Samsung Electronics.

ACKNOWLEDGEMENTS

I am indebted to a great number of individuals who have helped me along the way and I will now do my best to express my gratitude. I am very appreciating guidance of my advisor, professor Hyung-Soo Ahn. His extensive knowledge, as well as his love of science, makes me truly encourage exceptional mentor. My experiences with him will certainly guide me as I continue along in my career. I share the same sentiments for my co-advisor, professor Sam-Nyeong Lee, Dr. Henry. Ha, professor Min Yang, professor Joon Hwan Shim and Ji-Ho Chang. He has advised in my graduate studies as well, and I owe her a much debt of gratitude.

I would also like to thank the members of my laboratory: Dr. Kyung-Wha Kim, Hunsoo Jeon, Chung-Hyun Lee, Sang-Hyun Hong, In-Hye Heo, Eun-Joo Kim, Young-Hun Han. I am especially indebted to Dr. Kyung-Wha Kim and Hunsoo Jeon as they were my experimental advisor and helped me with draft of some presenting paper. Especially, Mr. Jeon has looked at my work from the point of view and thus has provided some supplement.

They also devoted themselves to helping me the basics of both mixed source hydride vapor phase epitaxy (MS-HVPE) and the gallium nitride material system. Throughout my Ph.D. studies, I worked by day and studied by night. I spent many long hours in the industry R&D laboratory, and have worked long wavelength related project for long times. Therefore their contributions to my work are far too numerous to mention. I'd also like to thank my colleagues in my company. Of course, they didn't support directly but advised sometimes when I need. Many of related friends also gave me vivid industry information.

And finally, I'd like to thank my wife, Mrs. Jung. She had complained a lot for being weekend widow because I studied most of the weekend and holiday to prepare dissertation. I sincerely apologize to her for leaving her alone and giving her burden of taking care of my son and daughter.